

Light Sheet Fluorescence Microscopy for Optical Detection
of Magnetic Resonance using the Nitrogen-Vacancy Defect
in Nanodiamonds within Whole Organisms

PhD Thesis

Petros Hadjichristodoulou

Nanobiophotonics

Department of Physics

University of Strathclyde, Glasgow

September 20, 2024

This thesis is the result of the author's original research. It has been composed by the author and has not been previously submitted for examination which has led to the award of a degree.

The copyright of this thesis belongs to the author under the terms of the United Kingdom Copyright Acts as qualified by University of Strathclyde Regulation 3.50. Due acknowledgement must always be made of the use of any material contained in, or derived from, this thesis.

Abstract

The research motivation for this thesis was the design, construction, and operation of a Light-sheet Fluorescent Microscope (LSFM) that is capable of imaging freely moving whole organisms, performing Optically Detected Magnetic Resonance (ODMR) measurements, and using Adaptive Optics (AO) elements.

The separation of illumination and detection paths in a LSFM allows it to be a highly adaptable microscope. A variety of LSFM designs have been presented in the literature, each designed to fulfill the specific imaging and sample requirements. This work presents an upright dual illumination single detection LSFM design. Two light-sheets are generated via cylindrical lenses, manipulated through a single Spatial Light Modulator (SLM), and are capable of illuminating a large volume, capturing freely moving *Caenorhabditis elegans*, or *C. elegans* at a cellular resolution.

C. elegans was chosen as an imaging sample due to its small size, optical transparency, and well known biology. Therefore, this work emphasised on the characterisation of the LSFM microscope rather than answering a biological question.

Fluorescent Nanodiamonds (FND) with a Nitrogen-Vacancy (NV) defect imaging is presented in this work. FNDs are biocompatible and offer an exceptional stability against photo-generated damage. FNDs imaging paves the way for the investigation of cell and whole organism tracking and identification leading to the examination of further biological processes. Additionally, the NV spin levels can be optically detected, when microwaves are applied, as spin transitions are observed as dips in fluorescence, leading to ODMR measurements. NV properties in combination with ODMR lead to temperature, magnetic field, and electric sensing.

This work demonstrates ODMR measurements using the detection path of the

Chapter 0. Abstract

LSFM with wide-field illumination and LS illumination. ODMR measurements are recorded when a Radio Frequency (RF) signal is applied to a NV centre and control its spin state. The effect of the RF signal power was examined showing a direct correlation of the RF signal power and the ODMR spectrum measurement performance. The effect of a magnetic field was also examined, showing magnetometry capabilities of the LSFM ODMR configuration.

Contents

Abstract	ii
List of Figures	vii
List of Tables	xxix
Acknowledgements	xxxiv
1 Introduction	2
1.1 Motivation	2
1.2 Introduction to Imaging Samples	4
1.3 Thesis Structure	6
2 Theory and Background Information	8
2.1 Optical Microscopy	8
2.2 Resolution	12
2.3 Fluorescence	15
2.4 Imaging Aberrations and Adaptive Optics	17
2.4.1 Introduction to Spatial Light Modulators	20
2.4.2 Deformable Mirror characterisation	23
2.4.3 Shack-Hartmann Wavefront Sensors	24
2.5 Phototoxicity and Photobleaching	25
2.6 Three Dimensional Imaging Principles	25
2.6.1 Confocal Microscopy	26
2.6.2 Spinning Disk Confocal Microscopy	27

Contents

2.7	Light-sheet Fluorescent Microscopy (LSFM)	28
2.7.1	Principles of Operation	28
2.7.2	LSFM FOV Enhancement	36
2.7.3	LSFM Design Configurations	38
2.7.4	LSFM Imaging Speed Improvement	38
2.7.5	LSFM Adaptive Optics Microscopes	41
2.8	Nitrogen-Vacancy Centers in Nanodiamond	42
2.8.1	Structure and Optical Properties	43
2.8.2	Nitrogen-Vacancy Centre in Magnetic Fields	45
2.8.3	Nitrogen-Vacancy sensing	45
2.8.4	Wide-field magnetometry and thermometry	49
2.9	Summary and Discussion	50
3	Light Sheet Fluorescent Microscope Design for Imaging Whole Living Organisms	53
3.1	Mathematical Modelling	54
3.1.1	Illumination Parameters	54
3.1.2	Detection Parameters	55
3.2	Optical Design	56
3.3	CAD Modelling and Mechanical Design	57
3.4	Large FOV Sample Holders Design	59
3.5	Microscope Control Hardware & Software	64
3.6	Summary and Discussion	69
4	Dual Illumination-Single Detection Light Sheet Fluorescent Microscope - Characterisation and Imaging	72
4.1	Imaging Platform	72
4.2	Methodology	74
4.2.1	Adaptive Optics Elements Calibration and Characterisation	74
4.2.2	Microscope Characterisation	78
4.2.3	Nano-Diamonds Imaging	87

Contents

4.2.4	<i>C. elegans</i> Imaging	88
4.3	Results	90
4.3.1	Nano-Diamonds Imaging	90
4.3.2	<i>C. elegans</i> Imaging	100
4.4	Summary and Discussion	106
5	Optically Detected Magnetic Resonance	111
5.1	Optically Detected Magnetic Resonance System Setup	111
5.2	ODMR Spectrum Measurement Technique	113
5.3	Methodology	118
5.3.1	Wide-field ODMR	118
5.3.2	Effect of RF Signal Power in Wide-field ODMR	119
5.3.3	LSFM ODMR	119
5.3.4	Effect of Magnetic field in LSFM ODMR	120
5.3.5	Effect of RF Signal Power in LSFM ODMR	120
5.4	Results	121
5.4.1	Wide-field ODMR	121
5.4.2	Effect of RF Signal Power in Wide-field ODMR	122
5.4.3	LSFM ODMR	125
5.4.4	Effect of Magnetic field on LSFM ODMR	128
5.4.5	Effect of RF Signal Power in LSFM ODMR	128
5.5	Summary and Discussion	130
6	Conclusions	133
6.1	Summary	133
6.2	Limitations	135
6.3	Future work	136
A	Python Coding - LSFM Mode in SLMtools	137
A.1	SLMtools LSFM Window	137
A.2	SLM dll Loading Code	144

Contents

B PrimeBSI Camera Troubleshooting	145
C ODMR Sample Preparation Protocol	147
Bibliography	147

List of Figures

1.1	<i>C. elegans</i> life cycle at 22°C. Fertilisation begins at time equals zero and eggs are laid 150 mins after fertilisation. The arrows indicate the time <i>C. elegans</i> spends at each developmental stage. The length of the animal is shown above each worm at every stage. The figure was extracted from WormAtlas.	5
1.2	<i>C. elegans</i> anatomy A) Anatomical features of a hermaphrodite <i>C. elegans</i> viewed laterally. Nerves (Dorsal Nerve Cord (DNC) and Ventral Nerve Cord (VNC)) and muscles run along the entire body of the <i>C. elegans</i> B) anatomical features of a male <i>C. elegans</i> viewed laterally when muscles and nerves are removed. The pharynx and intestine are shown. C) Cross-section through the anterior region of the <i>C. elegans</i> hermaphrodite. The location of sectioning is shown in a black line and an arrow at A). Epidermis surrounds the muscles enclosing the intestine. The figure was extracted from WormBook.	6

List of Figures

- 2.1 Optical microscopy imaging process. The upwards blue arrow represents the object. o_1 represents the the object point at the focal position of the objective lens while o_2 refers to the off-axis point of the same object. Light emitted by o_1 is represented with the red continuous lines and the light emitted by o_2 is shown as the red dashed lines. The beams emitted from each point of the object are parallel at the optical space between the objective and the tube lens. b_1 and b_2 is the projection of o_1 and o_2 respectively at the back focal plane of the tube lens. f_{obj} and f_{tl} is the focal length of the objective lens and the tube lens respectively. The figure was extracted from the work of K. Ulrich. 10
- 2.2 Resolution resolution criteria for two point sources. a) point sources just resolved according to Rayleigh criterion, b) not resolved point sources, where the two point sources cannot be discriminated c) resolved point sources, separated with a distance greater that the Rayleigh criterion. The figure was extracted from the work of T. Latychevskaia. 13
- 2.3 Representation of light intensity distribution of an illuminated single point near the optical axis. The lateral Airy pattern represents the light distribution at the image plane and the axial Airy pattern represent the distribution of light to a plane perpendicular to the image plane, with its maximum at the centre of the image plane. The figure was extracted from the work of K. Ulrich. 14
- 2.4 Jablonski diagram of a green fluorescent molecule. The upward arrows represent the high energy photons. Returning to the ground state can occur through any of the following ways: the fluorescent molecule will emit fluorescence (downwards arrow), or it can release energy as heat without photon emission (wavy downwards arrow), or it can return to ground state through an excited triplet state by emitting phosphorescence. The figure was extracted from the work of B. J. Thompson. 16

List of Figures

- 2.5 Normalised nitrogen-vacancy centre spectrum for a green wavelength excitation as recorded by S.R Nair et.al. Maximum emission occurs at a wavelength of 700 nm. The zero photon line is visible at 637nm. The excitation band is approximately 150nm. The data were extracted using WebPlotDigitizer. 17
- 2.6 Normalised mCherry fluorophore excitation and emission wavelengths. The absorption spectrum is shown in blue and the emission spectrum in orange. Maximum absorption occurs at 585nm and maximum emission at 609nm. The overlap between the absorption and emission does not affect imaging due to the introduction of optical filters in the detection path. The figure was extracted using data from FP Base related to the work of N. C. Shaner et al. 18
- 2.7 Refractive aberrations of a lens. Light is travelling from left to right in each of the diagrams. a) chromatic aberration describes the effect of rays of different wavelength (colour) focusing at a different point. b) Spherical aberration occurs when rays at the optical axis focus at a different location to rays at the periphery of the lens. c) Coma occurs when off-axis rays passing through the centre of the lens and rays passing through the periphery of the lens are not focused at the same location. d) Astigmatism takes place when rays passing through the vertical diameter and rays passing through the horizontal diameter are not focus at the same point. e) Image distortion is the phenomenon when the image plane is curved and not planar. The figure was extracted from the work of B. J. Thompson. 19
- 2.8 Spatial Light Modulator Structure. Green lines represent a wavefront. Blue arrows point towards the direction of the wavefront. The blue arrows pointing upwards represent the reflected light. The effect of the orientation of the crystal on the input wavefront is shown. The figure was extracted from the data-sheet of Meadowlark Optics. 21

List of Figures

2.9 Spatial Light Modulator Liquid Crystal Orientation. The SLM's coverglass is shown in blue and the liquid crystals in gray. n_e refers to the extraordinary index of refraction and n_o the ordinary index of refraction. a) No voltage is applied, liquid crystal molecules are parallel to the coverglass. Maximum difference between extraordinary and ordinary index of refraction. b) Maximum voltage is applied on the liquid crystals and the molecules are perpendicular to the coverglass. At this stage there is no difference between ordinary and extraordinary index of refraction. The figure was extracted from the data-sheet of Meadowlark Optics. 22

2.10 Deformable mirror feedback control loop (closed-loop configuration). Feedback from wavefront sensor is used to correct imaging aberrations. DM refers to Deformable Mirror and SH-WFS to Shack-Hartmann Wavefront Sensor. The figure was extracted from the work of G. Raju and N. Mazumder. 23

2.11 Shack-Hartmann Wavefront sensor principle of operation. A microlens array divides the wavefront into beams, which are focused on an imaging sensor. The imaging sensor reads the location of the beam. a) The reference beam used to estimate the desired beam location on the imaging sensor. b) distorted beam resulting in different beam locations on the imaging sensor (compared to the reference - shown as ΔX). The figure was extracted from the work of S. Vallmitjana et al. 24

2.12 Optical schematic of a basic confocal microscope. The function of the pinhole is shown with the illumination of the focal plane, the pinhole and the detection plane. The black dashed line represents the excitation beam which is focus on the sample. Only the light emitted at the focal position reaches the detector (green light), while the red dashed (emitted from an adjacent to the focal point position) and blue dashed (emitted from different focal plane) lines, representing light emitted from other position do not reach the detector. The figure was extracted from the work of K. Ulrich. 27

List of Figures

2.13 Spinning disk confocal microscope. a) Representation of a Nipkow disk embedded in a scanning microscope. Excitation and detection happens simultaneously at different regions of the Nipkow disk, b) pinhole structure image when the Nipkow disk is not rotating c) optical schematic of a spinning disk confocal microscope. The excitation beam is shown in gray and the detection path is shown in black. The figure was extracted from the work of K. Ulrich. 29

2.14 Light-sheet Fluorescent Microscope principle of operation. The fluorescent sample is positioned at the focal position of both the illumination and detection objectives. The excitation (shown with the blue arrow) and detection (shown with green arrow) are separated and perpendicular to each other. The light-sheet is shown in blue The area of the sample shown in green is collected by the detection objective. The figure was extracted from the work of O. E. Olarte. 30

2.15 Optical schematic of the two main light-sheet generation microscopes - a static light sheet and a scanned light sheet. The orange beam represents the top view and the blue beam represents the side view. The green beam represents fluorescence. a) a light sheet is generated when a beam with diameter b_d passes through a cylindrical lens. A beam expander (L_{T1} and L_{T2} lenses) adapts the diameter of the beam to b_h and focuses it at the back focal plane of the illumination objective O_{ill} . The detection objective O_{det} collects the excited fluorescence. The excited fluorescence passes through a tube lens, which focuses the excited beam on the camera. b) A light-sheet is generated by rapid scanning of the laser beam along the back focal plane of the L_{T1} lens axis. This way a "virtual" light-sheet is generated at the focal position of the detection objective. The figure was extracted from the work of K. Ulrich. 32

List of Figures

2.16 Illustration of two main types of light-sheets. a) static light sheet (SPIM) created when a laser beam passes through a cylindrical lens, b) virtual light sheet (DSLIM) created by rapidly scanning a laser beam. The figure was extracted from the work of M. Weber and J. Huisken. 33

2.17 Relationship between light-sheet thickness (resolution) and field of view when a light sheet is generated by a Gaussian beam with a diameter D . The thinnest part of the light sheet is $2w_0$. The thickest useful part of the light-sheet is $2 \times \sqrt{2}w_0$ and it is located at a distance Z_r from the centre of the light sheet which is the axial Rayleigh length. The FOV is equal to $2Z_r$. The figure was extracted from the work of O. E. Olarte et al. 33

2.18 Lateral and axial intensity distribution of a light sheet created by a Gaussian beam passing through a cylindrical lens. The large green arrow indicates the Gaussian beam passing through the cylindrical lens. The lateral resolution is marked with the green arrow and the axial resolution is shown with the red arrow, also shown as the Full Width Half Maximum (FWHM) of the Gaussian beam. The figure was extracted from the work of Y. Kim et al. 35

2.19 Light-sheet Fluorescent Microscopy volumetric image formation. Left) moving the sample through a stationary light-sheet, focused by the illumination objective OL_i , and a stationary detection objective (OL_d , b) Scan the light sheet through a stationary sample, while the detection objective follows the light-sheet to remain in focus. The figure was extracted from the work of K. Ulrich. 35

List of Figures

2.20	Light-sheet Fluorescent Microscopy objectives configuration. (a) single illumination single detection SPIM design with a vertical sample (b) Dual illumination single detection Multidirectional selective plane illumination microscopy (mSPIM) design with a vertical sample, (c) Dual illumination dual detection Simultaneous Multi-View selective plane illumination microscopy design with vertically mouted sample, (d) Ultramicroscope design, with a single detection objective in an upright configuration and two cylindrical lenses as illumination objectives. The sample is mounted horizontally, (e) Dual inverted selective plane illumination microscopy (diSPIM) design where the two objectives are used for both illumination and detection. Samples on coverslips are imaged with diSPIM, (f) Reflected light sheet microscopy where a small mirror close to the specimen is used to create an orthogonal light-sheet. The figure was extracted from the work of K. Ulrich	39
2.21	Volumetric imaging process using an ETL in the detection path and a scanning mirror in the illumination path. The figure was extracted from the work of F.O. Fahrbach et al.	40
2.22	a) Nanodiamond crystal lattice with an Nitrogen-Vacancy defect centre. Carbon atoms are represented in grey, the nitrogen atom is in blue and the vacancy in red. b) The coordinate axis of the Nitrogen-Vacancy centre. The z-axis defines the magnetic field sensing measurement axis.	43

List of Figures

2.23 Electronic structure of the Nitrogen-Vacancy centre. $|g\rangle$ represents the ground state, a spin-triplet state with m_s representing the spin projection along z -axis. D shows the zero-field splitting between the ground state sublevels and $m_s = \pm 1$ are degenerate at zero magnetic field (dashed line represents the energy). The solid lines represent the lifting of the degeneracy with the application of a magnetic field along the z -axis. $|e\rangle$ is the excited state (also a triplet) and the singlet state is represented by $|s\rangle$. Green lines represent the excitation with a green laser and the red lines represent the optical relaxation. The figure was extracted from the work of A. J. Tyler. 44

2.24 a) Optically detected magnetic resonance measurement of single Nitrogen-Vacancy centre with no magnetic field applied. When a microwave frequency is applied and shifts the Nitrogen-Vacancy centre from the $m_s=0$ state to the $m_s = \pm 1$, the photoluminescence intensity drops (R_0). C refers to the magnitude for resonance, which is the ratio of the off resonance count rate to the on resonance count rate. b) Zeeman splitting due to a magnetic field B_z that is applied at the z -axis of the NV centre. The two observed resonances correspond to each of the $m_s=0$ to $m_s = \pm 1$ transitions. $\Delta\nu_{NV}$ is used to characterise the resonance. The figure was extracted from the work of A. J. Tyler. 46

2.25 Optically detected magnetic resonance recordings of the Nitrogen-Vacancy centre defect for different local temperature changes. The greater the temperature, the smaller the value of the ground state splitting. The figure was extracted from the work of M. H. Alkahtani et al. 47

List of Figures

2.26	Optically detected magnetic resonance recordings of a single Nitrogen-Vacancy centre defect as the external magnetic field increases. The top represents the higher magnetic field applied while the bottom is the Optically detected magnetic resonance recording when there is no external magnetic field. ω_1 and ω_2 refer to the position of the Optically detected magnetic resonance lines. The figure was extracted from the work of M. H. Alkahtani et al.	48
2.27	Optically detected magnetic resonance recordings of the Nitrogen-Vacancy centre defect when voltage is applied to create an electric field. The voltage is applied on the electrodes of a microstructure on the diamond sample that creates an electric field. The figure was extracted from the work of M. H. Alkahtani et al.	49
3.1	Optical schematic of the adaptive light-sheet fluorescent microscopy microscope. An acousto-optic modulator was used for laser modulation, while a spatial light modulator conjugated with the back focal plane of the cylindrical lens was used for scanning the light-sheet. An upright detection, perpendicular to the light-sheet collects the excited fluorescence and a deformable mirror in combination with a Shack Hartmann wavefront sensor are correcting aberrations. Simultaneously the entire field of view can be imaged by a wide-field camera and illuminated via a white light LED. The figure is a representation of my work conducted in Inkscape using the ComponentLibrary created by A. Franzen.	58
3.2	Customised generic purpose sample holder, fixed on the imaging platform. M3 and M4 holes are used to clamp the sample on the holder. Dimensions of the base are 80 mm x 4 mm x 25 mm (width \times height \times depth) a) and b) are the top view and side view of the fixed generic purpose sample holder.	61
3.3	Generic sample holder mounting platform. M6 holes (red arrows) are used to mount the imaging platform on the z-stage and M3 holes (blue arrows) are used to mount the sample holder on the platform.	61

List of Figures

- 3.4 Microscope slide holder. a) Mounted on the platform, top view, b) Mounted on the platform, side view, c) Slide holder design with dimensions (width \times height \times depth) 80 mm \times 8 mm \times 30 mm. M3 holes are used to mount the holder on the mounting platform. The red arrow shows the direction that the slide is mounted on the holder 62
- 3.5 a) 45° Microscope slide holder with dimensions 60 mm \times 3 mm \times 15 mm (width \times height \times depth). The coverslip is permanently glued on the sample holder. b) Side view of the 45 degrees coverslip holder mounted on the imaging platform. 62
- 3.6 30 degrees angular coverslip holder. a) Permanent coverslip holder, where the coverslip will be glued on the holder. M3 holes are used to mount the holder on the sample platform. The dimensions (width \times height \times depth) of the coverslip holder are 23 mm \times 17 mm \times 33 mm. Side view of the assembled 30 degrees angular coverslip holder. 63
- 3.7 a) Multi-size angular coverslip holder for usage of coverslips with different thickness. Dimensions are 23 mm \times 18 mm \times 23 mm (width \times height \times depth). b) 45 degrees multi-size coverslip mounted on the imaging platform c) A cad model showing the the multi-size angular coverslip holder with a mounted 22mm \times 22mm coverslip. 63
- 3.8 Customised capillary holder design. a) Capillary holder of dimensions 24 mm \times 10 mm \times 24 mm (width \times height \times depth). A cut glass is glued at the sides of the holder to enclose the liquid used to match the refractive index of the capillary. M3 screws are used to mount the holder on the imaging platform b) Side view of the imaging platform with the mounted capillary holder. 64
- 3.9 Customised cuvette holder. a) Cuvette holder with dimensions (width \times height \times depth) 20 mm \times 8 mm \times 61 mm capable of housing cuvettes. M3 holes are used to mount the cuvette holder on the imaging platform b) and c) side view and top view of the cuvette holder mounted on the imaging platform 64

List of Figures

3.10 Customised cuvette designs. a) Used for volumetric imaging. Cut cover-glass pieces are glued in the two slides and on top of the cuvette to seal the sample, b) Cuvette that was used for imaging samples mounted in a capillary. Same sealing procedure is applied to be able to fill the cuvette with liquid matching the refractive index of the capillary. Dimensions for both cuvettes are 12.5 mm x 12.5 mm x 44.5 mm (width × height × depth) which is the same as standardised cuvettes. 65

3.11 a) b) and c) the 30 degrees sample holder, the coverslip holder and the cuvette holder mounted on the z-stage with the sample mounted on the z-stage and on the microscope. d),e) and f) The implementation of the z-stage with the sample attached at the imaging position. 65

3.12 SLMtools software without any adaptations. Geometry: controls the size of the hologram (red square). Pupils allow to increase or reduce the number of pupils in the hologram (blue square). Pupil allows control of the position of the selected pupil and its radius (green square). Zernike aberration window offers control over the aberration via Zernike polynomials (black square). 67

3.13 SLMtools software adapted to light-sheet scanning. Light-sheet control over the start and stop position of the scan as well as the scanning size is achieved through the light-sheet fluorescent microscopy window (black square). There is also the option to move the light-sheet at a selected position. 69

List of Figures

- 4.1 Optical setup of the dual illumination single detection light-sheet fluorescent microscope. A 532 nm laser is expanded (L1 and L2) to 6 mm and then split to create the two imaging paths. Both paths were refracted at the spatial light modulator (L3 and L4 conjugate the back focal plane of the cylindrical lens to the spatial light modulator screen) and pass through the cylindrical lenses to form two light-sheets. The excited fluorescence was collected by the detection objective and focused on a sCMOS camera. The figure is a representation of my work conducted in Inkscape using the ComponentLibrary created by A. Franzen. 73
- 4.2 Optical schematic of the spatial light modulator calibration setup. A 532 nm laser beam was expanded (L1 and L2) so that it covered the spatial light modulator's screen. L3 focused the refracted from the spatial light modulator beam on a photodiode power sensor. The half wave plate was used to achieve the desired polarisation alignment achieved by maximising the laser power at the photodiode. The figure was extracted from the Meadowlark data-sheet and it was created using Inkscape and the ComponentLibrary created by A. Franzen. 76
- 4.3 Normalised intensity of zeroth order diffraction of spatial light modulator with the greyscale patterns projected on the spatial light modulator. One of the stripes' greyscale value is set to 0 and the other varies from 0 to 255. The figure was extracted using data from the SLM calibration software provided by Meadowlark. 77
- 4.4 spatial light modulator look-up table for a 532 nm refraction. The Y-axis represents the phase shift, where 0 is referred to 0π and 1 to 2π . X-axis is the grayscale level applied on the spatial light modulator. The figure was extracted using data from the SLM calibration software provided by Meadowlark. 78

List of Figures

4.5 Optical schematic of the spatial light modulator scanning characterisation setup. L1 and L2 form a beam expander to cover the spatial light modulator’s screen. A halfwave plate ensures that the correct polarisation to achieve maximum refraction is applied, and a tube lens (L3) focuses the refracted beam on an iDS camera. The figure is a representation of my work conducted in Inkscape using the ComponentLibrary created by A. Franzen. 79

4.6 a) b) and c) Hologram projected on the spatial light modulator for a tilt coefficient of 0, 50 and 100 respectively. (d) The image of the diffracted beam for a tilt of 0. (e) The image of the diffracted beam for a tilt of 50. The shift of the 1st order of diffraction is 40 pixels which is translated to $234.4 \mu\text{m}$ and (f) The image of the diffracted beam for a tilt of 100. The shift of the 1st order of diffraction is 78 pixels which is translated to $457.8 \mu\text{m}$. Blue lines indicated the 0th order of diffraction and red lines the 1st order. The red and blue lines are used for representation of the pixel’s translation and they were not used for the extraction of the data plotted in Figure 4.8. 80

4.7 a) b) and c) Hologram projected on the spatial light modulator for a tip coefficient of 0, 50 and 100 respectively. (d) The image of the diffracted beam for a tip of 0. (e) The image of the diffracted beam for a tip of 50. The shift of the 1st order of diffraction is 40 pixels which is translated to $234.4 \mu\text{m}$ and (f) The image of the diffracted beam for a tip of 100. The shift of the 1st order of diffraction is 81 pixels which is translated to $474.5 \mu\text{m}$. Blue lines indicated the 0th order of diffraction and red lines the 1st order. The red and blue lines are used for representation of the pixel’s translation and they were not used for the extraction of the data plotted in Figure 4.8 81

4.8 Tip and tilt scan of the 1st order of refraction. The Zernike mode 1 amplitude varies from 0 to 100 in steps of 10 while the physical movement of the 1st order of refraction is measured. 81

List of Figures

4.9	Lens tissue light sheet illumination imaged with the light-sheet fluorescence microscope. a) A coloured lens tissue is fixed between two coverslips, glued together with nail varnish. b) The coloured lens tissue was imaged at an angle of 45° to image the light-sheet. c) Light-sheet image extracted through the coloured lens tissue.	82
4.10	Wide field, white light illumination of a $10\mu\text{m}$ calibration grid used to measure the field of view of the detection objective, using the light sheet fluorescent microscopy detection path.	83
4.11	a) Optical model of the Light-sheet fluorescent microscopy detection path in raytracing python module. The detection path is modelled with 25mm optics. The black vertical lines represent lenses and the gray and black dots represent apertures. b) Vignetting occurring due to blockers in the path. Red dots represent vignetting and green dots represent transmission. The figure was extracted using the RayTracing python library created by D. Côté.	84
4.12	a) Optical model of the detection path in raytracing python module with 50mm opto-mechanical components b) Vignetting of the imaging path. The figure was extracted using the RayTracing python library created by D. Côté.	84
4.13	a) Optical model of the detection path in raytracing python module with 50 mm opto-mechanical components including the camera's geometry b) Vignetting plot of the imaging path. The figure was extracted using the RayTracing python library created by D. Côté.	85

List of Figures

- 4.14 Fluorescent nanodiamond slide imaging with a 532nm wide-field illumination while the objective is scanning the sample. a) Image of the Nanodiamonds with the objective at the position $-200 \mu\text{m}$ in the z-direction, b) Image of the Nanodiamonds with the objective at the position $-100 \mu\text{m}$ in the z-direction, c) Image of the Nanodiamonds with the objective at the position $0 \mu\text{m}$ in the z-direction, d) Image of the Nanodiamonds with the objective at the position $100 \mu\text{m}$ in the z-direction, e) Image of the Nanodiamonds with the objective at the position $200 \mu\text{m}$ in the z-direction, f) Schematic showing the objective scanning characterisation strategy. The red and blue lines are used for representation of the pixel's translation and they were not used for the extraction of the data plotted in Figure 4.15 86
- 4.15 Light-sheet scanning characterisation in respect to the grating applied on the spatial light modulator. x-axis shows the applied grating and y-axis shows the corresponding light-sheet translation. a) Light sheet scanning of the reference illumination path, b) light-sheet scanning of the 2nd illumination path 87
- 4.16 Cuvette based *C. elegans* sample. The black arrow shows where the coverglass is placed to separate the *C. elegans* (green arrow) from pure agar (shown with the blue arrow). The cuvette's dimension is $12.5\text{mm} \times 12.5\text{mm} \times 45\text{mm}$ 89
- 4.17 Coverslip *C. elegans* sample. A coverglass was used as a base where a single worm or a small block of agar with *C. elegans* was placed on it. On top of the sample I add a drop of immersion oil and then the sample was sealed with a round coverslip and nail varnish. 90
- 4.18 3D image of 90nm nanodiamonds at a FOV of $1.5 \text{ mm} \times 1.55 \text{ mm}$ and a depth of $900 \mu\text{m}$ imaged using the light-sheet fluorescent microscope with single light-sheet illumination. The scanning step was $3 \mu\text{m}$. The grid is on 15micron scale for the x and y axes and $10 \mu\text{m}$ for the z-axis. 91

List of Figures

4.19	Plane images of nanodiamonds at depths of a) 135 μm , b) 465 μm and c)765 μm from the 900 μm scan. Aberrations at the edge of the field of view are observed within the entire sample depth.	92
4.20	Separation of the FOV into two regions (A and B, yellow circles) and four sub-regions (1, 2, 3, and 4, separated by the two red lines) to investigate the axial and lateral resolution within the entire field of view.	93
4.21	Axial resolutions of the light-sheet fluorescence microscopy at different depths with the reference arm light-sheet illumination imaging 90 nm fluorescent nanodiamonds. a) c), and d) Axial resolution for region A captured through a 300 μm (at depths of 45, 150, and 255 μm), 600 μm (at depths of 90, 300, and 510 μm), and 900 μm (at depths of 135, 450, and 765 μm) scans respectively. b), d), and f) Axial resolution for region B captured through a 300 μm (at depths of 45, 150, and 255 μm), 600 μm (at depths of 90, 300, and 510 μm), and 900 μm (at depths of 135, 450, and 765 μm) scans respectively.	94
4.22	Lateral resolutions of the light-sheet fluorescence microscopy at different depths with the reference arm light-sheet illumination imaging 90 nm fluorescent nanodiamonds.a) Lateral resolution of region A for a 300, 600 and 900 μm scan. b) Lateral resolution of region B for a 300, 600 and 900 μm scan.	95
4.23	Axial resolutions of the light-sheet fluorescence microscopy at different depths with the second arm light-sheet illumination imaging 90 nm fluorescent nanodiamonds. a) c), and d) Axial resolution for region A captured through a 300 μm (at depths of 45, 150, and 255 μm), 600 μm (at depths of 90, 300, and 510 μm), and 900 μm (at depths of 135, 450, and 765 μm) scans respectively. b), d), and f) Axial resolution for region B captured through a 300 μm (at depths of 45, 150, and 255 μm), 600 μm (at depths of 90, 300, and 510 μm), and 900 μm (at depths of 135, 450, and 765 μm) scans respectively.. . . .	96

List of Figures

4.24	Lateral resolutions of the light-sheet fluorescent microscopy at different depths with the second arm light-sheet illumination imaging 90 nm fluorescent nanodiamonds. a) Lateral resolution of region A for a 300, 600 and 900 μm scan. b) Lateral resolution of region B for a 300, 600 and 900 μm scan.	97
4.25	Division of the FOV in seven regions of interest to investigate the light-sheet thickness along the entire field of view.	98
4.26	a) Reference illumination arm and b) second illumination arm light-sheet thickness along the entire field of view of the light-sheet fluorescent microscope.	98
4.27	Dual illumination image acquisition using the light-sheet fluorescent microscope. Images in white refer to the images obtained when the light-sheet from path 1 is used for illumination, while green images represent images obtained with illumination from path 2.	99
4.28	Design of Plossl eyepiece. Two achromatic doublets are placed symmetrically with a small gap between them. The light is travelling from left to right.	100
4.29	a) Plossl lens focusing the image on the camera with the square grid at 1250 μm . b) Single lens focusing the image on the camera with the square grid at 1250 μm . The red and blue lines are used for representation of the field curvature measurement strategy and they were not used for the extraction of the data plotted in Figure 4.30	100
4.30	Comparison of a single lens and Plossl lens imaging along the field of view imaged using the detection path of the light-sheet fluorescent microscope.	101
4.31	Focal plane of <i>C. elegans</i> , strain xe1995, in agar imaged with the custom made light-sheet fluorescent microscope. The arrows point to the head, pharynx, terminal bulb, intestine and nerve ring of the worm.	102

List of Figures

- 4.32 *C. Elegans*, strain xe1995, imaged on a coverslip with water using the light-sheet fluorescent microscope. A young adult and an L2/L3 larvae are shown. The head and the nerve ring are shown with blue arrows. Embryos in the young adult are imaged and shown within the red square. 103
- 4.33 Optical section of a lx1960 strain *C.elegans* imaged on a coverslip with immersion oil using the light-sheet fluorescent microscope. The Figure was cropped so that only the nematode under investigation is shown. . . 104
- 4.34 Volumetric imaging of lx1960 strain *C.elegans* on a coverslip with a drop of immersion oil using the light-sheet fluorescent microscope. Grid size in x-direction is 145 μm , in the y-direction 160 μm and in the z-direction 65 μm 105
- 4.35 Freely moving xe1995 *C. elegans* imaging on a coverslip with immersion oil. Time duration of imaging sequence from the image a) to j) is 1 second. ai) to ji) is the same imaging sequence zoomed in on the moving *C. elegans* (red arrow). Time points = 100ms. 107
- 5.1 Optically detected magnetic resonance setup for wide-field and light-sheet fluorescence microscopy optically detected magnetic resonance measurements. 112
- 5.2 Wide-field Optically detected magnetic resonance sample. The nanodiamond sample is in the middle of the round coverslip enclosed with with nail varnish. A thin wire crosses the sample to deliver the RF signal to the nanodiamond sample. 113
- 5.3 Schematic of the wide-field optically detected magnetic resonance sample at the imaging plane of the light-sheet fluorescent microscope. A 532 nm 5 mW laser focused on the sample, through a 50 mm lens, illuminates the nanodiamond sample. The imaging path is the same as the detection path of the light-sheet fluorescent microscope described in Chapter 4. A 600 nm long pass filter is used in the imaging path. 114

List of Figures

- 5.4 Light-sheet fluorescent microscopy optically detected magnetic resonance sample. The same PCB used in the wide-field optically detected magnetic resonance is cut in half to set the nanodiamonds at a 45 degrees angle, required for light-sheet fluorescent microscopy illumination 115
- 5.5 Schematic of the light-sheet fluorescent microscopy optically detected magnetic resonance sample at the imaging plane of the light-sheet fluorescent microscope. The light-sheet fluorescent microscope's illumination path is used for the light-sheet illumination of the optically detected magnetic resonance sample. The imaging path is the same as the detection path of the light-sheet fluorescent microscope described in Chapter 4. A 600nm long-pass filter is used in the imaging path. 116
- 5.6 Wide-field optically detected magnetic resonance data. The red marks represent the fluorescence measurement and the continuous line represents the Lorentzian fit. Contrast is defined as the magnitude of the dip in the measured fluorescence. a) The sequence of optically detected magnetic resonance recording FND images for different applied RF signals. Regions where optically detected magnetic resonance data are extracted are shown. b) Entire field of view optically detected magnetic resonance. Contrast = 0.009 and $R^2 = 0.99$. c) optically detected magnetic resonance extracted from the blue region of interest. Contrast = 0.007 and $R^2 = 0.91$. d) optically detected magnetic resonance extracted from the yellow region of interest. Contrast = 0.0069 and $R^2 = 0.94$. e) optically detected magnetic resonance extracted from a single cluster of nanodiamonds, red circle. Contrast = 0.012 and $R^2 = 0.63$ 123
- 5.7 Effect of RF Sweeping frequency power on the wide-field optically detected magnetic resonance spectrum recording. x-axis indicates the power of the RF signal in dBm and the y-axis shows the normalised to one amplitude of the ODMR dip. Blue dots represent the measured data and the orange line represents a linear fit with $R^2=0.981$ 124

List of Figures

5.8 Wide-field optically detected magnetic resonance with different RF sweeping frequency power. The red marks represent the measured data points and the continuous line represents the Lorentzian fit. a) Entire field of view optically detected magnetic resonance with maximum RF power (6 dBm). The contrast of the ODMR spectrum is 0.008 and $R^2 = 0.99$. b) Entire field of view optically detected magnetic resonance with a power of (-14 dBm). The contrast of the ODMR spectrum is 0.0045 and $R^2 = 0.99$ 125

5.9 Light sheet fluorescent microscopy optically detected magnetic resonance recorded. The red marks represent the measured data points and the continuous line represents the Lorentzian fit. a) The sequence of ODMR recording nanodiamond images for different applied RF signals. Regions where optically detected magnetic resonance spectra were extracted are shown. b) Entire light-sheet optically detected magnetic resonance spectrum. Contrast = 0.01 and $R^2 = 0.99$. c) Top light-sheet region optically detected magnetic resonance spectrum (yellow region of interest). Contrast = 0.008 and $R^2 = 0.99$. d) Middle light-sheet region optically detected magnetic resonance spectrum (green region of interest). Contrast = 0.011 and $R^2 = 0.99$. e) bottom light-sheet region optically detected magnetic resonance spectrum (blue region of interest). Contrast=0.013 and $R^2 = 0.99$. f) Single nanodiamond cluster, red circle). Contrast = 0.012 and $R^2 = 0.98$ 127

List of Figures

5.10 Effect of a magnetic field on the Light sheet fluorescent microscopy optically detected magnetic resonance measurements. The red marks represent the measured data points and the continuous line represents the Lorentzian fit. a) The experimental methods for the examination of the effect of a magnet on optically detected magnetic resonance recordings, b) Magnet at a distance of 50 mm away from the sample. The contrast of the ODMR spectrum is 0.011 and $R^2 = 0.98$. c) Magnet 20 mm away from the sample. The contrast of the ODMR spectrum is 0.011 and $R^2 = 0.97$. d) Magnet at 5 mm away from the sample. The contrast of the ODMR spectrum is 0.008 and $R^2 = 0.94$ 129

5.11 Effect of RF Sweeping frequency power on the light-sheet fluorescent microscope optically detected magnetic resonance spectrum recording. x-axis indicates the power of the RF signal in dBm and the y-axis shows the normalised magnitude of the optically detected magnetic resonance dip. Blue dots represent the measured data, and the orange continuous line is the linear fit, $R^2 = 0.985$ 130

5.12 Light sheet fluorescent microscopy optically detected magnetic resonance with different RF sweeping frequency power. The red marks represent the measured data points and the continuous line represents the Lorentzian fit. a) Entire field of view optically detected magnetic resonance with RF power of 1 dBm. The contrast of the ODMR spectrum is 0.01 and $R^2 = 0.99$. b) Entire field of view optically detected magnetic resonance with a power of -29 dBm. The contrast of the ODMR spectrum is 0.017 and $R^2 = 0.98$ 131

B.1 The red dashed line shows the end exposure of the first row, triggering that the camera is ready to move to the next read. The gray dashed line represents the start of the trigger in, that triggers that the camera is ready for the next acquisition, and the green line shows the start of the next acquisition. a) First Row Mode. b) Any Row Mode. The figure was extracted using data from the Prime BSI manual [1]. 146

List of Tables

2.1	Summary of light-sheet fluorescent microscopy configurations listing their field of view and some of their biological applications.	40
3.1	The microscope control hardware. The camera, spatial light modulator, the analog input device, the computer, and the objective scanning stage are listed along with their specifications.	66
4.1	Summary of the axial and lateral resolutions of the light-sheet fluorescent microscope for 300 (μm), 600 (μm), and 900 (μm) scans for both illumination arms	109
5.1	ODMR data processing protocol using ImageJ	118
C.1	Fluorescent nanodiamond sample preparation procedure for ODMR measurements.	147

List of Tables

Acronyms

C. elegans *Caenorhabditis elegans*. 4

2D Two-Dimensional. 68

3D Three-Dimensional. 26

AC Alternating Current. 21

AO Adaptive Optics. 5, 20

BFP Back Focal Plane. 31

BS Beam Splitter. 74

CCD Charged-Coupled Device. 9

CGC *Caenorhabditis* Genetics Center. 88

CL Cylindrical Lens. 54

CMOS Complementary Metal Oxide Semiconductor. 9

CMS Corrected Multi-Sampling mode. 145

CPU Central Processing Unit. 66

CW Continuous Wave. 51

DAQ Data Acquisition. 66

DM Deformable mirrors. 23

Acronyms

DNC Dorsal Nerve Cord. 4

DOF Depth of Field. 13

DSLM Digitally Scanned Laser Light-sheet Microscopy. 31

FND Fluorescent Nanodiamonds. 3

FOV Field of View. 9

GPU Graphics Processing Unit. 66

GUI Graphical User Interface. 66

HDMI High-Definition Multimedia Interface. 68

LB Lysogeny Broth. 103

LED Light-Emitting Diode. 74

LS Light-Sheet. 31

LSFM Light-sheet Fluorescent Microscopy. 2

LUT Look-up Table. 75

mSPIM multi-directional Selective Plane Illumination Microscopy. 36

NA Numerical Aperture. 11

NI National Instruments. 68

NV Nitrogen-Vacancy. 3

ODMR Optically Detected Magnetic Resonance. 3

RAM Random-Access Memory. 66

RF Radio Frequency. 111

Acronyms

S-H WFS Shack-Hartmann Wavefront Sensor. 23

SIM Structured Illumination Microscopy. 26

SLM Spatial Light Modulator. 20

SNR Signal to Noise Ratio. 37

SPIM Selective Plane Illumination Microscopy. 31

STED Stimulated Emission Depletion. 26

TTL Transistor-Transistor-Logic. 117

VNC Ventral Nerve Cord. 4

Acknowledgements

Working for four years towards the completion of my PhD was a life changing experience. I believe it made me a better person both in my personal and professional life.

I wouldn't be able to go through this exceptional experience without my supervisor Dr. Brian Patton. I would initially like to thank you for giving me the opportunity to work on this project. Your guidance and advice helped me through every stage of my project and also helped me develop as a scientist. I knew I can rely on your advice from the initial steps of my project until the last day of my thesis writing.

I would also like to thank Dr. Graeme Johnstone for all the guidance over the initial phase of my project and always willing to help when asked. To my second supervisor, Professor Gail McConnell, I am thankful for reading my work and I appreciate all your comments and suggestions.

My warmest thanks to the NanBioPhotonics research group. I enjoyed working with you and I learned so many things from all of you. Thank you for your help and support.

Finally, I would like to give a special thanks my family for their understanding any support during all phases of my PhD and thank you for motivating me to complete this thesis writing.

Στους Νεφέλη και Παναγιώτη

Chapter 0. Acknowledgements

Chapter 1

Introduction

1.1 Motivation

By allowing us to look inside tissues and see the processes at work in individual cells, microscopy has long proved to be a powerful tool for biological research. Applying the advances in microscopy to whole animal imaging at cellular and sub-cellular resolution assists the ongoing research in understanding myriad biological processes and it will advance biological research [2,3]. Although whole *Drosophila* and *C. elegans* embryos have been imaged, it is very challenging to image freely moving whole organisms at such an imaging speed that motion artifacts do not appear. Increases in imaging speed, as well as total volume imaged, enables the investigation of organisms while they explore their environment, and the imaging of their interaction in a cellular and sub-cellular level [4] enables further investigation of neural activity [5]. Therefore, in this thesis I present my work on the design, construction and operation of a cellular resolution, optically sectioning, imaging system with a millimetric field of view, capable of imaging whole organisms. Although commercial millimetric Light-Sheet Fluorescent Microscopes (LSFM) (such as the ZEISS Lightsheet 7 [6]) exist, a custom made LSFM allowed me to design and build a microscope taking into consideration the sample that is going to be imaged and the specific requirements of optical-based sensing with nitrogen vacancy centres in diamond. A custom made microscope would also allow future adaptation such as introducing multiple illumination wavelengths, and relevantly easy,

Chapter 1. Introduction

replacing the detection sensor and tube lens. Therefore, a custom made microscope could follow technological advances (better sensors, objectives etc.). My “open” LSFM design allowed me to embed an Optically Detected Magnetic Resonance (ODMR) setup and perform LSFM ODMR measurements, which is reported for the first time in my work.

Combining the large volume imaging with imaging nanoscopic particles of diamond, Fluorescent Nanodiamonds (FND), paves the way to investigate further biological processes, such as long term tracking of specific features in individual cells and even whole freely moving organisms. This can be achieved because fluorescent nanodiamonds are exceptionally stable against both chemical and photo-generated damage and can remain in place in organisms without causing physiological damage [7], while being photostable with a bright colour centre. Nitrogen-Vacancy (NV) is the most studied type of fluorescent diamond centres because of their photophysical properties. The NV spin sublevels can be optically detected, with the simultaneous application of appropriate microwaves, with a technique known as ODMR, where spin transitions can be observed as dips in the fluorescence. Taking advantage of NV nanodiamond properties in combination with ODMR measurements, sensing of magnetic field, electric field and temperature can be conducted. Using the magnetic sensing and spin properties of the nitrogen-vacancy the location of the NV nanodiamond can be measured. Therefore, FNDs can be used to obtain more information when tracking cells and/or whole organisms. Consequently, embedding FND in cells and/or whole organisms can be used for *in vivo* sensing and thus pave the way for multiple biological applications [7–10]. Therefore, an ODMR measurement system is included in the microscope design.

I designed a microscope to image an organism that is biologically simple, widely researched and well known. Since this project is centered on the design and implementation of the microscope hardware, and since the Covid pandemic also had a significant impact, the image processing will be focused on the characterisation of the microscope, rather than a specific biological question. At the outset of the project there were already some protocols for labelling samples with nanodiamond [11] and more have emerged recently [12]. There is significant promise for *in vivo* nanodiamond imaging and ide-

ally *in vivo* sensing can be investigated. Hence I designed, constructed and operated a system that can achieve FND imaging, ODMR measurement and whole organism imaging; therefore, it should be capable of performing *in vivo* sensing and cell/whole organism tracking.

1.2 Introduction to Imaging Samples

Caenorhabditis elegans, or *C. elegans*, is chosen as an imaging sample. *C. elegans* is a transparent small roundworm that survives by consuming microbes, primarily bacteria. It has been widely used in biological research due to its small size, ease of propagation, stereotypical development and short life cycle. [13]. *C. elegans* has a cylindrical body, 1 mm long, with a diameter of 80 μm , and its cell diameter varies from 3 μm to 30 μm . Its life cycle is 14 to 21 days [13,14] and its speed of locomotion has been found to be within the range of 0.25-0.5 mm/s (it reduces as the animal is aging) [15]. The life cycle of *C. elegans* is shown in Figure 1.1, where the name of each stage along with its physical length and the time spent at that stage are shown. The anatomy of *C. elegans* is shown in Figure 1.2 where it is shown that despite its simplicity, hermaphrodites (Figure 1.2A) and males (Figure 1.2B) can be distinguished by the presence or absence of embryos. Figure 1.2A illustrates the Dorsal Nerve Cord (DNC) and the Ventral Nerve Cord (VNC) that runs along the entire worm, starting from the nerve ring. In Figure 1.2B, the nervous system and muscles are not illustrated, so that we have a clearer view on the pharynx and intestine. Examining the cross section of the *C. elegans* we can see that the cells at the outer layer form the epidermis, which surrounds the four muscle quadrants. The intestine and gonad are housed within the pseudocoelomic cavity. Ideally, the imaged cells within the whole organism of investigation are identified [17].

An imaging technique that is based on optically sectioning imaging with a wide field of view is LSFM. A LSFM that can image *C. elegans* and FNDs paves the way in imaging freely moving whole organisms within their environment. Additionally, LSFM ODMR measurements enables *in vivo* sensing of temperature, magnetic and electric field. Although a system that records ODMR measurements through light-sheet illumination has been reported [18,19], a LSFM ODMR has not been reported

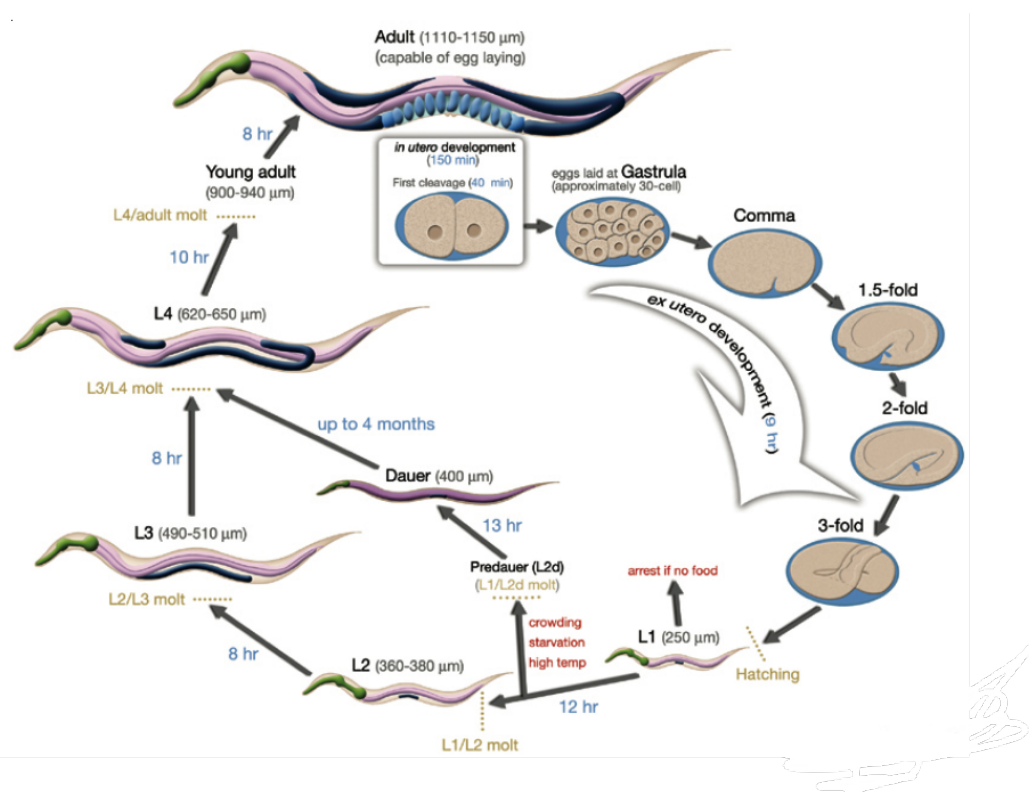


Figure 1.1: *C. elegans* life cycle at 22°C. Fertilisation begins at time equals zero and eggs are laid 150 mins after fertilisation. The arrows indicate the time *C. elegans* spends at each developmental stage. The length of the animal is shown above each worm at every stage. The figure was extracted from WormAtlas [16].

yet. Imaging FNDs also enables the identification and tracking of a single cell or organism [20–22]. One of the initial goals for this project, that got changed due to the impact of the pandemic, was to implement pattern recognition algorithms to images of organisms or cells that have been micro-injected with FND, thereby enabling long term tracking and identification of single cells within an organism or ensemble of cells.

When imaging in biological systems, the sample itself will introduce optical aberrations to the image that reduce the effectiveness of the microscope. A method to overcome such aberrations is Adaptive Optics (AO). Successful AO correction in a LSFM ODMR setup can improve fluorescence detection and thus provide more accurate ODMR measurements. This results in more accurate and precise temperature, magnetic field and electric field sensing as well as improving the LSFM imaging quality [23]. Therefore, adaptive optics elements were used in my design.

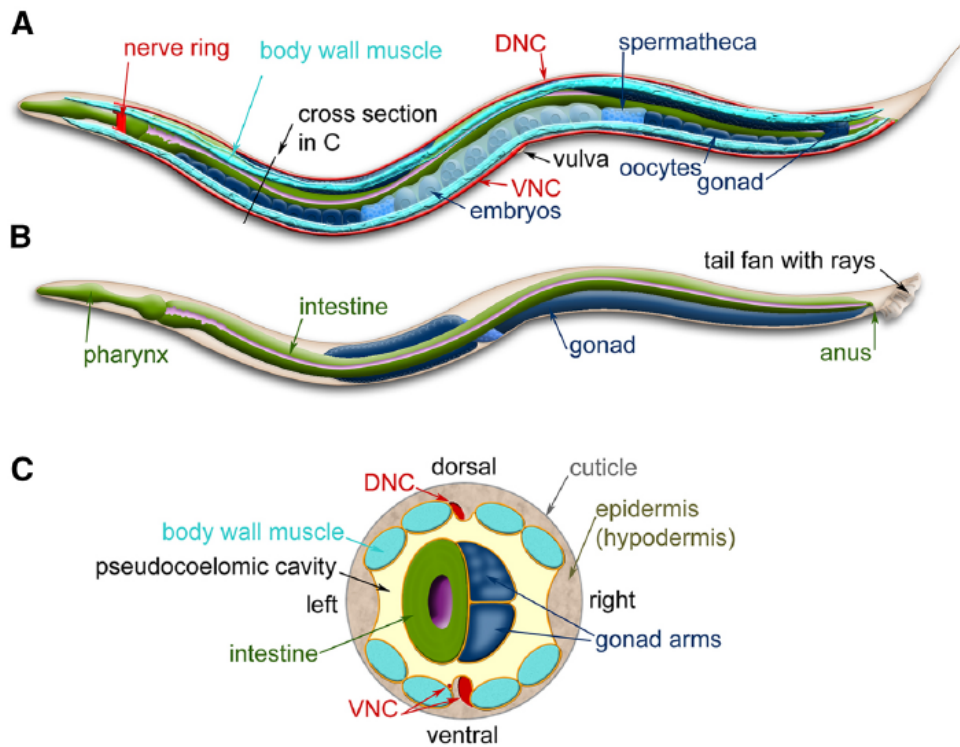


Figure 1.2: *C. elegans* anatomy A) Anatomical features of a hermaphrodite *C. elegans* viewed laterally. Nerves (Dorsal Nerve Cord (DNC) and Ventral Nerve Cord (VNC)) and muscles run along the entire body of the *C. elegans* B) anatomical features of a male *C. elegans* viewed laterally when muscles and nerves are removed. The pharynx and intestine are shown. C) Cross-section through the anterior region of the *C. elegans* hermaphrodite. The location of sectioning is shown in a black line and an arrow at A). Epidermis surrounds the muscles enclosing the intestine. The figure was extracted from WormBook [17].

1.3 Thesis Structure

In this thesis I demonstrate ways to design, construct, characterise and operate a light-sheet fluorescent microscope that incorporates adaptive optics technologies to image through living tissue. I developed a LSFM that extract volumetric datasets of FNDs and freely moving whole organisms and I have developed an ODMR measurement setup that conducts wide-field and LSFM measurements.

My work is divided into three categories: the theoretical background, the experimental setup and results, and the conclusions. The fundamental principles required for the conduction of the project are presented in Chapters 2. Chapter 2 describes

Chapter 1. Introduction

concepts of fluorescent microscopy, volumetric imaging and adaptive optics techniques. Additionally in Chapter 2 the up to date light-sheet fluorescent microscopes in the literature are investigated from an imaging volume and speed viewpoint and presents an introduction into Nitrogen-vacancy.

The experimental setup and results are examined in Chapters 3, 4, and 5. In Chapter 3, I present the design and development of a dual illumination single detection light sheet fluorescent microscope in which the excitation and detection beam paths both incorporate adaptive elements. The characterisation of my system and imaging of nanodiamonds and whole freely moving organisms is presented in Chapter 4. Chapter 5 describes the optically detected magnetic resonance measurement setup and presents wide-field and light sheet ODMR spectra recorded using my system.

The last part is conclusions: In Chapter 6, the achievements of the thesis are summarised. In the future work section, work that could be done in the future that could improve the imaging quality, as well provide additional useful information for further biological research is presented.

Chapter 2

Theory and Background Information

In this chapter the fundamental concepts of fluorescence microscopy are presented. Initially, the geometrical optics required for the understanding of light microscope construction are described. Volumetric imaging techniques, including their capabilities and limitations, are then presented, with an emphasis in LSFM. Additionally, LSFM imaging techniques are reviewed. LSFM imaging techniques are investigated regarding their imaging volume and their imaging speed. Adaptive optics techniques applied on a LSFM microscope to improve imaging quality were also considered.

The theoretical background explained in this chapter is necessary for the design and construction of a LSFM capable of imaging whole living organisms in cellular resolution, with a millimetre-scale FOV. The required information for the implementation of an ODMR spectrum measurement setup on the LSFM microscope is also explained in this Chapter.

2.1 Optical Microscopy

A light microscope consists of two sets of components that constitute the illumination and the imaging paths. The simplest form of a light microscope imaging sub-system can be created by two lenses; the objective lens and the tube lens. The objective lens

produces an image of the object at infinity (for an infinity corrected lens), while the tube lens focuses the image into the primary image plane. The specimen is located at the front focal plane of the objective lens. This configuration is shown in Figure 2.1. The objective lens transforms the light emitted from the object's on axis point o_1 into a set of light beams travelling parallel to the optical axis. The tube lens focuses the light on the detector (typically a Charged-Coupled Device (CCD) or Complementary Metal Oxide Semiconductor (CMOS) device in modern microscopes) or imaging plane for the eyepiece. On the other hand, light emitted from the point o_2 creates two additional beams, the central ray rc and the parallel ray rp . The o_2 point is projected on the primary image plane, in the back focal plane of the tube lens, at the point b_2 , which is the intersection of the rc' and rp' beams. The space between the objective lens and the tube lens is called infinity space and it is where all beams emitted from each point of the object are parallel to each other.

As observed, the size of the elements impact the achievable the Field of View (FOV). Modelling of the imaging path can enable an estimate of the size of the beam along the whole imaging path and thus enable proper selection of elements and elements' positioning to avoid vignetting [25]

Raytracing [25,26], a Python library, was used to model optical systems in my work (the simulations are shown in Section 4.2.2). Raytracing module, an optical system modelling module, is based on the ray matrix formalism (ABCD matrices). Through the ABCD matrices the effect of finite-sized lenses and apertures can be estimated. [25]. In the ray matrix formalism, each ray along the optical path is described as

$$r = \begin{bmatrix} y \\ \theta \end{bmatrix} \quad (2.1)$$

where y refers to the height of the ray with respect to the optical axis and θ refers to the angle the ray makes with the optical axis. Each optical element is described as

$$M = \begin{bmatrix} A & B \\ C & D \end{bmatrix} \quad (2.2)$$

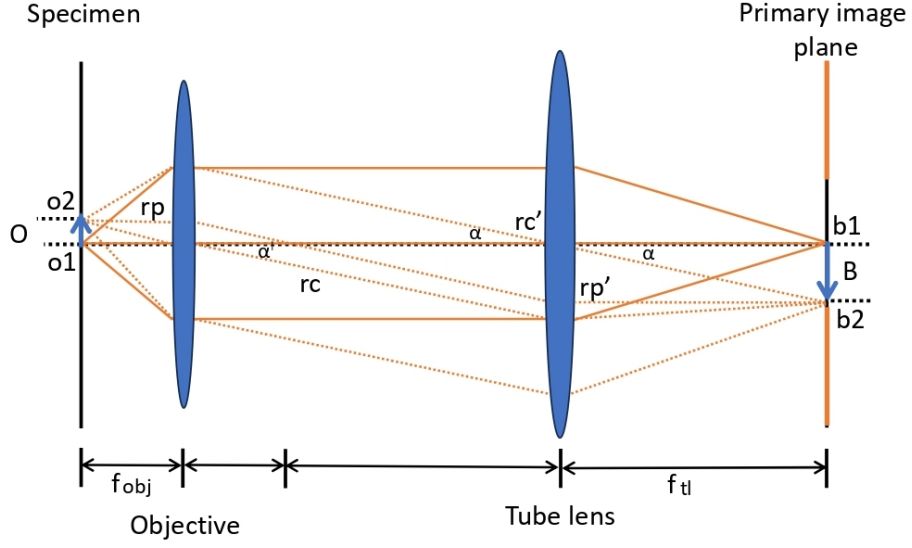


Figure 2.1: Optical microscopy imaging process. The upwards blue arrow represents the object. o_1 represents the the object point at the focal position of the objective lens while o_2 refers to the off-axis point of the same object. Light emitted by o_1 is represented with the red continuous lines and the light emitted by o_2 is shown as the red dashed lines. The beams emitted from each point of the object are parallel at the optical space between the objective and the tube lens. b_1 and b_2 is the projection of o_1 and o_2 respectively at the back focal plane of the tube lens. f_{obj} and f_{tl} is the focal length of the objective lens and the tube lens respectively. The figure was extracted from the work of K. Ulrich [24].

A ray r will be transformed into r' after passing through an optical element (or a series of optical elements). When ray r passes through a series of optical elements,

$$r' = M_i, \dots M_3 M_2 M_1 r = M_r \quad (2.3)$$

Therefore,

$$y' = Ay + B\theta \quad (2.4)$$

$$\theta' = Cy + D\theta \quad (2.5)$$

Each optical element is represented by a 2×2 matrix. For my model only propagation through free space and transmission through thin lens were used; Therefore, free space

propagation at a distance d is represented as $\begin{bmatrix} 1 & d \\ 0 & 1 \end{bmatrix}$, while the transmission through a thin lens with a focal length f is represented as $\begin{bmatrix} 1 & 0 \\ -1/f & 1 \end{bmatrix}$. Additionally, the raytracing module allows the placement of apertures which block rays outside their diameter. By having appropriate size apertures coincide with our mirrors, we are also able to check for mirror clipping.

The magnification M of a light microscope is defined as

$$M = B/O \quad (2.6)$$

where, O is the distance between o_1 and o_2 and B is the distance between between the equivalent imaged points b_1 and b_2 . From Figure 2.1 it can be seen that

$$\tan \alpha = O/f_{obj} = B/f_{tl} \quad (2.7)$$

where, f_{obj} is the focal length of the objective lens and f_{tl} is the focal length of the tube lens. Therefore the magnification of a two lens system can be defined as

$$M = f_{tl}/f_{obj}. \quad (2.8)$$

The main objective lens characteristics, that have a crucial role in the design of an optical microscope, are the angular aperture, the field number and the focal length of the objective. Angular aperture is the total angular opening of the objective, which is the maximum angle at which the objective lens can collect light emitted from the object. The half of the angular aperture, α , is used to define the Numerical Aperture (NA) of the objective, which is expressed as

$$NA = n \sin a \quad (2.9)$$

where, n is the refractive index of the medium between the lens and the object. On the other hand, the field number of the objective refers to the diameter, in millimeters, of

the aperture called field stop. The field stop is used to cut the peripheral regions with low field performance. The field number and the magnification are used to define the FOV of the objective at the sample as

$$FOV = s/M_{obj} \quad (2.10)$$

where s is the field number of the objective and M_{obj} its magnification [24]. Obtaining all the above information regarding an objective is crucial for the selection of the most suitable detection objective for a microscope since it will establish the FOV and resolution of the microscope.

2.2 Resolution

Two objects can be resolved when they can be discriminated from each other [24]. According to the Rayleigh criterion, two point sources are regarded as just resolved when the zero-order diffraction maximum of one diffraction pattern coincides with the first minimum of the other. For a distance between the zero-order diffraction maxima of two diffraction patterns less than the Rayleigh distance, we consider the two point sources as not resolved. Two source points are considered completely resolved when the distance between the zero-order diffraction maximum of the one diffraction pattern coincides with the first-order diffraction maximum of the other, as shown in Figure 2.2 [27].

The image of a source point corresponds to the intensity distribution I_r , which is described by the Airy function that can be expressed as

$$I(r) = I_0 \left[\frac{J_1\left(\frac{2\pi r \sin \alpha}{\lambda}\right)}{\frac{2\pi r \sin \alpha}{\lambda}} \right]^2 \quad (2.11)$$

where J_1 is a Bessel function of the first order and α is the half opening angle of the objective. By applying the Rayleigh criterion to two point sources with such intensity distribution and knowing that the zero crossing of the Bessel function $J_1(x)$ is at $x=3.83$,

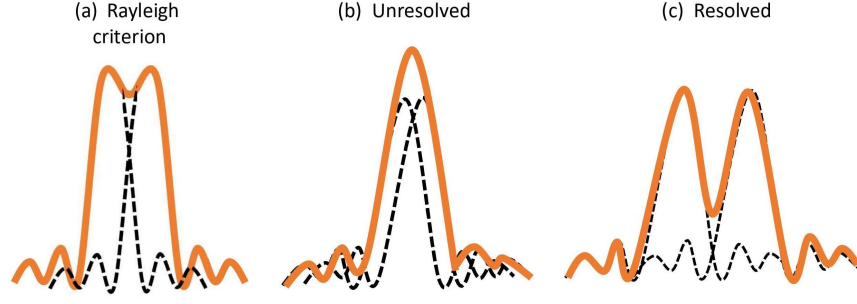


Figure 2.2: Resolution resolution criteria for two point sources. a) point sources just resolved according to Rayleigh criterion, b) not resolved point sources, where the two point sources cannot be discriminated c) resolved point sources, separated with a distance greater that the Rayleigh criterion. The figure was extracted from the work of T. Latychevskaia [27].

the Rayleigh range and thus the lateral resolution can be expressed as

$$r_{lateral} = \frac{0.61n\lambda}{NA} \quad (2.12)$$

The Rayleigh criterion can be proved by solving the Bessel function for $x=3.83$ as

$$\frac{2\pi r \sin \alpha}{\lambda} = 3.85 \Rightarrow r = \frac{3.85\lambda}{2\pi \sin \alpha} = \frac{0.61\lambda}{NA} \quad (2.13)$$

The axial intensity distribution of a point source is described by the sinc function. Applying the Rayleigh criterion to two source points with such intensity distribution the axial resolution is expressed as [24]

$$r_{axial} = \frac{2n\lambda}{NA^2} \quad (2.14)$$

The depth of view refers to the vertical distance that the object stage with a point source must be moved so that the image shifts from the central intensity maximum to its first minimum. Therefore the Depth of Field (DOF) can be defined as

$$DOF = 2r_{axial} \quad (2.15)$$

A representation of lateral and axial light distribution is shown in Figure 2.3 [24, 28]

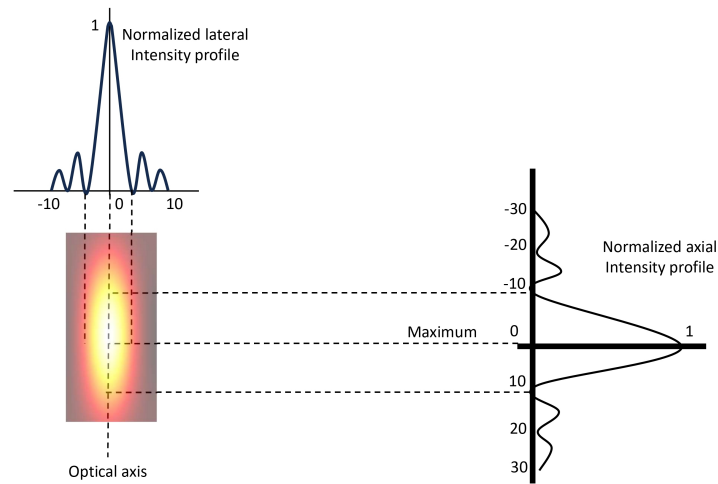


Figure 2.3: Representation of light intensity distribution of an illuminated single point near the optical axis. The lateral Airy pattern represents the light distribution at the image plane and the axial Airy pattern represent the distribution of light to a plane perpendicular to the image plane, with its maximum at the centre of the image plane. The figure was extracted from the work of K. Ulrich [24]

Two source points can be optically separated laterally or axially at Rayleigh distances without being discriminated at the imaging side. To properly transfer the information required, to achieve the two source point discrimination, to an imaging sensor, information theory should be applied. Information theory states that the sampling rate should be high enough to satisfy the Nyquist criterion [24]. In practice, this means that the sampling interval should be at least twice as fine as the desired resolution. For example, to image with $10 \mu\text{m}$ resolution, the microscope should be able to detect $5 \mu\text{m}$. Nyquist theorem is also applied for the selection of the pixel size of the detector or the determination of the microscope's magnification. Multiplying the lateral resolution calculated by two will result in the sampling interval required to obtain the given lateral resolution. The physical pixel size of the detector should be equal to the sampling interval multiplied by the magnification M . This way all the required structural

information will be passed to the imaging sensor.

2.3 Fluorescence

Fluorescence is the emission of photons by molecules or nano-crystals whose electrons are stimulated to a higher excitation state by radiant energy from an outside source. Typically, they absorb photons of a given energy and emit photons at a lower energy and longer wavelength [24,29]. This difference in the wavelength is called Stokes shift [30].

Because of the energy loss during that process, the emitted fluorescent photon's wavelength is longer than the excitation photon that was absorbed by the molecule. This process is graphically illustrated by the Jablonski diagram, as shown in Figure 2.4. As shown, there are two excited states categories, the singlet state - which is described above, and the triplet excited state. Excited above the ground state electrons may enter the triplet excited state, through inter-system crossing. Molecules with electrons within this state are chemically reactive, which leads to photo-bleaching. Absorption and emission during fluorescence happens almost simultaneously, thus there is no longer fluorescence after the excitation stops [29].

Within the scope of this work, FND and fluorescence from the fluorescent reporter molecule mCherry were imaged. FND shows great promise for examination of complex biological processes. Its ability to produce bright and stable fluorescence (due to various atomic impurities in their structure) [31], low toxicity, chemical stability and photostability in tandem with the capability to detect changes in magnetic fields, electric fields, and temperature makes FND ideal for tracking and localizing individual drugs, proteins, nucleic acids, and small molecules [7].

FNDs absorb a wavelength of ≈ 560 nm and emit fluorescence from 637nm (which is the wavelength of the zero photon line for NV^-) to 800nm with a peak at ≈ 700 nm. (the zero photon line occurs because of the electronic transition from the excited state to the ground state without any interaction with photons) [32,34–36]. The biocompatibility and stability of FND in the body has been investigated by feeding and injecting 120nm FND to *C. elegans*. FND that were fed to the worm remain lumen for few hours before they were discarded by the nematode. When FNDs were injected to the worm

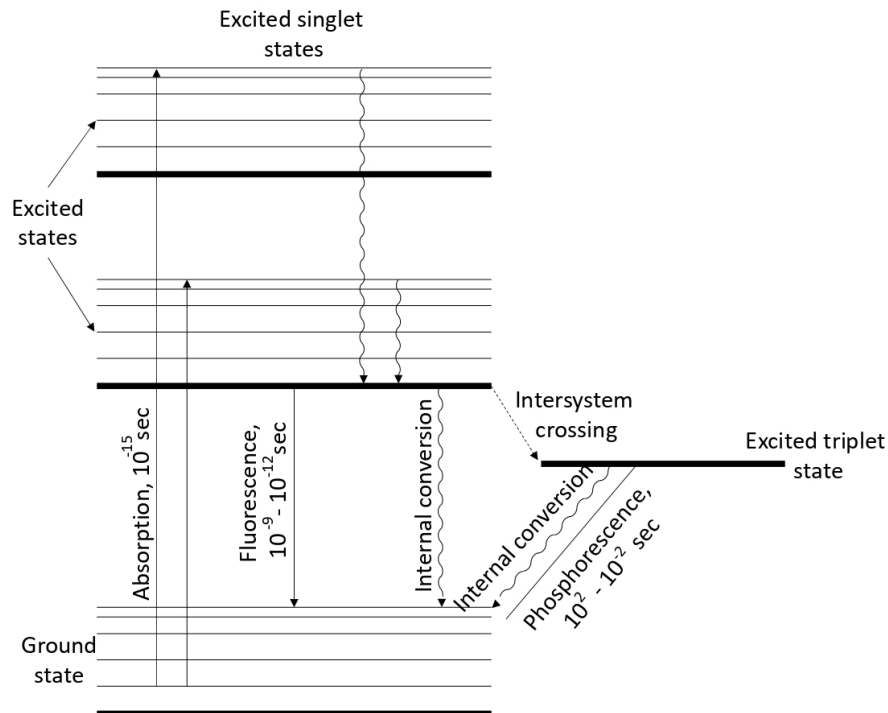


Figure 2.4: Jablonski diagram of a green fluorescent molecule. The upward arrows represent the high energy photons. Returning to the ground state can occur through any of the following ways: the fluorescent molecule will emit fluorescence (downwards arrow), or it can release energy as heat without photon emission (wavy downwards arrow), or it can return to ground state through an excited triplet state by emitting phosphorescence. The figure was extracted from the work of B. J. Thompson [29].

gonads, they were stable in the nematode's cells and allowed long-term observations of FNDs. Additionally, FNDs were transferred into the larvae and offspring with no impact on the reproduction or the survival of the worm [37,38]

mCherry absorption and fluorescence emission spectra is shown in Figure 2.6 where the Stokes shift can be observed in the wavelength difference between the absorption and emission peaks. FND NV emission with an excitation of a green wavelength laser is shown in Figure 2.5 .

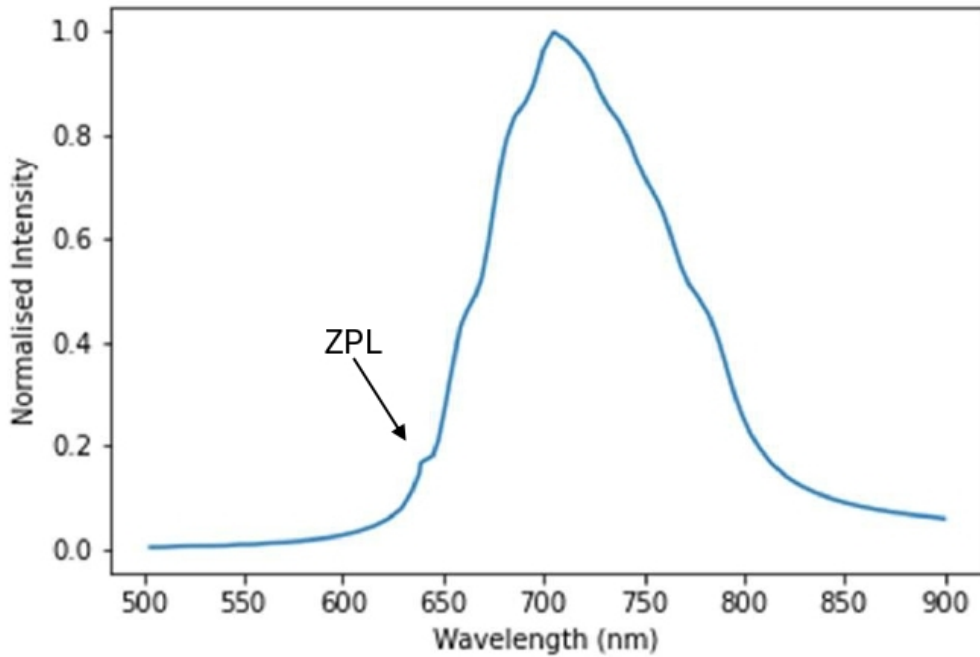


Figure 2.5: Normalised nitrogen-vacancy centre spectrum for a green wavelength excitation as recorded by S.R Nair et.al [32]. Maximum emission occurs at a wavelength of 700 nm. The zero photon line is visible at 637nm. The excitation band is approximately 150nm. The data were extracted using WebPlotDigitizer [33]

2.4 Imaging Aberrations and Adaptive Optics

The lenses required for microscopy are not perfect; therefore, they cause imaging aberrations. The most important aberrations of concern are the chromatic, spherical, coma, astigmatism, curvature of field, and distortion aberrations. The effect of each aberration is shown in Figure 2.7

Optical aberrations can be categorised as on-axis and off-axis aberrations. Chromatic and spherical aberrations constitute the on axis aberrations while coma, astigmatism, field curvature and distortion are off-axis aberrations. Chromatic aberration occurs because light with different wavelengths is refracted differently by the lens. As a result the focal point for different wavelengths will not be the same. To correct chromatic aberrations, imaging systems are designed with multiple elements of differing refractive index. This is a topic outwith the scope of this project, however we

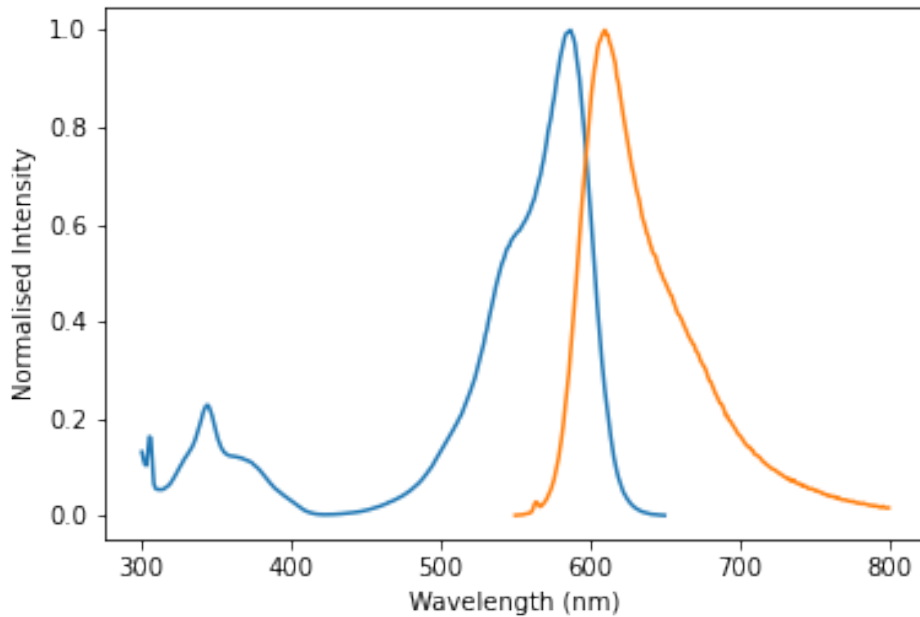


Figure 2.6: Normalised mCherry fluorophore excitation and emission wavelengths. The absorption spectrum is shown in blue and the emission spectrum in orange. Maximum absorption occurs at 585nm and maximum emission at 609nm. [29, 39]. The overlap between the absorption and emission does not affect imaging due to the introduction of optical filters in the detection path. The figure was extracted using data from FP Base related to the work of N. C. Shaner et al [39].

do employ achromatic doublets where appropriate to help lessen chromatic aberration. Spherical aberration occurs because the amount a ray is refracted is related to the sine of the angle of refraction; there is a different focal point for light rays of significantly different angles of incidence unless careful optical design is performed to correct for this. The result is the appearance of series of rings around an in-focus point source of light and the extension of the PSF in the axial direction.

On the other hand, when rays passing through the edge of the lens are focused closer to the optic axis compared to the rays passing through the centre of the lens, a focused point source looks like a comet with the tail extending towards the periphery of the field. This is an off-axis aberration called coma. Another off-axis aberration is astigmatism. Astigmatism occurs when rays passing through the horizontal and vertical diameter of the lens are focused at two different axial positions. The result is that

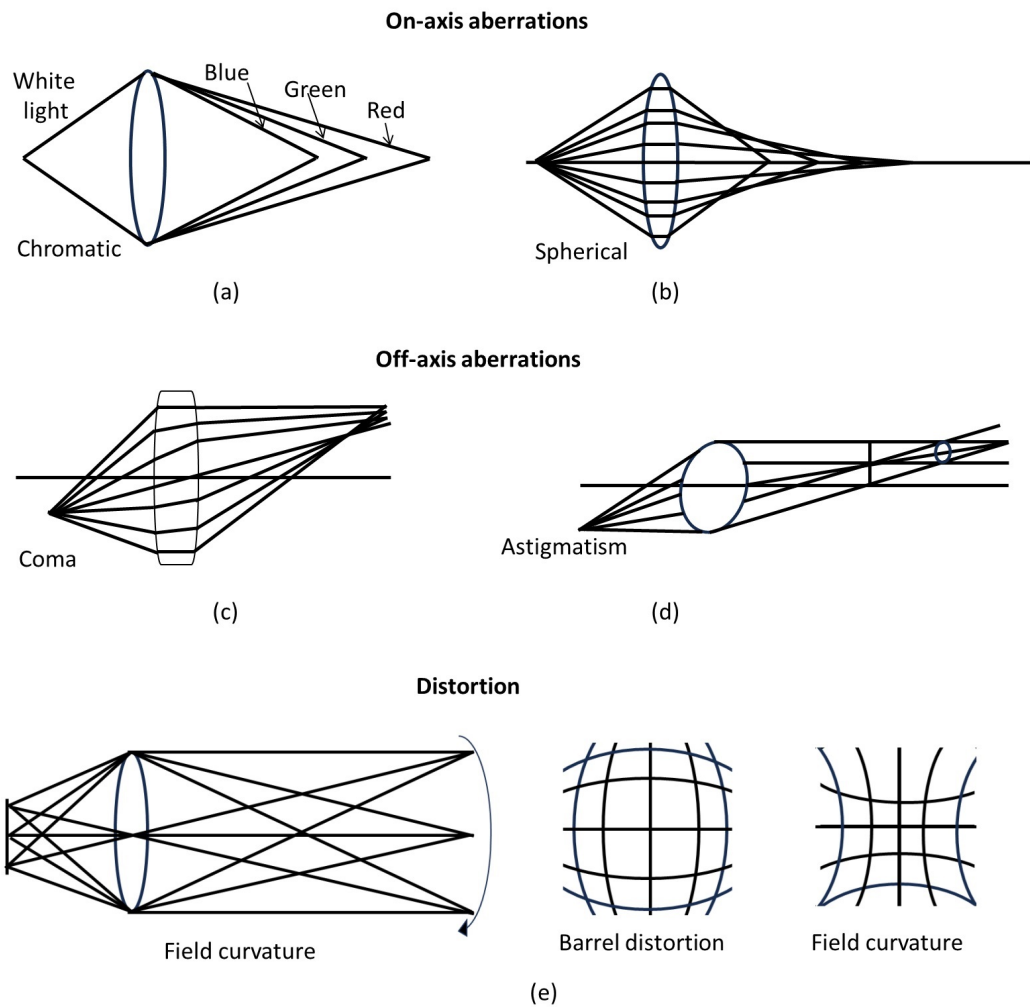


Figure 2.7: Refractive aberrations of a lens. Light is travelling from left to right in each of the diagrams. a) chromatic aberration describes the effect of rays of different wavelength (colour) focusing at a different point. b) Spherical aberration occurs when rays at the optical axis focus at a different location to rays at the periphery of the lens. c) coma occurs when off-axis rays passing through the centre of the lens and rays passing through the periphery of the lens are not focused at the same location. d) Astigmatism takes place when rays passing through the vertical diameter and rays passing through the horizontal diameter are not focus at the same point. e) Image distortion is the phenomenon when the image plane is curved and not planar The figure was extracted from the work of B. J. Thompson [29].

the focused image of a point object is shown as an extended circular patch (elliptical). Astigmatism is corrected by proper lens mounting and alignment. When the image plane is not flat, but instead has a concave spherical shape, it is indication of field curvature. This results in an image that cannot be focused simultaneously on a flat surface such as an imaging chip. Finally, distortion is the aberration that occurs when the focus position of the object image shifts laterally in the imaging plane when increasing the displacement of the object from the optical axis. This results in a nonlinear magnification in the image from the centre to the peripheral field. When the magnification is increasing pincushion distortion is observed, while when the magnification decreases, barrel distortion is observed. Correction of field curvature and distortion is achieved by objective lens and tube lens designs (Plossl lens design) [29, 40–42].

There are several methods for aberration correction; however, the effect of aberrations can never be completely removed. In addition to the aberrations caused by the optical system, the sample itself causes aberration, which has a negative effect on imaging resolution and imaging quality. Therefore, Adaptive Optics (AO) have been introduced into microscopy to improve aberration correction and increase the imaging quality and resolution [43]. AO is a technique using dynamically re-configurable optical elements in combination to aberration measurement to correct aberrations [44].

In this work adaptive optics elements were used for the manipulation of the illumination beam while aberration correction is not applied in the imaging path, although the foundation work has paved the way for aberration corrections in the future. This sub-chapter explores key AO technologies, namely the spatial light modulator, the deformable mirror and the Shack-Hartmann Wavefront Sensor.

2.4.1 Introduction to Spatial Light Modulators

Spatial Light Modulators (SLM) are based on a liquid crystal array, where the liquid crystal molecules can be manipulated either by optical or electrical means, changing their orientation. The behaviour of the SLM makes it widely used in optics for phase modulation, adaptive optics and beam shaping [45–48]. Additionally, SLMs are used in super resolution techniques such as STED microscopy and SIM [49]

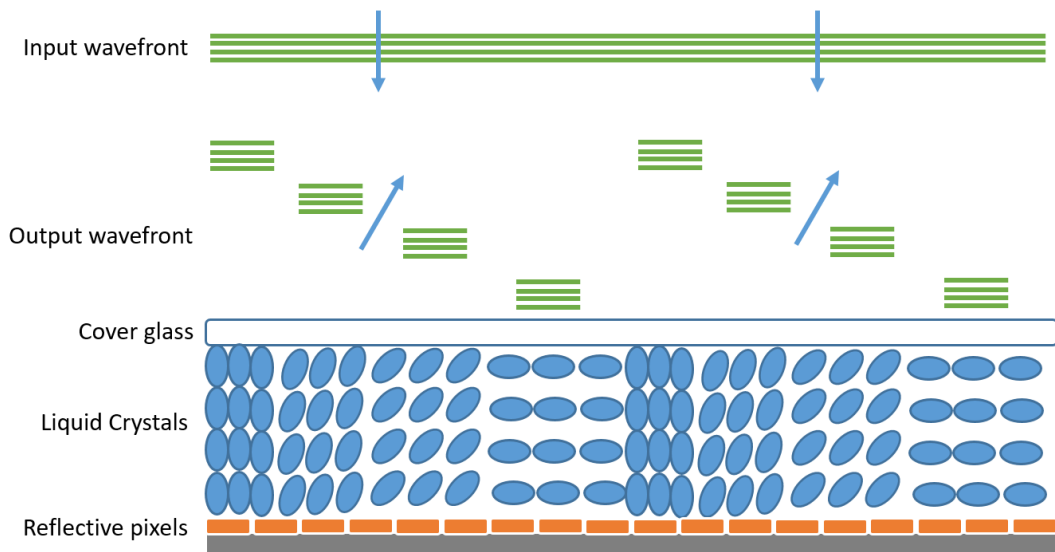


Figure 2.8: Spatial Light Modulator Structure. Green lines represent a wavefront. Blue arrows point towards the direction of the wavefront. The blue arrows pointing upwards represent the reflected light. The effect of the orientation of the crystal on the input wavefront is shown. The figure was extracted from the data-sheet of Meadowlark Optics [50].

SLM is capable of modulating light through a fixed pixel pattern. By applying an Alternating Current (AC) voltage to each pixel an electric field between the pixel and the cover glass is produced. The resulted electric field changes the optical properties of the liquid crystal layers, by changing their refractive index. The fact that each pixel is independently controlled enables the phase pattern generation by applying different voltages onto each pixel. An intrinsic section of the SLM is shown in Figure 2.8. As shown, a polarised light passes through the cover glass and liquid crystal layer. The light is reflected from the pixel electrodes and returns on the same path. If the reflected light is not polarized, voltage controlled light modulation would not be achieved since the light will not be parallel to the extraordinary axis [50]. In summary, the liquid crystal has the orientation birefringence, and the SLM is constructed so that this birefringence is observed consistently across the whole device.

SLMs, akin to every wave-plate, have a slow (extraordinary) axis and a fast (ordinary) axis, both being perpendicular to the beam direction and to each other [51]. The fast axis has a lower refraction index (n_o), resulting in a faster travelling light, while

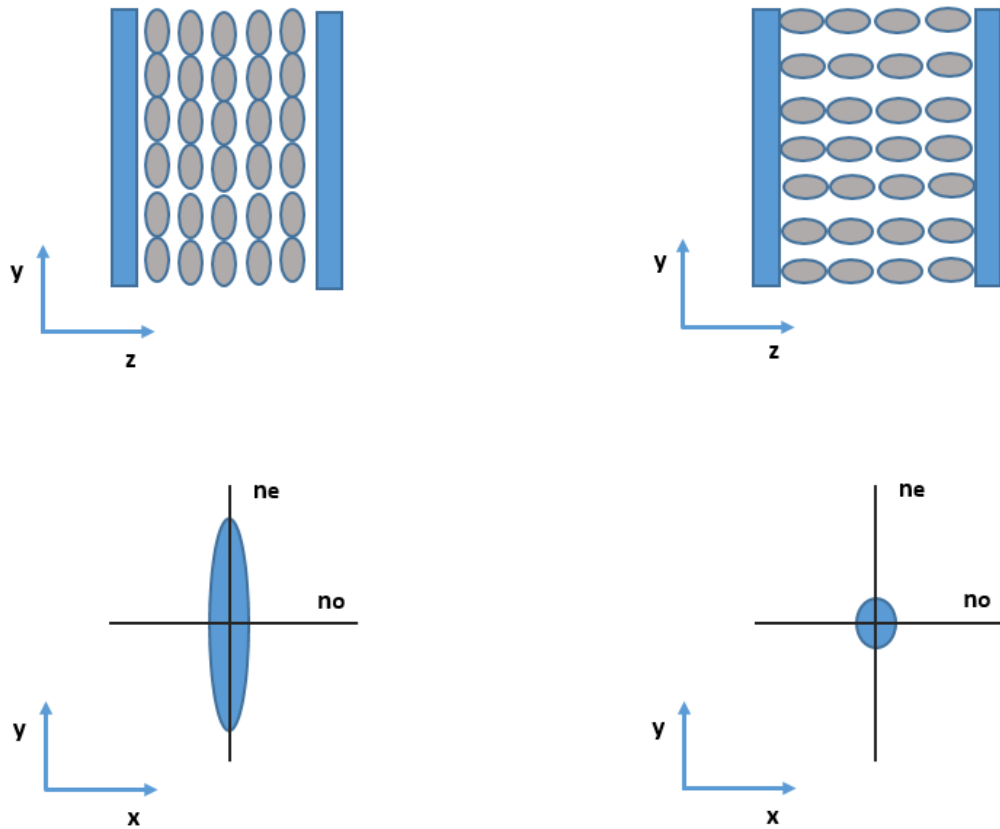


Figure 2.9: Spatial Light Modulator Liquid Crystal Orientation. The SLM's coverglass is shown in blue and the liquid crystals in gray. n_e refers to the extraordinary index of refraction and n_o the ordinary index of refraction. a) No voltage is applied, liquid crystal molecules are parallel to the coverglass. Maximum difference between extraordinary and ordinary index of refraction. b) Maximum voltage is applied on the liquid crystals and the molecules are perpendicular to the coverglass. At this stage there is no difference between ordinary and extraordinary index of refraction. The figure was extracted from the data-sheet of Meadowlark Optics [50].

the light passing through the slow axis encounters a higher refraction index (n_e) and thus travels slower. SLMs achieve phase modulation by manipulating the extraordinary refractive index. For the sake of simplicity, the case of no voltage and maximum voltage have been examined, as shown in figure 2.9. In the case where voltage equals to zero, the liquid crystal molecules are parallel to the cover glass, hence, maximising of the extraordinary refractive index and consequently maximising the phase retardation. In contrast, when the voltage applied to the pixel array is maximised the difference

between the extraordinary and ordinary refractive indices is approaching zero, leading the phase delay to its minimum. To achieve phase modulation the light polarisation should be parallel to the extraordinary axis [50]. Due to structural anomalies of the SLM, calibration is required to achieve the desired operation, as discussed in Chapter 4.

2.4.2 Deformable Mirror characterisation

A Deformable Mirror (DM) is a device capable of manipulating its reflecting surface when voltage is applied [52]. Therefore it can manipulate the phase of a light beam by varying the optical path length across the mirror's surface. Similar to the calibration of an SLM, a flat surface can be achieved by calibrating the DM. When a feedback control loop (closed-loop) is used for wavefont correction, calibration is not required. In control theory, a feedback loop takes into consideration the output of a system and

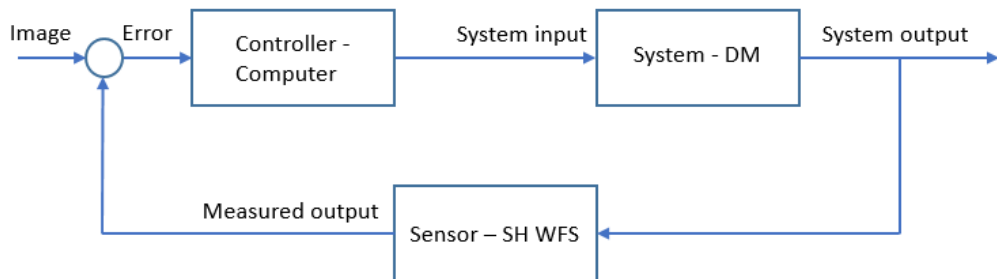


Figure 2.10: Deformable mirror feedback control loop (closed-loop configuration). Feedback from wavefront sensor is used to correct imaging aberrations .DM refers to Deformable Mirror and SH-WFS to Shack-Hartmann Wavefront Sensor. The figure was extracted from the work of G. Raju and N. Mazumder [53].

modifies its performance to achieve the desired output. Fundamentally, this is achieved by a controller, a sensor and the controlled system in a configuration as shown in Figure 2.10. The deformable mirror control system consists of the computer used for the microscope operation as a controller, a Shack-Hartmann Wavefront Sensor (S-H WFS) and a deformable mirror.

2.4.3 Shack-Hartmann Wavefront Sensors

Hartmann testing device has been initially used for telescope optics control. However, it has been modified to be used in adaptive optics. The fundamental principle of operation is based on the projection of an image of the exit pupil onto an array of identical lenses (lenslet), where each lens produces an image on the detector [54–57].

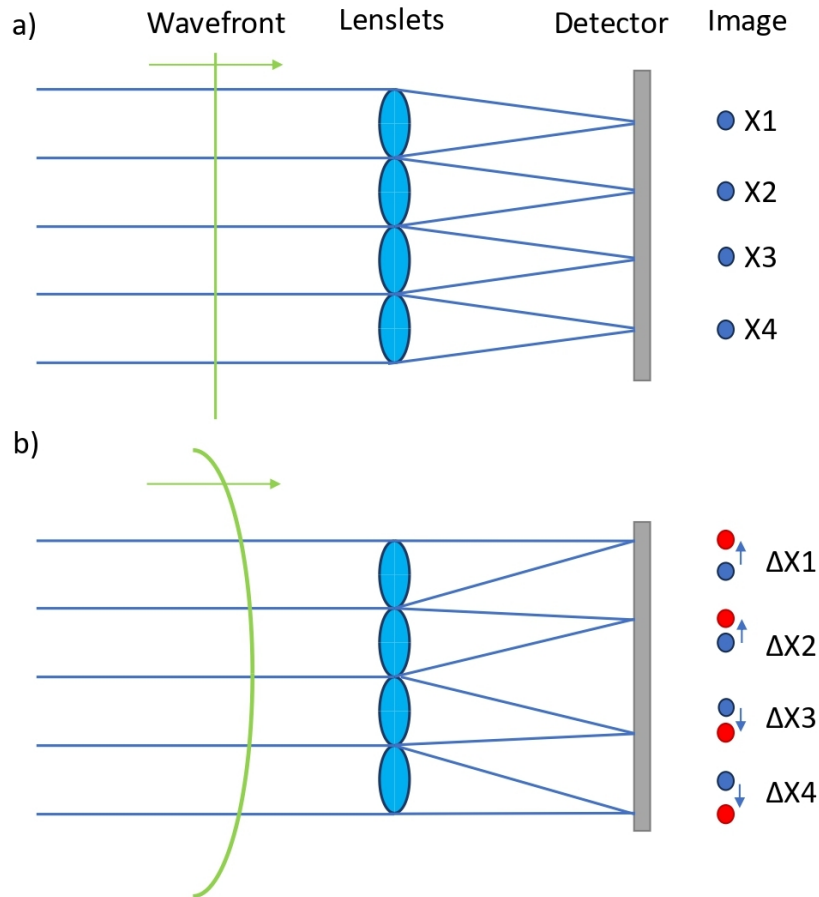


Figure 2.11: Shack-Hartmann Wavefront sensor principle of operation. A microlens array divides the wavefront into beams, which are focused on an imaging sensor. The imaging sensor reads the location of the beam. a) The reference beam used to estimate the desired beam location on the imaging sensor. b) distorted beam resulting in different beam locations on the imaging sensor (compared to the reference - shown as ΔX). The figure was extracted from the work of S. Vallmitjana et al [56].

Incoming wavefronts are divided on the basis of their structure. When a plane wavefront is imaged all focal points follow the lenslet array's geometry and are projected at

their nominal position (Figure 2.11a). Therefore, displaced focal points indicate a distorted wavefront (Figure 2.11b). Measuring that displacement leads to the calculation of the wavefront slopes. A S-H WFS measures the wavefront gradients, paving the way to the reconstruction of the wavefront [57, 58].

2.5 Phototoxicity and Photobleaching

Advancement in microscopy enabled real time imaging and resolution improvements in imaging whole cells [59], tissues [60, 61], and organisms [62], having large impact on biology research. Improving the resolution, the imaging speed and the signal to noise ratio, while imaging deeper into the sample, requires high light doses that the imaged biological specimen is not experiencing in its natural environment. This has a negative effect on the imaged sample, called photo-toxicity [63]. Phototoxicity can impair sample physiology, and even kill the sample [64].

Photobleaching, on the other hand refers to the process at which a gradual loss of fluorescence intensity occurs. This effect occurs because the exciting light photochemically destroys the fluorescent dye. This is an irreversible process [24]. Photobleaching highly depends on the molecular structure of the fluorophore. Some fluorophores have a very low number of excitation and emission cycles while others can go millions of cycles before bleaching [65] and FND has effectively no photobleaching at the light levels used for most microscopes.

Investigating living specimen has a major impact on advances in understanding of biology, therefore imaging techniques limiting photodamage and photo-bleaching are in high demand [24, 63].

2.6 Three Dimensional Imaging Principles

In its simplest form, wide-field fluorescence microscopy uses an appropriate light source to excite a sample, filters, an objective, a tube lens, and an imaging sensor. Wide-field fluorescence microscopy is a relatively simple, low cost, microscope that provides good resolution both laterally in the imaging plane and temporally. However, all the emission

light generated travels through the sample in the axial direction (Z-axis), resulting in a poor axial resolution and limited optical sectioning capabilities [66]. Therefore, to overcome such limitations, optical sectioning microscopes were developed, allowing diffraction-limited three dimensional imaging from cells to whole living organisms [24].

This projects aims in imaging whole organisms at cellular resolution without investigating sub-cellular features; therefore, Three-Dimensional (3D) super-resolution imaging techniques, such as Stimulated Emission Depletion (STED) microscopy and Structured Illumination Microscopy (SIM) are not reviewed.

2.6.1 Confocal Microscopy

Confocal microscopy is based on the use of two pinholes, one to restrict the excitation beam and the other to restrict the detection beam, both blocking out of focus light. When a coherent laser beam is used for excitation, the excitation pinhole can be removed. Confocal microscopy principles are illustrated through the schematic in Figure 2.12. The main components of a basic confocal microscope are a laser, a beam expander, a dichroic mirror that splits the excitation light from fluorescence, an objective lens, a tube lens, a pinhole and an imaging lens. A laser beam is expanded to the designed beam size through a series of lenses. The expanded beam is then reflected by the dichroic mirror and by passing through the objective lens, it focuses on the focal plane. Fluorescent light emitted by the sample is collected by the same objective lens, passes through the dichroic mirror and a pinhole, positioned at the image plane of the sample, and it is focused on a detector.

The pinhole at the image plane of the sample blocks the out of focus light and thus improves resolution and the signal to noise ratio of the received information. On the other hand, confocal microscopy is still diffraction limited and to form an image scanning is required. Spatial information is obtained by scanning either the beam or by moving the sample relative to a stationary beam. Even with high speed scanning techniques, the imaging time per frame is often slower than wide-field microscopy [24].

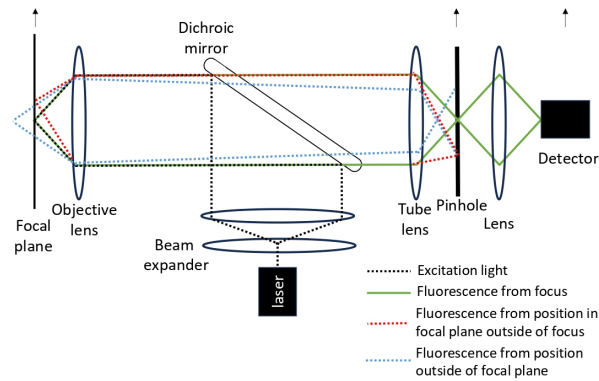


Figure 2.12: Optical schematic of a basic confocal microscope. The function of the pinhole is shown with the illumination of the focal plane, the pinhole and the detection plane. The black dashed line represents the excitation beam which is focus on the sample. Only the light emitted at the focal position reaches the detector (green light), while the red dashed (emitted from an adjacent to the focal point position) and blue dashed (emitted from different focal plate) lines, representing light emitted from other position do not reach the detector. The figure was extracted from the work of K. Ulrich [24].

2.6.2 Spinning Disk Confocal Microscopy

Spinning disk confocal microscopy improves the imaging speed of confocal microscopy while maintaining its advantages by scanning multiple pinholes across the sample. This is achieved by placing a disk with a series of holes (Nipkow disk) arranged as shown in Figure 2.13 (a), and imaged as shown in Figure 2.13 (b), in front of an image. Only the light that is in front of a hole pass through the disk. When the pinholes are in conjugate with the image plane of the objective, every point of the sample can be scanned with a high speed, compared to confocal microscopy. The optical schematic of the spinning disk confocal microscope is very similar to the laser scanning confocal microscope's, as shown in Figure 2.13 (c). The only difference is that the excitation beam passes through

the disk and thus it splits into an array of beams, each producing a separate beam for illumination. Confocal detection and image construction by assembling each fluorescent signal from the different pinholes is achieved by using the same set of pinholes for excitation and detection, as shown in Figure 2.13c. To properly reconstruct an image, the frame rate of the camera is synchronised with the rotation frequency of the Nipkow disk [24].

Spinning disk confocal microscopy achieves a higher imaging speed while maintaining a good lateral resolution, compared to confocal microscopy; however, cross-talk among the pinholes occurs. Cross-talk refers to the event when light from out of focus region, blocked by a specific pinhole, passes through an adjacent pinhole, resulting in the decreasing of the axial resolution. Scanning through multiple pinholes, the excitation power is more distributed both spatially and temporally, thus reducing the effect of photobleaching and phototoxicity, making spinning disk confocal microscopy a powerful tool for investigating various biological questions [24].

2.7 Light-sheet Fluorescent Microscopy (LSFM)

2.7.1 Principles of Operation

Light-sheet fluorescence microscopy takes advantage of the ability to separate the excitation and detection optical paths. The illumination path is the one responsible for a plane-wise illumination of the sample with a thin light sheet. The wide-field fluorescence extracted by the sample is then collected at the detection path, which is perpendicular to the illumination path (illustrated in Figure 2.14). As a result, imaging an optical section of the sample without out-of-focus light is achieved [4,67]. In order to create a uniform illumination and to illuminate the sample from different perspectives (form a 3D image of the sample), either the sample is scanned through a stationary light-sheet or the light sheet is digitally scanned through the sample [68]. Imaging with a single illumination and single detection LSFM will result in low quality image due to the effect of shadowing. To improve the performance of the microscope a second detection path and/or illumination path is applied to achieve a dual side detection and/or illumina-

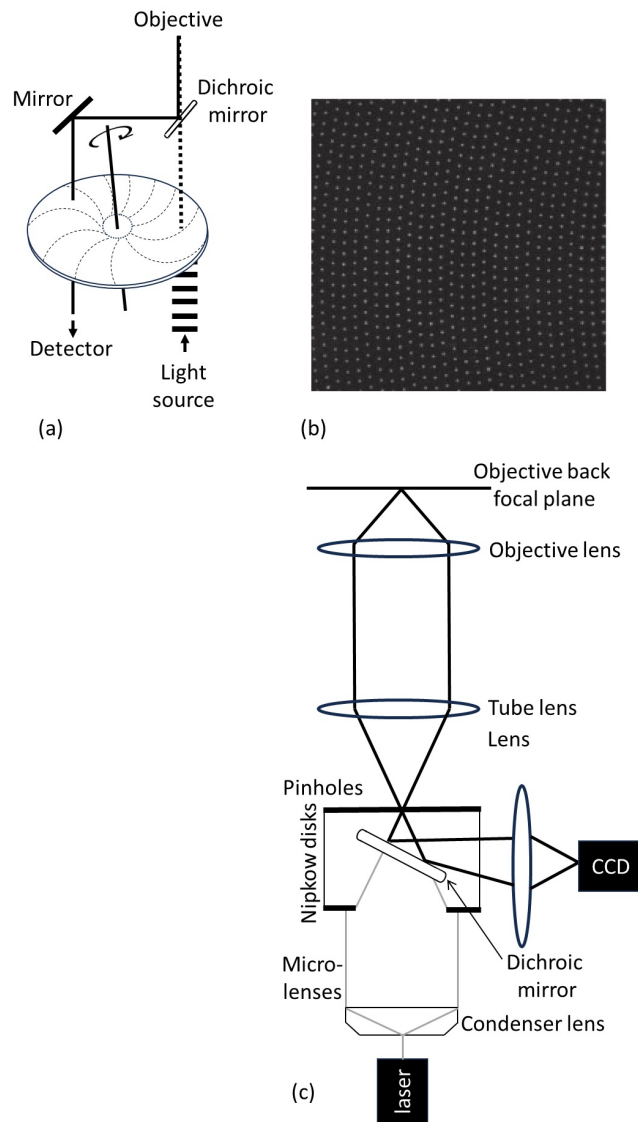


Figure 2.13: Spinning disk confocal microscope. a) Representation of a Nipkow disk embedded in a scanning microscope. Excitation and detection happens simultaneously at different regions of the Nipkow disk, b) pinhole structure image when the Nipkow disk is not rotating c) optical schematic of a spinning disk confocal microscope. The excitation beam is shown in gray and the detection path is shown in black. The figure was extracted from the work of K. Ulrich [24].

tion [4]. Illuminating the sample from two opposite directions, and fusing the received data, image degradation in the light-sheet propagation axis is reduced [67].

The fact that the sample is illuminated by a thin light-sheet and the capturing

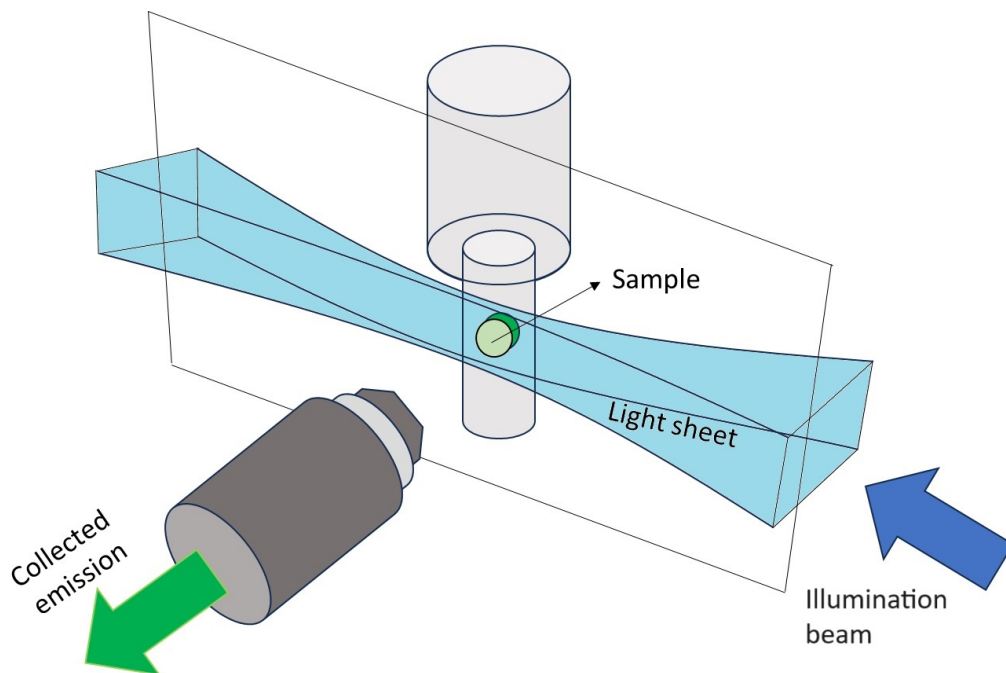


Figure 2.14: Light-sheet Fluorescent Microscope principle of operation. The fluorescent sample is positioned at the focal position of both the illumination and detection objectives. The excitation (shown with the blue arrow) and detection (shown with green arrow) are separated and perpendicular to each other. The light-sheet is shown in blue. The area of the sample shown in green is collected by the detection objective. The figure was extracted from the work of O. E. Olarte [67].

of fluorescent light is very efficient, not only makes LSFM a high resolution optical imaging device but also reduces photobleaching and phototoxicity. However, isotropic imaging, achieved when spatial resolution is the same in all directions [69], with a LSFM is very challenging due to its geometry. The orthogonal geometry of the detection and illumination paths limits the selection of the illumination and detection objectives since bulky objectives cannot be brought close to each other; therefore, the focal positions of the two objectives will not be at the same location. Despite the limitations due to the geometry of the objectives, isotropic LSFM have been reported in the literature.

Light-sheet Generation and Image Formation

There are two methods of LS generation. The first one is called Selective Plane

Illumination Microscopy (SPIM) and it is based on the creation of a LS using a cylindrical lens, as shown in Figure 2.15 (a). The second one is called Digitally Scanned Light-Sheet Microscopy (DSLM). The principle of operation in this case is based on the quick moving, compared to the camera integration time, of a focused beam at the focal plane of the detection lens, hence forming a virtual LS, illustrated in Figure 2.15 (b).

The basic optical schematic for both the SPIM and DSLM is shown in Figure 2.15. In SPIM, a static LS is created when a laser beam with diameter d_b passes through a cylindrical lens L_{cl} where the Light-Sheet (LS) is formed. The LS then passes through a beam expander (L_{T1}, L_{T2}) to control its height d_h and focuses the light sheet to the Back Focal Plane (BFP) of the illumination objective O_{Li} . The illumination objective focuses the light sheet on the focal plane of the detection objective O_{Ld} , which collects the excited fluorescence. Removing the cylindrical lens from a SPIM microscope and adding a fast scanning mirror results in a DSLM. A fast scanning of a laser beam at the back focal plane of $LT1$ results in the generation of a virtual LS in the focal plane of the detection objective [24, 70]. The difference between the two LS generation methods is observed in Figure 2.15, where the the illumination beam is coloured in orange for the top view representation, and in blue for the side view representation. Both the static and virtual LSs are shown in Figure 2.16.

In both cases the LS's shape at the focal plane of the detection objective is the same, as shown in Figure 2.17. The FOV and the LS thickness are dependent on the beam characteristics and thus on the illumination objective used. The Rayleigh range defines the FOV, while the thickness of the LS defines the axial resolution, only when the thickness of the LS is greater than the axial resolution of the detection objective [67]. Since in LSFM, the excitation and collection arms are uncoupled, the lateral resolution of a LSFM microscope is defined by the detection objective used. If isotropic imaging is required, the thickness of the light sheet should be equal to the lateral resolution of the detection objective (lateral and axial directions are shown in Figure 2.18).

The FOV of the LSFM microscope is given by the Rayleigh length Z_r , which is the distance from the waist to the plane where the beam diameter is equal to $\sqrt{2}w_0$,

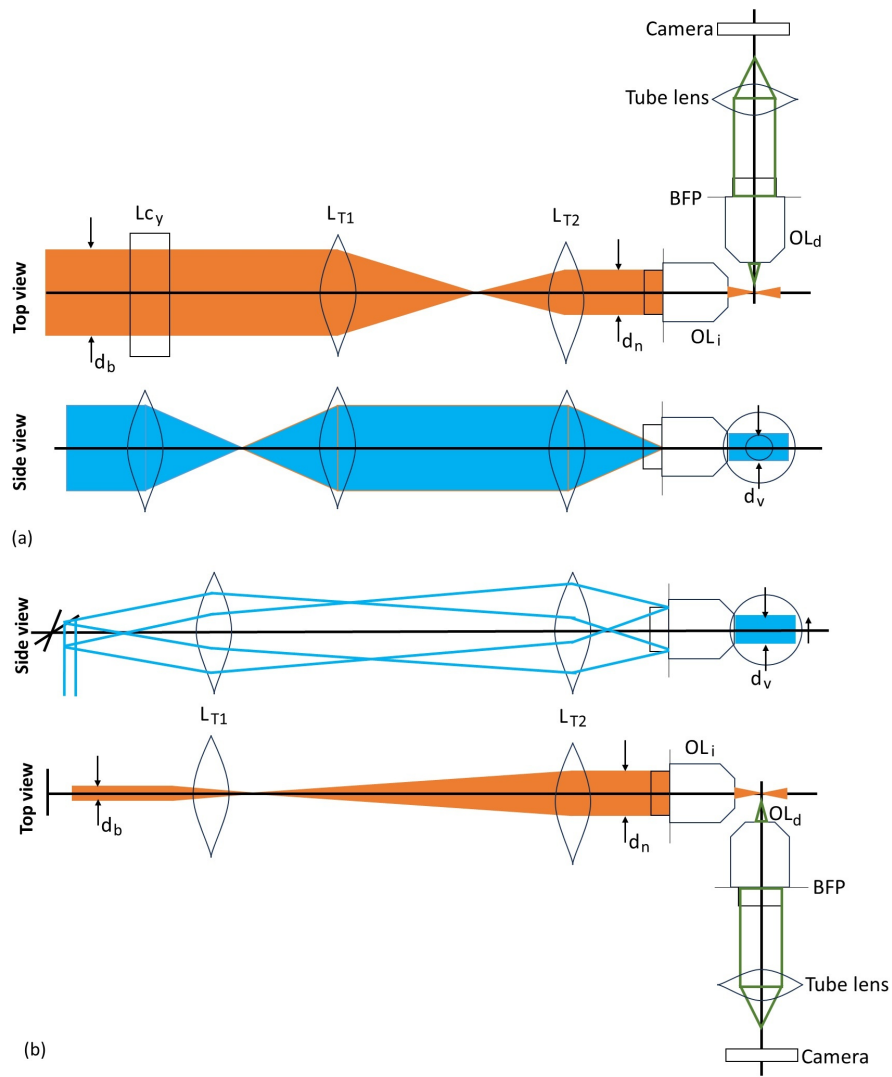


Figure 2.15: Optical schematic of the two main light-sheet generation microscopes - a static light sheet and a scanned light sheet. The orange beam represents the top view and the blue beam represents the side view. The green beam represents fluorescence. a) a light sheet is generated when a beam with diameter b_d passes through a cylindrical lens. A beam expander (L_{T1} and L_{T2} lenses) adapts the diameter of the beam to b_h and focuses it at the back focal plane of the illumination objective O_{ill} . The detection objective O_{det} collects the excited fluorescence. The excited fluorescence passes through a tube lens, which focuses the excited beam on the camera. b) A light-sheet is generated by rapid scanning of the laser beam along the back focal plane of the L_{T1} lens axis. This way a "virtual" light-sheet is generated at the focal position of the detection objective. The figure was extracted from the work of K. Ulrich [24].

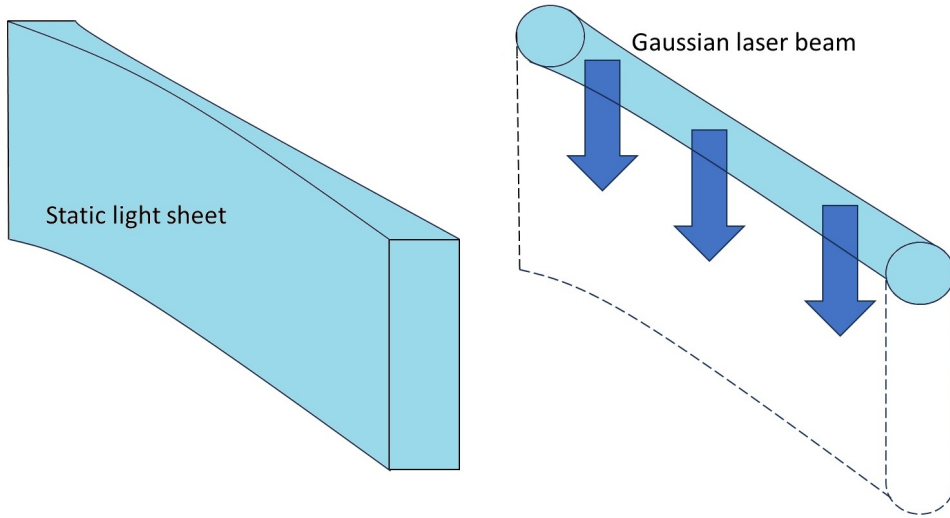


Figure 2.16: Illustration of two main types of light-sheets. a) static light sheet (SPIM) created when a laser beam passes through a cylindrical lens, b) virtual light sheet (DSLM) created by rapidly scanning a laser beam. The figure was extracted from the work of M. Weber and J. Huisken [70].

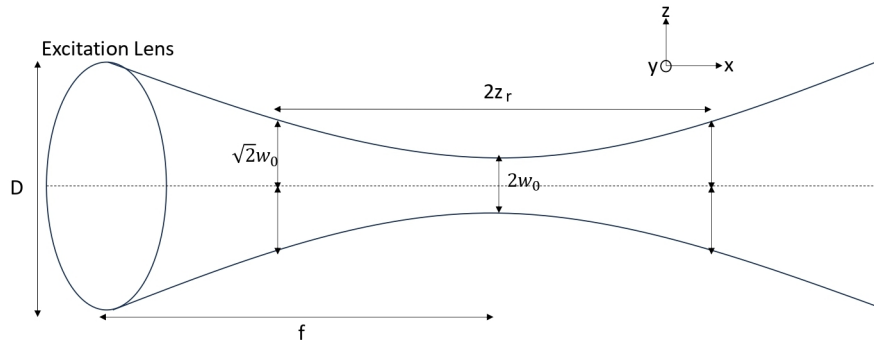


Figure 2.17: Relationship between light-sheet thickness (resolution) and field of view when a light sheet is generated by a Gaussian beam with a diameter D . The thinnest part of the light sheet is $2w_0$. The thickest useful part of the light-sheet is $2 \times \sqrt{2}w_0$ and it is located at a distance Z_r from the centre of the light sheet which is the axial Rayleigh length. The FOV is equal to $2Z_r$. The figure was extracted from the work of O. E. Olarte et al [67].

where w_0 is defined as the half distance of the waist of the LS. Herein, the LSFM FOV can be expressed as the central lobe of a sinc^2 function [30], and thus is modelled as:

$$FOV_{ill} = \frac{1.78 \times n \times \lambda_{ill}}{NA_{ill}^2} \quad (2.16)$$

where, n is the refractive index of the medium between objective lens and the sample, λ_{ill} is the illumination wavelength and NA_{ill}^2 is referred to the illumination's numerical aperture [24, 67].

The axial resolution of the LSFM is either determined by the detection objective (the axial resolution of the detection objective - shown in Chapter 2) or by the thickness of the LS. The larger value between the two properties determines the axial resolution. For millimetric illumination (low illumination NA, and thus longer, thicker LS) and cellular resolution (higher detection NA) the LS will set the axial resolution of the microscope (the mathematical model is described in Chapter 3). Therefore, the axial resolution of the microscope is equal to $2\omega_0$. The LS thickness can be calculated by applying the Rayleigh criterion, and thus the lateral resolution of the LSFM is expressed as

$$D_{beam} = \frac{1.22 \times \lambda_{ill}}{NA_{ill}} \quad (2.17)$$

So far the creation of a stationary light sheet and consequently, 2D imaging is discussed. To achieve 3D imaging, either the sample is moved through a stationary LS or the LS scans a stationary sample. The simplest form of LSFM volumetric imaging is achieved by translating the sample along the detection axis, through a light sheet, focused on the focal plane of the detection objective. This way all optics in the detection arm remain stationary. Acquiring z-stacks using this method limits both the imaging speed as well as the sample that can be imaged. The imaging speed is limited by the speed a sample can be moved without changing its physiology. To overcome such limitation, a LS is scanned through a static sample, with the detection objective being synchronised with the LS in such a way that the LS is kept in focus with the detection objective. This way, fragile samples as well as freely moving living organisms can be imaged [24, 67].

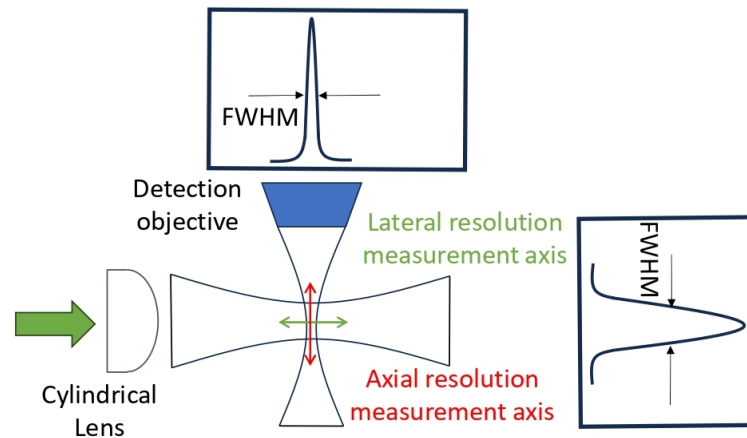


Figure 2.18: Lateral and axial intensity distribution of a light sheet created by a Gaussian beam passing through a cylindrical lens. The large green arrow indicates the Gaussian beam passing through the cylindrical lens. The lateral resolution is marked with the green arrow and the axial resolution is shown with the red arrow, also shown as the Full Width Half Maximum (FWHM) of the Gaussian beam. The figure was extracted from the work of Y. Kim et al [71].

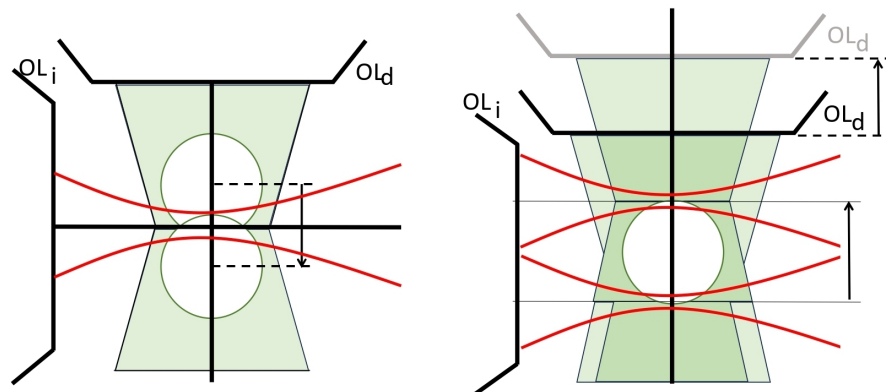


Figure 2.19: Light-sheet Fluorescent Microscopy volumetric image formation. Left) moving the sample through a stationary light-sheet, focused by the illumination objective OL_i , and a stationary detection objective (OL_d , b) Scan the light sheet through a stationary sample, while the detection objective follows the light-sheet to remain in focus. The figure was extracted from the work of K. Ulrich [24].

2.7.2 LSFM FOV Enhancement

In this sub-chapter several LSFM techniques are going to be investigated from a "FOV size" point of view. Chronologically, the first LSFM technique was the SPIM [72] in which a cylindrical lens creates the LS. A plane-wise static illumination occurs, which illuminates only the focal plane of the detection path, hence there is no generation of out of focus fluorescence. Due to the efficiency of the illumination the photodamage and photobleaching are reduced, paving the way to long-term fluorescence imaging of an entire embryo without any effect on its health. A comparison between the effect of photodamage and photobleaching between confocal microscopy and LSFM is found at [73]. On the other hand, due to the static illumination on an entire plane, artefacts appear. This occurs due to the refraction, scattering and absorption of coherent light within the tissue. This effect is minimal on optically transparent specimens, hence it is suitable for my project [4]. To overcome the drawbacks of SPIM, multi-directional SPIM (mSPIM) and dual-beam illumination have been introduced. In the mSPIM configuration, the LS is pivoted, at the imaging plane, at its focus, leading to the reduction of the shadowing in the excitation path, occurring due to the absorption in the specimen. In dual-beam illumination, the scattering effect is limited by illuminating the sample from the opposite direction [74]. Both single illumination and dual illumination configurations can be used for freely moving whole organisms. For millimetric FOV imaging dual-illumination would be beneficial not only because of the reduction of the scattering but also because at dual illumination the axial resolution is improved by a $\sqrt{2}$, assuming the FOV is the same. This is because each of the two beams illuminates only half of the FOV in the direction of propagation of the light sheet with the required axial resolution - the waist of each beam is therefore a quarter of the way into the field of view. Counter propagating beams can then cover the whole FOV as if it were half the size. This can be proved as follows, from equation 3.1 $NA = \sqrt{\frac{1.78\lambda}{FOV}}$. Applying that in equation 2.7, the resolution for a single beam illumination is equal to $r_1 = \frac{0.61\lambda}{\sqrt{\frac{1.78\lambda}{FOV}}}$ while for dual-beam illumination resolution is $r_2 = \frac{0.61\lambda}{\sqrt{\frac{1.78\lambda}{FOV/2}}}$; therefore, $\frac{r_1}{r_2} = \sqrt{2}$, which indicates the resolution improvements at dual beam illumination.

The second major category of LSFM is the DSLM. Because the time on target is

reduced due to the scanning of the laser (the imaging plane is illuminated partially, reducing the time the beam dwells at each pixel within the (longer) frame integration time), laser peak power increases as the desired FOV increases, to keep a constant Signal to Noise Ratio (SNR) [4,67] [75]. The laser power increase can cause fluorophore saturation and/or photodamage in transparent samples [67,76]. Therefore DLSM is more suitable for optically dense samples (densely fluorescent specimens [77]). When imaging highly dense samples scattering is increased and the image quality is reduced. Improvement methods are reported in the literature [78,79]; however, I will not discuss it further here since a SPIM configuration is superior for our application because I am interested in imaging optically an transparent sample.

LSFM's success to offer *in toto* cell resolution of embryos is primarily based on multiview imaging. Multiview imaging is the process whereby a single image is generated from multiple sub images that have differing illumination conditions. It improves axial resolution since the data from the highest resolved portion of each sub-image is used in the final image. Initially, multiview imaging has been achieved by rotation of the sample though the LS [4]. However, this sets a major bottleneck in the speed of the system, since high rotational speeds have a major impact on the viability of the specimen under investigation. Multiview imaging by sample rotation was not applied in my work, since the observation of *C. elegans* movement is of high importance, and hence the specimen cannot be moved [4].

To avoid sample rotation a second illumination path has been added to the SPIM design. Such a design can either simultaneously or sequentially illuminate the sample. Simultaneous illumination can be used in transparent specimens, since there is minimal LS degradation. For simultaneous illumination it's also important that the structures of interest are sparse, so that there's a low probability of the thicker parts of the light sheets exciting fluorescence out of the thinnest plane of the other light sheets. Sequential dual-beam illumination is used for scattering samples, where there is LS degradation [80]. By illuminating the sample with a dual-beam illumination, half of the FOV needs to be covered by each illumination path and thus the resolution increases by $\sqrt{2}$ (mSPIM) (Figure 2.20 (b)). Dual illumination reduces the rotations required for

each scan to one. Sample rotation is eliminated by introducing a second detection path in the LSFM setup (Figure 2.20c). Theoretically, this setup improves the optical coverage of the system since imaging of the sample will occur from two directions [4].

2.7.3 LSFM Design Configurations

By investigating the existing LSFM design, it can be concluded that LSFM is a flexible microscope that can be adapted and customised to answer a wide range of biological applications. The major LSFM objectives configurations are shown in Figure 2.20.

A single detection, single illumination SPIM setup is shown in Figure 2.20 (a). The orthogonal configuration limits the choice of objectives since the size of high NA objectives does not allow them to be placed close to each other. Additionally, this configuration results in sample shadowing, an undesired effect of LSFM imaging. To limit the effect of shadowing, a dual illumination single detection LSFM has been designed (Figure 2.20 (b)). This paved the way for multi-view imaging and imaging larger samples. Naturally, the next improvement of a LSFM system was to include a second detection objective. A dual illumination dual detection LSFM can record two opposite views of the sample simultaneously, and thus getting a step closer to isotropic imaging. As the interest in investigating larger sample increases, LSFM has been adapted in such a way that, large organisms, mouse brains and cleared samples can be imaged. This is achieved by constructing an upright dual illumination single detection LSFM, where the illumination objectives are replaced with low NA cylindrical lenses, as shown in Figure 2.20 (d). Finally, to image cell cultures or samples mounted on a coverslip, inverted LSFM configurations have been developed (Figure 2.20 (e)) [4, 24, 71,81,82]. A summary of the investigated LSFM objectives configurations, emphasising on their biological application is listed in Table 2.1.

2.7.4 LSFM Imaging Speed Improvement

Imaging speed can be an important characteristic of a microscope. From a biological point of view it is equally important to image structure as it is to image function and capture biological processes. The bottleneck for the overall speed of the system is the

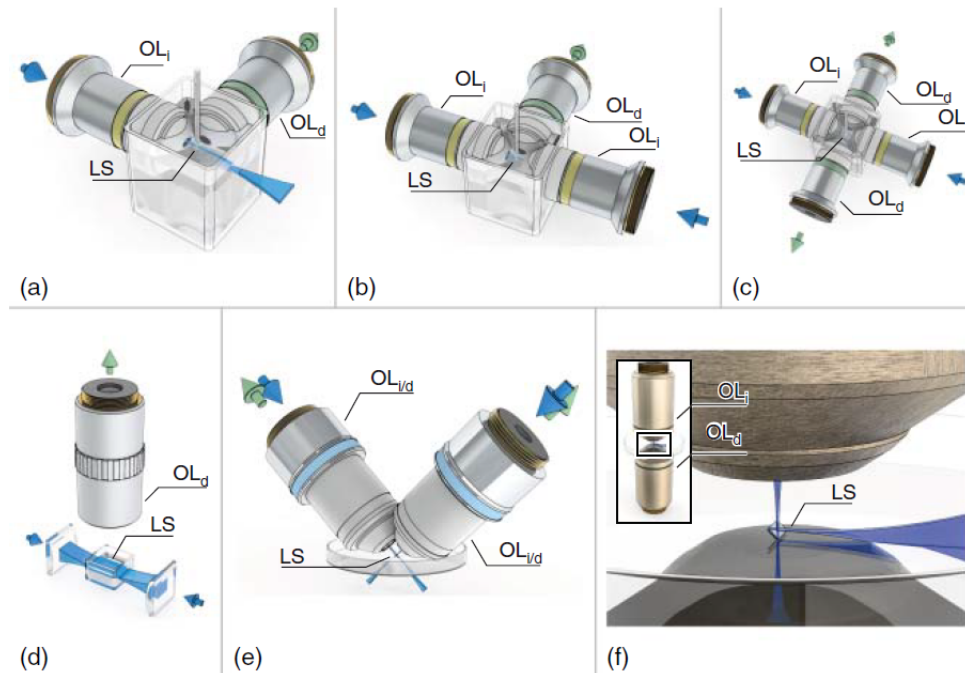


Figure 2.20: Light-sheet Fluorescent Microscopy objectives configuration. (a) single illumination single detection SPIM design with a vertical sample (b) Dual illumination single detection Multidirectional selective plane illumination microscopy (mSPIM) design with a vertical sample, (c) Dual illumination dual detection Simultaneous Multi-View selective plane illumination microscopy design with vertically mouted sample, (d) Ultramicroscope design, with a single detection objective in an upright configuration and two cylindrical lenses as illumination objectives. The sample is mounted horizontally, (e) Dual inverted selective plane illumination microscopy (diSPIM) design where the two objectives are used for both illumination and detection. Samples on coverslips are imaged with diSPIM, (f) Reflected light sheet microscopy where a small mirror close to the specimen is used to create an orthogonal light-sheet. The figure was extracted from the work of K. Ulrich [24].

mechanical movement of the sample (to reach multiview imaging). Immobilizing the sample and reaching multiview imaging through sample scanning will translate that bottleneck to the scanning speed and ultimately to the data acquisition speed of the camera. An investigation within the literature revealed that there exists two methods to achieve such imaging speed. Initially, an electrical tunable lens in combination with a scan mirror can be used to scan a LS through the sample. Both the tubable lens and the scan mirror are required to align and scan the LS on the imaging plane of the LSFM

LSFM Configuration	FOV	Ideal Sample
SPIM (Figure 2.20(a))	100-500 μm	Small transparent embryos
DSLM (Figure 2.20(a))	100-500 μm	Small embryos
mSPIM (Figure 2.20(b))	100-500 μm	Small transparent embryos
Multi-View SPIM (Figure 2.20(c))	250 μm - 1mm	Long term <i>in toto</i> <i>Drosophila</i> embryogenesis
Simultaneous Multi-View LSFM (Figure 2.20(c))	250 μm -1mm	Long term <i>in toto</i> <i>Drosophila</i> and zebrafish embryogenesis
Ultramicroscope (Figure 2.20d)	500 μm -2mm	Cleared tissue
Inverted SPIM (Figure 2.20e)	50-300 μm	Long term <i>in toto</i> <i>C. elegans</i> embryogenesis.
Dual-View Inverted SPIM (Figure 2.20e)	50-300 μm	Long term <i>in toto</i> <i>C. elegans</i> embryogenesis.

Table 2.1: Summary of light-sheet fluorescent microscopy configurations listing their field of view and some of their biological applications [4, 83]

microscope. SPIM and dual illumination SPIM have been modified to implement that feature [84, 85]. The volumetric imaging process using an ETL in the detection path and a scanning mirror in the illumination path is shown in Figure 2.21 The scanning mirror is responsible for scanning the LS, while the ETL ensures the projection of the illuminated plane on the camera. A second method used to increase the scanning speed

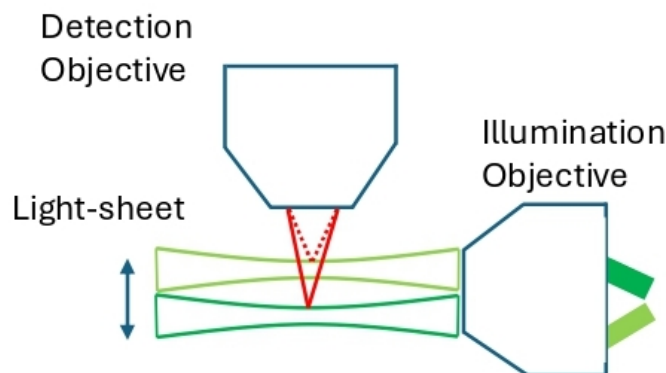


Figure 2.21: Volumetric imaging process using an ETL in the detection path and a scanning mirror in the illumination path. The figure was extracted from the work of F.O. Fahrbach et al [86].

is to apply wavefront coding to a light sheet microscope. This technology is achieved by

placing a suitable phase mask at the exit pupil of the objective lens and it will make the system capable of producing optical sections from out-of-focus planes. By extending the depth of field of the detection optics, fewer illuminations are required since a thicker LS can still give the desired depth information in the detection arm [87, 88]. Our research group has experience with adaptive optics; therefore AO elements were used to allow scanning of the light sheet [89]. The SLM used sets the imaging speed of the constructed microscope to 40 frames per second, which is the refresh rate of the SLM at its maximum resolution.

2.7.5 LSFM Adaptive Optics Microscopes

As every optical setup, the performance of LSFM suffers from aberrations, scattering and absorption. One of the key technologies we wanted to incorporate, in order to reduce the effect of aberrations and improve performance, is AO.

DM and SLM are the main components introduced to an optical system to apply adaptive optics. The nature of a LSFM microscope allows using simultaneously both an SLM and a DM, one in the illumination path and one in the detection path [90]. An SLM has been introduced in the illumination path, where by taking feedback from a second camera, the LS could be manipulated to improve the axial resolution [90]. Additionally, a DM has been placed in the detection path, with the main system's camera as a sensor, it was capable to control the focal plane of the microscope [91]. An SLM in the illumination path can also do AO corrections. As shown in the work of D. Wilding, [92], an SLM has been introduced in the illumination path to correct phase aberrations, which also improves the axial resolution of the LSFM. SLMs in the detection path can also manipulate the geometry of the LS and simulate the work of two galvo-scanners. The work of L.A. Royer [93] demonstrates a LS with highly manipulated geometry achieved by two galvo-scanners in the illumination path. Theoretically this can also be done with two SLMs, however there is a major effect on the system's cost and imaging speed. SLMs are used mainly in the illumination path since their operation is highly correlated to the wavelength and polarisation of the beam to be corrected (discussed in Chapter 4), hence it would have caused problems due to emission being

non-polarised for our applications if placed in the detection path.

An SLM can improve the adaptability of the microscope (use various beams for the LS generation - Bessel, Airy, Lattice) and also improve the axial resolution by correcting for aberrations and shaping the LS [94]. Moreover an SLM can modulate the LS, leading to imaging with different methods, such as structured illumination, pivoting, auto-focusing and DSLM, with the same microscope which would improve the multi-functionality of the microscope [95]. Combining an SLM in the illumination path and a construction of the illumination path with a cage system would allow having different conjugation between the SLM and the focal plane of the illumination objective, providing control over the LS thickness [95]. The drawback of the SLM is that it limits the imaging speed to its refresh rate.

As demonstrated by D. Wilding et al [90] and R. Jorand et. al [96] AO corrections in the detection path can be achieved by a DM. The combination of a DM in the detection path and a S-H WFS can correct for wavefront errors and thus improving imaging quality. As described in Chapter 2, Microscopes are typically designed for specific imaging conditions, the addition of AO allows a degree of reconfiguration without needing to rebuild the instrument. As such, it widens the range of samples which can be imaged with that sample, and is highly beneficial for researchers.

2.8 Nitrogen-Vacancy Centers in Nanodiamond

Pure diamond consists entirely of carbon atoms. Synthetic and natural diamonds can host various impurities, such as different atoms in the place of atoms in the diamond lattice or vacancies. The NV defect consists of a nitrogen atom at one of the carbon sites in the diamond lattice and a vacancy in one of the adjacent sites. The two most commonly observed charge states of the NV centre are the neutral and single negative charge; in this thesis NV centre will refer to the negative state of the NV centre since there is an emission spectrum difference between the neutral and negative states and the microscope was built to observe the negative state. This is because NV sensing relies on the spin properties of the negative state [97–100].

2.8.1 Structure and Optical Properties

A substitutional nitrogen atom and vacancy pair forms the NV centre. A diamond crystal lattice with a NV defect in its centre is shown in Figure 2.22 (a) and the NV centre quantisation z-axis is shown in Figure 2.22 (b).

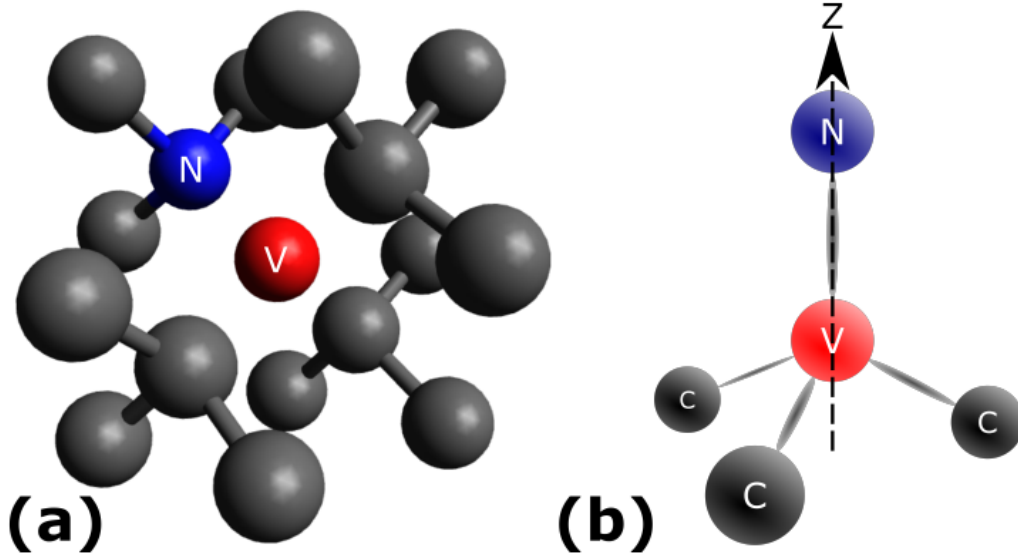


Figure 2.22: a) Nanodiamonds lattice with an Nitrogen-Vacancy defect centre. Carbon atoms are represented in grey, the nitrogen atom is in blue and the vacancy in red. b) The coordinate axis of the Nitrogen-Vacancy centre. The z-axis defines the magnetic field sensing measurement axis. The figure was extracted from the work of A. J. Tyler [97].

The electronic structure of the NV defect is shown in Figure 2.23. The ground state $|g\rangle$, a spin-triplet, is split into three spin sublevels. The $m_s = \pm 1$ sub-levels are degenerate at zero magnetic field, and $m_s=0$ state at lower energy. The splitting between $m_s = \pm 1$ and $m_s=0$ is 2.87GHz. An optically excited NV centre reaches its excited state $|e\rangle$, also a spin-triplet state. The optical decay lifetime of the excited state is about 12 ns in FND [101]. There are also two metastable singlet states shown as $|s\rangle$. The metastable singlet states allow the NV centre defect to be optically spin polarised through the application of light. Illuminating the NV centre with a wavelength between 450-610nm drives the defect to the excited state. The excited state relaxes optically, resulting in photoluminescence (637-850nm). Relaxation can

also occur via the singlet states which does not result in emission in the 637-850nm band. The relaxation through the singlet states depends on the spin state of the NV centre. When the spin is in the $m_s = \pm 1$ sublevel, the probability of relaxation via the single state is higher while the spin decays out of the singlet state to the ground $m_s=0$ substate; therefore, the NV centre can be optically spin-polarised [97–100].

As described above, the photoluminescence of the NV centre is spin-dependent. The decay via the singlet state is non-radiative, and the probability of decay through the singlet state depends on the spin projection on the NV centre (high probability for the $m_s = \pm 1$ sublevel and low probability for $m_s = 0$). Low probability of non-radiative decay will appear brighter; therefore, the relaxation through the singlet state enables the optical readout of the spin state by optical means by detecting the photoluminescence intensity [97–100, 102].

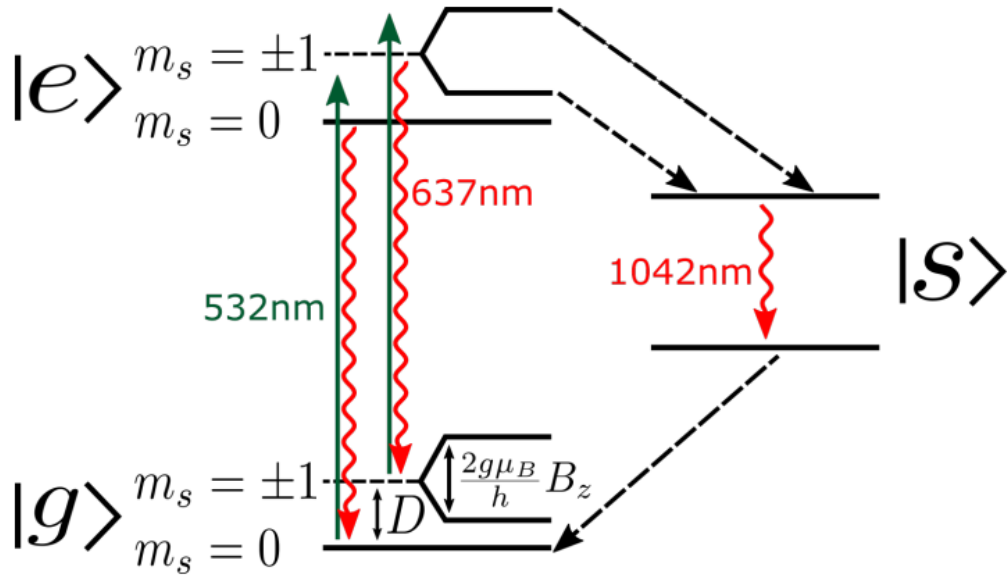


Figure 2.23: Electronic structure of the Nitrogen-Vacancy centre. $|g\rangle$ represents the ground state, a spin-triplet state with m_s representing the spin projection along z -axis. D shows the zero-field splitting between the ground state sublevels and $m_s = \pm 1$ are degenerate at zero magnetic field (dashed line represents the energy). The solid lines represent the lifting of the degeneracy with the application of a magnetic field along the z -axis. $|e\rangle$ is the excited state (also a triplet) and the singlet state is represented by $|s\rangle$. Green lines represent the excitation with a green laser and the red lines represent the optical relaxation. The figure was extracted from the work of A. J. Tyler [97].

2.8.2 Nitrogen-Vacancy Centre in Magnetic Fields

NV centres can be used for magnetic field sensing by detecting the Zeeman splitting of the NV centre-ground state. This can be achieved by recording the photoluminescence intensity while microwave frequencies close to the zero-field transition are swept. Figure 2.24 a) shows the photoluminescence intensity when no external magnetic field is applied. When an on-axis (z-axis or NV centre axis) magnetic field is applied, Zeeman splitting is observed, as shown in Figure 2.24. The greater the magnetic field, the greater the separation of the two intensity dips in photoluminescence [97,99,100].

Equation 2.18 describes the transition frequencies between the $m_s=0$ state and the $m_s = \pm 1$ state.

$$\nu_{\pm} = D \pm g\mu_B B_z/h \quad (2.18)$$

D refers to the axial zero-field splitting parameter (equal to 2.87GHz at room temperature and zero magnetic field [103]), B_z is an on-axis magnetic field, and g , μ_B are fundamental constants. The detection of the transition frequencies the magnetic field applied can be calculated. Hence, NV centres can be used magnetic field sensing [97–100,104].

2.8.3 Nitrogen-Vacancy sensing

FNDs are excellent candidates for sub-cellular sensing because of their photostability, biocompatibility and sensitivity to temperature, magnetic field and electric field [7,31,38]. NV centres have been used to detect electric fields, temperature, and magnetic fields with nanoscale spatial resolution [103,105].

Among others, an example of the interaction of temperature, magnetic field and electric field on the ODMR recordings as presented by Masfer H. Alkahtani et al [7] are shown in Figures 2.25, 2.26 and 2.27 respectively. As shown in Figure 2.25 an increase of the local temperature of the nanodiamond translates to the movement of the zero-field splitting of the ground state towards smaller values. This occurs because of the crystal expansion during the increase of the temperature. A temperature sensitivity of $1.8\text{mK}/\sqrt{\text{Hz}}$ in pure bulk diamond and a sensitivity of $200\text{mK}/\sqrt{\text{Hz}}$ in living

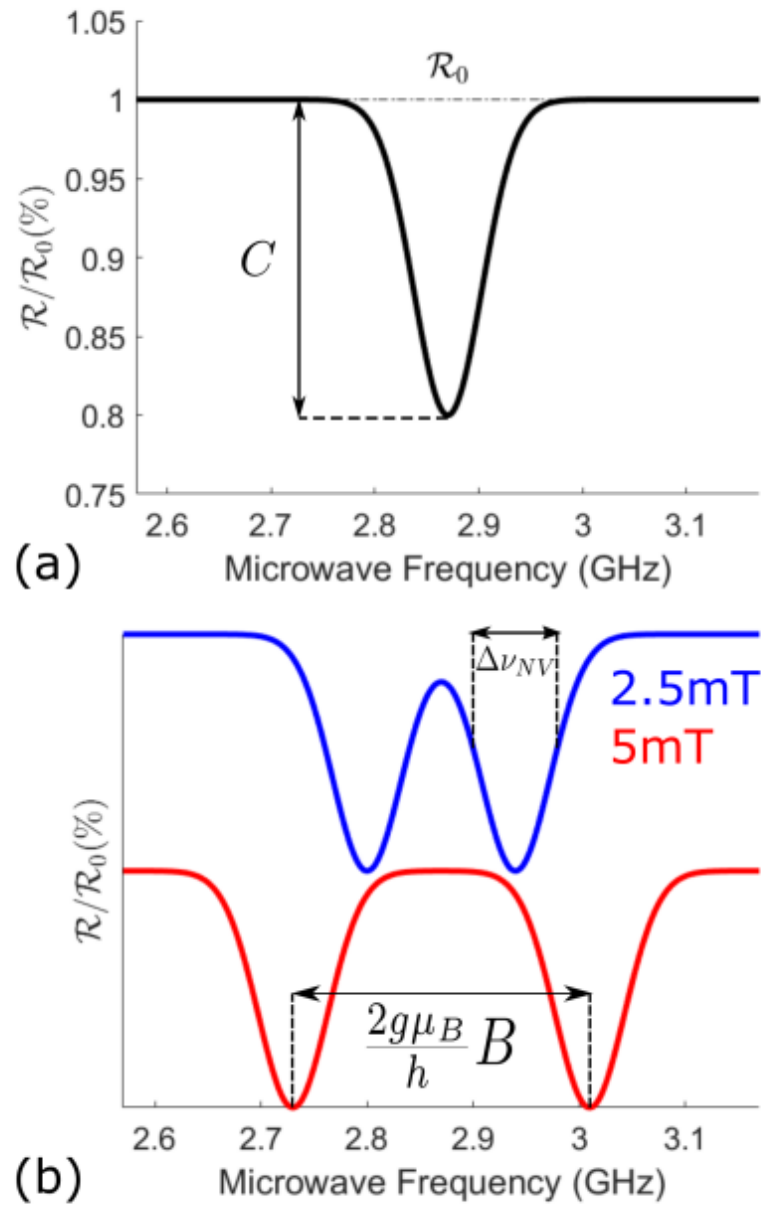


Figure 2.24: a) Optically detected magnetic resonance measurement of single Nitrogen-Vacancy centre with no magnetic field applied. When a microwave frequency is applied and shifts the Nitrogen-Vacancy centre from the $m_s=0$ state to the $m_s = \pm 1$, the photoluminescence intensity drops (R_0). C refers to the magnitude for resonance, which is the ratio of the off resonance count rate to the on resonance count rate. b) Zeeman splitting due to a magnetic field B_z that is applied at the z-axis of the NV centre. The two observed resonances correspond to each of the $m_s=0$ to $m_s = \pm 1$ transitions. $\Delta\nu_{NV}$ is used to characterise the resonance. The figure was extracted from the work of A. J. Tyler [97].

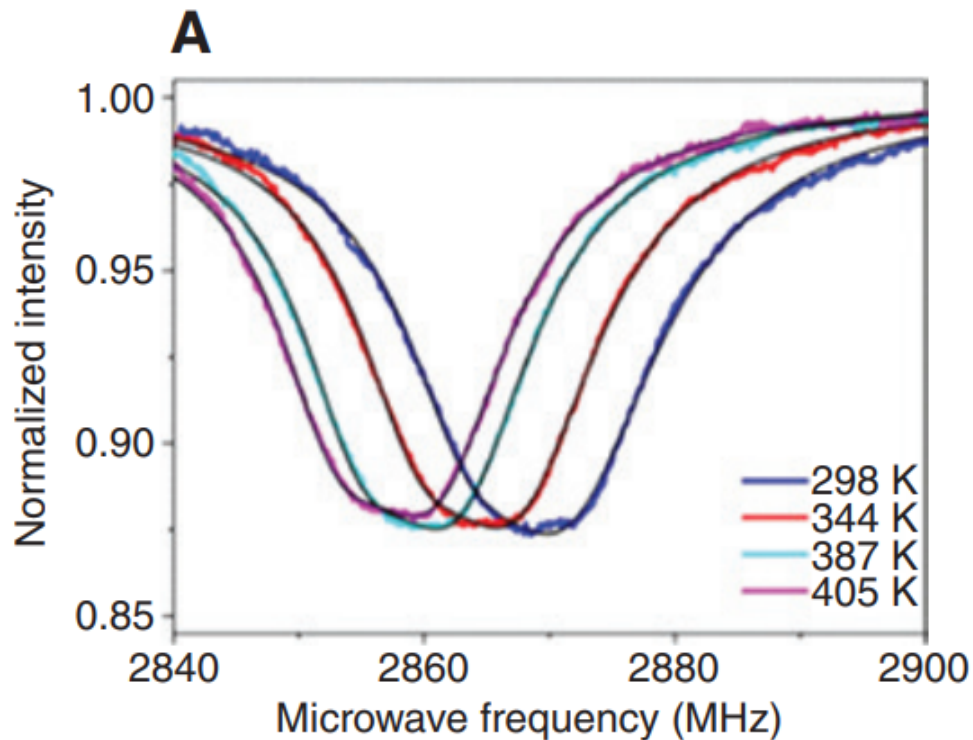


Figure 2.25: Optically detected magnetic resonance recordings of the Nitrogen-Vacancy centre defect for different local temperature changes. The greater the temperature, the smaller the value of the ground state splitting. The figure was extracted from the work of M. H. Alkahtani et al [7].

cells have been reported; therefore ODMR frequency is temperature depended and can be used for thermometry. The larger spin line-width in nanodiamond compared to bulk diamond decreases the observed sensitivity in the experiments on living cells [7]. Subcellular temperature measurement is a method of investigating temperature-related phenomena, such as the variation of cell-death types in photothermal cancer therapy, cellular thermotaxis and cellular level thermogenesis [106]

Figure 2.26 shows the effect of an external magnetic field on the ODMR measurement of a single NV centre. A single resonance appears when at zero external magnetic field. When an external magnetic field is applied, two dips are presented. The magnetic field can be measured from the position of these two dips, since as the external magnetic field increases the position of the two dips changes. This is valid for magnetic fields

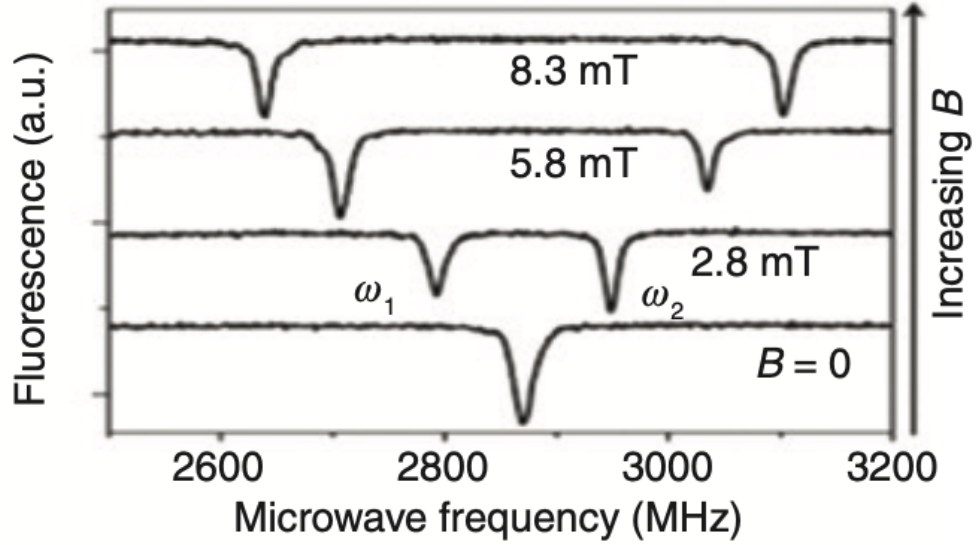


Figure 2.26: Optically detected magnetic resonance recordings of a single Nitrogen-Vacancy centre defect as the external magnetic field increases. The top represents the higher magnetic field applied while the bottom is the Optically detected magnetic resonance recording when there is no external magnetic field. ω_1 and ω_2 refer to the position of the Optically detected magnetic resonance lines. The figure was extracted from the work of M. H. Alkahtani et al [7].

axial to the z -axis of the NV centre, parallel to the z -axis of the optical microscope. In the case of non-axial magnetic fields the ODMR dips can move in the same directions. Magnetic field sensing can be used for monitoring neuron firing [7].

The electric field sensitivity has been investigated by applying controlled voltage to a gold microstructure that has been fabricated by lithography and placed directly on a bulk nanodiamond sample containing NV centre defects. As shown in Figure 2.27, the electric field introduces shifts in the spin sub-level. It has been found that a resonance line shift of 28.4kHz occurs for an electric field of 3000 V/cm while an electric field sensitivity is $202 \text{ V/cm}\sqrt{\text{Hz}}$ [7]. Electric field sensing can be used for monitoring membrane potentials.

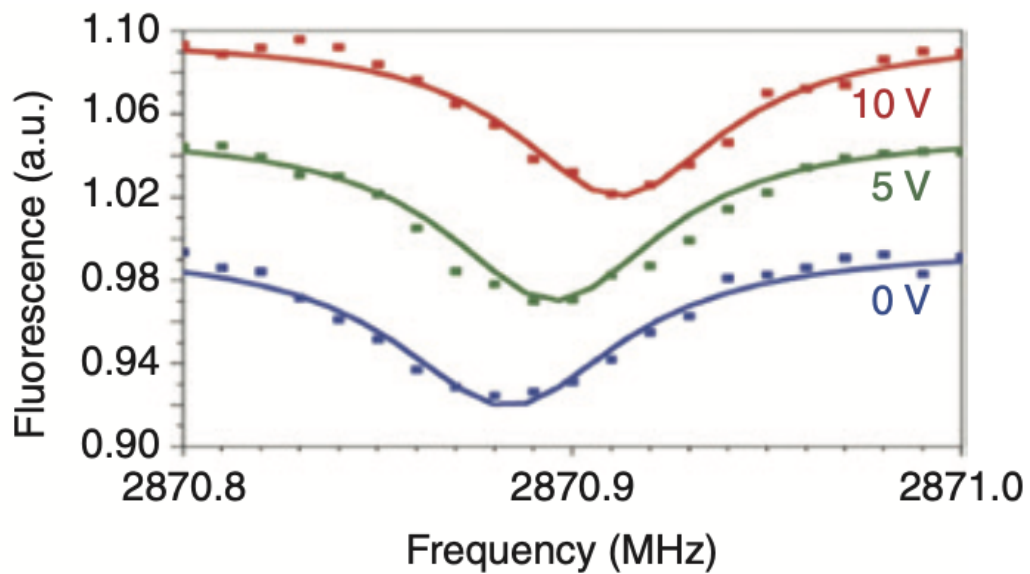


Figure 2.27: Optically detected magnetic resonance recordings of the Nitrogen-Vacancy centre defect when voltage is applied to create an electric field. The voltage is applied on the electrodes of a microstructure on the diamond sample that creates an electric field. The figure was extracted from the work of M. H. Alkahtani et al [7].

2.8.4 Wide-field magnetometry and thermometry

Magnetometry and thermometry using NV defects can be achieved because ODMR of electron spin in diamond NV defects is sensitive to both external magnetic fields and temperature. ODMR measurements can be recorded either with a photon counter control detection or a camera based wide-field detection. Confocal-based ODMR measurement emphasises on extracting information from a single FND, while wide-field can get data simultaneously from multiple FNDs within a large FOV [106]. Therefore, wide-field ODMR reduces the ODMR measurement time compared to confocal scanning [103]. The time-limitation of confocal-point scanning arises from the fact that confocal relies on a moving spot to excite fluorescence. Even with a short pixel dwell time it is time consuming to acquire an image. In wide-field illumination, there is no scanning beam; therefore the acquisition time is a function of the exposure time of the camera.

Wide-field magnetometry setup consists of a wide-field imaging subsystem, a microwave delivery subsystem and an external magnetic field control subsystem. Simple

imaging systems of a detection objective, a tube lens, and an imaging sensor can be used to extract ODMR [103]. The ODMR microwave system consists of signal generators, RF switches, attenuators and RF amplifiers [12, 103]. Magnetic field control can be achieved by current-controlled electromagnets [105]. The orientation of the magnetic field in respect to the NV z-axis has an effect on the ODMR signal. The position and angle dependence of the NV centre z-axis on the applied magnetic field and the frequency of resonance pairs can be used to reconstruct the magnetic field vector [103]. A wide-field ODMR in an imaging area of $300\mu\text{m} \times 250\mu\text{m}$ is reported in [103, 105]

Wide-field thermometry setup is similar to the magnetometry setup, but instead of a magnetic field control subsystem a heater controller is used [106]. Y. Nishimura et al. [106] compared confocal-based temperature measurement to wide-field thermometry in living cells. Their work present a method of wide-field temperature measurement that achieves the same performance as the confocal thermometry. This paves the way for further investigation of wide-field ODMR and LSFM, a 3D wide-field imaging technique, ODMR, in applications such as real-time thermometry of living cells, regions of a living cell, and a whole living organism [106]. LSFM ODMR could provide temperature and magnetic field measurements in the entire volume of a sample.

2.9 Summary and Discussion

The fundamental principles of fluorescence microscopy are described in this Chapter. Concepts such as image formation, magnification and imaging resolution, required for the design of a microscope are described. The necessity of 3D imaging techniques is presented along with volumetric imaging techniques that can achieve cellular resolution. The purpose of this research is to image freely moving living organisms in a millimetric FOV, with a cellular resolution at a relevantly high imaging speed. Confocal microscopy results in a high resolution imaging, but lacks in imaging speed. Spinning disk confocal microscopy images at a high rate [107] but it is limited on the FOV that can be imaged (less than 1mm FOV) [108]. LSFM is chosen because it fulfills the imaging criteria. The geometry of the LSFM also allows the application of AO for light modulation and aberration corrections. Imaging improvements at the depth of view of interest ($100\mu\text{m}$)

have been reported in the literature; therefore, an AO LSFM was investigated [109–113].

Additionally, in this Chapter the major LSFM configurations have been investigated to identify which one, or combinations, is the most suitable for millimetric imaging of optically transparent living organisms at cellular resolution. It is found that each of the described techniques has advantages and limitations. The LSFM configuration of my microscope was decided by the samples of interest for this project (*C. elegans* and FNDs). An upright LSFM configuration was selected because it enables imaging of freely moving *C. elegans*. Imaging was achieved through a single detection arm and dual-beam illumination, illuminating the sample sequentially. This way we overcome the effect of shadowing and simultaneously improve the imaging resolution, compared to a single-beam illumination LSFM.

Adaptive elements were implemented in both imaging paths. An SLM was embedded in the illumination path and a DM in the detection path. Initially the SLM implemented LS scanning, but further software development and hardware calibration would allow it to perform AO corrections and imaging with different beams (Bessel, Lattice, Airy). A DM in the detection arm could improve imaging quality by applying AO corrections and with wavefront coding. We identified a suitable DM and calibrated it for use in the microscope, however the impacts of Covid mean that AO correction with a DM in this microscope is still a task for the future. Both AO elements offer adaptability regarding the application of the microscope. An ODMR setup was also implemented to the microscope for wide-field and LSFM ODMR measurements. Although the imaging techniques and microscope configurations used existed, my research combined ultra large FOV (2mm) and DOF (0.9mm) with AO elements in both the detection and illumination paths, capable of conducting LSFM ODMR measurements, which has never been reported.

In continuous Wave (CW) ODMR, the NV centre defect can be prepared in the $m_s=0$ by continuous optical illumination. By applying a resonant microwave field, the defect is driven in the $m_s = \pm 1$ substate. When excited at this state the probability of non-radiative relaxation is higher. When applying a range of microwave frequencies, the resonance is detected by the decrease of photoluminescence intensity. The opti-

cal detection of the spin state enables the detection of Zeeman shifts in the spectral position of the $m_s = \pm 1$ states resulting in the ODMR spectrum. [97,98,100]. External parameters that affect the CW-ODMR spectrum quality are the microwave power (microwave heating [114], ohmic heating [115], power broadening), the laser power (excitation rate), and the microwave sweeping method and pace. Laser power should be high enough to ensure spin polarisation. A very high laser power would have a negative impact on the ODMR contrast since the optical excitation would be relevantly high compared to the microwave excitation, and thus the difference between the $|m_s = 0\rangle$ and $|m_s = \pm 1\rangle$ will be less. Microwave power increasing would initially improve the contrast of the ODMR spectrum and at a point it will reach a saturation of the spin transition [116].

Pulsed ODMR typically offers better sensitivity, compared to CW ODMR, at the expense of complexity [117] since precise calibration and strict synchronisation of hardware is required [118]. Several sequences can result in pulsed ODMR; however, the most common to all sequences is a first laser pulse that sets the system in the $|m_s = 0\rangle$ state, followed by a period of microwave pulses for spin manipulation, and a second laser pulse that extracts information from the $|m_s = 0\rangle$ and $|m_s = \pm 1\rangle$ states through the optical emission intensity. Optimisation of the ODMR spectrum from pulse-ODMR depends on the pulsed protocols used [116].

LSFM pulsed ODMR was initially considered. An AOM was included in the initial LSFM design to allow laser pulsing and thus enable pulsed ODMR spectrum recordings; however, due to hardware limitations (described in Section 5.1) the LSFM pulsed ODMR experiments were not conducted. Pulsed ODMR sequences were not further investigated since the work presented in chapter 4 emphasises on CW ODMR.

Chapter 3

Light Sheet Fluorescent Microscope Design for Imaging Whole Living Organisms

Recent research presented living *C. elegans* LSFM imaging [119, 120]. In both cases the *C. elegans* was anaesthetised, and fixed for imaging. A detection objective of NA 1.0 was used in both cases, providing a submicron lateral resolution, and a few microns axial resolution. This axial resolution is related to the detection objective. If the LS's thickness is greater than the axial resolution of the detection objective, the LS thickness determines the axial resolution of the LSFM. Such detection objective limits the imaging FOV, therefore sample translation is required to obtain a full image of a 350 μm larvae [120]. Both works presented a single illumination beam, single detection arm LSFM, where sample rotation is essential for multiview imaging.

Both works of J. Van Krugten et al. [119] and Jayson J. Smith et al. [120] presented an exceptional imaging of anaesthetised *C. elegans*; however after few hours the physiology changes due to starvation. My work investigates imaging *C. elegans* for the L1 larvae stage (about 250 μm long) to adults (1 mm long) freely moving in their feeding environment. This enables the investigation of further biological processes in living organisms.

This chapter presents the design of a custom made LSFM that can image freely

moving whole organisms at a cellular resolution. The design includes the mathematical modelling of the LSFM, the selection of optical elements and hardware, the control software and the custom made 3D printed sample holders.

3.1 Mathematical Modelling

As explained in Chapter 2 a dual illumination, single detection LSFM in an ultramicroscope configuration is the most suitable for our application; therefore, my design is based on an ultramicroscope configuration. This microscope is designed to image freely moving *C. elegans*, a 1 mm ground-worm. Therefore, a FOV of 2 mm is required to capture the movement of the sample of interest. Dual illumination means that each illumination arm will have a FOV of 2mm×1mm in propagation, and thus the total FOV of the microscope is 2 mm. My design is based on the information provided in Chapter 2.

3.1.1 Illumination Parameters

Applying an illumination beam wavelength (532 nm), and the desired FOV (1 mm for each illumination side) in Equation 3.1, the numerical aperture of the illumination objective has been calculated to be $NA_{ill} = 0.03$.

The light sheet thickness can be then calculated either at the edge of the FOV or at centre of the FOV. For my mathematical modelling, the beam diameter and thus the LS thickness is calculated at the edge of the FOV using equation 3.2. With an illumination NA of 0.03, the LS thickness at the edge of the FOV is 21.6 μm . The illumination NA of our system is low enough that a Cylindrical Lens (CL) can be used to focus the LS on the sample instead of an objective lens. The CL focal length can be calculated by:

$$f_{CL} = \frac{D_p}{2 \times NA_{ill}} \quad (3.1)$$

where, D_p is the diameter of the beam at the entrance pupil of the system. Due to system requirements that are going to be discussed later in this Chapter the diameter of the beam at the entrance of the cylindrical lens is 6 mm. Therefore, a 100 mm

cylindrical lens is required to achieve a 0.03 illumination NA.

3.1.2 Detection Parameters

The detection arm of the system is mathematically modelled to achieve isotropic imaging, where the axial resolution is equal to the lateral resolution. Hence, by setting the axial resolution of the detection arm equal to the LS's width at the edge of the FOV (equation 4.2) we can calculate the NA of the detection path. The axial resolution of the detection arm is defined as:

$$R_{detaxial} = 1.78 \times \frac{n \times \lambda_{det}}{NA_{det}^2} \quad (3.2)$$

where, λ_{det} is the detection wavelength, while the NA_{det} is the numerical aperture of the detection objective. Therefore, the detection objective NA can be calculated by:

$$NA_{det} = \sqrt{\epsilon \times \frac{1.78 \times n}{1.22} \times NA_{ill}} \quad (3.3)$$

where $\epsilon = \lambda_{em}/\lambda_{ill}$. The NA of the detection objective is calculated to be 0.24. The lateral resolution can then be calculated by equation 2.7. The lateral resolution of the detection objective of 0.24 NA is 1.8 μm . However, we decided to sacrifice isotropic imaging to achieve a better lateral resolution. We were imaging with a detection objective of 0.4 NA and a focal length of 16.45 mm. This results in an axial resolution of 7.79 μm , when imaging through air, and a lateral resolution of 1.06 μm .

To digitise images, minimum sample of a Nyquist rate is required (described in Section 2.2); therefore, considering the Nyquist criterion, modeled pixel size can be represented as [121]:

$$R_T = 2 \times pixelsize_i \quad (3.4)$$

where, $pixelsize_i$ is the size of the imaged pixel. Thus, the imaged pixel size is 0.53 μm . The formula used to estimate the minimum required magnification of the detection

path is given by:

$$M = \frac{\text{camera pixel size}}{\text{image pixel size}} \quad (3.5)$$

Since we decided to use a PrimeBSI camera with a $6.5\mu\text{m}$ pixels, a magnification of 12.6 was required to image with such resolution. However, the result of the multiplication of the magnification to the FOV of the image (FOV_I) should be able to be projected to the size of the detection sensor (FOV_d). Therefore, the FOV generated by the detection system should satisfy the following formula.

$$FOV_d = FOV_i \times M \quad (3.6)$$

So, a magnification of 12.6, as calculated above, will result in a FOV of 1.085 mm. Since I am interested in a 2 mm FOV and I am willing to sacrifice sampling and resolution as long as the resolution remains in the $3\mu\text{m}$ - $30\mu\text{m}$ window, the magnification of our system is set to 6.65. Finally the focal length of the tube lens was calculated using Equation 2.3. A tube lens with a focal length of 110mm was required to achieve such a magnification.

3.2 Optical Design

The optical schematic of the adaptive LSFM designed in Inkscape software is shown in Figure 3.1. A laser (CNI 532 nm 300 mW single longitudinal mode laser) was used for fluorescence excitation, while an acousto-optic modulator (M1205-T80L-2, 488 nm-633 nm) was included to modulate the laser beam. The beam was expanded by a 1:5 achromatic lens system L1 (f=25 mm, Thorlabs) and L2 (f=125 mm, Thorlabs), polarised (GTH10M-A, Thorlabs) and split (CCM1-BS013/M 50:50, Thorlabs) to create dual illumination. Both illumination beams were transmitted to the SLM (1920x1152 XY Phase Series, Meadowlark Optics) by passing through a half-wave plate (AHWP10M-600, Thorlabs). The SLM was conjugate to the back focal plane of the CL (LJ1567L1-1-f=100mm, Thorlabs) through a 1:1 4f system L3 (f=200 mm, Thorlabs) and L4 (f=200

mm, Thorlabs), so the tilt the SLM induces becomes a shift at the front focal plane, hence two LSs were illuminating the sample. Two corner cube reflecting prism mirrors (MRAK25-P01, Thorlabs) were used, one to bring the two beams close enough to each other, so that they can both be refracted at the same SLM, and the second one, to push them apart to achieve the desired two side illumination (both illumination arms are identical) with a single SLM. The detection objective (C Epiplan-Apochromat 10x/0.4, Zeiss) was in an upright configuration, perpendicular to the LSs, and its back focal plane was conjugated with the position of the DM through a 1:1.2 4f system L5 ($f=250$ mm, Thorlabs) and L6 ($f=200$ mm, Thorlabs). The imaging is achieved by an sCMOS camera (PRIME BSI) with a TL L7 ($f=100$ mm) and an optical long-pass filter (FELH0550/FELH0600/FELH0650) in the path. The three long-pass filters were mounted on a rotation filter wheel, enabling switching among the three, depending on the imaging sample.

Through my project planning, a cost effective DM that does not guarantee stability in an open loop configuration was used. Therefore, to ensure repeatability, DM surface monitoring was required. I designed surface monitoring setup, for the DM, using a S-H WFS (sCMOS camera CS2100M, Thorlabs and a lenslet array MLA300-14AR-M, Thorlabs) and a laser (CPS405, thorlabs), used for illumination. A beam expander 2:1 L11 ($f=100$ mm) and L12 ($f=50$ mm) ensures the illumination of the entire DM surface and a 4f system 1:2 L13 ($f=250$ mm) and L14 ($f=125$ mm) conjugates the DM with the back focal plane of the lenslet array. This creates a feedback DM feedback control loop, where its performance is controlled by the wavefront sensor and not by the supplier's software.

3.3 CAD Modelling and Mechanical Design

To finalise the microscope's design process, a mechanical design that consists of an optical breadboard mounted vertically on an optical table was adopted. To verify the feasibility of the microscope's construction, the optomechanical components required to realise my design were identified and a 3D computer model was generated in Sketchup

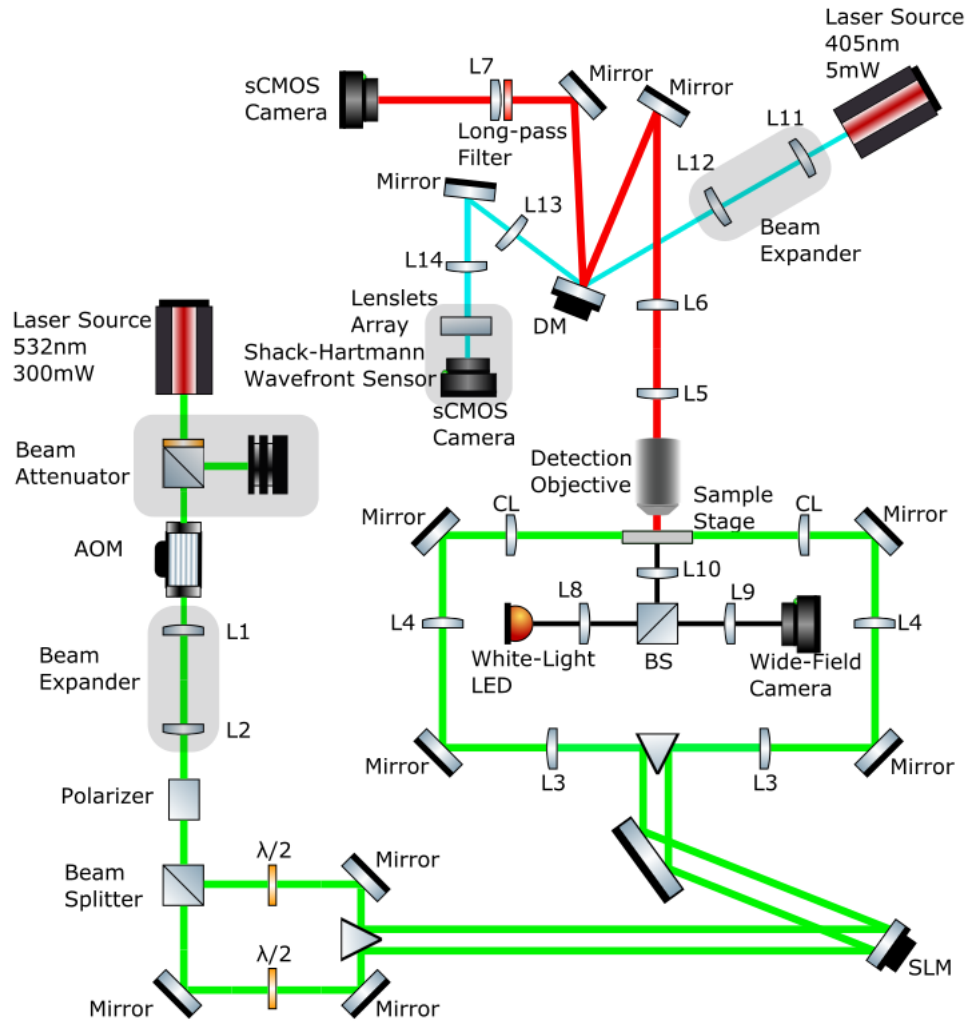


Figure 3.1: Optical schematic of the adaptive light-sheet fluorescent microscope. An acousto-optic modulator was used for laser modulation, while a spatial light modulator conjugated with the back focal plane of the cylindrical lens was used for scanning the light-sheet. An upright detection, perpendicular to the light-sheet collects the excited fluorescence and a deformable mirror in combination with a Shack Hartmann wavefront sensor are correcting aberrations. Simultaneously the entire field of view can be imaged by a wide-field camera and illuminated via a white light LED. The figure is a representation of my work conducted in Inkscape using the ComponentLibrary created by A. Franzen [122]

[123].

The vertical breadboard was mounted on the optical table via two vertical brackets

for breadboards and a 66 mm rail to reduce vibrations. Both the illumination and detection paths were designed for optics with a diameter of 25 mm and mounted on the table through 25 mm pedestal pillar posts in such a way that the optical path is 150 mm above the optical table and 80 mm away from the vertical breadboard. All lenses were mounted on XY translation mounts, whilst the cylindrical lenses were mounted on a kinematic mount and on a single direction stage to ease the microscope's alignment. The objective was designed to allow the required refocussing the the Z plane when performing 3D imaging. Additionally, the sample was mounted on an XY linear stage with 13 mm translation and an aperture of 57.1 mm in combination with a vertical travel stage (LJ750/M - Ø2.64" Compact Lab Jack, 1" Vertical Travel). This allowed wide field imaging by illuminating underneath the sample in addition to the light sheet imaging. The finalisation of the CAD model paves the way to the LSFM microscope construction.

3.4 Large FOV Sample Holders Design

The multi-purpose nature of this work required an adaptable sample holder. The aim was to design a sample holder that allowed imaging coverslips of various sizes (18x18 mm, 22x22 mm, 50x22 mm) and different angles (0°, 30° and 45°), microscope slides, capillaries, and cuvettes. Imaging coverslips at different angles are used to characterise the light sheet (this is shown in more detail in Chapter 4). Flat coverslips and microscope slides were suitable for single plane wide-field imaging, while cuvettes were used for volumetric imaging. Due to the diversity of the samples, imaging FND on a cover-slip, FND in agar, *C. elegans* on coverslip and *C. elegans* in agar, a platform that was mounted on the sample's z stage and brings the sample at the imaging level was considered.

A sample holder where the sample was fixed on a threaded hole platform was considered (Figure 3.2). However, this design blocked the wide field imaging as well as it limited the imaging of samples at an angle, as required for the microscope characterisation, due to the short working distance of the detection objective (5.4mm). I designed a platform where smaller sample holders, specifically designed for each sample, can be

Chapter 3. Light Sheet Fluorescent Microscope Design for Imaging Whole Living Organisms

attached (Figure 3.3). At first, a microscope slide holder was designed, as shown in Figure 3.4. This holder was used to image NDs and *C. elegans* in wide-field as well as to perform wide-field ODMR measurements. A sample holder capable of holding a slide at 45° was also modelled (illustrated in Figure 3.5). This was used for LSFM ODMR measurements and for *C. elegans* imaging. Coverslip holders at an angle of 30° and 45° were used for the initial LS characterisation. A design where the coverslip was glued on the holder is shown in Figure 3.6 and a design where coverslips of different sizes were slide into the holder is shown in Figure 3.7. Additionally, a glass capillary holder was designed as shown in Figure 3.8 and Figure 3.10 (b). The sample was inserted in the capillary and then sealed. The capillary was then placed in the tube sample holder and the sample holder was filled with glycerol to reduce the refractive index mismatch between glass and air. Coverslips were glued at the sides of the sample holder to seal the glycerol. A cuvette holder was designed (Figure 3.9) in addition to custom made 3D printed cuvettes (Figure 3.10). The platform as well as the microscope slide holder, cuvette holder and angular holder mounted on the microscope's imaging path are illustrated in Figure 3.11. All the designs are modelled in SketchUp and printed by the research's group 3D printer (S5 Ultimaker, S5 Material Station, which provides a 0.25mm resolution and 6.9 micron accuracy) with a PLA filament.

The geometry of the LSFM makes it challenging to have a universal sample holder. A custom made sample mount was designed for each experiment. The group's 3D printer made this a low cost and rapid process.

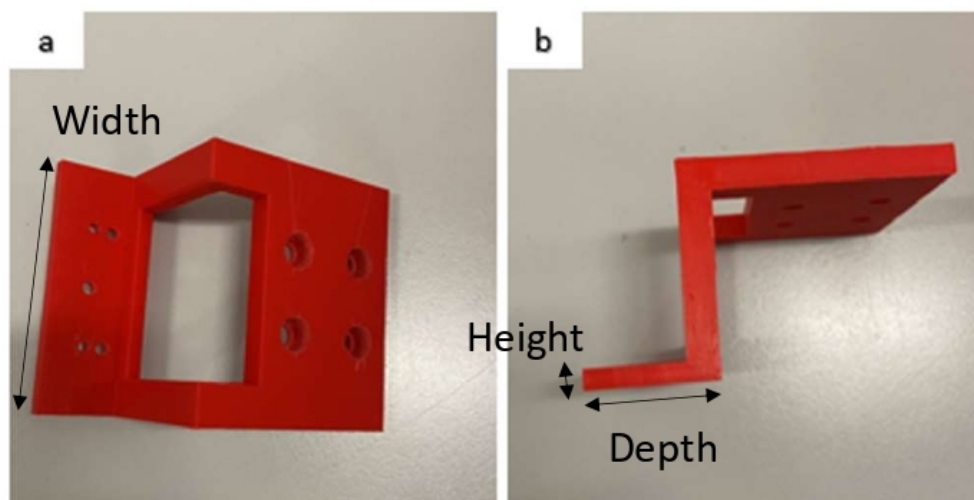


Figure 3.2: Customised generic purpose sample holder, fixed on the imaging platform. M3 and M4 holes are used to clamp the sample on the holder. Dimensions of the base are 80 mm x 4 mm x 25 mm (width × height × depth) a) and b) are the top view and side view of the fixed generic purpose sample holder.

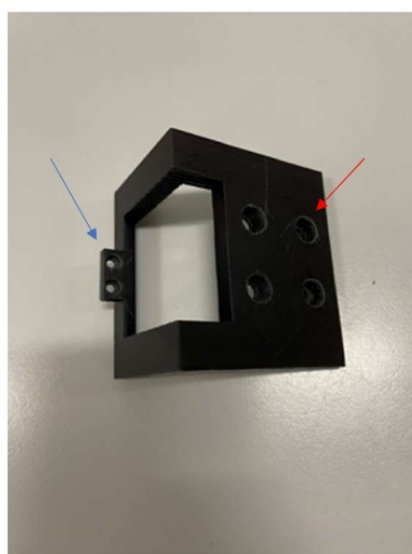


Figure 3.3: Generic sample holder mounting platform. M6 holes (red arrows) are used to mount the imaging platform on the z-stage and M3 holes (blue arrows) are used to mount the sample holder on the platform.

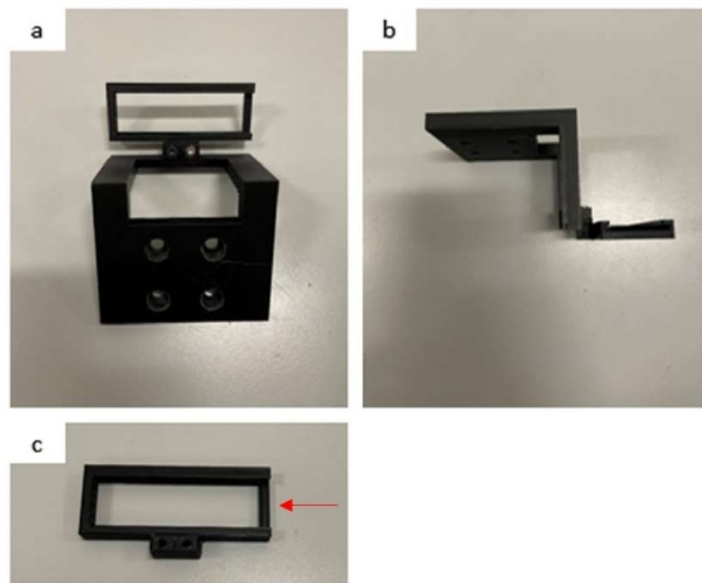


Figure 3.4: Microscope slide holder. a) Mounted on the platform, top view, b) Mounted on the platform, side view, c) Slide holder design with dimensions (width \times height \times depth) 80 mm \times 8 mm \times 30 mm. M3 holes are used to mount the holder on the mounting platform. The red arrow shows the direction that the slide is mounted on the holder

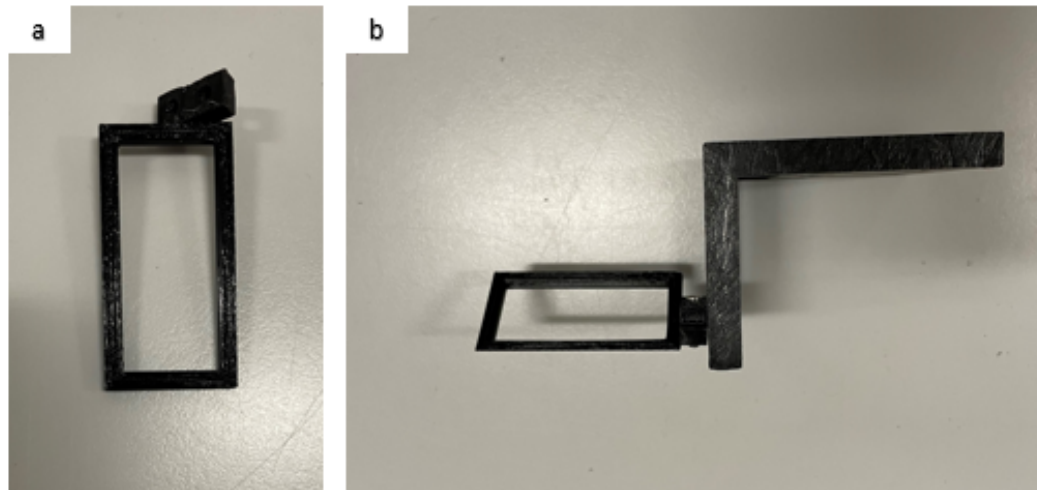


Figure 3.5: a) 45° Microscope slide holder with dimensions 60 mm \times 3 mm \times 15 mm (width \times height \times depth). The coverslip is permanently glued on the sample holder. b) Side view of the 45 degrees coverslip holder mounted on the imaging platform.

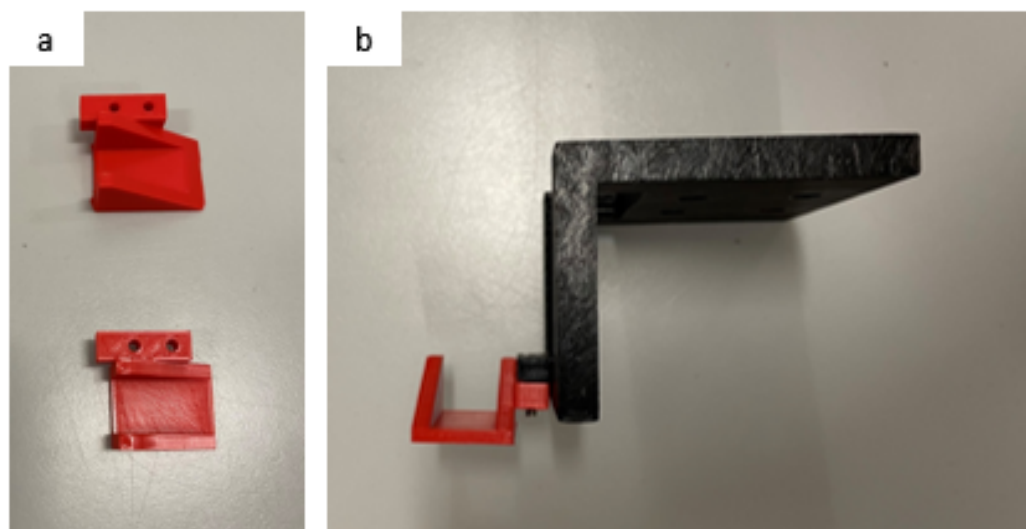


Figure 3.6: 30 degrees angular coverslip holder. a) Permanent coverslip holder, where the coverslip will be glued on the holder. M3 holes are used to mount the holder on the sample platform. The dimensions (width \times height \times depth) of the coverslip holder are 23 mm \times 17 mm \times 33 mm. Side view of the assembled 30 degrees angular coverslip holder.

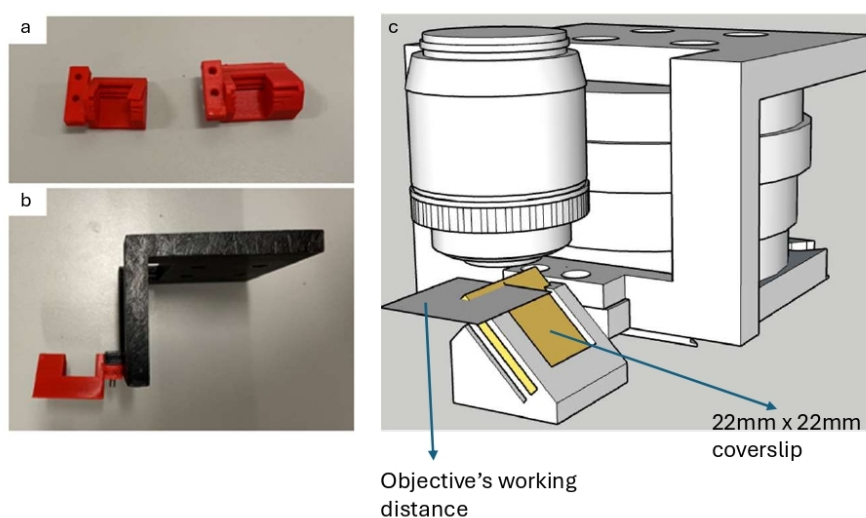


Figure 3.7: a) Multi-size angular coverslip holder for usage of coverslips with different thickness. Dimensions are 23 mm \times 18 mm \times 23 mm (width \times height \times depth). b) 45 degrees multi-size coverslip mounted on the imaging platform c) A cad model showing the the multi-size angular coverslip holder with a mounted 22mm \times 22mm coverslip.

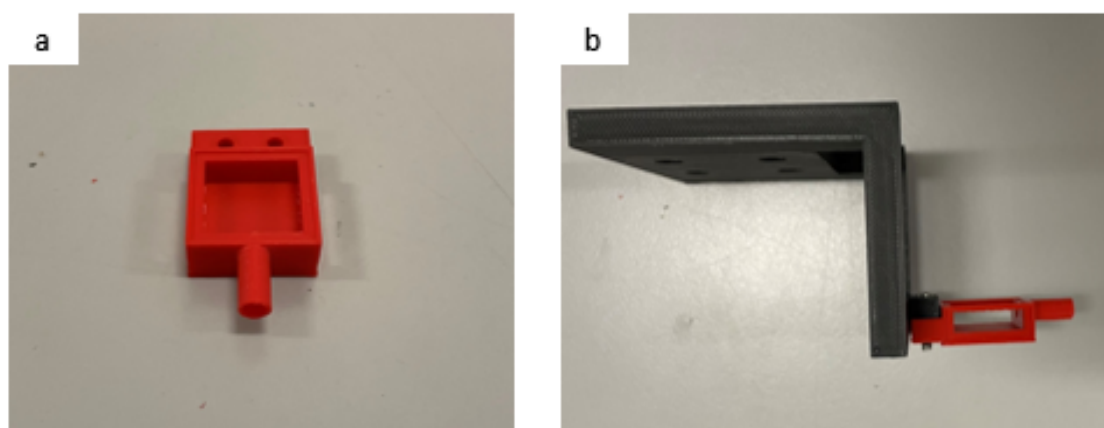


Figure 3.8: Customised capillary holder design. a) Capillary holder of dimensions 24 mm x 10 mm x 24 mm (width x height x depth). A cut glass is glued at the sides of the holder to enclose the liquid used to match the refractive index of the capillary. M3 screws are used to mount the holder on the imaging platform b) Side view of the imaging platform with the mounted capillary holder.

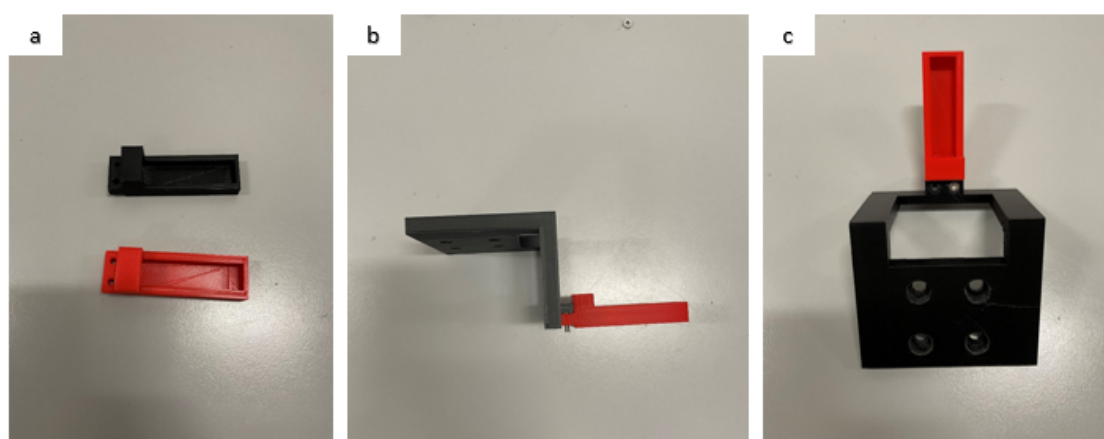


Figure 3.9: Customised cuvette holder. a) Cuvette holder with dimensions (width x height x depth) 20 mm x 8 mm x 61 mm capable of housing cuvettes. M3 holes are used to mount the cuvette holder on the imaging platform b) and c) side view and top view of the cuvette holder mounted on the imaging platform

3.5 Microscope Control Hardware & Software

My LSFM was controlled through a computer system capable of handling the large amount of data (5Mb per frame) and hardware components fast enough to achieve high imaging speed (above 40 fps). This way the computer will not add a bottleneck on

Chapter 3. Light Sheet Fluorescent Microscope Design for Imaging Whole Living Organisms

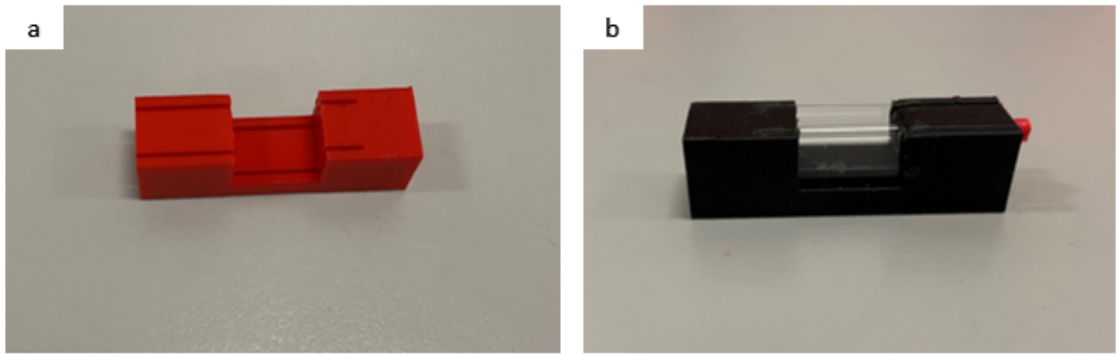


Figure 3.10: Customised cuvette designs. a) Used for volumetric imaging. Cut cover-glass pieces are glued in the two slides and on top of the cuvette to seal the sample, b) Cuvette that was used for imaging samples mounted in a capillary. Same sealing procedure is applied to be able to fill the cuvette with liquid matching the refractive index of the capillary. Dimensions for both cuvettes are 12.5 mm x 12.5 mm x 44.5 mm (width x height x depth) which is the same as standardised cuvettes.

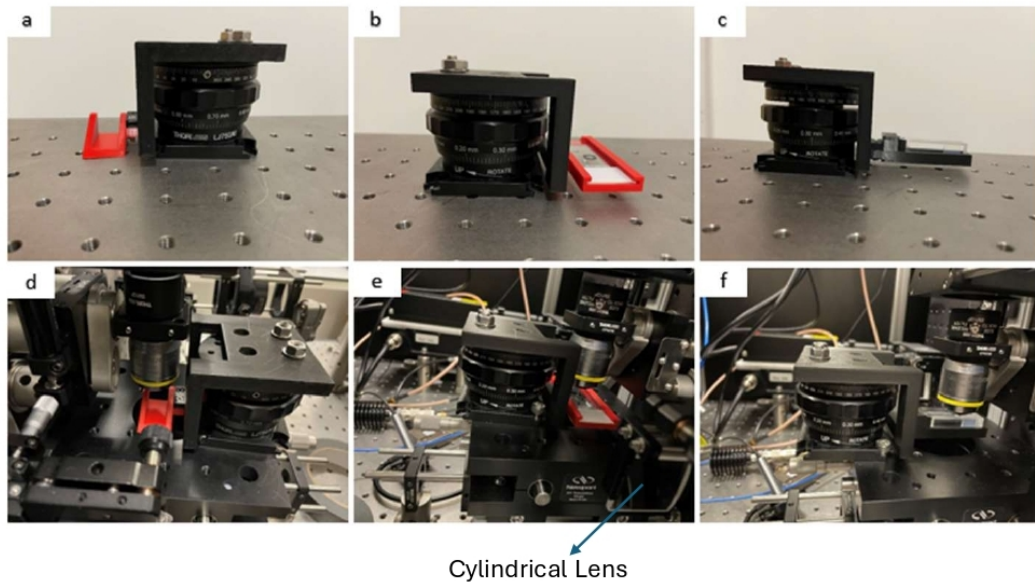


Figure 3.11: a) b) and c) the 30 degrees sample holder, the coverslip holder and the cuvette holder mounted on the z-stage with the sample mounted on the z-stage and on the microscope. d),e) and f) The implementation of the z-stage with the sample attached at the imaging position.

the LSFM microscope. The hardware components used for the control of the designed LSFM microscope are listed in Table 3.1

The computer system supports the large size images that are going to be extracted

Chapter 3. Light Sheet Fluorescent Microscope Design for Imaging Whole Living Organisms

Camera

PrimeBSI, 95% Quantum efficiency, 43.5 fps at 16-bit/12-bit(CMS),
63 fps at 11-bit

Light sheet scanning

Meadowlark SLM - 1920×1152 ,
19ms LC response time, 31 Hz frame rate.

I/O device

NI PCIe-6323, 16 analog input channels, 250kS/s sample rate,
4 Analog Output channels, 719-900kS/s update rate and 48 Digital I/O channels
BNC-2110 terminal

Computer

Graphics Card: MSI GeForce RTX 2070 Ventus 8192MB PCI-Express
RAM: Corsair Vengeance LPX 32GB (2x16GB) DDR4 PC4-21300C16 2666MHz
M2 SSD: Intel 660P 512GB M.2-2280 PCI-e 3.0 x 4 NVMe QLC 3D NAND SSD
SSD: Samsung 1TB 860 QVO SSD 2.5" SATA 6Gbps 64 Layer 3D V-NAND SSD
Internal Hard Drive: Seagate 8TB IronWolf NAS 7200RPM 256MB Cache
Power Supply: Kolink Continuum 1200W 80 Plus Platinum Modular
Processor: AMD Ryzen Threadripper Twelve Core 2920X 4.3GHz (Socket TR4)
Motherboard: Gigabyte X399 Aorus Pro AMD X399 (Socket TR4) ATX

Objective stage

Dover Motion DOF5, 5mm travel, 1000g max load, 5nm position holding stability,
15ms step and settle time

Table 3.1: The microscope control hardware. The camera, spatial light modulator, the analog input device, the computer, and the objective scanning stage are listed along with their specifications.

from the LSFM due to the large Random-Access Memory (RAM) and storage memory(64GB), while the Central Processing Unit (CPU) and Graphics Processing Unit (GPU) offer fast image processing capabilities. High imaging speed was ensured by the selection of a camera and an SLM with a high frame rate, and a fast Data Acquisition (DAQ) card and focusing objective stage (all specifications are listed in table 3.1).

The software control of the microscope was based on Python. Python was chosen due to its rapid users expansion the past few years in combination with its open source nature. Initially we considered adapting an open source software called Qudi [124]. Qudi is python based software capable of controlling laboratory experiments, based on three modules, the hardware, the logic and the Graphical User Interface (GUI). The modules are controlled through a core code and called through a configuration file. The hardware modules are the translation of hardware to software language, the logic

Chapter 3. Light Sheet Fluorescent Microscope Design for Imaging Whole Living Organisms

modules are used to control the hardware in order to perform the desired function, while GUI modules are responsible for the control over the logic modules and the illumination of the experiments' results. Despite the fact that we coded the hardware module for the camera and the DAQ card, it was very challenging to hardware code for the DM, and to write the adaptive optics logic code. Therefore, we decided to use μ manager [125] as an imaging software and SLMtools [126] as the SLM control and light sheet scanning software. The exploration of QUDI as control software was performed in the initial stages of the COVID lockdown and it was only when we regained access to the lab that we realised its limits for our specific application and moved to MicroManager.

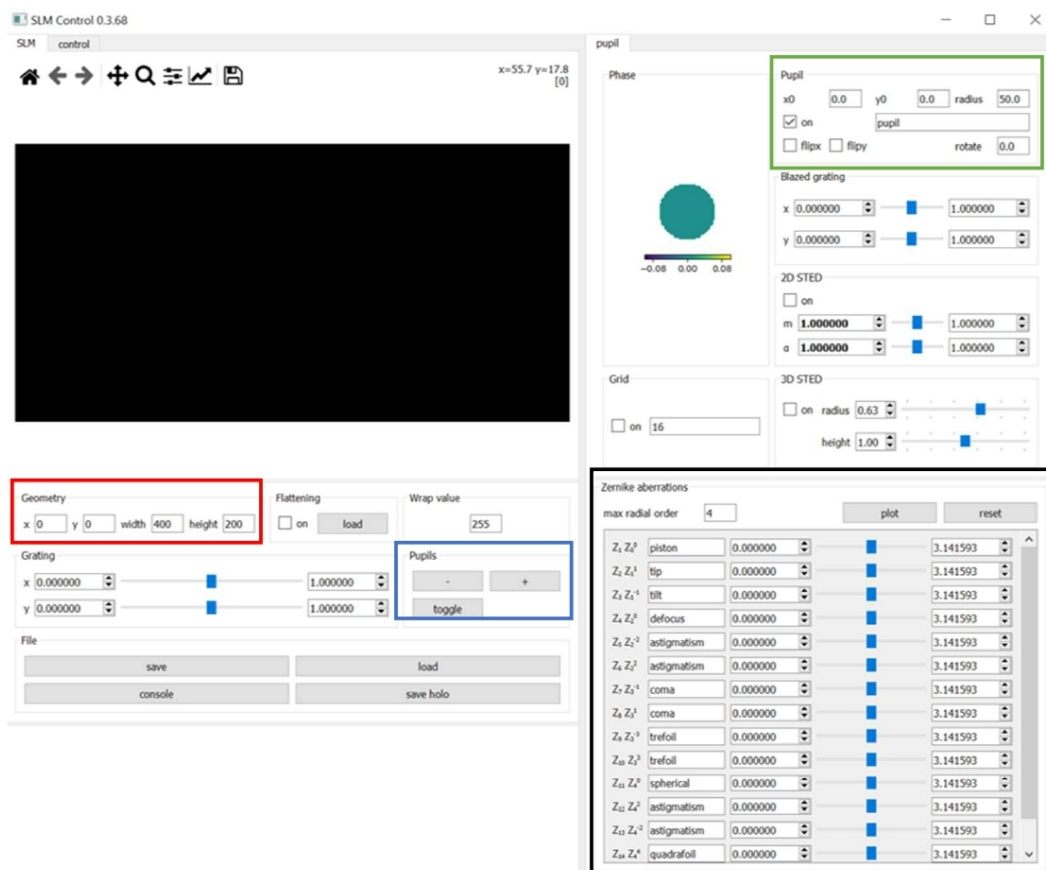


Figure 3.12: SLMtools software without any adaptations. Geometry: controls the size of the hologram (red square). Pupils allow to increase or reduce the number of pupils in the hologram (blue square). Pupil allows control of the position of the selected pupil and its radius (green square). Zernike aberration window offers control over the aberration via Zernike polynomials (black square). [126].

SLMtools is a Python based software that enables control over a SLM connected to the computer via an High-Definition Multimedia Interface (HDMI) connection. The control of the SLM is done through the GUI shown in Figure 3.12. The principle of operation is based on the fact that when the SLM is connected to a computer via an HDMI connection, the computer sees it as a second monitor. Hence, a hologram is projected on the SLM as it would have been projected on a second monitor. SLM control is achieved by manipulating this hologram. The positioning of the hologram as well as its dimensions are controlled from the “Geometry” window, while the position of the pupil and radius specified at the ”Pupil” window. Pupils refer to the aperture on the SLM that the selected grating is applied on. Additionally, the grating of the hologram’s background is set at the “Grating” window, and the pupil’s grating at the ”Blazed grating” window. Pupils can be added and removed from the ”Pupils” window. The original SLMtools code offers aberration control via Zernike polynomials, it supports multiple pupils over the same SLM window and it supports Two-Dimensional (2D) and 3D STED phase masks. The fact that this software allows control of an HDMI connected SLM and can manipulate several pupils on a single SLM makes it perfect for our application, since our SLM is an HDMI connected SLM and we are reflecting both illumination beams from the same SLM, thus multi-pupil control is mandated.

Light sheet manipulation was achieved by adapting the SLMtools code and introducing the ”LSFM” window, as shown in Figure 3.13. A custom written python code ensured hardware synchronisation. This was achieved by investigating the LS’s position in response to the grating applied on the SLM (more information is presented in Section 4.2). I set a scanning module where the user can select the start and end position of the light sheet as well as the scanning step size in μm . Additionally, the ”goto” option is included where the user can directly drive the light sheet to a specific z location. Scanning and imaging synchronisation is achieved by setting the same start, end and step size in both the SLMtools and micromanager. By running both software, micromanager moves the detection objective at the correct position and waits for a trigger to capture an image. SLMtools moves the light sheet at the imaging position and then triggers the camera through the National Instruments (NI) DAQ card. The

Chapter 3. Light Sheet Fluorescent Microscope Design for Imaging Whole Living Organisms

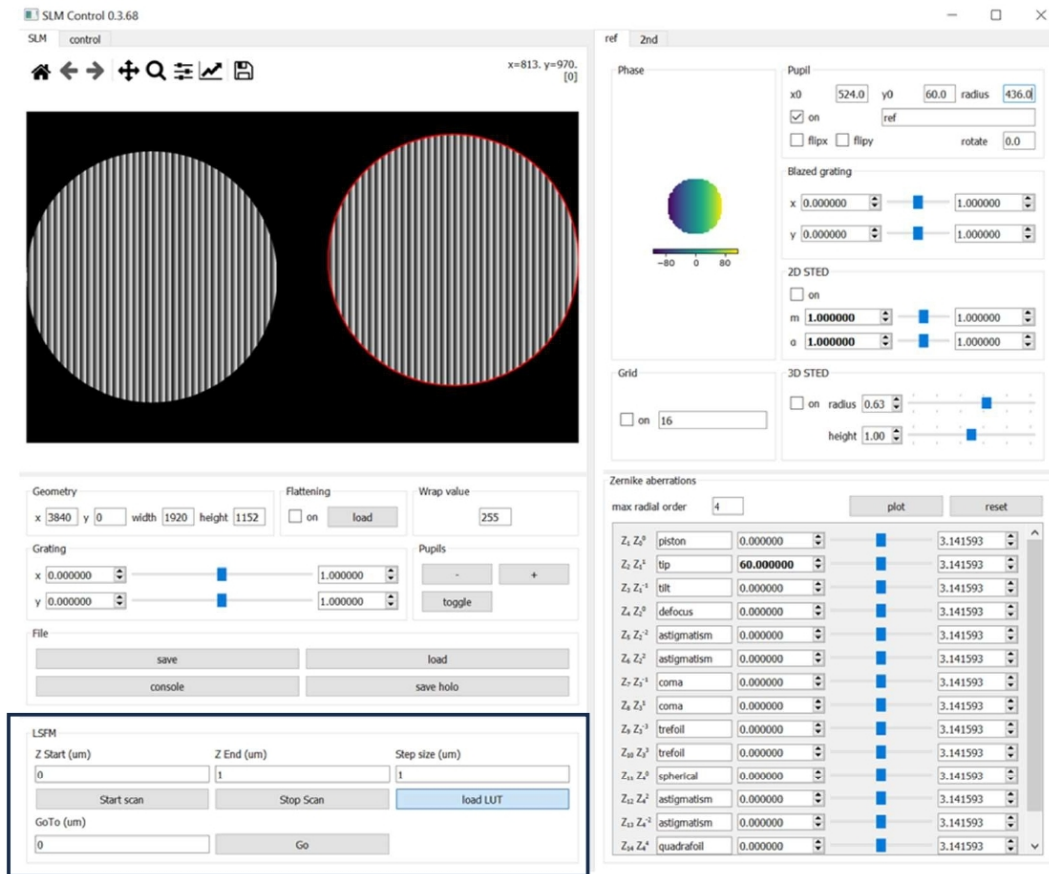


Figure 3.13: SLMtools software adapted to light-sheet scanning. Light-sheet control over the start and stop position of the scan as well as the scanning size is achieved through the light-sheet fluorescent microscopy window (black square). There is also the option to move the light-sheet at a selected position.

image is then captured, the objective is moved and next trigger is expected. This runs in a loop until the scan is completed.

3.6 Summary and Discussion

In this Chapter I present the methodology of designing a conventional LSFM (single illumination beam and single detection) and a dual illumination beam and single detection LSFM. The sample of interest, FOV, resolution and level of accepted anisotropy lead to the selection of suitable optical elements. The sample's optical specifications (transparency) assists in the selection of LS generation, with DSLM being favourable for

Chapter 3. Light Sheet Fluorescent Microscope Design for Imaging Whole Living Organisms

optically dense samples and SPIM being more suitable for optically transparent samples [4, 67]. The biological question or the application of the microscope contributes in the selection of a FOV, resolution, level of anisotropy and imaging sensor, which are used to calculate the NAs of the illumination and detection objectives, the magnification and the focal length. The method of optical elements selections described in this chapters assumes that conventional illumination and detection objectives are used. However, objectives such as Mesolens can be used in LSFM configurations. Mesolens is a 0.47 NA objective that offers a 6 mm FOV with 700 nm lateral and 7 μm axial resolution [127]. LS mesoscopy was presented by E. Battistella et al [128] where a Gaussian LS and an Airy LS illuminate 4.4 mm and 3 mm FOV respectively with and Airy LS thickness of 7.8 μm and a Gaussian LS thickness of 36.8 μm . This demonstrates the level of flexibility and adaptability of LSFM and shows that a plethora of biological questions can be investigated with LSFM.

I designed a LSFM with dual-illumination beam and single detection with a FOV of 2mm. Due to the low NA required to illuminate such a FOV (NA 0.03) the CL directly illuminates the FOV without the necessity of an additional illumination objective. A LS with a thickness of 21 μm at the edge of the FOV and 14.9 μm at the centre of the FOV was formed. A detection objective with NA 0.4, magnification of $\times 10$ and field number of 25 was selected. This detection objective allowed a lateral resolution of 1.06 μm and a axial resolution of 7.79 μm ; however, the since the LS thickness was greater than the axial resolution of the detection objective, the LSFM axial resolution was determined by the LS thickness. A compromise of resolution was made to ensure a FOV of 2 mm, limiting the lateral resolution of the microscope to 2.12 μm .

Adaptive elements were included in my design. A SLM in the illumination path was responsible for the modulation of the illumination beam and it would also allow AO corrections. A DM was positioned in the detection path for further AO corrections. Although a LSFM with a large FOV, where the LSs are directly illuminating the FOV without an illumination objective was reported [129] and AO elements have been reported in the illumination [95] and detection arm [91], a combination of the three has not been reported yet. The adaptability offered by the SLM in the illumination

Chapter 3. Light Sheet Fluorescent Microscope Design for Imaging Whole Living Organisms

path and the DM in the detection could lead to the development of a "smart" adaptive LSFM [130]. Real-time analysis of the sample could determine the most suitable LS generation (DSLIM, SPIM) method and beam used (Gaussian, Bessel, Airy) to achieve the maximum capability of the microscope. The SLM's modulation capabilities would allow such an operation.

The software used for the control of the LS was based on SLMtools. SLMtools was adapted to enable scanning of the LS and the detection objective so that the two are in focus during the scanning operation. However, the software limited the refresh rate of the SLM to 10 frames per second, which determined the imaging speed of the LSFM.

Due to Covid lock-downs my access to the lab was limited, therefore; some of the microscope design features were not able to be fully implemented and tested. The DM as well as the wide-field imaging configuration were not implemented in the microscope and the laser modulation is achieved through the SLM and not an AOM (LSFM microscope is described in Chapter 4).

Chapter 4

Dual Illumination-Single Detection Light Sheet Fluorescent Microscope - Characterisation and Imaging

In this chapter I present the constructed dual illumination single detection microscope. The microscope incorporates AO elements; therefore, the SLM calibration and characterisation along with the stability characterisation of the DM is presented. The microscope characterisation method and the resulted specifications are also presented in this chapter. Finally, volumetric imaging of ND and *C. elegans* is shown.

4.1 Imaging Platform

The dual illumination, single detection LSFM I constructed and used for imaging of *C. elegans* and NDs is shown in Figure 4.1. Comparing the constructed microscope shown in Figure 4.1 with the microscope design shown in Figure 3.1, we can observe that there are three differences. Since the SLM was used to select which path the illumination was following, the AOM was not included into the illumination path. Instead the SLM was used for modulation. This is sufficient for initial testing and CW ODMR experiments,

Chapter 4. Dual Illumination-Single Detection Light Sheet Fluorescent Microscope - Characterisation and Imaging

but when pulsed-excitation schemes are attempted, it will be necessary to add the AOM to the optical path as the required sub-microsecond pulses are far outside the capabilities of the SLM

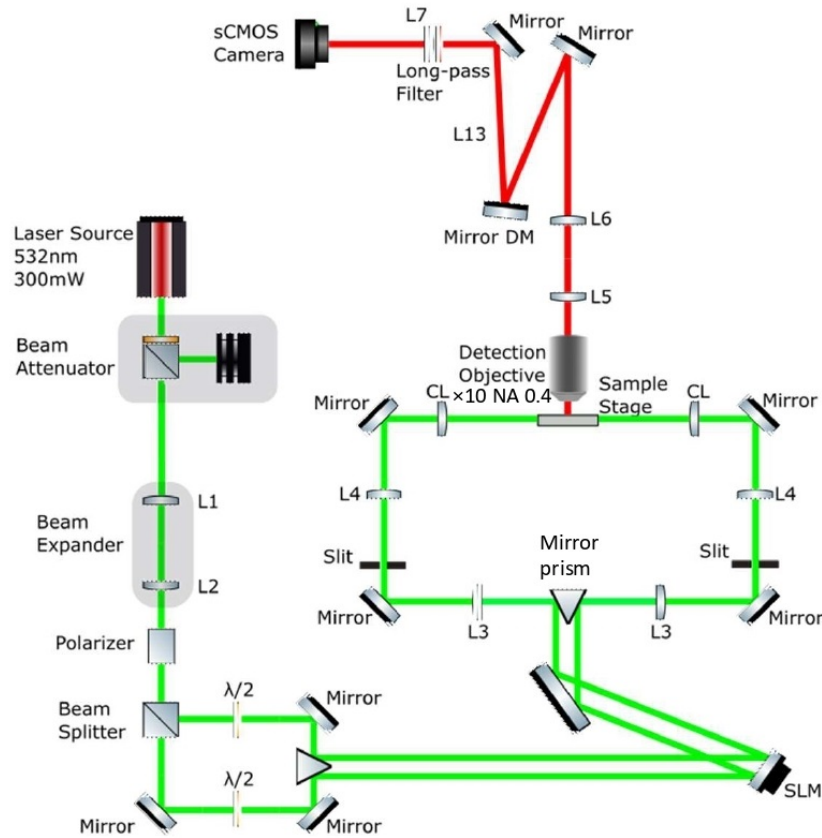


Figure 4.1: Optical setup of the dual illumination single detection light-sheet fluorescent microscope. A 532 nm laser is expanded (L1 and L2) to 6 mm and then split to create the two imaging paths. Both paths were refracted at the spatial light modulator (L3 and L4 conjugate the back focal plane of the cylindrical lens to the spatial light modulator screen) and pass through the cylindrical lenses to form two light-sheets. The excited fluorescence was collected by the detection objective and focused on a sCMOS camera. The figure is a representation of my work conducted in Inkscape using the ComponentLibrary created by A. Franzen [122]

Laser modulation was achieved through the SLM. When a specific hologram was projected on the SLM, the reflected beams were driven out of the illumination path and blocked by a mechanically adjustable slit. The mechanically adjustable slit was

placed at the focal position of L3 in each path. Hence, when a grating on the SLM shifted the beam, the beam was blocked by the slit. The beam passes through the aperture only at a selected SLM grating. To ensure that only the 1st refraction order of the SLM passes through the opening of the slit, a lens and a camera were used to image the mechanical slit surface, via a drop-in mirror. The slit was opened so that many diffraction orders pass through. When closing the slit, one by one the diffraction orders are blocked. At a certain opening, only the 1st diffraction order was imaged. The first diffraction order was used for phase modulation, since the first diffraction order provides maximum efficiency when a phase grating is projected on the SLM [131]. Additionally, the wide-field imaging setup (L8, L9, L10, Beam Splitter (BS), white Light-Emitting Diode (LED), and a camera) was replaced with a 532 nm 5 mW power laser, used for the alignment of the detection path as well as the conduction of wide-field ODMR measurements (discussed in Chapter 5). Following our experimental procedure, initial tests were done with a mirror at the position of the DM to avoid problems with DM control being mistaken for alignment issues with the microscope overall. This is a common approach with AO microscopes; the AO elements have a maximum capacity to correct for aberrations, so it makes sense to align the microscope as well as possible before introducing them. Unfortunately, the severe restrictions on lab access imposed by the COVID lockdowns meant that I was not able to reach the stage where we placed the DM in the microscope. A DM can be embedded in the microscope without any changes, by replacing the mirror, shown as "mirror DM" in Figure 4.1, with a DM.

4.2 Methodology

4.2.1 Adaptive Optics Elements Calibration and Characterisation

SLM calibration

SLMs are not achromatic because the index of refraction changes for different wavelengths. As a result, an SLM designed to give 2π phase stroke at a specific wavelength will provide a phase stroke less than 2π for longer wavelengths and more than 2π phase

Chapter 4. Dual Illumination-Single Detection Light Sheet Fluorescent Microscope - Characterisation and Imaging

stroke for shorter wavelengths. Therefore, a wavelength dependent calibration is required every time the wavelength is changed. The calibration will ensure that the input greyscale levels of 0 to 255 (since this is an 8-bit device) linearly map phase delays of 0 to 2π [132].

The SLM calibration procedure recommended by the SLM supplier was used and described below [133]. The SLM calibration optical setup is shown in Figure 4.2. The beam expander was used to expand the beam so that it illuminates the entire active area of the SLM. The half-wave plate was required for polarisation alignment and a lens focused the refracted beam on a photodiode power sensor.

The calibration procedure starts by projecting images of phase grating stripes to the SLM. One of the stripes' greyscale value was set to 0 and the other varies from 0 to 255, which is the maximum greyscale level. The width of each stripe was 8 pixels, which is small enough to ensure separation between the 0th and 1st order of diffraction, as indicated by the SLM's manufacturer. The power intensity of the 0th order was then measured for each greyscale variation. The 0th order was used for global calibration as indicated at the calibration protocol [132].

The resulted normalised to one SLM calibration raw data is shown in Figure 4.3. Greyscale 0 refers to a fully black image, where greyscale 255 refers to a fully white grating. The first minimum indicates the greyscale required to achieve a phase shift of π while the second peak indicates the greyscale required to achieve a 2π phase shift.

The SLM was calibrated for phase shifts from 0 to 2π . The intensity measurements, raw data, were converted to phase and normalised from 0 to 2π . The obtained phase was unwrapped and a curve fit has been applied. The final stage was the extraction of the Look-up Table (LUT) where 0 to 1 refers to 0 to 2π (Figure 4.4). This procedure was done automatically by a software provided by the SLM supplier. The results of the SLM calibration are shown in Section 4.2.

SLM Beam Scanning Characterisation

The LS scanning through the sample was achieved through the SLM when Zernike polynomials were applied. Zernike mode 1, tip and tilt, was projected to scan in the

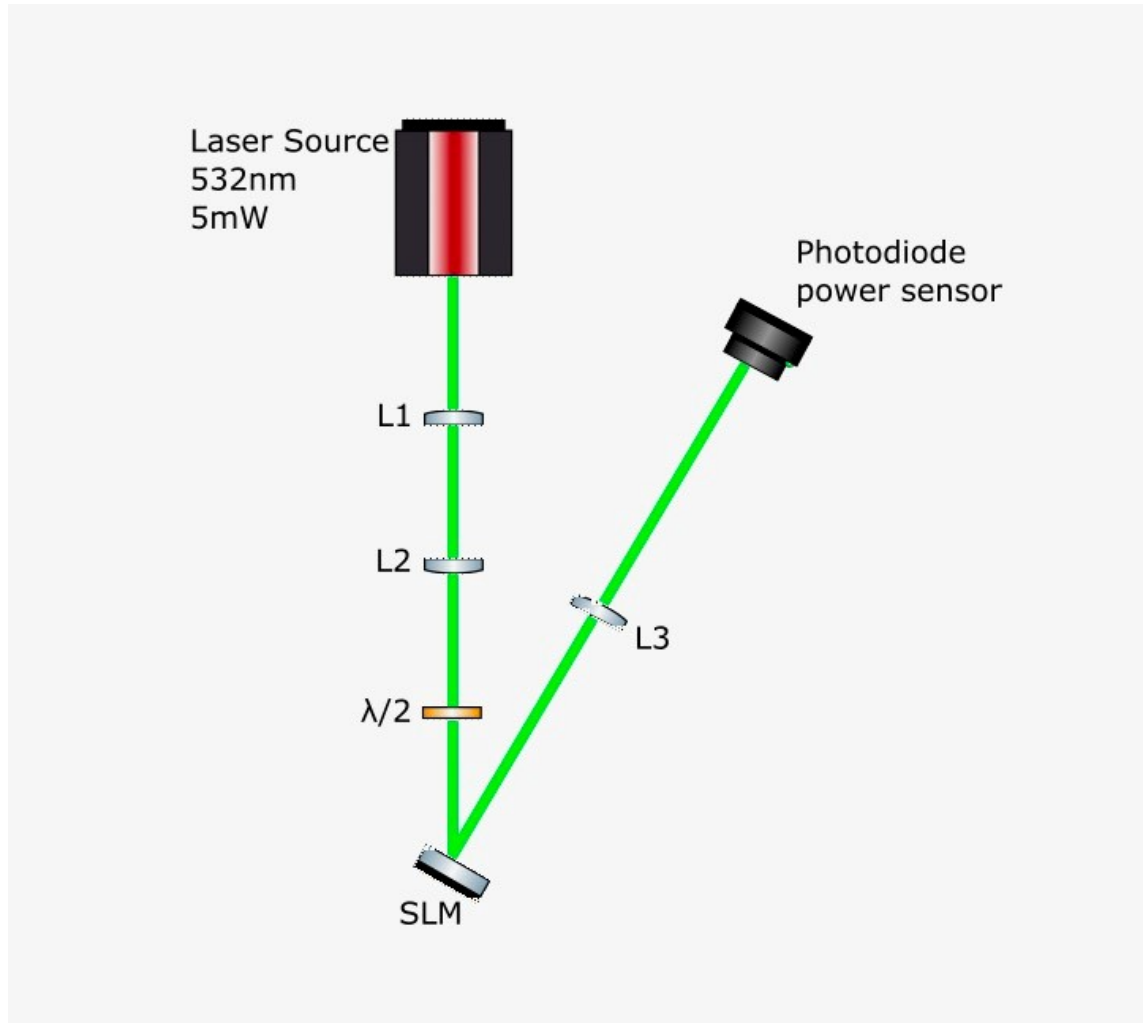


Figure 4.2: Optical schematic of the spatial light modulator calibration setup. A 532 nm laser beam was expanded (L1 and L2) so that it covered the spatial light modulator's screen. L3 focused the refracted from the spatial light modulator beam on a photodiode power sensor. The half wave plate was used to achieve the desired polarisation alignment achieved by maximising the laser power at the photodiode [132]. The figure was extracted from the Meadowlark data-sheet [132] and it was created using Inkscape and the ComponentLibrary created by A. Franzen [122]

x and y direction respectively (see Figure 4.6 and Figure 4.7). The Zernike amplitude was selected and applied through the SLMtools software [89, 126, 134, 135].

The optical schematic of the SLM scanning characterisation setup is shown in Figure 4.5. The SLM scanning characterisation setup is similar to the SLM calibration setup, their only difference is that a camera was used for the scanning characterisation instead

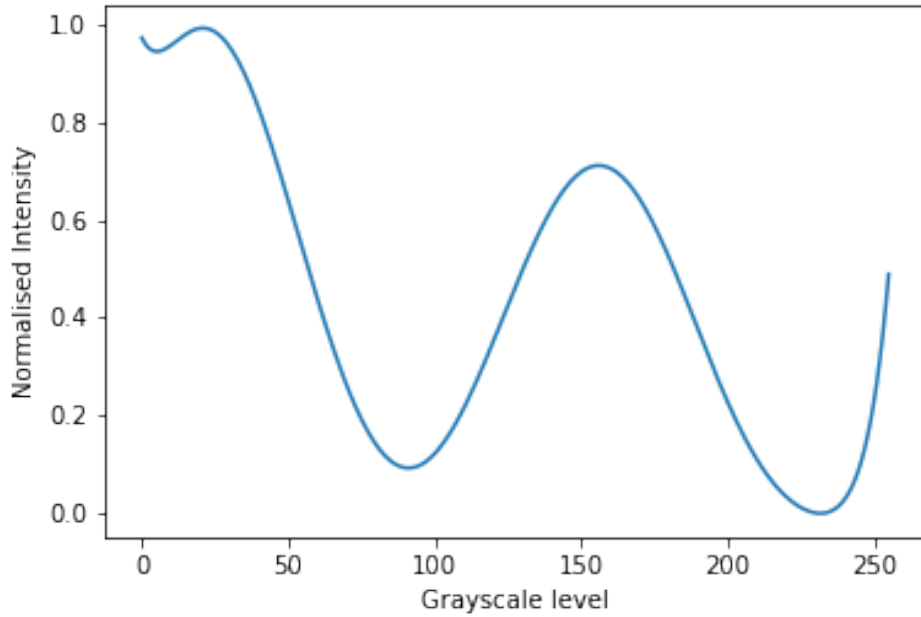


Figure 4.3: Normalised intensity of zeroth order diffraction of spatial light modulator with the grayscale patterns projected on the spatial light modulator. One of the stripes' grayscale value is set to 0 and the other varies from 0 to 255. The figure was extracted using data from the SLM calibration software provided by Meadowlark.

of a photodiode. Initially, all aberration amplitudes were set to zero, and then the Zernike mode 1- (tilt) amplitude was increased in steps of 10, within a range of 0-100. Tip was also investigated by setting all aberration amplitudes to zero and then increase Zernike mode 1+ (tip) amplitude in steps of 10, starting from zero and ending at 100.

The refracted beam imaged, in respect to the hologram applied on the SLM, for both tip and tilt is shown in Figures 4.6 and 4.7

The distance between the 0th order and the 1st order were initially measured in pixels and then translated into physical movement (μm), by multiplying the number of pixels measured to the physical size of each pixel (pixel size equals to $5.86 \mu\text{m}$, and plotted (Figure 4.8). The pixel shift was determined by plotting the linear profile of the imaged diffracted beam and measuring the distance (in pixels) from the 0th order beam peak intensity to the 1st order beam peak intensity. Since the laser beam's size is greater than one pixel (it is equal to 10 pixels), the middle point of each laser beam,

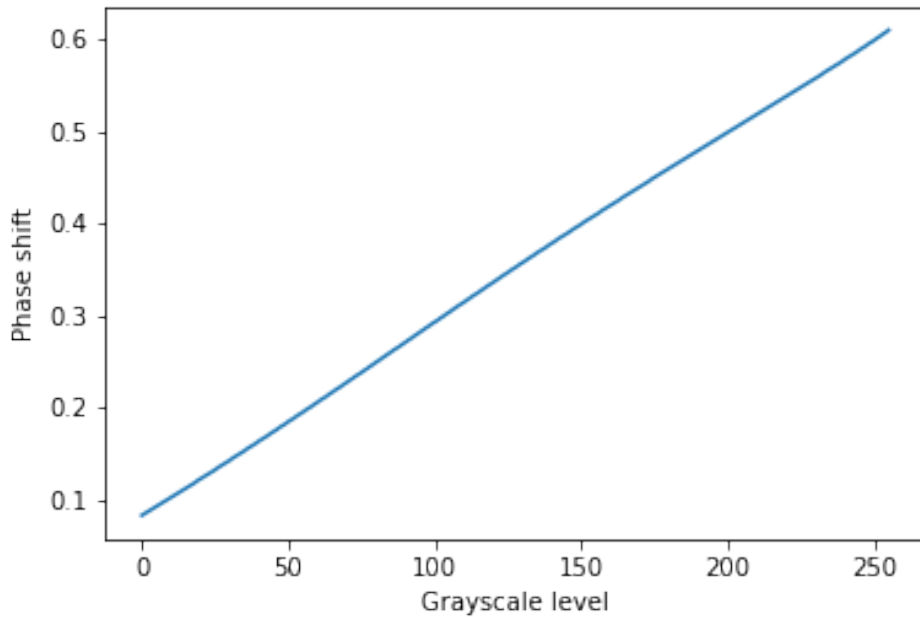


Figure 4.4: spatial light modulator look-up table for a 532 nm refraction. The Y-axis represents the phase shift, where 0 is referred to 0π and 1 to 2π . X-axis is the grayscale level applied on the spatial light modulator. The figure was extracted using data from the SLM calibration software provided by Meadowlark.

for both the 0th and 1st diffraction orders, were used to measure the pixel's shift. The measurement was repeated three times with identical results; therefore the error is not included in Figure 4.8

As shown, linear scanning of a beam in both the x and y directions was achieved. For LSFM imaging only scanning in the y-direction was used to illuminate the sample. In the LSFM imaging configuration, the y-axis defined on the SLM software corresponds to the z-axis of the detection arm.

4.2.2 Microscope Characterisation

The first step of the LSFM microscope characterisation was to ensure that LS illumination was achieved. This was investigated by imaging a coloured lens tissue at 45° (Figure 4.9). The sample was made by colouring a lens tissue with highlighter. To ensure that the highlighter soaked lens tissue was flat, the lens tissue was fixed between

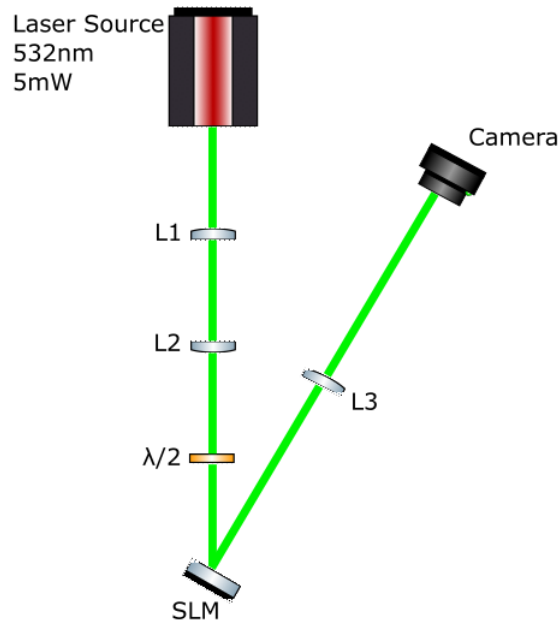


Figure 4.5: Optical schematic of the spatial light modulator scanning characterisation setup. L1 and L2 form a beam expander to cover the spatial light modulator’s screen. A halfwave plate ensures that the correct polarisation to achieve maximum refraction is applied, and a tube lens (L3) focuses the refracted beam on an iDS camera. The figure is a representation of my work conducted in Inkscape using the ComponentLibrary created by A. Franzen [122].

to two coverslips. The coverslips were held together with nail varnish. The image of the highlighter soaked lens tissue when the illumination beam was focused on it is shown in Figure 4.9. This image was expected since only the tissue illuminated by the LS was imaged.

To calculate the FOV of the microscope and magnification a $10\ \mu\text{m}$ calibration grid was imaged, with white light illumination, as shown in Figure 4.10.

Each calibration grid square consists of 10 pixels. Therefore each pixels corresponds to $1\ \mu\text{m}$. With a camera pixel size of $6.5\ \mu\text{m}$ we saw that the magnification of the microscope was, as designed, 6.5. Also, it was observed that image illumination was projected on 1570 pixels, showing that the FOV was 1.57 mm. The FOV was designed to be 2 mm; therefore, this was an indication that there was clipping in the detection path.

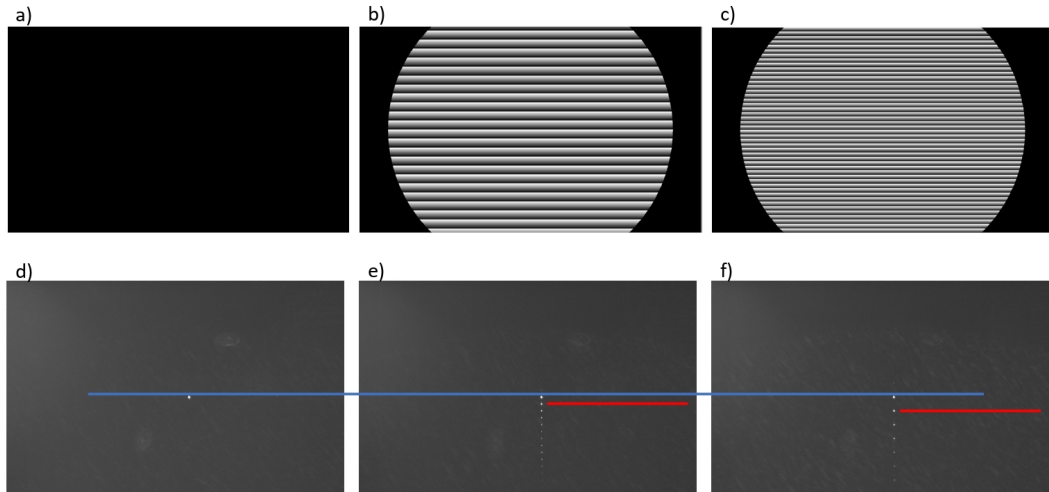


Figure 4.6: a) b) and c) Hologram projected on the spatial light modulator for a tilt coefficient of 0, 50 and 100 respectively. (d) The image of the diffracted beam for a tilt of 0. (e) The image of the diffracted beam for a tilt of 50. The shift of the 1st order of diffraction is 40 pixels which is translated to $234.4 \mu\text{m}$ and (f) The image of the diffracted beam for a tilt of 100. The shift of the 1st order of diffraction is 78 pixels which is translated to $457.8 \mu\text{m}$. Blue lines indicated the 0th order of diffraction and red lines the 1st order. The red and blue lines are used for representation of the pixel's translation and they were not used for the extraction of the data plotted in Figure 4.8.

To identify the element or elements that cause clipping an optical simulation of the detection path was conducted. Each optical element along with the physical distance between each set of elements were implemented in raytracing (see Section 2.1). The model of the detection path was then formed and used to extract the efficiency of the optical model, pointing to the location that causes vignetting. Additionally, the magnification and FOV was calculated. Initially, the detection path was designed with 25 mm diameter optics. When the detection path was modelled a large loss due to vignetting (26.6%) was observed (shown in Figure 4.11). Raytracing [25] showed that there was blockage in the detection path from the 45 degrees-orientation mirror mounts used in the periscope section of the detection paths well as a sub-set of the lens mounts and cage plates used for the construction of the microscope. Therefore all the components causing a blockage in the detection path were replaced with 50 mm diameter optical and opto-mechanical components. The 50 mm detection path model is shown in Figure 4.12 As observed, the loss due to vignetting was reduced to 3.1%. The

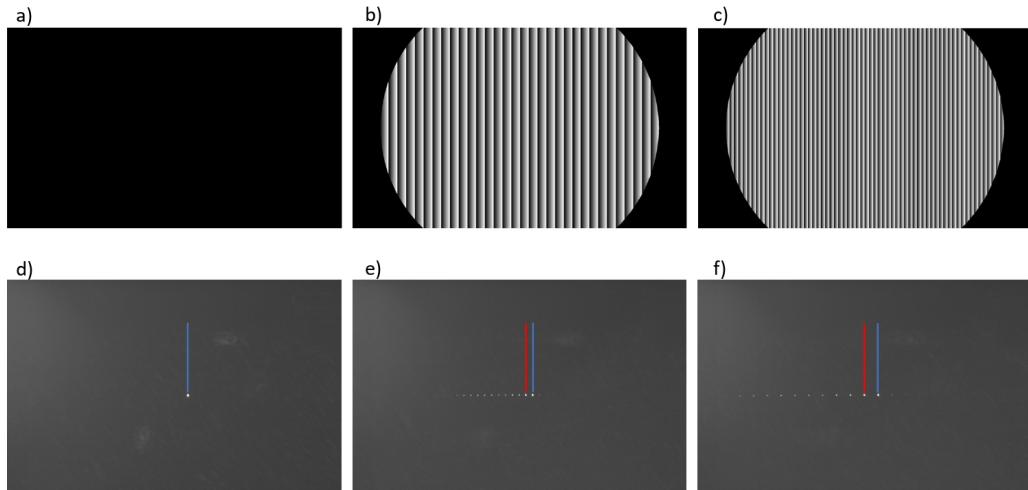


Figure 4.7: a) b) and c) Hologram projected on the spatial light modulator for a tip coefficient of 0, 50 and 100 respectively. (d) The image of the diffracted beam for a tip of 0. (e) The image of the diffracted beam for a tip of 50. The shift of the 1st order of diffraction is 40 pixels which is translated to $234.4 \mu\text{m}$ and (f) The image of the diffracted beam for a tip of 100. The shift of the 1st order of diffraction is 81 pixels which is translated to $474.5 \mu\text{m}$. Blue lines indicated the 0th order of diffraction and red lines the 1st order. The red and blue lines are used for representation of the pixel's translation and they were not used for the extraction of the data plotted in Figure 4.8

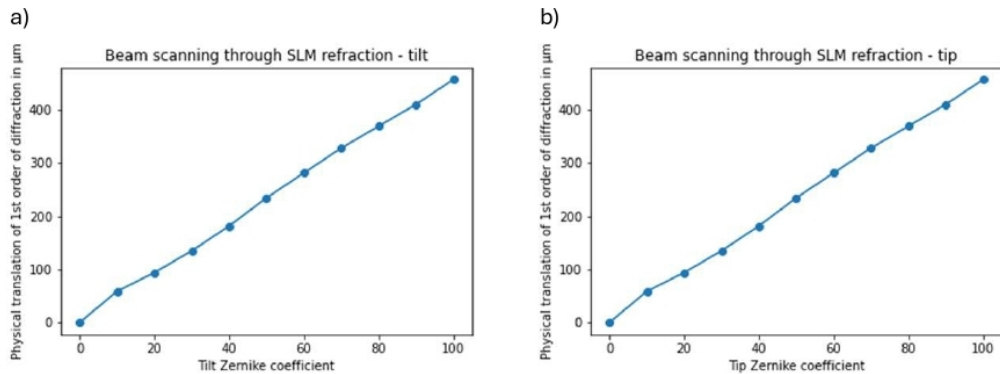


Figure 4.8: Tip and tilt scan of the 1st order of refraction. The Zernike mode 1 amplitude varies from 0 to 100 in steps of 10 while the physical movement of the 1st order of refraction is measured.

raytracing modelling of our system with the 50 mm optics confirmed that we should have a 2 mm FOV. However, when we replaced the optics and measured again, the resulting FOV was only slightly improved, to 1.6 mm. Deeper investigation on the detection path revealed that the distance between the outer surface of the camera's c-

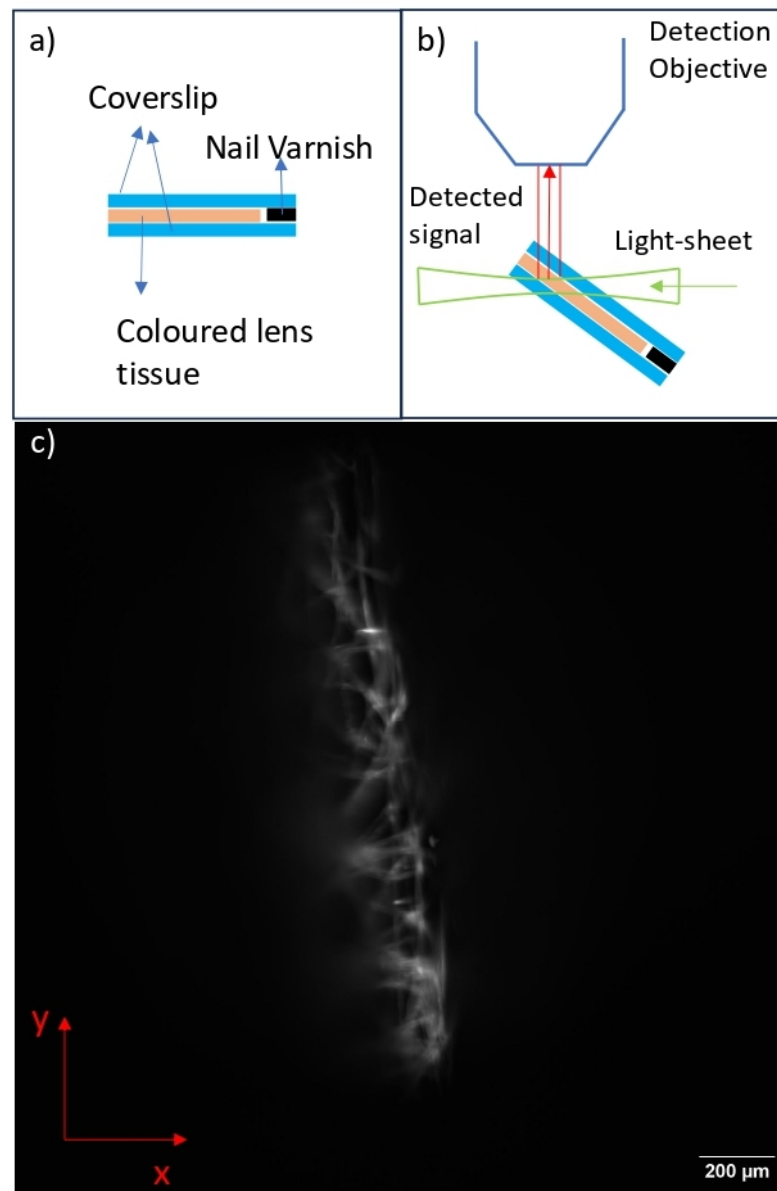


Figure 4.9: Lens tissue light sheet illumination imaged with the light-sheet fluorescence microscope. a) A coloured lens tissue is fixed between two coverslips, glued together with nail varnish. b) The coloured lens tissue was imaged at an angle of 45° to image the light-sheet. c) Light-sheet image extracted through the coloured lens tissue.

mount hardware (which can be used to directly attach suitable imaging lenses or filters) and the actual sensor (which, in agreement with the c mount standard) is located 17.5 mm in front of the mount's surface was not included in previous models. Including the

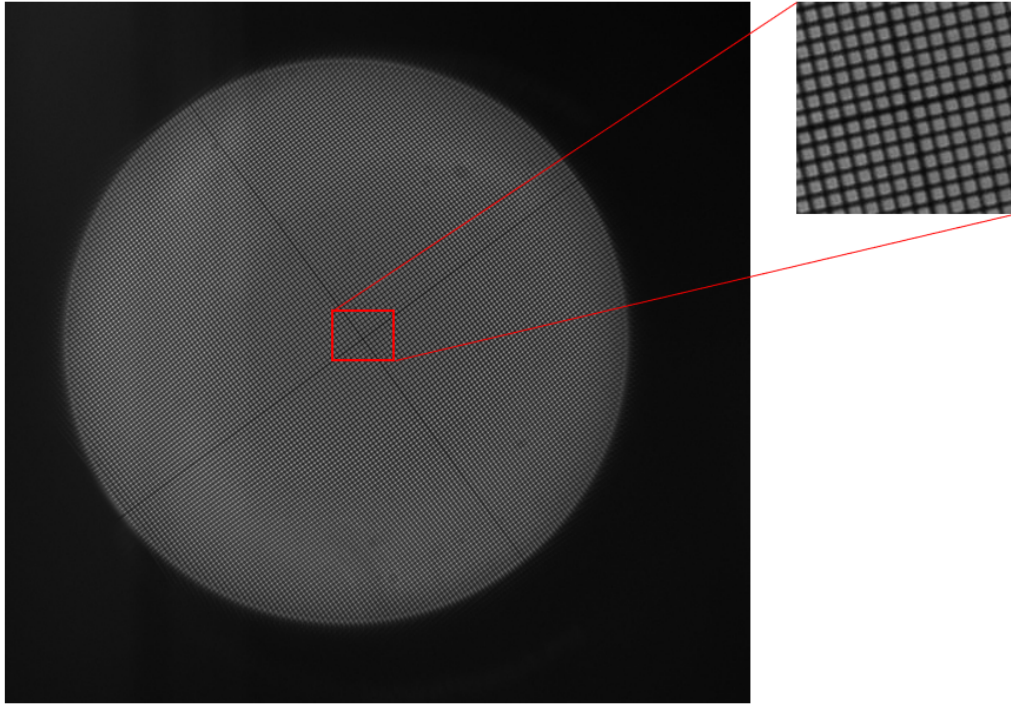


Figure 4.10: Wide field, white light illumination of a $10\mu\text{m}$ calibration grid used to measure the field of view of the detection objective, using the light sheet fluorescent microscopy detection path.

camera's geometry within the model, it was shown that the loss of FOV was caused by the camera's c mount (Figure 4.13)

The FOV of the model, where the camera's geometry was included, was 1.53 mm, which agrees with the actual LSFM FOV observed. All similar specifications cameras use c mounts; therefore, the option of changing a camera was not considered. A solution considered was to include two more lenses within the detection path. The space from the DM to the sCMOS camera is an optically infinite space; therefore, by introducing two lenses and form a beam expander of magnification $M=3$, we will need a tube lens with 3 times longer focal length to maintain the same magnification. The distance between the TL and the camera will be 3 times longer and thus the camera's mount will not cause a blockage. However, due to time limitation, this could not be applied. Hence, all the experiments and imaging are conducted within a FOV equal to 1.53mm. There are some other imaging artefacts that arise from the vignetting due to the camera

Chapter 4. Dual Illumination-Single Detection Light Sheet Fluorescent Microscope - Characterisation and Imaging

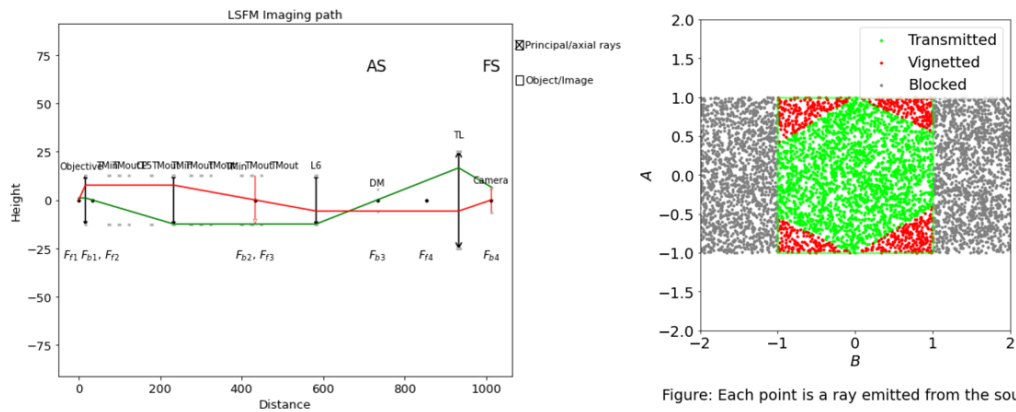


Figure 4.11: a) Optical model of the Light-sheet fluorescent microscopy detection path in raytracing python module. The detection path is modelled with 25mm optics. The black vertical lines represent lenses and the gray and black dots represent apertures. b) Vignetting occurring due to blockers in the path. Red dots represent vignetting and green dots represent transmission. The figure was extracted using the RayTracing python library created by D. Côté [26].

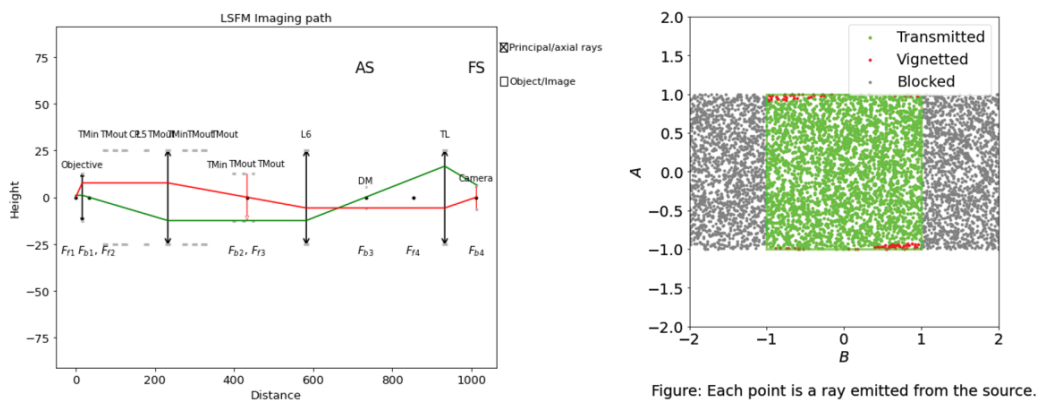


Figure 4.12: a) Optical model of the detection path in raytracing python module with 50mm opto-mechanical components b) Vignetting of the imaging path. The figure was extracted using the RayTracing python library created by D. Côté [26].

mount and we will point them out when then occur in the data presented in the thesis.

To investigate the accuracy of the objective's scanning stage, a FND slide sample was imaged at an angle of 30° with a wide-field illumination via the low power 532 nm laser described in section 4.2.2. The sample preparation is described in Section 4.2.3. The sample was mounted on the angular mount shown in Figure 3.7 and it was set

Chapter 4. Dual Illumination-Single Detection Light Sheet Fluorescent Microscope - Characterisation and Imaging

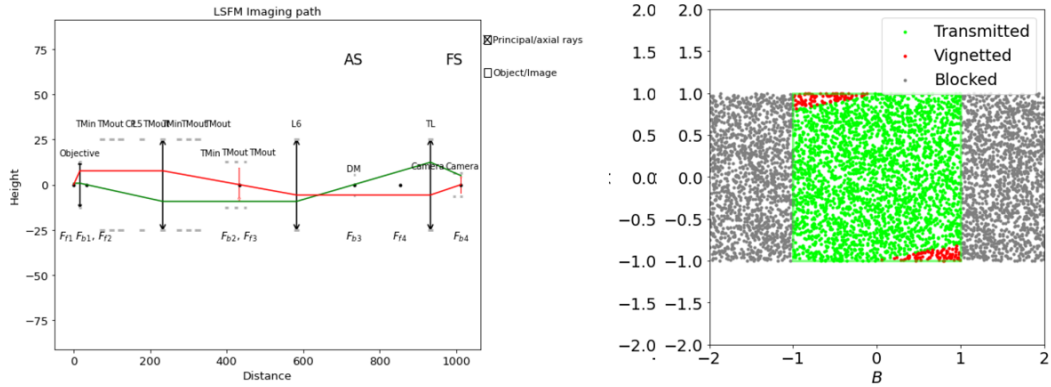


Figure 4.13: a) Optical model of the detection path in raytracing python module with 50 mm opto-mechanical components including the camera's geometry b) Vignetting plot of the imaging path. The figure was extracted using the RayTracing python library created by D. Côté [26].

for imaging. The objective was moved in steps of $50 \mu\text{m}$, starting from $-200 \mu\text{m}$ and ending at $200 \mu\text{m}$, with 0 being the reference position of the LS. The objective moves in the z-direction, perpendicular to the imaging plane. The vertical movement of the objective results in lateral focal shifts because the angle between the sample and the imaging plane is 30 degrees. During this characterisation procedure, the LS remained stationary. For each step an image was captured and the centre of the in-focus plane was estimated for each image as shown in Figure 4.14. A stack was created listing all the captured images. The lateral focal shifts were measured by examining the entire images' profiles. A sharp change between bright and dark pixels indicated the in-focus region. The pixels at the centre of this regions were used to measure the lateral focal shifts. Knowing that the sample was at 30° and by measuring the translation of the focus (parallel to the optical plane), we calculated the actual translation of the detection objective. To calculate the error of my measurements, each measurement was repeated five times. The obtained measurements presented a standard error of 0.94%, which considering that the centre of the focal plane is estimated empirically, presents an accurate objective scanning [136].

Ensuring that the focal plane of the objective was synchronised with the LS was of crucial importance. Therefore, the position of the light sheet in respect to the grating

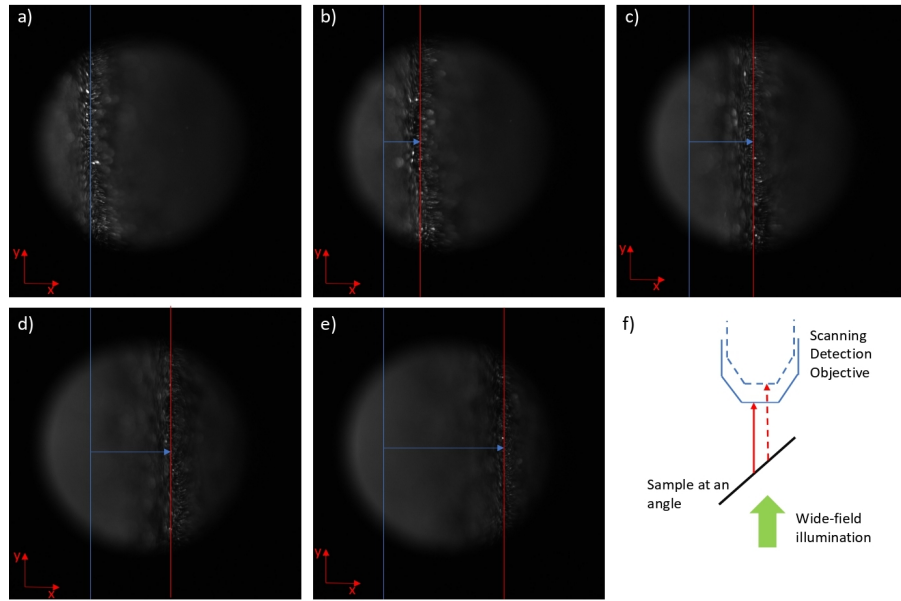


Figure 4.14: Fluorescent nanodiamond slide imaging with a 532nm wide-field illumination while the objective is scanning the sample. a) Image of the Nanodiamonds with the objective at the position $-200 \mu\text{m}$ in the z-direction, b) Image of the Nanodiamonds with the objective at the position $-100 \mu\text{m}$ in the z-direction, c) Image of the Nanodiamonds with the objective at the position $0 \mu\text{m}$ in the z-direction, d) Image of the Nanodiamonds with the objective at the position $100 \mu\text{m}$ in the z-direction, e) Image of the Nanodiamonds with the objective at the position $200 \mu\text{m}$ in the z-direction, f) Schematic showing the objective scanning characterisation strategy. The red and blue lines are used for representation of the pixel's translation and they were not used for the extraction of the data plotted in Figure 4.15

applied on the SLM was examined. This was achieved by placing CMOS camera (uEye iDS) at the focal position of the LS and, by including neutral density filters to protect the camera, imaging the LS. The tilt grating of the SLM was swept from -100 to 100 in steps of 10 . The LS translation caused by the change in the grating projected on the SLM was measured by estimating the position of the LS for each grating applied on the SLM. The shift of the LS was initially measured in pixels and then translated into μm . The resulted plots are shown in Figure 4.15. As it can be observed in Figure 4.15 the LS translation is not perfectly linear in respect with the grating applied on the SLM. This could be a result of the uncertainties within the calibration process. The camera used to image the in-focus LS was mounted on the imaging system through an optomechanical cage system; therefore, the calibration progress was not adapted to

Chapter 4. Dual Illumination-Single Detection Light Sheet Fluorescent Microscope - Characterisation and Imaging

the angle of the LS nor the angle of the camera. Additionally, the estimation of the focal line was achieved by linearly plotting the profile of the in-focus light sheet. Since the LS thickness is greater than the camera's pixel size, there is an uncertainty in the placement of the focal line. Knowing the scanning capabilities of the objective's stage

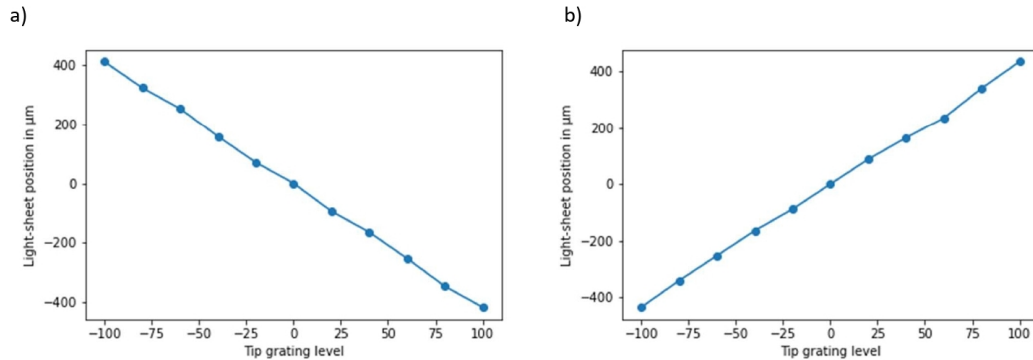


Figure 4.15: Light-sheet scanning characterisation in respect to the grating applied on the spatial light modulator. x-axis shows the applied grating and y-axis shows the corresponding light-sheet translation. a) Light sheet scanning of the reference illumination path, b) light-sheet scanning of the 2nd illumination path

and the effect of the grating projected on the SLM on the LS's position, the SLMtools software was modified so that the objective's focal position is synchronised with the position of the LS.

4.2.3 Nano-Diamonds Imaging

Nano-Diamond Samples Preparation

FND imaging was conducted on FNDs mounted either on a coverslip or in an optically transparent cuvette. To make the ND slide sample, FNDs were mixed with distilled water at a 1:100 ratio (90nm ND, Sigma-Aldrich 798150). When mixed, 10 μL of the mixture was dispensed on a coverslip. A pipette was used to continuously spread the liquid containing the FNDs across the coverslip until the water is evaporated (this can be done with the coverslip being placed on a hotplate at 40-50 degrees Celsius to speed up the evaporation process). Then 10-20 μL of distilled water or objective immersion oil was added on the top of the FNDs. A second coverslip was then placed on the top

Chapter 4. Dual Illumination-Single Detection Light Sheet Fluorescent Microscope - Characterisation and Imaging

of the oil or water. Few minutes were given for the sample to settle, and then it was sealed with nail varnish. When the nail varnish is hardened the sample is ready to be used.

The same FND was used to make a cuvette sample by mixing ND with agarose and then dispensing it in a cuvette for imaging. High optical quality cuvettes were required to avoid compromising imaging, thus we used the CV10Q7F Thorlabs 700 μL cuvettes, made with synthetic quartz glass. Initially an 1% agarose in water was heated in a microwave to form the agarose solution. NDs were added to the dissolved agarose at a ratio of 1:100. Because the agarose is liquid only at a high temperature a hotplate stirrer was used to keep the agarose liquid (set at 90 degrees Celsius) and the ND were mixed with the agarose using a vortex. The ND/agarose was inserted into an optically transparent cuvette. The cuvette was then sealed with nail varnish and the sample was ready to be imaged.

4.2.4 *C. elegans* Imaging

The protocol used for growing and freezing *C. elegans* was the one found at Worm-Book.org, as suggested by the *C. elegans* supplier [137], while the freezing *E. coli* protocol followed was suggested by Thermofisher [138]. The *C. elegans* supplier was the Caenorhabditis Genetics Center (CGC) at the University of Minnesota [139] and the strains used for imaging are the XE1995 and LX1960. XE1995 strain genotype is `wplIs98 [it 1pB::Chrimson::SL2::mCherry + odr-1p::RFP]` and it was chosen because of the red fluorescent protein (RFP) tag. RFP relative absorption compared to the peak is 49% with the illumination of a 532nm laser [140]. The LX1960 genotype is `vsIs172 [lin-11(enhaner)::pes-10p::GCaMP5 + lin-11(enhaner)::pes-10p::mCherry + lin-15(+)]`. The mCherry in both strains allowed the imaging of neurons. mCherry can be excited with the 532 nm laser used at the LSFM microscope; however, at 532 nm excitation mCherry is excited with 40% efficiency [141].

Sample Preparation

Three different samples of *C. elegans* were prepared and imaged with the LSFM microscope. A sample preparation method was based on the enclosure of a block of agar, 40 mm×10 mm×3 mm, seeded with *E. coli* and living *C. elegans* in a cuvette [137]. The sample used for imaging is shown in Figure 4.16. The block of agar is placed in a cuvette. To cover the gap of air formed, since the agar block is thinner than the cuvette, a cut cover glass is placed on top of the seeded agar. On top of the coverglass, 1% agar in water is placed to fill the rest of the cuvette and thus stabilise the sample.

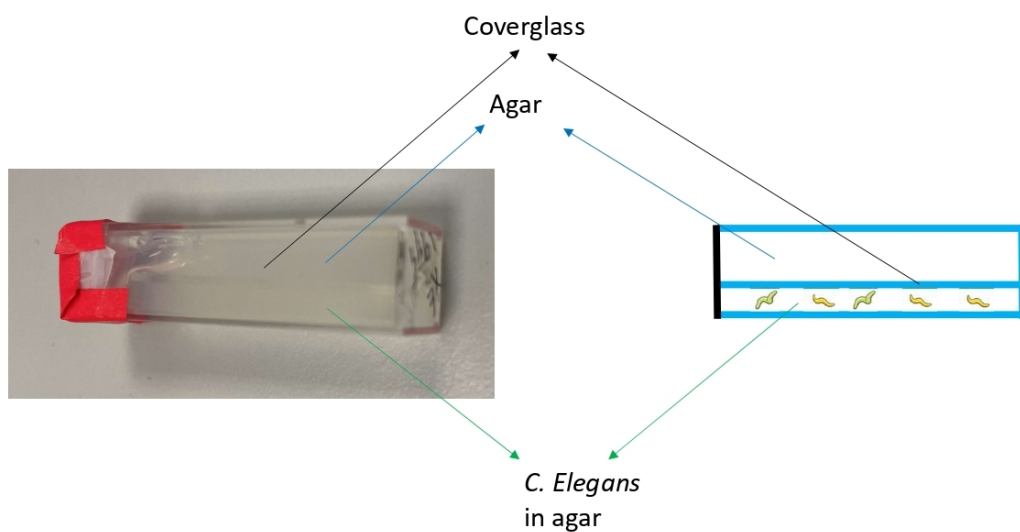


Figure 4.16: Cuvette based *C. elegans* sample. The black arrow shows where the coverglass is placed to separate the *C. elegans* (green arrow) from pure agar (shown with the blue arrow). The cuvette's dimension is 12.5mm×12.5mm×45mm

The other two samples were based on coverslip imaging, one with water and the other with immersion oil. To create the sample, a very small amount of worms or a single worm were moved from the petri plate to a coverglass [142], as described below.. A drop of water or immersion oil was then added on top of the worm and then the sample was sealed by placing a coverslip on the top and applying nail varnish and parafilm [143, 144]. The coverslip *C. elegans* sample is shown in Figure 4.17. To ensure that worms are transferred on the coverglass, the *C. elegans* culture was observed under a stereomicroscope. As the *C. elegans* culture consisted of worms at

different development stages, large worms were identified and transferred either by the "chunking" method, or by using tweezers to transfer a single worm.

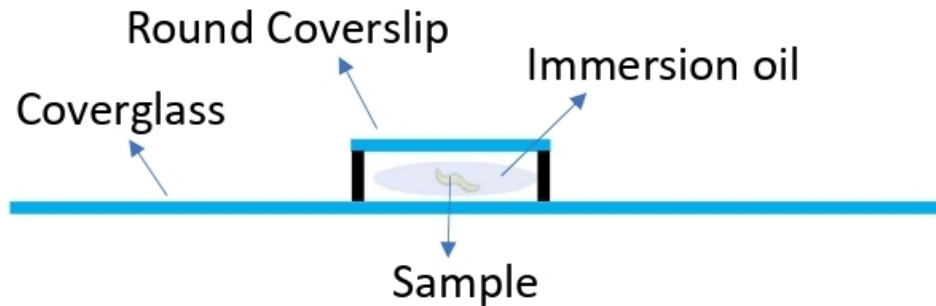


Figure 4.17: Coverslip *C. elegans* sample. A coverglass was used as a base where a single worm or a small block of agar with *C. elegans* was placed on it. On top of the sample I add a drop of immersion oil and then the sample was sealed with a round coverslip and nail varnish.

4.3 Results

4.3.1 Nano-Diamonds Imaging

Volumetric Imaging

The volumetric imaging capabilities were examined by imaging 90nm nanodiamonds in a cuvette. To push the microscope to its imaging capabilities, the depth of imaging acquired was increased until signal was not detected. Initially a $300\mu\text{m}$ depth scan was conducted followed by a $600\mu\text{m}$ and a $900\mu\text{m}$, the last being the limit of the depth of imaging. A $900\mu\text{m}$ depth scan is shown in Figure 4.18, where the imaging plane at depths of $135\mu\text{m}$, $465\mu\text{m}$ and $765\mu\text{m}$ are shown in Figure 4.19. The shape of the PSFs imply that there is significant spherical aberration which was expected since there was no refractive index matching nor a method of correction. As observed, a field curvature-like effect is presented, either due to the aberrations introduced by the tube lens, or by the vignetting at the camera's c-mount. An attempt to correct the field curvature is done by replacing the tube lens with a Plossl eyepiece (more information in Section 4.2.2); however, no improvement was observed, indicating that the cause

of distortion is most likely the vignetting at the c-mount of the camera (See Section 4.2.2).

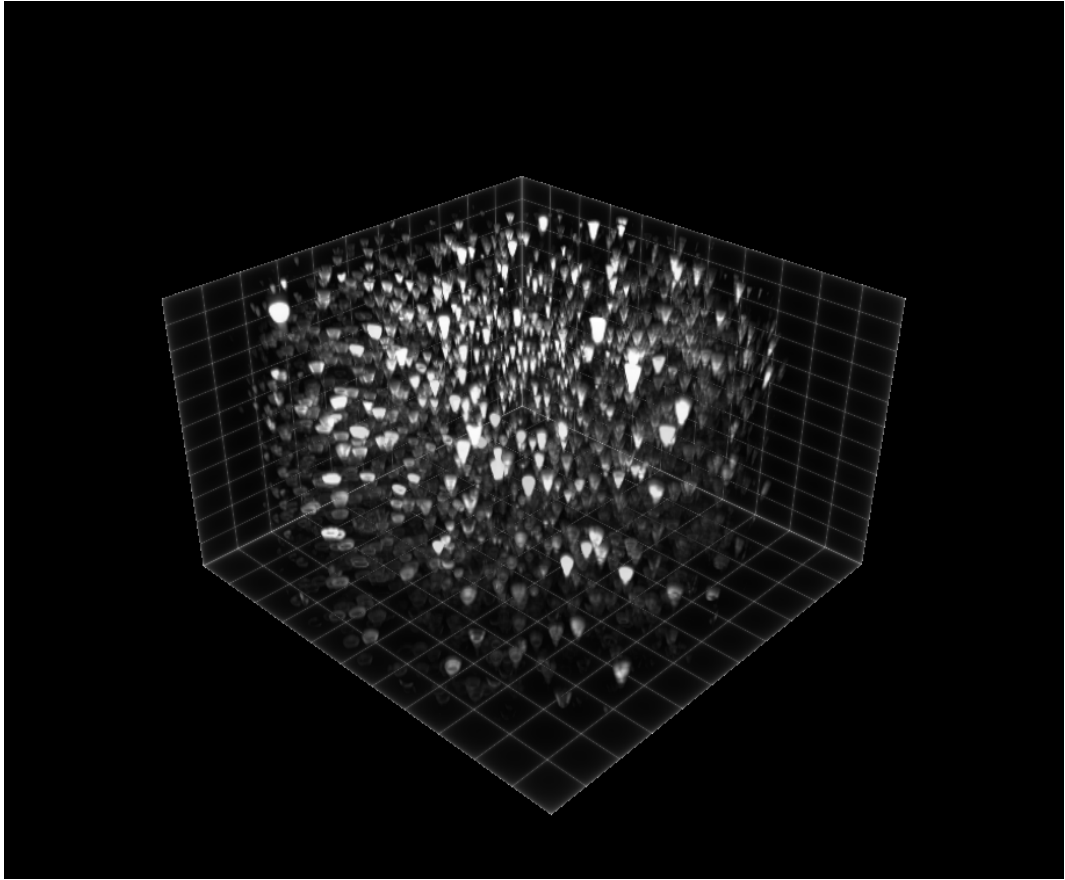


Figure 4.18: 3D image of 90nm nanodiamonds at a FOV of 1.5 mm x 1.55 mm and a depth of 900 μm imaged using the light-sheet fluorescent microscope with single light-sheet illumination. The scanning step was 3 μm . The grid is on 15micron scale for the x and y axes and 10 μm for the z-axis.

To calculate the axial and lateral resolutions, the FOV has been divided into two regions. Each region is subdivided into four sub-regions as shown in Figure 4.20. The yellow circles form the two regions and the red lines form the four sub-regions.

The axial resolution was calculated by isolating four low intensity FND within each region. I used low intensity features that were of the order of the PSF size in the hope that they were sub-diffraction sized single FND or single-digit clusters of FND. Then the z-profile was extracted using ImageJ. Gaussian fits to the z-profiles were used to determine the axial FWHM. A mean of the four FWHMs determined the axial

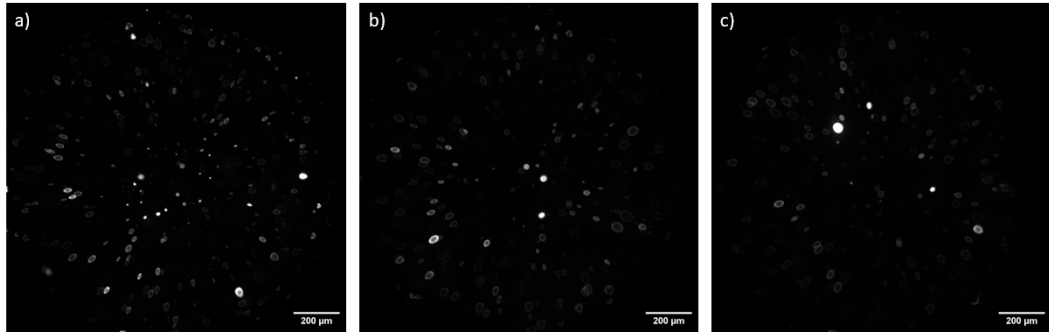


Figure 4.19: Plane images of nanodiamonds at depths of a) $135\mu\text{m}$, b) $465\mu\text{m}$ and c) $765\mu\text{m}$ from the $900\mu\text{m}$ scan. Aberrations at the edge of the field of view are observed within the entire sample depth.

resolution in each region and the standard error was used to estimate the error of my measurements. Measurements of the axial resolution were made at different depths for all three scans. The same sample was imaged at three different depth scanning ranges. The first scanning range was from 0 to $300\mu\text{m}$, the second from 0 to $600\mu\text{m}$ and the third from 0 to $900\mu\text{m}$. For the $300\mu\text{m}$ scan the axial resolution is examine at depths of $45\mu\text{m}$, $150\mu\text{m}$ and $255\mu\text{m}$. For the $600\mu\text{m}$ scan the depths investigated are $90\mu\text{m}$, $300\mu\text{m}$ and $510\mu\text{m}$, while for the $900\mu\text{m}$ scan the depths where the axial resolution is recorded are $135\mu\text{m}$, $450\mu\text{m}$ and $765\mu\text{m}$. The axial resolution at different depths has been acquired. The lateral resolution was estimated by calculating the xy FWHM for each of the grid's squares using the LuckyProfiler imageJ plugin [145]. LuckyProfiler calculates the FWHM of the PSF considering all the planes of a stack; therefore, I did not examine xy-axis PSF for different imaging depths. The axial and lateral resolutions for the reference arm are shown in Figures 4.21 and 4.22 respectively. The axial and lateral resolutions for the second illumination arm are shown in Figures 4.23 and 4.24 respectively. To examine the LS thickness, a series of images were acquired with a stationary LS while scanning the detection objective. The scan started from $-150\mu\text{m}$ and ended at $150\mu\text{m}$ with 0 the position that the detection objective recorded FNDs peak intensity. Z-axis profiles were extracted and a Gaussian fit was applied to measure the LS thickness. The FOV was divided in seven regions along the y-axis (see Figure 4.9) to measure the thickness of the LS along the entire FOV. The FOV separation is

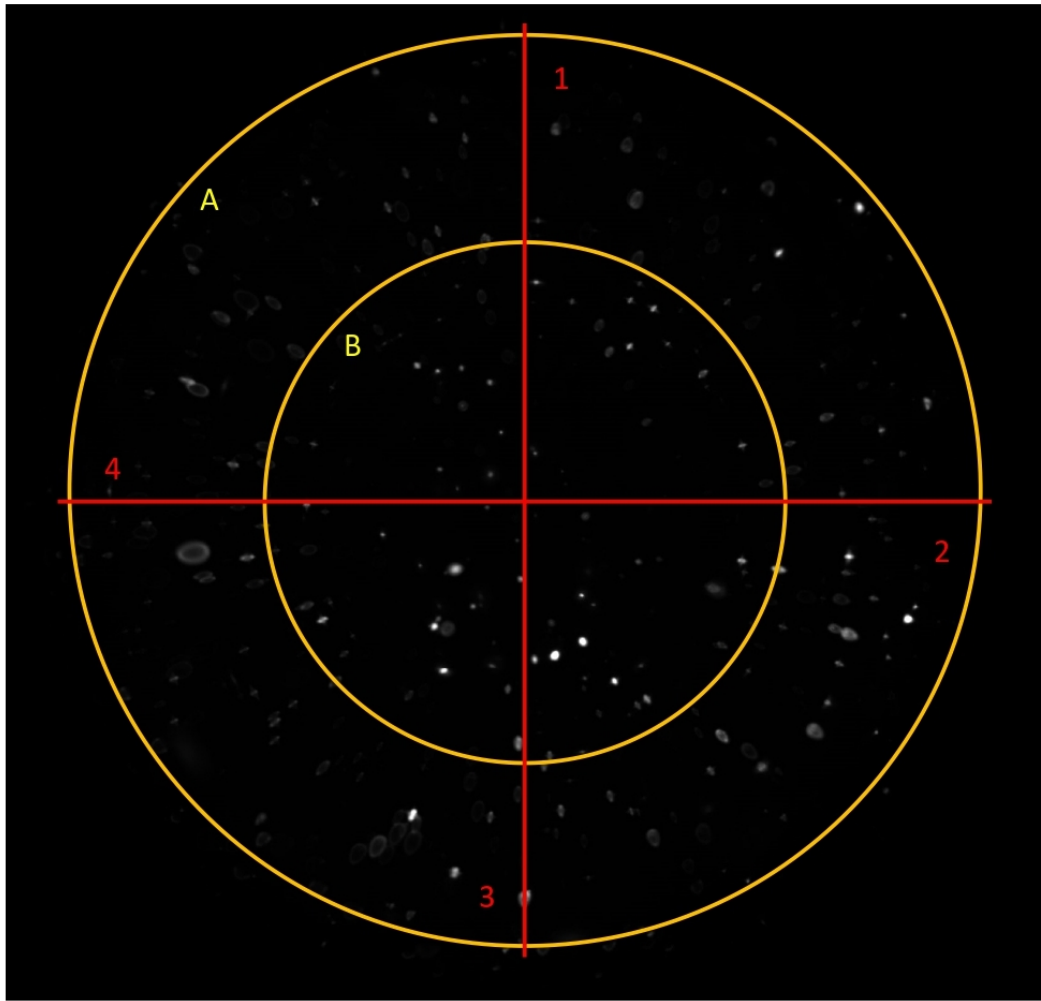


Figure 4.20: Separation of the FOV into two regions (A and B, yellow circles) and four sub-regions (1, 2, 3, and 4, separated by the two red lines) to investigate the axial and lateral resolution within the entire field of view.

shown in Figure 4.25 The reference path LS thickness and the second path LS thickness are shown in Figure 4.26. Four FNDs or FND clusters were examined in each region to estimate the uncertainty in this measurement.

Synchronised dual illumination imaging

The imaging distortion presented at the edge of the FOV cancels out the benefit of larger FOV imaging offered by the dual LS illumination, because increasing the illuminated FOV will not result in an increase of the imaged FOV. This is not due to the

Chapter 4. Dual Illumination-Single Detection Light Sheet Fluorescent Microscope - Characterisation and Imaging

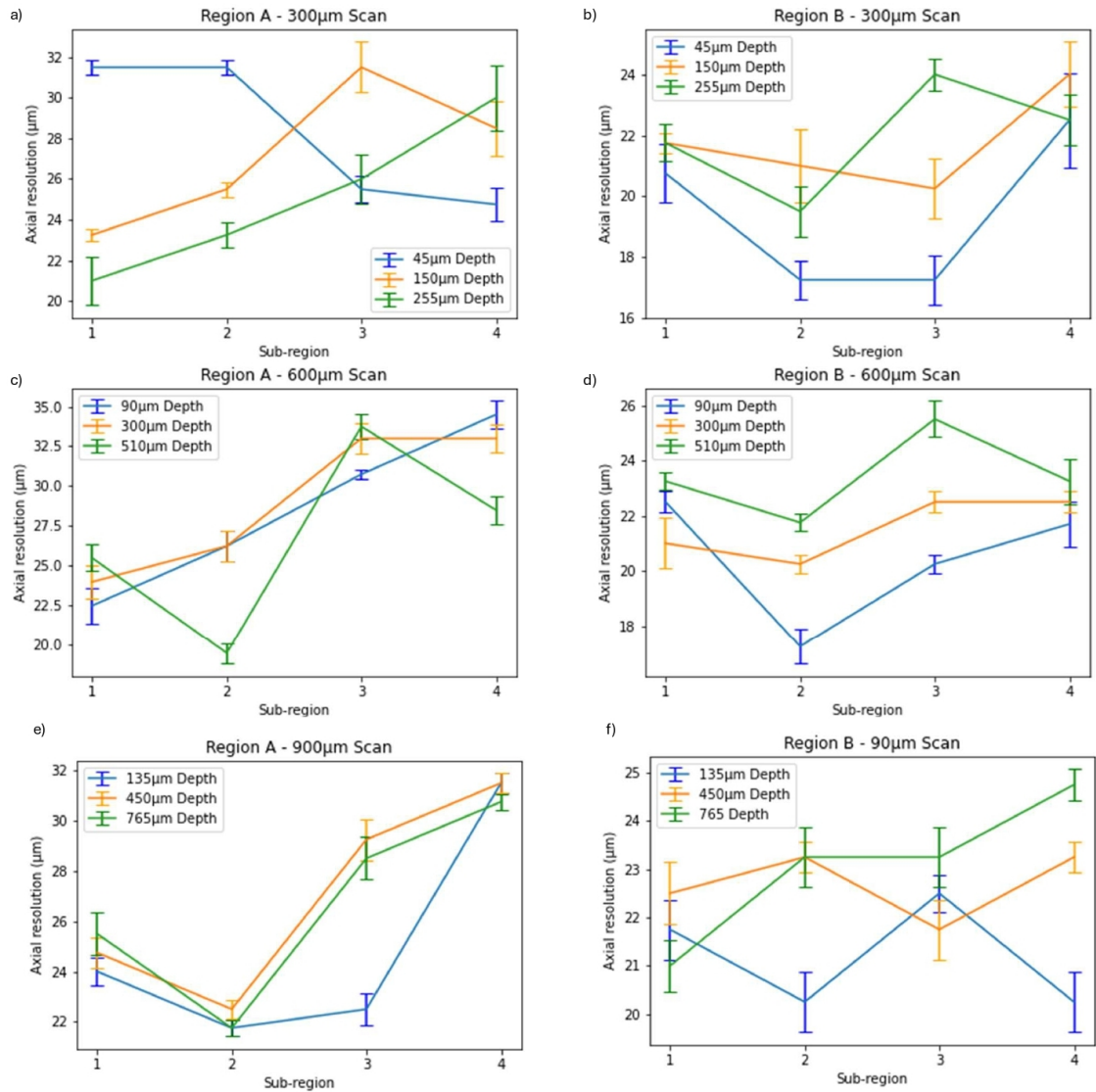


Figure 4.21: Axial resolutions of the light-sheet fluorescence microscopy at different depths with the reference arm light-sheet illumination imaging 90 nm fluorescent nanodiamonds. a) c), and d) Axial resolution for region A captured through a 300 μm (at depths of 45, 150, and 255 μm), 600 μm (at depths of 90, 300, and 510 μm), and 900 μm (at depths of 135, 450, and 765 μm) scans respectively. b), d), and f) Axial resolution for region B captured through a 300 μm (at depths of 45, 150, and 255 μm), 600 μm (at depths of 90, 300, and 510 μm), and 900 μm (at depths of 135, 450, and 765 μm) scans respectively.

nature of dual illumination LSFM, but because of the vignetting in the imaging path of our microscope (solutions to overcome this problem are described in Section 4.2.3). Therefore, all the data acquisition occurred under a single illumination LS. To examine

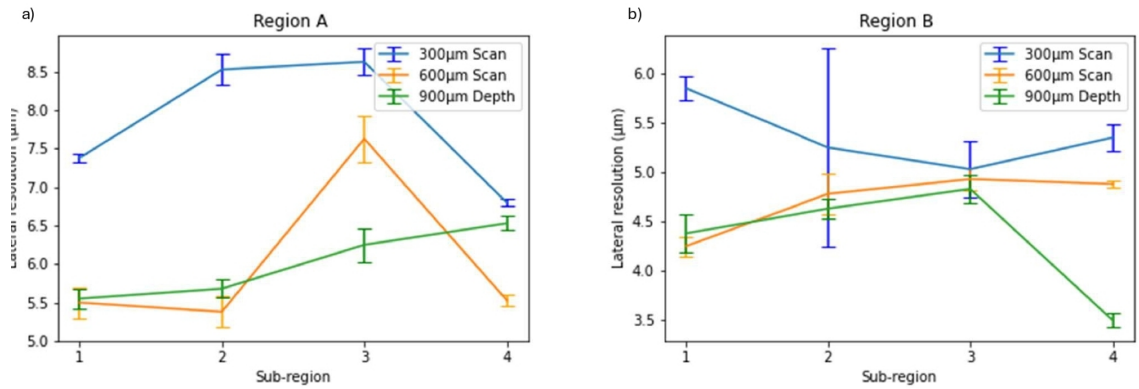


Figure 4.22: Lateral resolutions of the light-sheet fluorescence microscopy at different depths with the reference arm light-sheet illumination imaging 90 nm fluorescent nanodiamonds. a) Lateral resolution of region A for a 300, 600 and 900 μm scan. b) Lateral resolution of region B for a 300, 600 and 900 μm scan.

the synchronisation of the two LSs, both LSs were aligned and focused at the centre of the FOV. All scans conducted for the volumetric imaging of NDs are repeated with dual illumination and the images acquired for each illumination path were compared at various imaging depths. Figure 4.27 shows imaging planes when the reference path is used for illumination (a,b,c) and when the second path is illuminating (d,e,f). Figure 4.27a) and d) are at a depth of 60 μm , Figure 4.27 b) and e) are at a depth of 150 μm while Figure 4.27 c) and f) are at a depth of 240 μm . In Figure 4.27 g), h), and i) the overlay between a) and d), b) and e), and c) and f) is shown respectively. As shown, the LSFM microscope was capable of synchronised dual-illumination volumetric imaging.

Image correction

The acquired images show a field curvature-like effect. To investigate whether this is actual field curvature or if it is formed by the blockage occurring at the camera's mount different tube lenses were examined. In other applications, a Plossl eye-piece configuration, used as a tube lens, was found to reduce the effect optical aberrations (including field curvature) and improve imaging performance [146,147]. The work of V. Voleti et.al showed improvement of a LSFM microscope performance when introducing a Plossl lens in the detection path of the microscope [146]. Plossl lenses are made by placing two achromatic doublets symmetrically around a small air gap as shown in

Chapter 4. Dual Illumination-Single Detection Light Sheet Fluorescent Microscope - Characterisation and Imaging

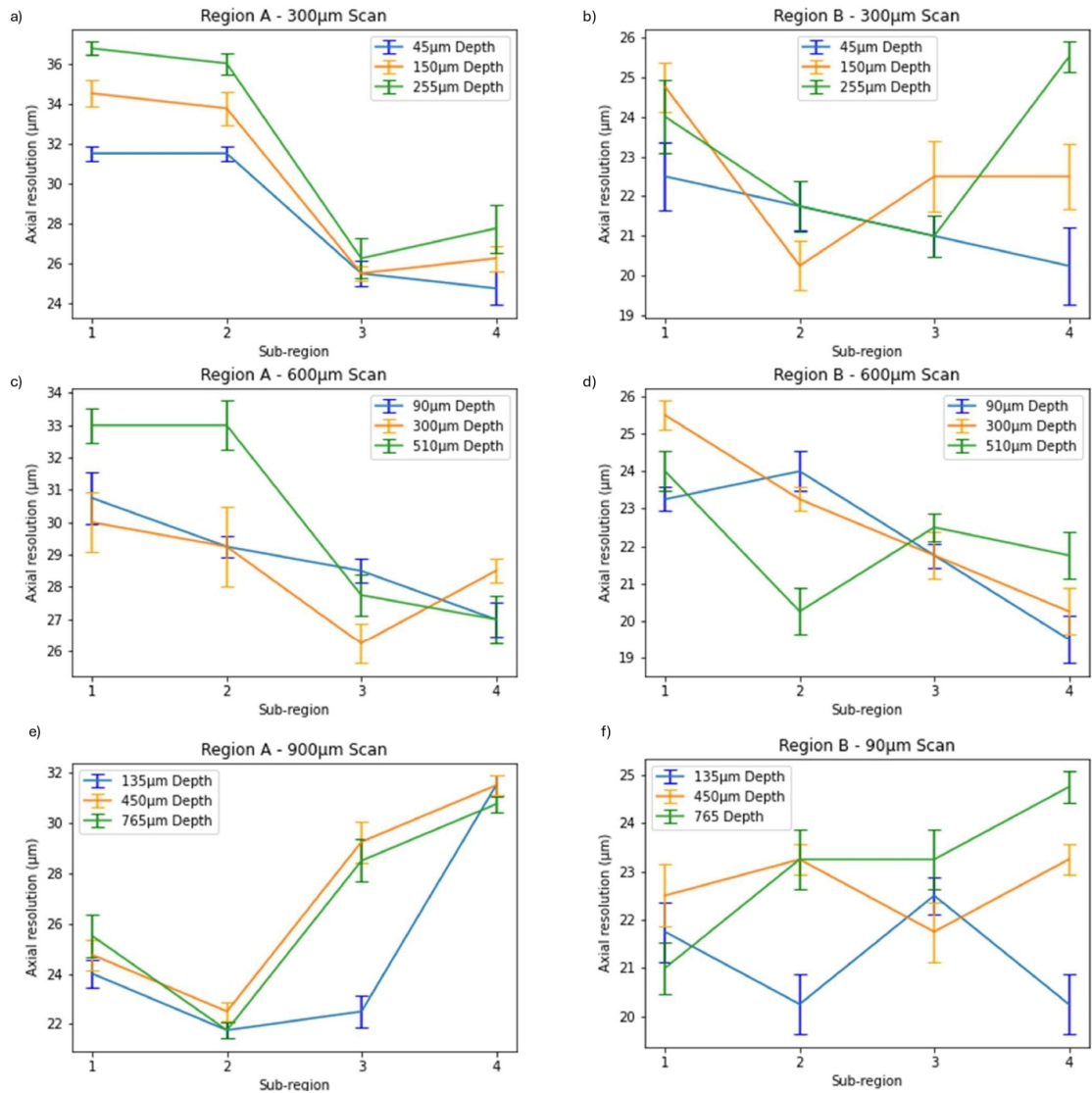


Figure 4.23: Axial resolutions of the light-sheet fluorescence microscopy at different depths with the second arm light-sheet illumination imaging 90 nm fluorescent nanodiamonds. a) c), and d) Axial resolution for region A captured through a 300 μm (at depths of 45, 150, and 255 μm), 600 μm (at depths of 90, 300, and 510 μm), and 900 μm (at depths of 135, 450, and 765 μm) scans respectively. b), d), and f) Axial resolution for region B captured through a 300 μm (at depths of 45, 150, and 255 μm), 600 μm (at depths of 90, 300, and 510 μm), and 900 μm (at depths of 135, 450, and 765 μm) scans respectively..

Figure 4.28 [148].

The overall focal length of the Plossl tube lens is the half of the focal length of each of the doublets. Since we wanted to check if there was any improvement in the imaging

Chapter 4. Dual Illumination-Single Detection Light Sheet Fluorescent Microscope - Characterisation and Imaging

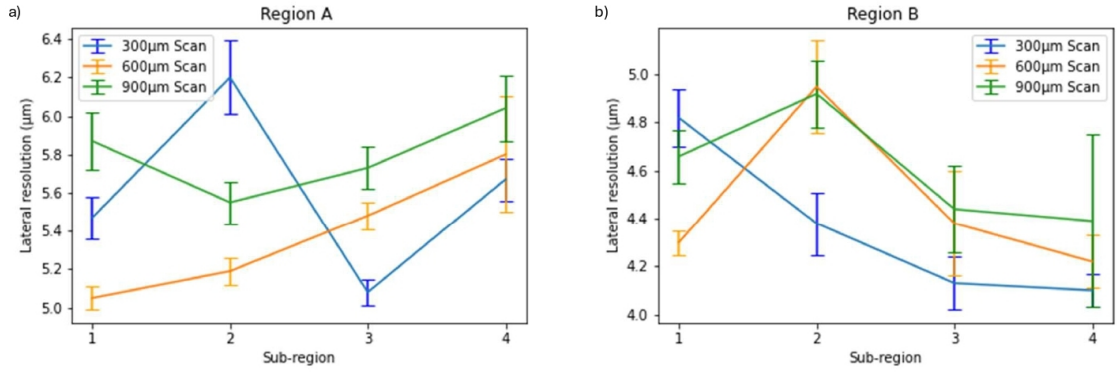


Figure 4.24: Lateral resolutions of the light-sheet fluorescent microscopy at different depths with the second arm light-sheet illumination imaging 90 nm fluorescent nanodiamonds. a) Lateral resolution of region A for a 300, 600 and 900 μm scan. b) Lateral resolution of region B for a 300, 600 and 900 μm scan.

with the use of a Plossl lens, we constructed a 90mm effective focal length Plossl lens from two 180mm lenses that were available to us. The difference in effective focal length (90mm versus the original design's 80mm) was not expected to be important.

To investigate whether the Plossl eyepiece corrects for the distortion observed at edge of the FOV, a grid calibration sample was used. The examination of the effect of the Plossl eyepiece was based on moving a straight line (formed at the edge of the square grid) across the y-axis of the FOV; therefore, a distortion at the edge of the FOV would be observed, if present. Assuming the bottom edge of the FOV is pixel 0, the sample is moved from 0 to 1250 in steps of 250 pixels, with pixel 1250 being at the top of the FOV. Figure 4.29 shows the field curvature measurement strategy. The top of the microscope's FOV is shown (pixel 1250) with a Plossl lens focusing the image on the camera (Figure 4.29a) and with a single lens focusing on the camera (Figure 4.29b). To measure the effect of field curvature a two parallel lines were drawn. One line passes through points A and B (see Figure 4.29), which represent the square grid at the edge of the FOV. The second line passes through point C so that there is only one point of intersection. The distance between the two lines, and thus the effect of field curvature, is shown in Figure 4.30. To identify points A, B, and C the linear profile plot was used in ImageJ. By selecting the live data option on the profile plot and moving the line manually, the points of intersection of the line with the square grids were found. Points

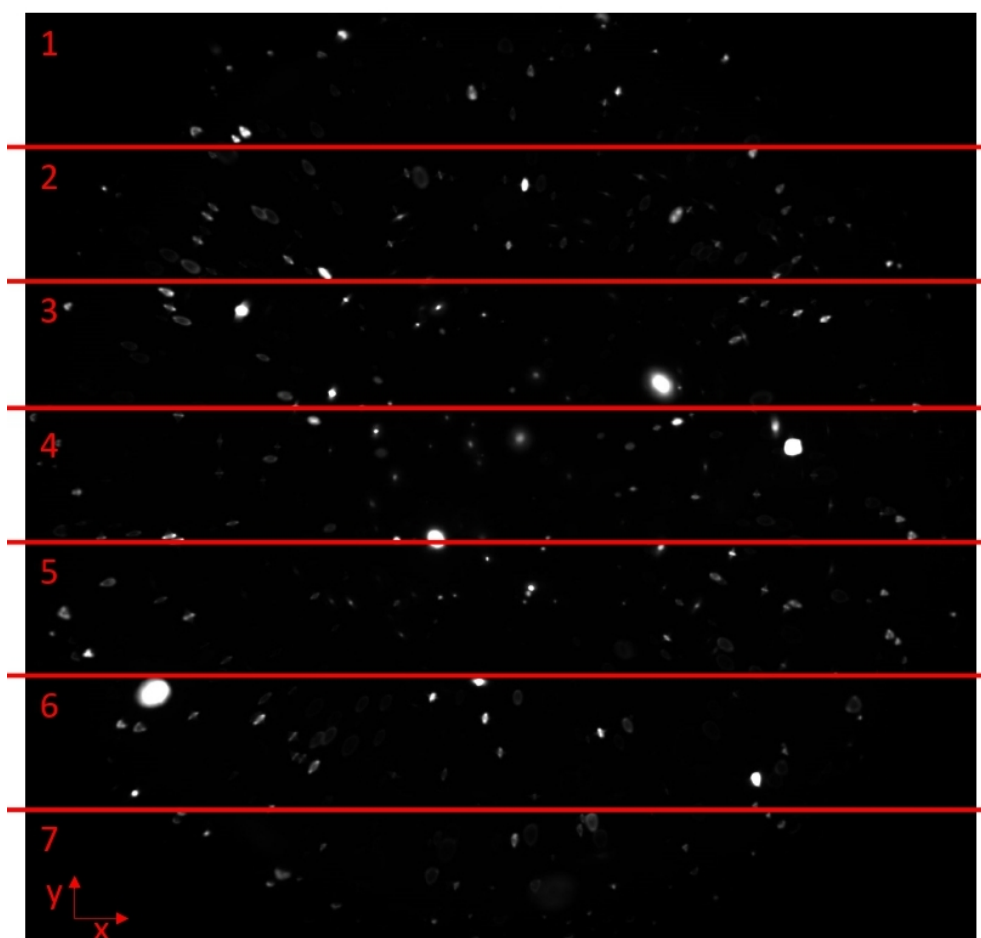


Figure 4.25: Division of the FOV in seven regions of interest to investigate the light-sheet thickness along the entire field of view.

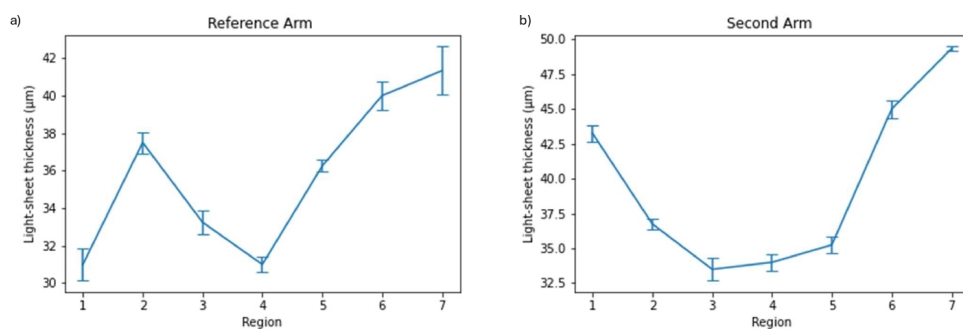


Figure 4.26: a) Reference illumination arm and b) second illumination arm light-sheet thickness along the entire field of view of the light-sheet fluorescent microscope.

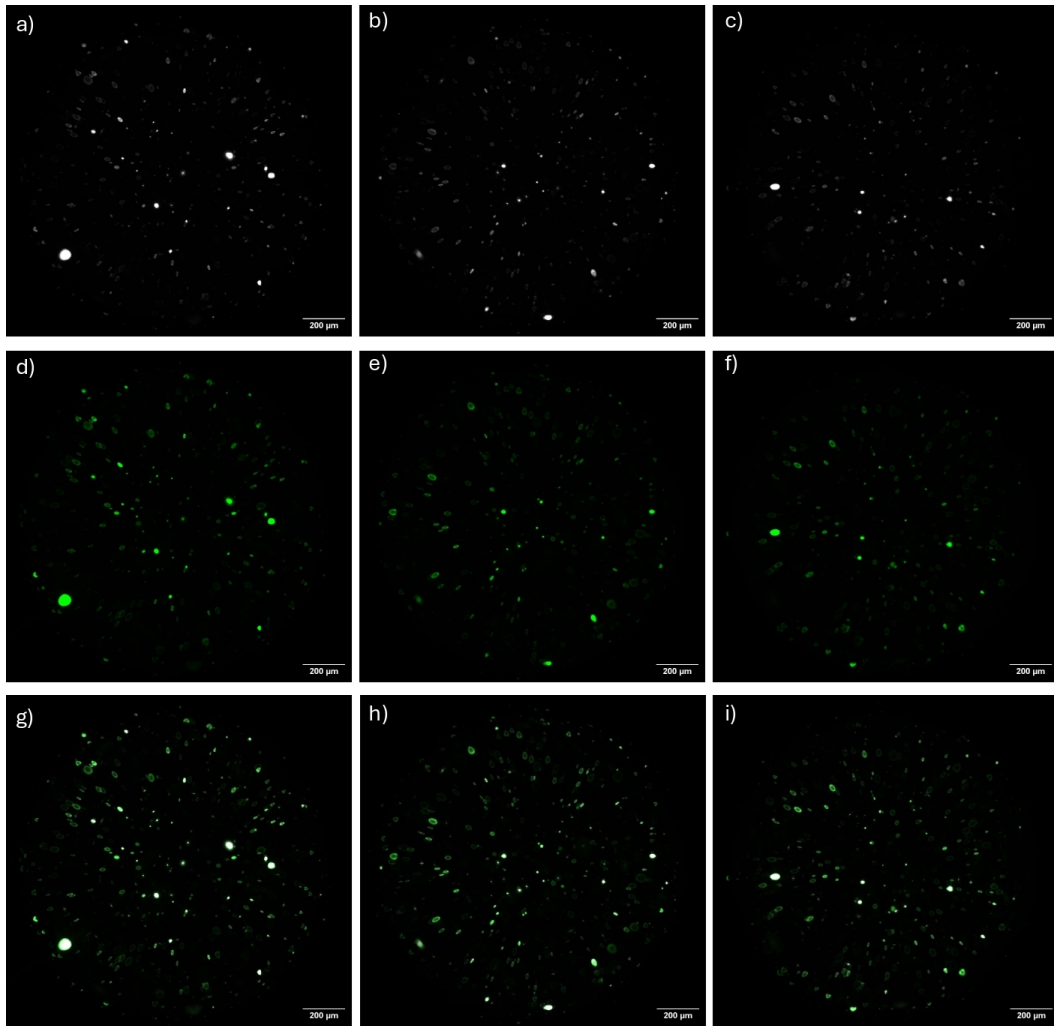


Figure 4.27: Dual illumination image acquisition using the light-sheet fluorescent microscope. Images in white refer to the images obtained when the light-sheet from path 1 is used for illumination, while green images represent images obtained with illumination from path 2.

A, B and C, were identified empirically, which would introduce an uncertainty in the measurement.

As shown, the Plossl lens does not reduce the effect of field curvature, but it adds barrel distortion. Therefore, it is believed that the camera blockage cause the observed imaging distortion. This requires further investigation to be clearly shown, however the impact on field of view alone makes investigation of how to remove the camera-mount induced vignetting an important future work.

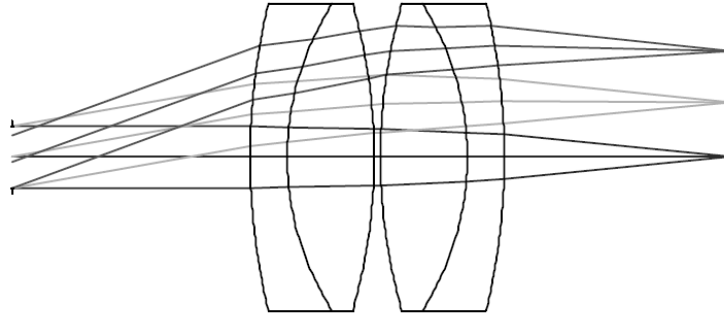


Figure 4.28: Design of Plossl eyepiece. Two achromatic doublets are placed symmetrically with a small gap between them. The light is travelling from left to right. The figure was extracted using the work of M. Laikin [149].

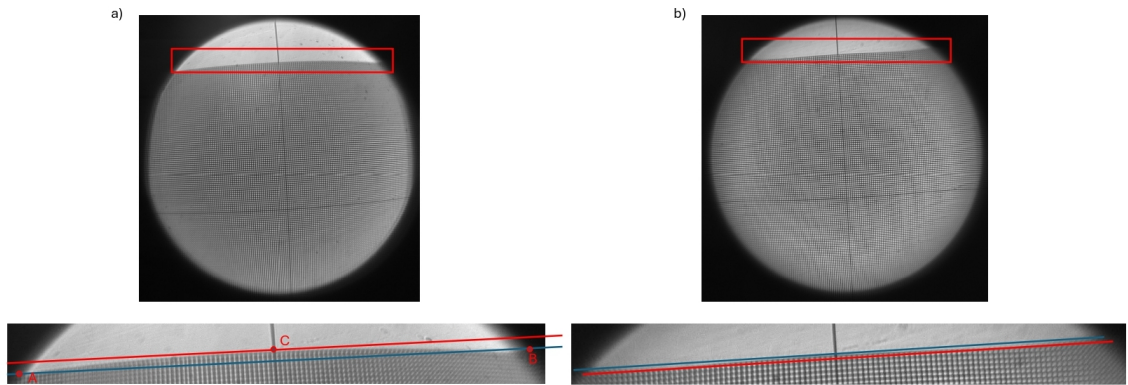


Figure 4.29: a) Plossl lens focusing the image on the camera with the square grid at $1250 \mu\text{m}$. b) Single lens focusing the image on the camera with the square grid at $1250 \mu\text{m}$. The red and blue lines are used for representation of the field curvature measurement strategy and they were not used for the extraction of the data plotted in Figure 4.30

4.3.2 *C. elegans* Imaging

Volumetric imaging

Volumetric images were obtained by scanning through the sample from 0 to $300 \mu\text{m}$ in the z-direction, with 0 being the plane closer to the detection objective and $300 \mu\text{m}$ being the furthest away from the detection objective. The scanning step size was $3 \mu\text{m}$.

In Figure 4.31 the in-focus image of a *C. elegans*, strain-xe1995 mounted in a cu-

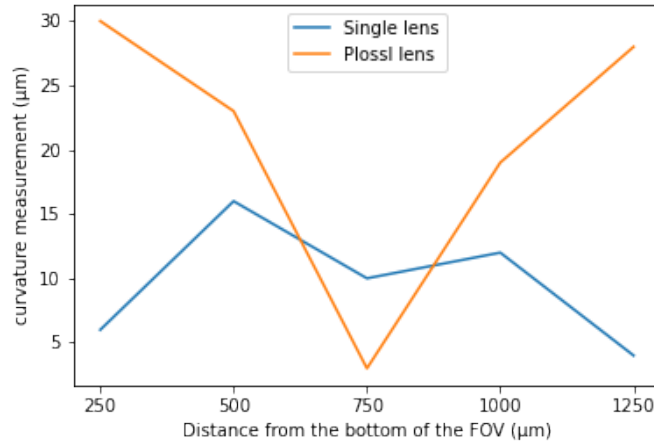


Figure 4.30: Comparison of a single lens and Plossl lens imaging along the field of view imaged using the detection path of the light-sheet fluorescent microscope.

vette, is shown. The worm is $434 \mu\text{m}$ long with a maximum diameter of $19 \mu\text{m}$. The LuckyProfile ImageJ plugin was used to determine the imaged cells' size. The region from the pharynx to the head was investigated and it was found that the lateral resolution was $3.5 \mu\text{m}$. According to the worm's size, this is an L2 to L3 larvae. According to the CGC [139], in the xe1995 strain mCherry, is expressed in the neurons of the *C. elegans*. Comparing *C. elegans* images from the literature, with those from my LSFM (Fig 4.31), anatomical features of the imaged *C. Elegans* were identified. It is shown that the head of the worm is at the top of Figure 4.31. The pharynx, the terminal bulb of the pharynx and the intestine can be identified. The brightest area on the worm is assumed to be the nerve ring since the largest collection of neurons is around the nerve ring and it is anatomically close to that bright spot [37] [13, 150–152].

Investigating the volumetric imaging capabilities of the LSFM microscope, it was found that the cuvette sample results in distorted 3D imaging. This is because the image is obtained through non-transparent agar and the worm is imaged at a depth of 2 mm, with 0 being the edge of the cuvette closer to the detection objective [153, 154]. Although 1% agar in water is non-scattering, in this case, the agar contains Lysogeny broth (LB) and *E. Coli*, which results in scattering [155].

To reduce scattering, a *C. elegans* on coverslip was imaged. A *C. elegans*, strain

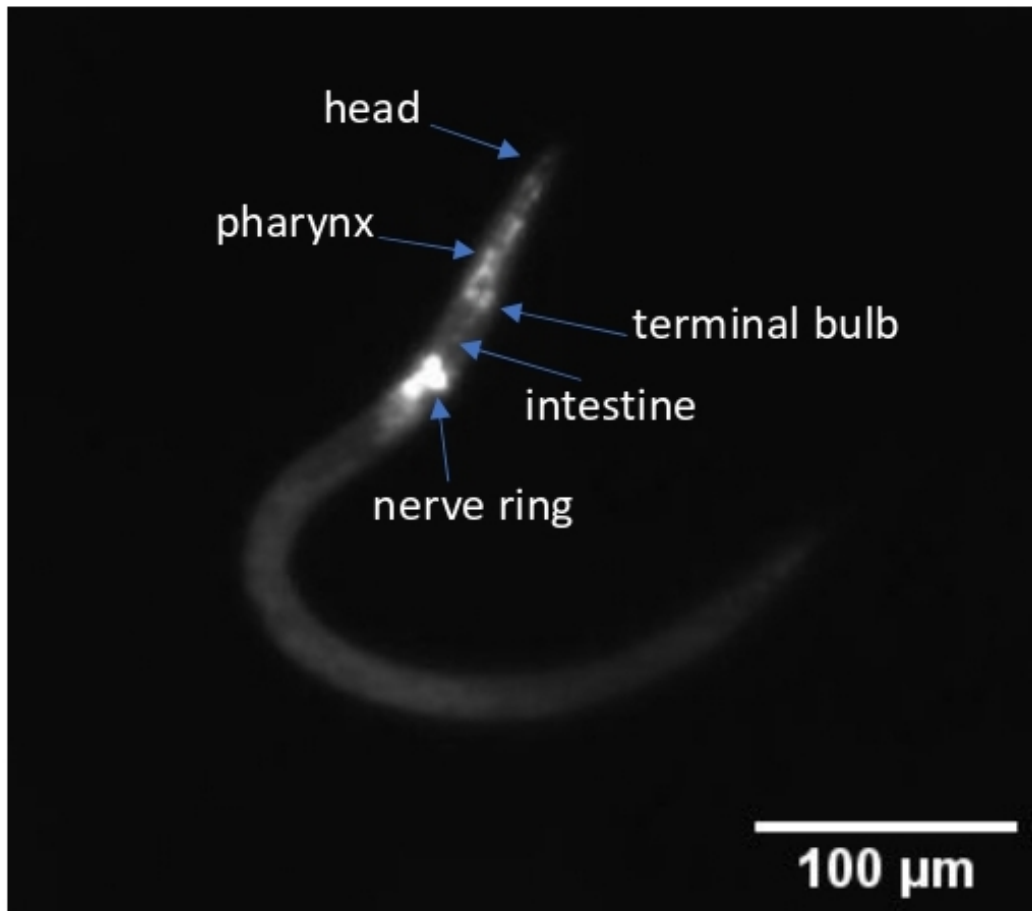


Figure 4.31: Focal plane of *C. elegans*, strain xe1995, in agar imaged with the custom made light-sheet fluorescent microscope. The arrows point to the head, pharynx, terminal bulb, intestine and nerve ring of the worm.

xe1995, mounted on a coverslip and sealed after 10 μl of water was dropped on the sample is shown in Figure 4.32. Two worms are observed, a large one which is 848 μm long worm with a diameter of 58 μm and a smaller one with a length of 450 μm and a diameter of 15 μm . A young adult and an L2 to L3 worms were imaged. It is also found that cells of approximately 6 μm can be imaged (using Luckyproffier imageJ plug-in). Comparing the imaged *C.elegans* to the anatomy of the worm described in Figure 1.2 and imaged *C. elegans* in the literature, it can be assumed that the head and the nerve ring for both worms are spotted. Embryos might be imaged in the young adults. Embryos are considered to be imaged, since the shapes spotted, and assumed

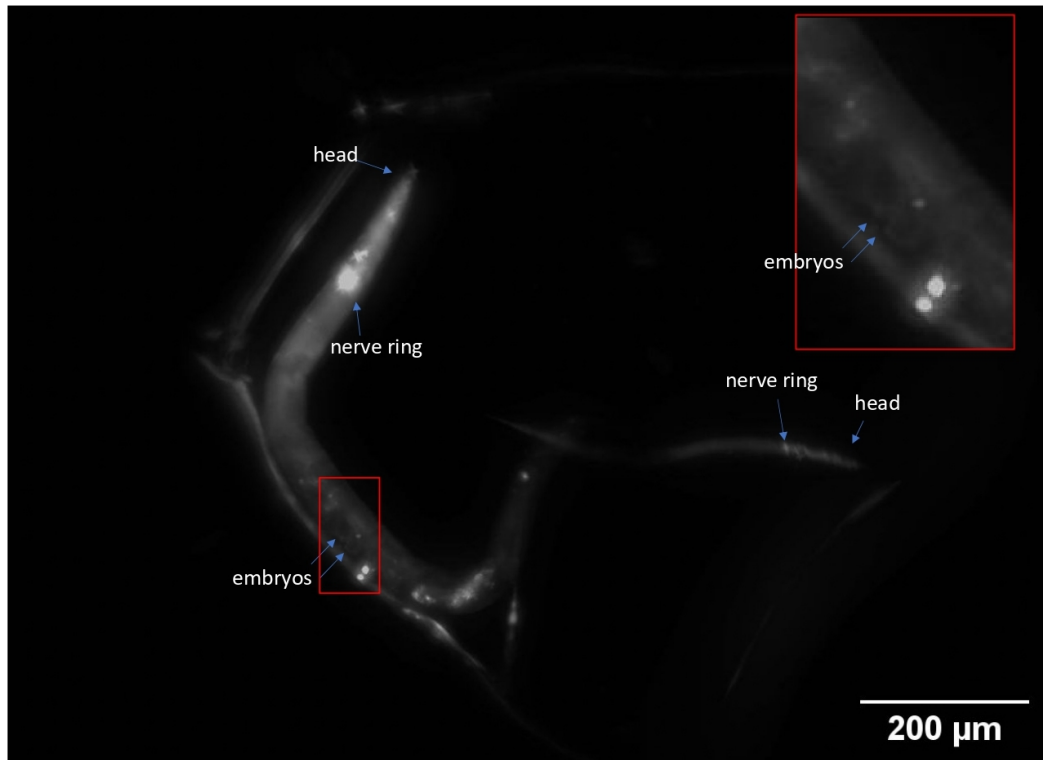


Figure 4.32: *C. Elegans*, strain xe1995, imaged on a coverslip with water using the light-sheet fluorescent microscope. A young adult and an L2/L3 larvae are shown. The head and the nerve ring are shown with blue arrows. Embryos in the young adult are imaged and shown within the red square.

to be embryos, fit the location and shape of embryos in adult worms. Additionally, a significant amount of agar is observed around the worms. As found in the cuvette sample imaging, agar with Lysogeny Broth (LB) and *E. Coli*, results in scattering. This comes from the "chunk" worm transfer method. The effect of scattering is significantly reduced compared to imaging through a cuvette filled with agar; however, there is still scattering observed. The effect of the light's interaction with the water-agar (with LB broth and *E. Coli*) is shown in Figure 4.32, where the bright elongated region to the left of the nematode is the boundary between water and agar formed either by the reflection of the excited fluorescence between water and agar or the reflection of fluorescence between water and the coverglass.

A *C. elegans* sample where the worm is on the top of the coverglass and sealed with a coverslip after a drop of immersion oil is dropped on top of the sample was prepared. A

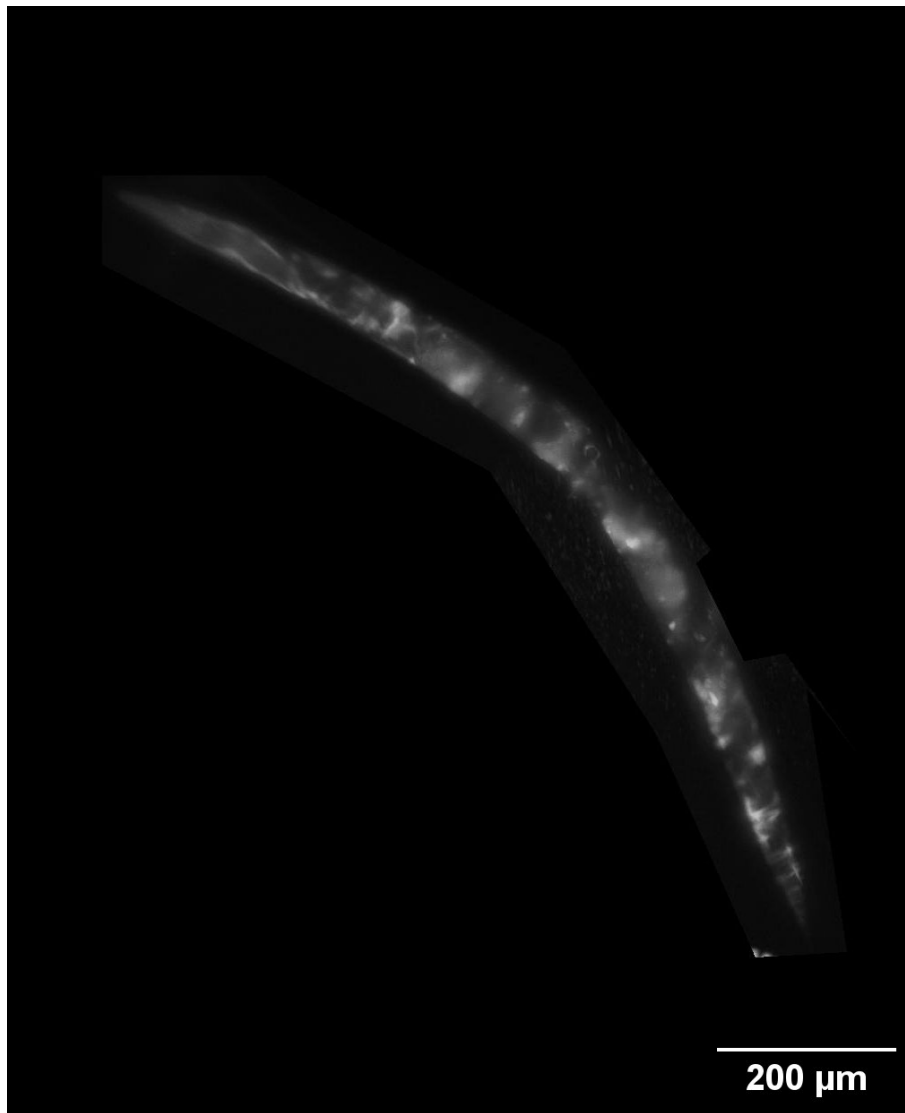


Figure 4.33: Optical section of a lx1960 strain *C.elegans* imaged on a coverslip with immersion oil using the light-sheet fluorescent microscope. The Figure was cropped so that only the nematode under investigation is shown.

single worm has been transferred on the coverslip using two needles. Figure 4.33 shows a *C. elegans*, strain LX1960. The length of the worm is 1142 μm and its diameter is 60 μm . Agar is not observed around the worm and a clearer 3D image was achieved (shown in Figure 4.34).

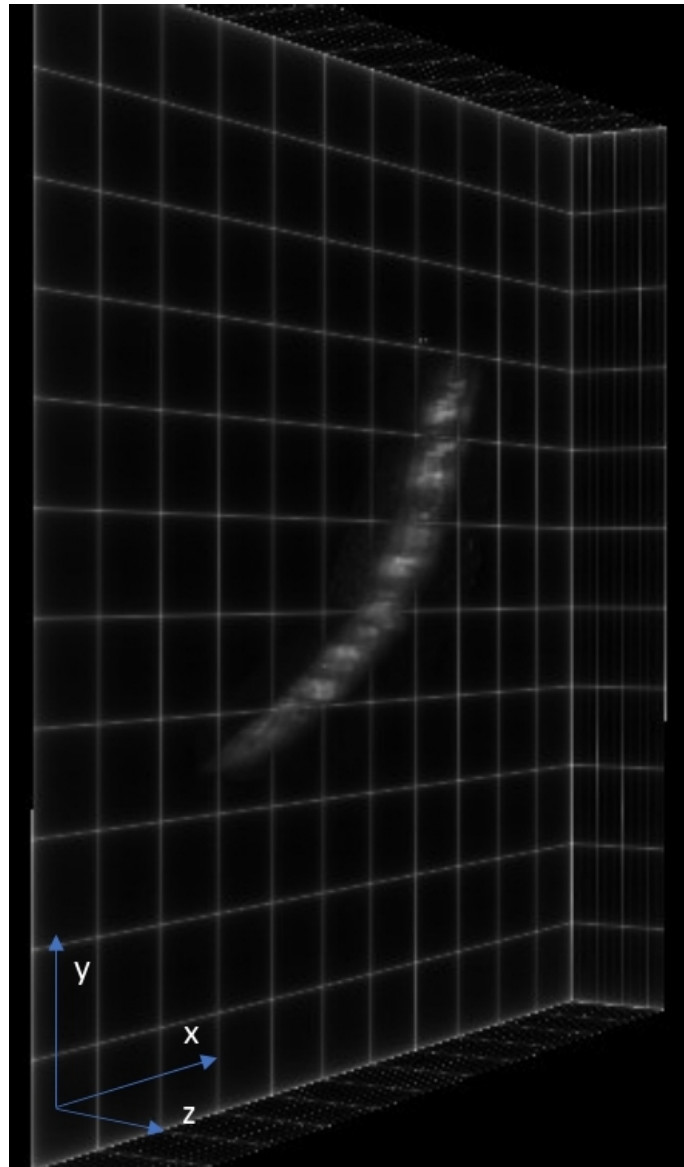


Figure 4.34: Volumetric imaging of lx1960 strain *C.elegans* on a coverslip with a drop of immersion oil using the light-sheet fluorescent microscope. Grid size in x-direction is $145\ \mu\text{m}$, in the y-direction $160\ \mu\text{m}$ and in the z-direction $65\ \mu\text{m}$.

Freely moving samples

A *C. elegans* sample was made by placing worms on a coverglass, dropping $50\ \mu\text{l}$ of immersion oil on top of the worms. A coverslip is placed on top of the worms and oil and sealing it with nail varnish and parafilm. Moving *C. elegans* were identified within the sample after a $300\ \mu\text{m}$ scan, in steps of $3\ \mu\text{m}$ was made. Figure 4.35 shows a

Chapter 4. Dual Illumination-Single Detection Light Sheet Fluorescent Microscope - Characterisation and Imaging

series of images captures at an 100ms interval and 3 μm z-direction scans (z-direction is parallel to the detection objective). Three worms are observed; worm 1 is 243 μm long and its diameter is 15 μm , shown with the red arrow. Worm 2 is 678 μm long and its diameter is 59 μm , shown with the blue arrow, and worm 3 is 164 μm long and its diameter is 13 μm , shown with a yellow arrow. Cells of sizes 4 μm to 5 μm are observed in all 3 worms. Among the Figures 4.35 a) to j) movement of *C. elegans* is observed, shown in the zoomed images ai) to ji).

4.4 Summary and Discussion

In this Chapter I present the LSFM microscope I constructed along with the SLM calibration, its characterisation, and imaging capabilities. SLMs were used for laser scanning and refocusing in microscopy [95, 156]. In my study, a SLM was used for laser scanning and modulation, and it is shown that it can achieve an accurate LS scanning. The SLM calibration procedure followed was the one suggested by the SLM supplier [132, 133].

The FOV of the LSFM was measured to be 1.6 mm. Due to the difference between the measured FOV and the modelled FOV (2 mm) further investigation of the detection path was conducted. The LSFM detection path was modelled using Raytracing [25] and it was found that vignetting occurs at the c-mount of the camera. To ensure that vignetting was causing the reduction of the FOV, the aperture that simulates the c-mount of the camera in Raytracing was removed. The resulted simulation showed that a 2 mm FOV would have been achieved without the vignetting. This finding agrees with the literature, since reduction of FOV due to vignetting was previously reported [157].

The lateral and axial resolution of the LSFM were measured through the volumetric imaging of 90 nm NDs. Three volumetric scans were conducted at different scanning ranges were made, a 300 μm , a 600 μm , and a 900 μm , with a scanning step size of 3 μm , and a single LS illumination. Spherical aberration was observed in all three scans. Less aberrations are observed in the centre of the FOV and, while aberrations increase at the edge of the FOV. Similar aberrations were observed in the work of Y.

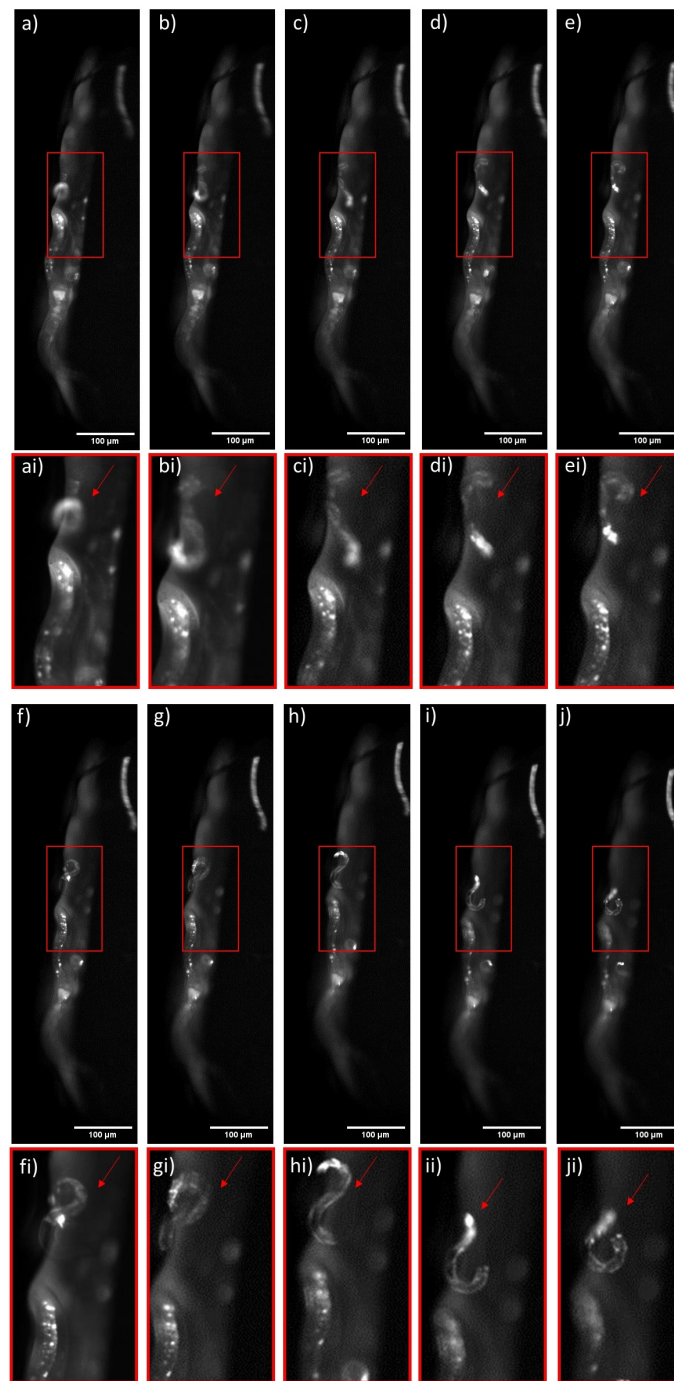


Figure 4.35: Freely moving xe1995 *C. elegans* imaging on a coverslip with immersion oil. Time duration of imaging sequence from the image a) to j) is 1 second. ai) to ji) is the same imaging sequence zoomed in on the moving *C. elegans* (red arrow). Time points = 100ms.

Chapter 4. Dual Illumination-Single Detection Light Sheet Fluorescent Microscope - Characterisation and Imaging

Liu et.al [158], where a volume of $499 \times 499 \times 192 \mu\text{m}^3$ of 200 nm fluorescent beads was imaged. However, the aberrations in that study were caused by an electrically tunable lens (ETL) in the detection path. In the work of Y. Liu et.al the ETL was used to increase the imaging speed of a LSFM by eliminating the scanning of the detection objective. The ETL causes aberrations, mainly spherical aberration, in large volumes as the focusing is deviated from the working distance of the detection objective [86]. An attempt to correct the aberrations involved the replacement of the TL with a Plossl lens; however, no improvements were achieved. Field curvature was observed within the data (barrel distortion) [29], probably being caused by the tube lens [86]. AO in the detection path of the LSFM would be capable of aberration and field curvature correction as shown in the work of Y. Liu et.al [158].

To measure the lateral and axial resolutions of the LSFM microscope, the FOV was divided into two regions, region A and region B (Figure 4.20). Region A represents the outer FOV, with increased aberrations, while region B represents the centre of the FOV and has a diameter of 1 mm. Since the imaging was conducted with a single illumination LS, the diameter of the region B was chosen to be equal to the effective FOV of a single LS. Lateral and axial resolutions were measured for both the illumination arms in 300 μm , 600 μm and 900 μm scans. The measured resolutions for all scans in different depths are shown in Table ?? and Table ?? for the reference and the second illumination arms respectively. The averaged lateral and axial resolutions, at the two regions, for both illumination arm are summarised in Table 4.1. As observed, there was a significant difference between regions A and B, for both lateral and axial resolutions, while imaging depth had less impact on both resolutions. Lateral and axial resolutions improvement varied from 16% to 31% comparing A to B. The resolution improvements were expected since region B is the effective FOV of the LS and there is much less aberrations in region B compared to region A. Scanning depth had a change in axial and lateral resolutions between 0% and 8%, with an exception of the lateral resolution of the 300 μm scan of the reference LS.

The lateral resolution of the reference path, in region B, varied from 4.33 μm to 5.38 μm and the lateral resolution of the second path in region B varied from 4.36 μm to

Chapter 4. Dual Illumination-Single Detection Light Sheet Fluorescent Microscope - Characterisation and Imaging

Reference Light-sheet				
	Region A		Region B	
Scan	Lateral res. (μm)	Axial res. (μm)	Lateral res. (μm)	Axial res. (μm)
300 μm	7.83 \pm 0.12	25.94 \pm 0.95	5.38 \pm 0.2	21.04 \pm 0.86
600 μm	6.0 \pm 0.19	28.13 \pm 0.86	4.71 \pm 0.11	21.81 \pm 0.52
900 μm	6.0 \pm 0.14	26.19 \pm 0.53	4.33 \pm 0.12	22.31 \pm 0.52
Second Light-sheet				
	Region A		Region B	
scan	Lateral res. (μm)	Axial res. (μm)	Lateral res. (μm)	Axial res. (μm)
300 μm	5.6 \pm 0.12	30 \pm 0.63	4.36 \pm 0.1	22.31 \pm 0.7
600 μm	5.38 \pm 0.12	29.18 \pm 0.65	4.49 \pm 0.14	22.3 \pm 0.5
900 μm	5.8 \pm 0.13	30.13 \pm 0.45	4.6 \pm 0.2	20.75 \pm 0.5

Table 4.1: Summary of the axial and lateral resolutions of the light-sheet fluorescent microscope for 300 (μm), 600 (μm), and 900 (μm) scans for both illumination arms

4.6 μm . The mathematically calculated lateral resolution that the detection objective can image is 2.12 μm . The difference between the theoretical value and the measured value could be because of the spherical aberration and field curvature in the detection path.

The axial resolution of the LSFM microscope was determined by the thickness of the LS (see Chapter 3). In region B the axial resolution varies from 20.75 μm to 22.32 μm , which is expected since the LSFM was designed to have an axial resolution of 21 μm at the edge of its effective FOV. This is the maximum thickness of the LS that is used for imaging and it is equal to $2\sqrt{2}\omega_0$. The thinnest part of the light sheet that is equal to $2\omega_0$; therefore, the thinnest part of the light sheet is equal to $21\mu\text{m}/\sqrt{2}=14.8$ μm . This explains the axial resolutions measured to be below 21 μm shown in Tables ?? ??.

To directly measure the thickness of the LS, a stationary LS was illuminating a ND cuvette sample. An imaging stack was obtained by scanning the detection objective. The axial resolution measured along the illumination direction would give the thickness of the light-sheet. The results are shown in Tables ?? ?. As shown, the measured thickness of the LS is significantly above the theoretical value, but the LS focuses at the centre of the FOV (minimum LS thickness measured at the centre of the FOV). Since we know that the LS thickness is close to 21 μm , as measured at characterisation

Chapter 4. Dual Illumination-Single Detection Light Sheet Fluorescent Microscope - Characterisation and Imaging

of the LSM, the LS thickness measurements were conducted on an out of focus LS. The thickness minimised in the centre of the FOV because of the aberrations in region A.

The biological specimen imaging capabilities of the LSM were examined by imaging freely moving *C. elegans*. Comparing the obtained images to the literature, anatomical features such as the head, pharynx, intestine, nerve ring, and embryos were identified [37, 150–152, 159, 160]. Three nematode samples were tested. Initially, a block of LB broth with agar cultured with *E. Coli* and *C. elegans* was positioned in a cuvette. An in focus nematode was imaged; however 3D data could not be extracted due to aberrations. A second sample was made with a small block of LB broth with agar cultured with *E. Coli* and as few as possible *C. elegans* was placed on a slide along with a drop of water and sealed with a coverglass. Water was used to ensure that there is no air gap between the slide and the coverglass and to protect the specimen [161]. 3D reconstruction is challenging with this sample, because fluorescence is reflected either on the water/agar or the water/coverglass boundary causing imaging distortions. To investigate the effect of the water to coverglass reflection, a nematode sample in a coverslip with a drop of immersion oil was prepared. Immersion oil matches the refractive index of glass, therefore reflections between immersion oil and glass are minimised. The resulted imaging presented a volumetric imaging of *C. Elegans* without aberrations.

Chapter 5

Optically Detected Magnetic Resonance

Chapters 3 and 4 demonstrate a LSFM that can excite fluorescent nanodiamonds, either mounted on a coverslip or in a cuvette, and then detect fluorescence photons. A RF system that can output high frequency microwave signal is required to control the NV spin state and thus record ODMR spectrum measurements.

In this chapter I present the Radio Frequency (RF) system that was implemented on my LSFM microscope to obtain CW ODMR spectrum measurements in both wide-field and LSFM imaging. The effect of a magnetic field and the RF signal power on the CW ODMR spectrum were examined.

5.1 Optically Detected Magnetic Resonance System Setup

In general the CW ODMR measurement setup consists of microwave generation and delivery and optical subsystems. The RF setup used in our group consists of a sweeping frequency RF signal generator (R&S SMB 100A), which generates the RF signal that was swept around the axial zero-field splitting parameter (equal to 2.87 GHz). A second RF signal generator (AARONIA AG) was used as the reference for the acquisition scheme described in section 5.1. To deliver the required RF signal power a 40dB amplifier was used (Microwave Amps AM64-2.7-3.1-40-40) and to prevent reflections

from returning to the amplifier a circulator (PE83CR1004) and an attenuator were introduced into the RF sub-system. The switching between the two signal generators was achieved with an RF switch (ZASWA-2-50DR+) [12,97].

The diagram of the ODMR setup is shown at Figure 5.1. The imaging system was the detection path of the LSFM described in Chapter 3; however, ODMR spectrum measurements could not be extracted using the Prime BSI camera (the camera which was used for whole organism and FND imaging). Therefore, the Prime BSI camera was replaced with a Thorlabs CS235MU (the troubleshooting of Prime BSI camera is presented in Appendix B). To achieve wide-field CW ODMR a 5 mW laser was used to illuminate the sample from underneath while for the CW LSFM ODMR, LSFM illumination was used (50 mW). Both the sweeping frequency signal generator and the reference RF generator were connected to the RF switch. The RF switch output was connected to the input of the amplifier and the RF output of the amplifier was connected to the circulator. Both the RF attenuator and the FND sample were connected at the circulator in such a way that the sample sees the amplified signal generated and the attenuator receives any signal that passes through the circulator. Last, the sample was terminated with a 50 Ohm terminator to ensure impedance matching and thus maximise the signal power. An DAQ (National Instruments) was used to synchronise the ODMR data extraction [12].

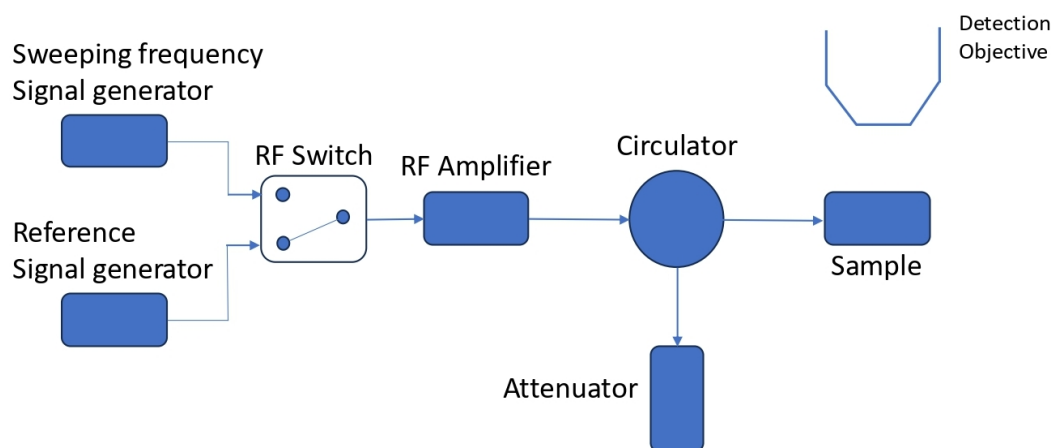


Figure 5.1: Optically detected magnetic resonance setup for wide-field and light-sheet fluorescence microscopy optically detected magnetic resonance measurements.

The FND sample for wide-field ODMR and LSFM ODMR are shown in Figures 5.2 and 5.4 respectively. A custom made 3D printing mount was made in both cases to ensure that the sample can be mounted on the LSFM microscope stage. The optical schematic of the wide-field ODMR and the LSFM ODMR are shown in Figure 5.3 and Figure 5.5 respectively.

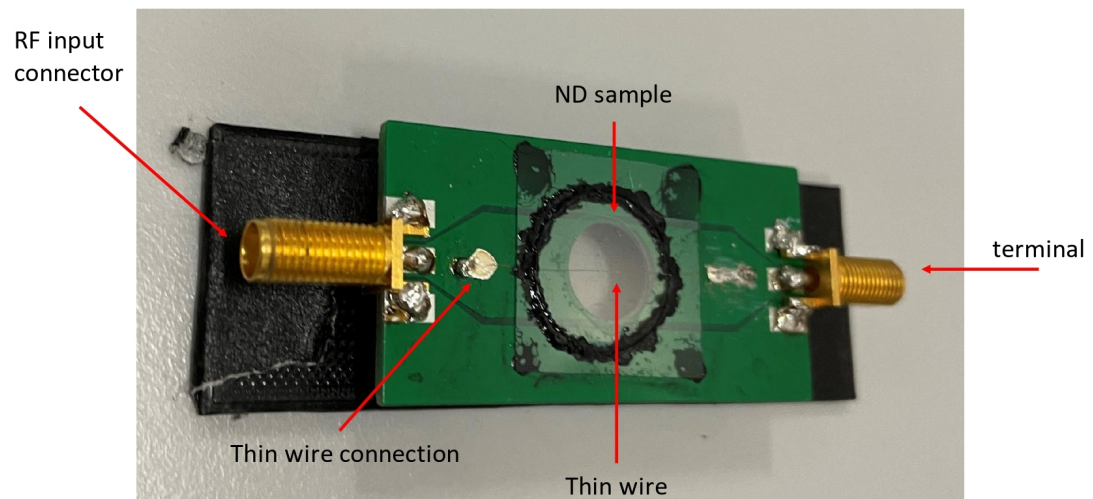


Figure 5.2: Wide-field Optically detected magnetic resonance sample. The nanodiamond sample is in the middle of the round coverslip enclosed with with nail varnish. A thin wire crosses the sample to deliver the RF signal to the nanodiamond sample.

In both the wide-field and LSFM ODMR a custom made PCB was used to transfer the RF signal to the nanodiamonds through a thin copper wire [12]. The only difference between the two is that the PCB for the LSFM ODMR is cut in half to be able to illuminate the sample with the light sheet. The sample preparation process is presented Appendix C.

5.2 ODMR Spectrum Measurement Technique

CW ODMR spectrum measurement starts with continuous optical and microwave excitation of a FND sample. The CW ODMR spectrum is recorded by capturing the optical emission, in respect to the swept microwave frequency, with a sCMOS camera.

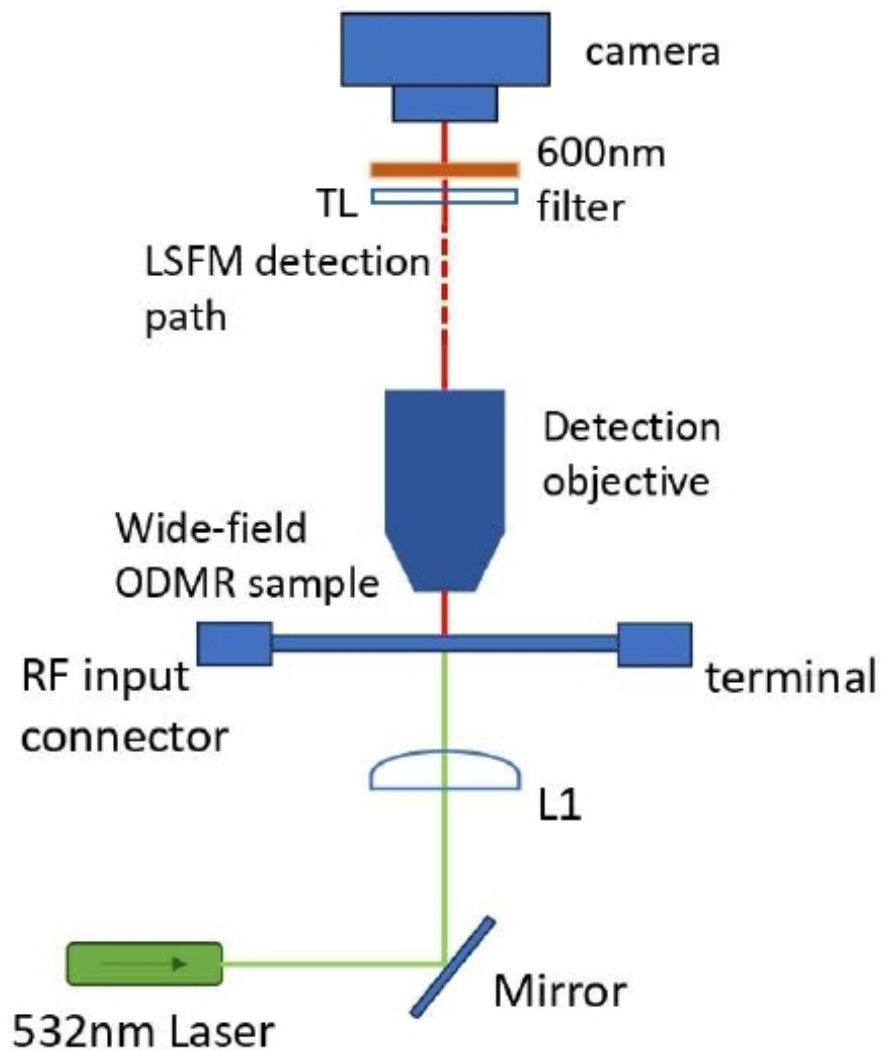


Figure 5.3: Schematic of the wide-field optically detected magnetic resonance sample at the imaging plane of the light-sheet fluorescent microscope. A 532 nm 5 mW laser focused on the sample, through a 50 mm lens, illuminates the nanodiamond sample. The imaging path is the same as the detection path of the light-sheet fluorescent microscope described in Chapter 4. A 600 nm long pass filter is used in the imaging path.

Each image captured by the sCMOS camera is correlated to a single microwave frequency. An initial ODMR spectrum can be obtained by plotting the intensity (either of the entire FOV, a specific ROI, or a single FND) vs microwave frequency. Fluorescent dips in the optical intensity are indications of reaching spin resonances [116].

Microwave frequency change was achieved through the sweeping frequency capa-

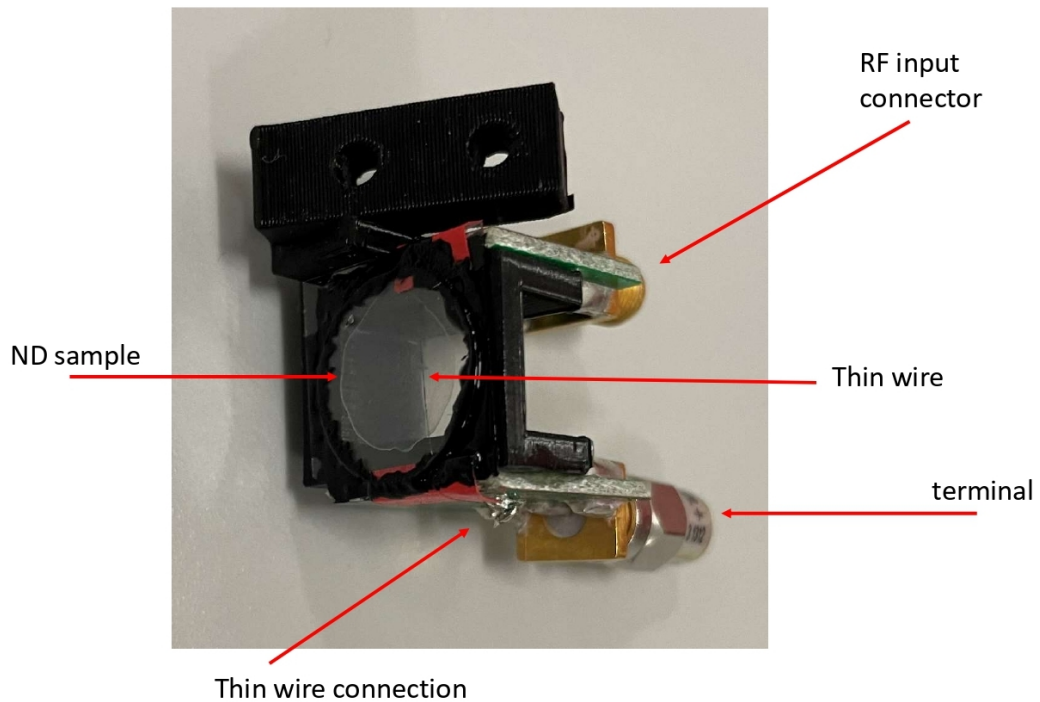


Figure 5.4: Light-sheet fluorescent microscopy optically detected magnetic resonance sample. The same PCB used in the wide-field optically detected magnetic resonance is cut in half to set the nanodiamonds at a 45 degrees angle, required for light-sheet fluorescent microscopy illumination

bilities of the microwave source. A minimum and maximum frequency were selected as well as the scanning step size. As mention in Section 2.8.2, frequencies of interest were around 2.87 GHz; therefore the initial ODMR spectrum measurements were conducted with minimum and maximum frequencies of 2.75 GHz and 2.95 GHz respectively. The minimum and maximum frequencies were selected empirically (experienced with ODMR spectrum measurements within our research group) to ensure that the fluorescent dips were captured. To scan the 200 MHz window a step size of 0.8 MHz was initially selected. Since we were aware of the sample, we knew that we are over-sampling, but we wanted to test the quality of the measured ODMR spectrum. In biosensing applications, we would expect to change the parameters of the acquisition according to the requirements of the specific experiment, such as speed of measurement or the size of the expected change in the ODMR spectrum.

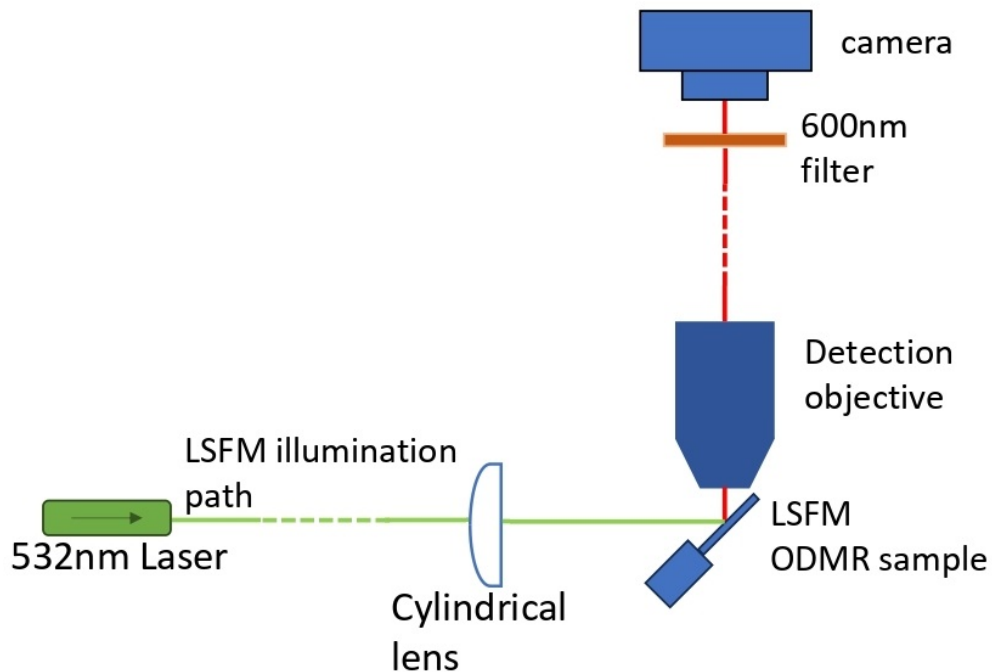


Figure 5.5: Schematic of the light-sheet fluorescent microscope optically detected magnetic resonance sample at the imaging plane of the light-sheet fluorescent microscope. The light-sheet fluorescent microscope’s illumination path is used for the light-sheet illumination of the optically detected magnetic resonance sample. The imaging path is the same as the detection path of the light-sheet fluorescent microscope described in Chapter 4. A 600nm long-pass filter is used in the imaging path.

To improve the SNR the “N P” averaging strategy was adopted [116]. Let P be the number of frequency points measured (for example, a minimum frequency of 2.75 GHz, a maximum frequency of 2.95 GHz, and a step size of 2 MHz result in $P=101$) and N and then N is the number of repetitions of each frequency before moving to the next frequency. An image was captured for each repetition. Each microwave signal was repeated N times before moving to the next signal. This process was repeated P times. Alternatively, a “P N” averaging strategy could be used, where an entire scan of P frequencies is conducted with an image being captured for each microwave frequency, and then this process is repeated N times. The “P N” method requires a high time resolution to dynamically resolve pulses, thus making it challenging to be used with a camera. The typical camera frame rate does not allow the isolation of

signals from each pulse [116]. Initially, an ODMR spectrum was recorded with $N=50$.

Further improvements of the ODMR spectrum measurement were achieved by applying a referencing protocol, developed within our group. The ODMR spectrum measurement using the referencing protocol corrects for variations, such as ohmic heating and sample drifting, occurring between each measurement [162]. The referencing protocol states that for every image capture at a given microwave frequency a second reference image will be captured at a fixed microwave frequency known to be off-resonant with the NV centre. We typically also choose it to be out of the frequency band being swept in the ODMR spectrum. The reference microwave frequency was selected to be 2.75 GHz. The collected ODMR spectrum measurement was then divided by the reference data resulting in the normalised ODMR spectrum. The work of R. Corbyn shows the improvement of the referencing protocol [12].

The ODMR data synchronisation strategy started with a Transistor-Transistor-Logic (TTL) pulse, from our DAQ card, triggering the sweeping frequency microwave signal generator. Image acquisition begins with a second TTL pulse, on a different DAQ channel, triggering the camera. Once the first ODMR image is obtained a camera trigger output confirmed that the camera is ready for the next image. A third TTL output channel controls the RF switch used to select whether the sample is seeing the reference or sweeping microwave signal generator. Another image is acquired with the switch on this alternate setting - this allows us to take successive, alternating reference and signal images. This process was repeated until the ODMR spectrum data was obtained. Initial examination of ODMR recording was conducted in post-processing using ImageJ. The ImageJ data processing sequence is shown in Table 5.1. The ODMR spectra presented in this Chapter were the output of an ODMR processing python code developed within the research group where a Lorentzian function fit was applied on the ODMR spectrum measurements.

The final ODMR spectrum data consisted of P (number of frequency scans) \times N (number of repetitions) \times two (referencing) images. The size of the single frame imaged through wide-field ODMR spectrum measurement was 720 kb, while for the LSFM ODMR spectrum measurement, the frame size was 440 kb. A wide-field ODMR

Step	Action
1	Upload dataset to ImageJ
2	Deinterleave to split the reference from the sweeping frequency
3	Normalise the data to 1 by dividing the reference to the sweeping frequency data
4	Average the number of repeats for each measurement
5	Data visualisation by z-axis profile

Table 5.1: ODMR data processing protocol using ImageJ

spectrum dataset size of 100 sweeping frequencies and 10 repetitions would be 1.44 Gb. The temporal resolution of the ODMR spectrum measurement is equal to the frame time $\times P \times N \times \text{two}$. The Thorlabs CS235MU sCMOS offers a frame time of 25 ms; therefore, an ODMR spectrum measurement, with the characteristics described above, is recorded in 50s. The selection of repetitions N and the step size should be carefully selected to minimise the data size and improve ODMR spectrum measurement temporal resolution. The ODMR spectrum acquisition time (calculated to be 50s for the initial ODMR spectrum measurement) can be significantly improved with an ODMR measurement system optimisation. The aim of the initial ODMR spectrum recording was to extract the highest quality data; therefore oversampling and multiple averages were used.

5.3 Methodology

The general CW ODMR spectrum measurement procedure started with the positioning of the sample at the focal plane of the LSFM detection objective. The sample was adjusted to ensure the collection of maximum emission from the NV centres.

5.3.1 Wide-field ODMR

Wide-field ODMR spectrum measurements were recorded with the illumination of a FND sample prepared for ODMR measurements (Figure 5.2) with a 5 mW laser focused on the sample. ODMR recordings were extracted from the entire FOV, $471 \mu\text{m} \times 416 \mu\text{m}$, from two $100 \mu\text{m} \times 100 \mu\text{m}$ regions of interest and from a single FND cluster (Figure 5.6). The axial zero-field splitting parameter, equal to 2.87 GHz, should be included

within the scanning range to observe a fluorescence dip. The sweeping frequency and reference signal power is 6 dBm. The results of these scans are presented in Section 5.4.1

5.3.2 Effect of RF Signal Power in Wide-field ODMR

Here I investigated the effect of the RF signal power on the wide-field ODMR spectrum recordings. Wide field ODMR spectrum measurements were recorded with a continuous illumination of the FND sample and a microwave frequency sweeping, starting from 2.81 GHz and ending at 2.93 GHz. The scanning step was 10 MHz. For each scanning frequency and reference frequency, 100 images were captured, i.e. repetitions N equals to 100.

The entire FOV was used to extract ODMR recordings and the scanning step is larger compared to the wide-field ODMR reported in Section 5.3.1 because here I was interested only in the amplitude of the fluorescent dip. Since a relevantly large step size was selected, the number of repeats N was chosen to be 100 to improve the ODMR spectrum measurement without sacrificing temporal resolution, compared to the wide-field ODMR experiment.

The effect of the RF signal power on the ODMR fluorescent dip was examined by conducting ODMR measurements while reducing the signal power by 5 dBm for each measurement. The maximum signal power used for ODMR detection was 6 dBm. ODMR was no longer detectable for a signal power of -44 dBm. The results are shown in Section 5.4.2

5.3.3 LSFM ODMR

LSFM ODMR spectrum measurement was achieved by the continuous LS illumination of a FND sample (shown in Figure 5.4) with a 50 mW laser at a wavelength of 532 nm. The LS illumination of the FND sample is shown in Figure 5.9a) where a FOV of $1200 \times 200 \mu\text{m}$ was illuminated. ODMR measurements were extracted from the entire FOV, three $200 \times 200 \mu\text{m}$ regions of interests (top, middle and bottom of the FOV - see Figure 5.9a) and from a single FND cluster. The sweeping frequency scan started from

2.78 GHz and ended at 2.93 GHz, with a scanning step size of 5 MHz, and 100 point repeats. The maximum, minimum microwave frequencies, and step size were chosen to create a smaller scanning window with a larger step size, compared to the wide-field ODMR experiment, since we were aware of the sample and knew that ODMR spectrum would be captured within this range at a step size of 5 MHz. A relatively high number of repeats was selected to obtain a good SNR. Both the reference and the sweeping frequency powers were 6 dBm. The results are shown in Section 5.4.3

5.3.4 Effect of Magnetic field in LSFM ODMR

To investigate whether NV properties can be detected through LSFM ODMR, the effect of a magnetic field on the ODMR spectra was examined. A magnet was placed 50 mm away from the FND LSFM ODMR sample and moved closer to the sample in steps of 5 mm. Since we were looking to see if we could observe the expected Zeeman splitting of the ODMR peaks and did not yet want to measure the absolute field strength, we did not use a calibrated magnet, but a small, high field one obtained from an online retailer. An ODMR measurement was recorded for each step. The sweeping frequency scan started at 2.7 GHz and ended at 3 GHz, with a scanning step of 5MHz. For each frequency change 20 images were captured. A larger range of frequency was covered to ensure that the fluorescent dip will be captured when a high magnetic field is applied.

The experimental methodology is shown in Figure 5.10a) and the obtained ODMR spectra for a distance between the magnet and the sample of 50 mm, 20 mm and 5 mm is shown in Figure 5.10 b), c) and d). The results of this experiment are shown in Section 5.4.4.

5.3.5 Effect of RF Signal Power in LSFM ODMR

To investigate the effect of the RF signal power on the LSFM ODMR, the signal power has been set to 6 dBm (which is the maximum power our system can deliver to the sample). The signal power is reduced in steps of 5 dBm and an ODMR measurement was recorded for every signal power reduction. The scanning range of the sweeping frequency was 2.8 GHz to 2.93 GHz at a scanning step of 10 MHz and a point repetition

equal to 100. The minimum and maximum microwave frequencies, and scan size were selected to be the same as the investigation of the effect of RF signal power in wide-field ODMR, since we knew that these parameters would result in an observable ODMR spectrum. The results of this experiment are shown in Section 5.4.5.

5.4 Results

Due to the delays occurred from the troubleshooting of the Prime BSI camera, the results presented in this Section were obtained the last week of my laboratory access. I emphasised my work on presenting working principles; further investigation would lead to the examination of the effect of SNR to the ODMR spectrum contrast, the examination of magnetometry sensitivity, the effect of temperature on the ODMR spectra, and the volumetric LSFM ODMR spectrum measurement.

5.4.1 Wide-field ODMR

The ODMR spectrum fluorescent dip recorded at my measurements was significantly less than previously reported ODMR measurements. This could be because of the laser power used for illumination [163], the microwave power, or the background noise [164]. I used a 5 mW laser which was focused on a $471\ \mu\text{m} \times 416\ \mu\text{m}$ FOV and a fluorescent dip of 0.985 was recorded on an FND cluster (Figure 5.6 e). For comparison, when looking in the literature, ODMR fluorescent dip of 0.92 was recorded with a 40 mW laser focused on a single crystal [165]. As described in Section 2.9, as the sample illumination laser's power increases, the contrast of the ODMR spectrum will improve; however, further increase of the power will have a negative effect on the contrast of the ODMR spectrum. On the other hand, as the microwave power increases, the ODMR spectrum contrast will improve and at a given microwave power it will saturate. To maximise the contrast from a laser and microwave power approach, further investigation is required. As shown in the work of Y. Nishimura et al [164], the background noise reduces the contrast of the ODMR spectrum. Sources of background noise in my ODMR spectrum measurement configuration could be non-fluorescent background,

low fluorescent contrast, or the sample preparation protocol. Further investigation is required to achieve system optimisation. Even if the magnitude of the fluorescent dip, observed in the ODMR spectrum, is smaller than expected, a good signal to noise ratio on the curves was obtained; therefore, there's optimism that good sensitivity on sensing applications will still be possible.

The ODMR spectrum of different regions within the FOV are shown in Figure 5.6. The fluorescence signal is shown in respect to the applied RF frequency on the FND sample [165]. When sensing within a millimetric FOV with multiple NV centres the sensitivity of the ODMR measurement is decreased because of the averaging of signals received from many NVs with different orientations [97]. Consequently, the ODMR spectrum extracted from a single cluster presents two distinct fluorescence dips while the entire FOV and region of interests ODMR spectrum presents one. Since there is no external magnetic field, the two fluorescent dips are a result of the strain splitting.

Investigating the time required to obtain wide-field ODMR compared to confocal point scanning ODMR, it was found that the frame time of a single acquisition of a single frequency of a confocal CW ODMR spectrum measurement was 10ms [12], where information from a single FND was extracted. My system presents a frame time of 220 ms for a single acquisition of a single frequency; however, the difference between the confocal point scanning ODRM and wide-field ODMR, which makes wide-field ODMR “faster”, is that ODMR measurements of hundreds of FNDs or clusters of FNDs are recorded simultaneously [166]. A frame time of 25 ms could be achieved with my ODMR spectrum measurement setup; however, hardware synchronisation problems lead to a 100ms delay before, and 100 ms delay after an image capture.

5.4.2 Effect of RF Signal Power in Wide-field ODMR

The fluorescent dip amplitude recorded in ODMR spectra measurements with respect to the sweeping frequency signal power is shown in Figure 5.7. The reference signal power remains at 6 dBm through the experiment. As observed, the reduction of the signal power has a dramatic effect on the ODMR amplitude. The RF signal passes through a thin wire, placed close to the region of interest, and achieves spin manipulation [105];

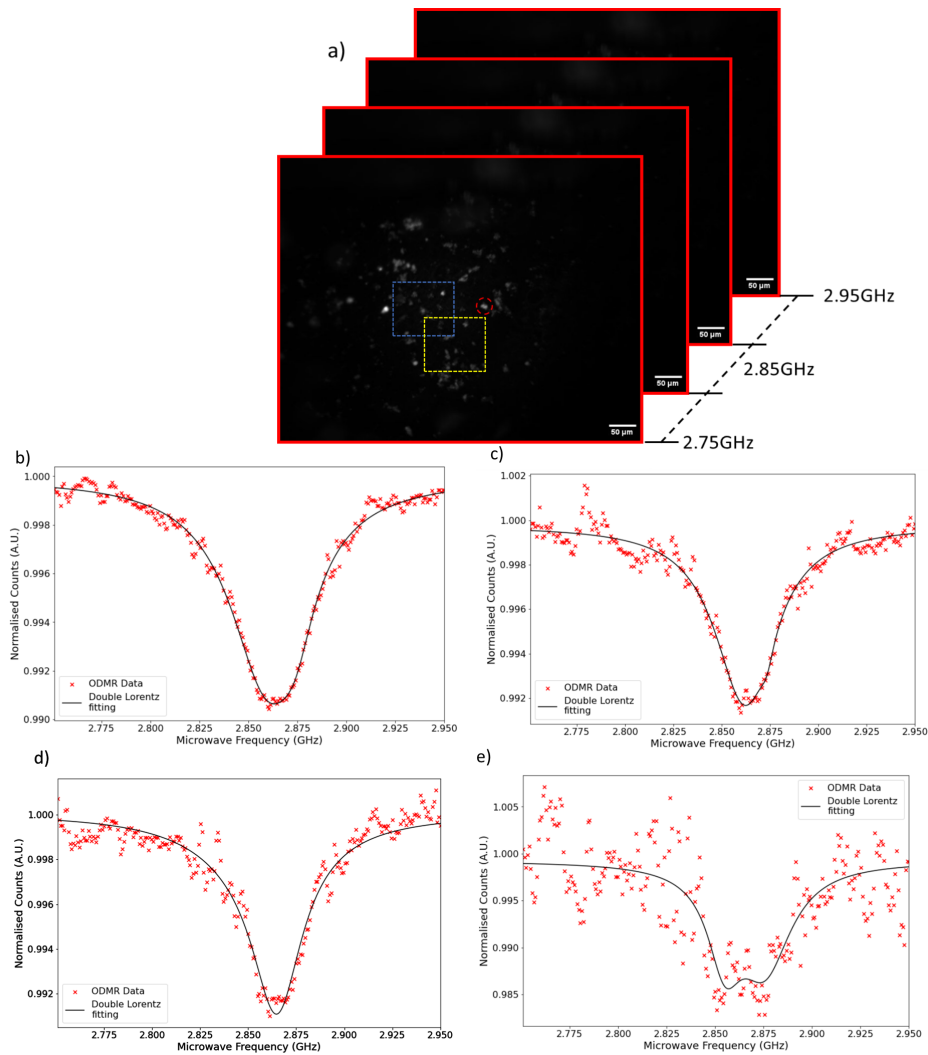


Figure 5.6: Wide-field optically detected magnetic resonance data. The red marks represent the fluorescence measurement and the continuous line represents the Lorentzian fit. Contrast is defined as the magnitude of the dip in the measured fluorescence. a) The sequence of optically detected magnetic resonance recording FND images for different applied RF signals. Regions where optically detected magnetic resonance data are extracted are shown. b) Entire field of view optically detected magnetic resonance. Contrast = 0.009 and $R^2 = 0.99$. c) optically detected magnetic resonance extracted from the blue region of interest. Contrast = 0.007 and $R^2 = 0.91$. d) optically detected magnetic resonance extracted from the yellow region of interest. Contrast = 0.0069 and $R^2 = 0.94$. e) optically detected magnetic resonance extracted from a single cluster of nanodiamonds, red circle. Contrast = 0.012 and $R^2 = 0.63$.

therefore at a low enough signal power spin manipulation is not accomplished and thus ODMR spectra cannot be detected. The recorded data, shown in Figure 5.7,

are following a sine-wave or an s-shape form. Such a result is expected since a similar response was recorded by H. Babashah et al [116] when the effect of the ODMR contrast in respect the the MW signal power was investigated. Further investigation is required to link the data form to either the data normalisation processing (due to the ODMR referencing protocol applied) or to the way the hardware frequency sweeping is applied since the performance of the RF hardware used in the ODMR spectrum measurement setup is not linear.

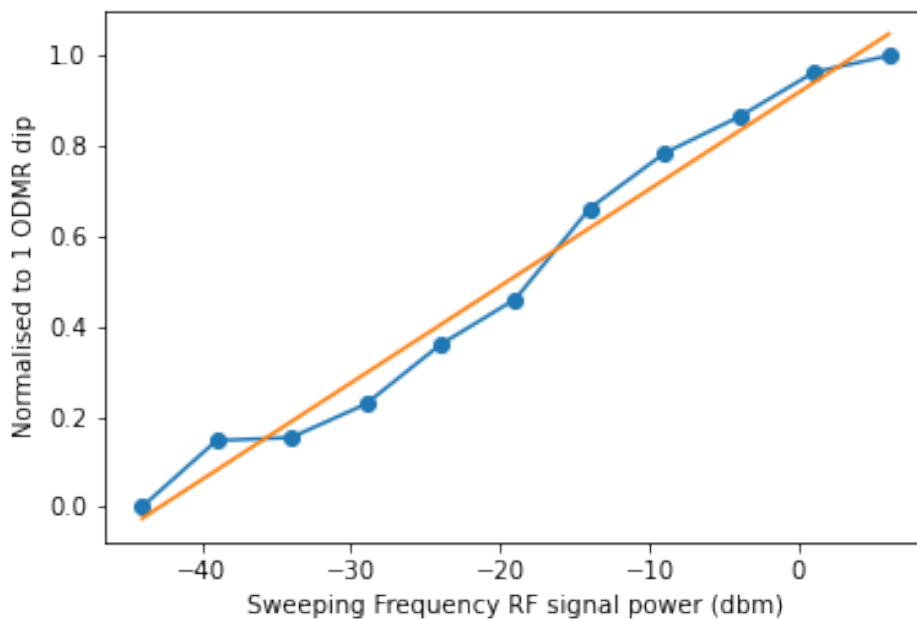


Figure 5.7: Effect of RF Sweeping frequency power on the wide-field optically detected magnetic resonance spectrum recording. x-axis indicates the power of the RF signal in dBm and the y-axis shows the normalised to one amplitude of the ODMR dip. Blue dots represent the measured data and the orange line represents a linear fit with $R^2=0.981$.

The ODMR spectra recorded for 6 dBm and -14 dBm sweeping frequency signal power are shown in Figure 5.8. As expected, a reduction in contrast was observed; however, more information information was extracted from Figure 5.6b. As shown, in the ODMR spectrum obtained when the sweeping frequency RF signal power was reduced the two peaks of the fluorescent dip are much more clearly resolved. Additionally, the

peaks are steeper at -14dBm, resulting in a narrower linewidth, which increases the sensitivity of CW ODMR measurement.

The sensitivity of ODMR spectrum depends on the contrast and the linewidth of the fluorescent dip recorded [167]. As described in Section 2.9, the FND illumination laser power and the microwave power have a major impact on contrast and fluorescent dip linewidth. Typically, both contrast and linewidth should improve with higher microwave power [167]; however, since laser power also affects the sensitivity of ODMR, system optimisation including ODMR spectrum measurements with different settings of microwave and laser power should be conducted.

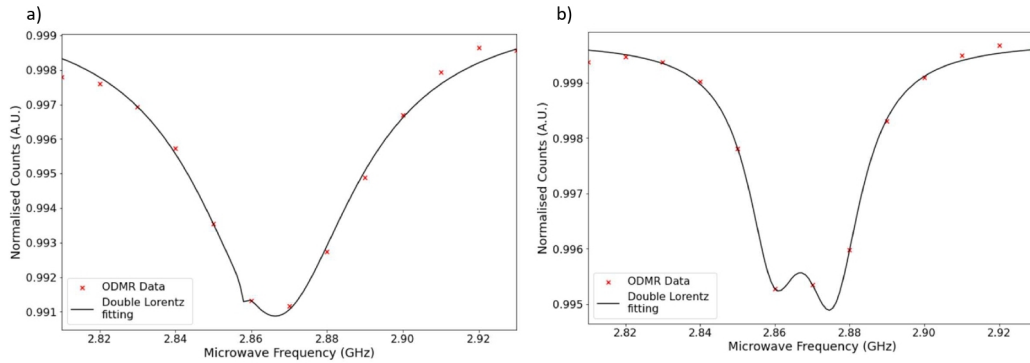


Figure 5.8: Wide-field optically detected magnetic resonance with different RF sweeping frequency power. The red marks represent the measured data points and the continuous line represents the Lorentzian fit. a) Entire field of view optically detected magnetic resonance with maximum RF power (6 dBm). The contrast of the ODMR spectrum is 0.008 and $R^2 = 0.99$. b) Entire field of view optically detected magnetic resonance with a power of (-14 dBm). The contrast of the ODMR spectrum is 0.0045 and $R^2 = 0.99$.

5.4.3 LSFM ODMR

Albeit the fact that the laser power is 10 times higher than the laser power used for the wide-field ODMR (since the LS illumination is used to excite the sample, see Chapter 3.2), the contrast of the LSFM ODMR spectra was similar to the contrast of the wide-field ODMR spectra. The large FOV of the LSFM ODMR and the fact that the LS extends over 6 mm (this is the beam thickness required to generate a LS with the desired specifications - described in Section 3.1.1) are among the factors that were limiting the illumination intensity and thus the amplitude of the fluorescence dip. As

discussed in Section 5.4.1, the background noise has a major effect on the contrast of the ODMR spectrum measurement.

Fluorescence dips extracted from the entire FOV, from single FND clusters and from the edges and middle of the FOV are shown in Figure 5.9. LSFM ODMR has never been reported before, and the fact that ODMR spectra can be recorded at such large FOV, compared to current wide-field ODMR [105,106,166], as well as from various sub-regions and single clusters, could pave the way to fast 3D *in-vivo* sensing of freely moving living organisms and thus enabling the investigation of various biological processes. Further investigation is required to optimise the LSFM ODMR spectrum measurement system. The power of the laser and the microwaves should be adjusted to maximise contrast and the background noise should be reduced.

Zeeman splitting can not be observed in any of the LSFM ODMR spectra. This could be either because a larger step size was used (5 MHz) compared to the step size used for the wide-field ODMR spectra measurements (0.8 MHz), or because the ROI and single FND/or FND cluster were selected manually. The optimisation of the LSFM ODMR spectrum should be followed by a series of experiments to determine the optimal number of repeats and step size.

The LSFM ODMR spectrum showed a shift of the fluorescent dip to frequencies lower than 2.87 GHz. This may be a result from the increase in the sample's temperature. Approximately, the same frequency shift was observed in the wide-field ODMR spectrum. The entire wide-field ODMR data consisted of 2,500 images, while the LSFM ODMR data consisted of 3,000 images; therefore the data acquisition time of the wide-field ODMR data was 9 minutes and 10 seconds. The LSFM ODMR data acquisition time was 11 minutes. Both 11 minutes and 9m10s of microwave and ohmic heating resulted in a similar sample temperature. A series of ODMR measurements at controlled temperatures would enable a temperature calibration of the system and thus show whether this shift of the resonance frequency related to sample heating.

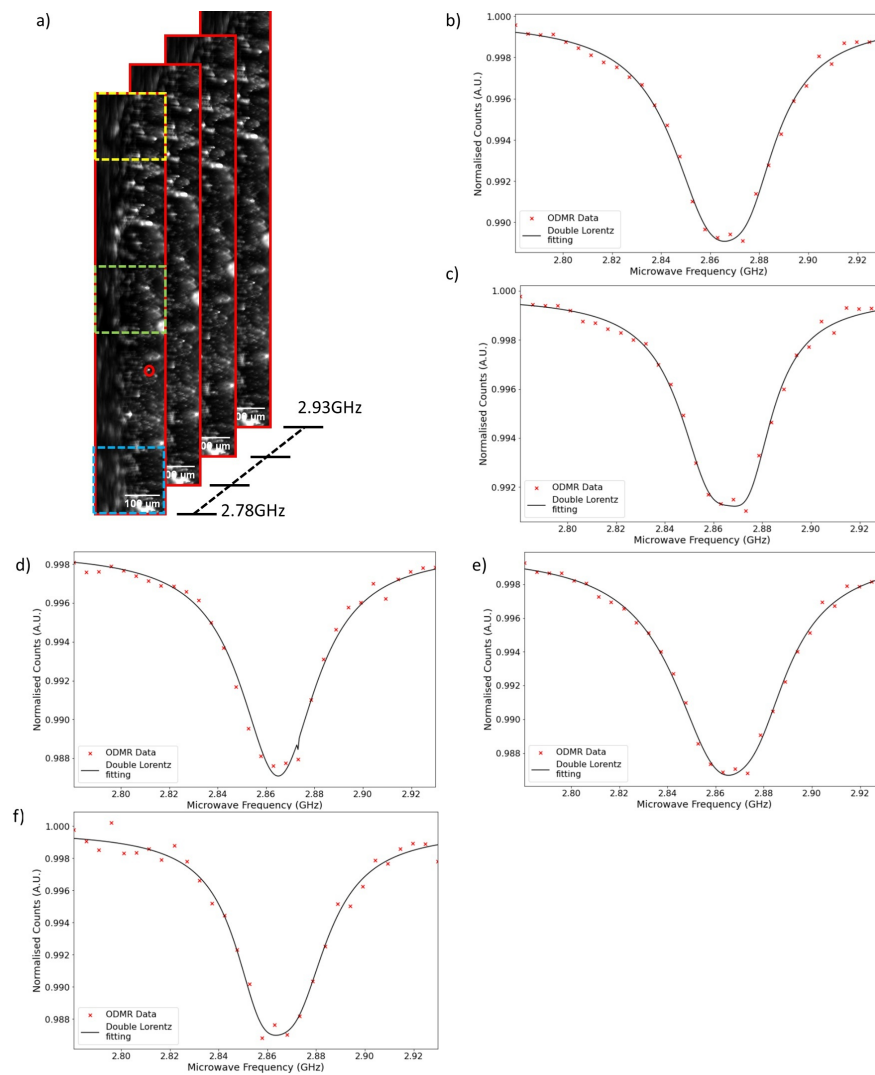


Figure 5.9: Light sheet fluorescent microscopy optically detected magnetic resonance recorded. The red marks represent the measured data points and the continuous line represents the Lorentzian fit. a) The sequence of ODMR recording nanodiamond images for different applied RF signals. Regions where optically detected magnetic resonance spectra were extracted are shown. b) Entire light-sheet optically detected magnetic resonance spectrum. Contrast = 0.01 and $R^2 = 0.99$. c) Top light-sheet region optically detected magnetic resonance spectrum (yellow region of interest). Contrast = 0.008 and $R^2 = 0.99$. d) Middle light-sheet region optically detected magnetic resonance spectrum (green region of interest). Contrast = 0.011 and $R^2 = 0.99$. e) bottom light-sheet region optically detected magnetic resonance spectrum (blue region of interest). Contrast=0.013 and $R^2 = 0.99$. f) Single nanodiamond cluster, red circle). Contrast = 0.012 and $R^2 = 0.98$.

5.4.4 Effect of Magnetic field on LSFM ODMR

The effect of the magnetic field in the LSFM ODMR spectrum was examined by moving a magnet towards the FND sample. For each movement step an ODMR spectrum was recorded. The range of movement was 50 mm to 5 mm away from the sample and the magnet movement step size was 5 mm. The experiment showed that as the magnet was moved closer to the sample the magnetic field increased. The ODMR spectra recorded with the magnet being at the furthest away from the sample (50 mm) presents two fluorescent dips. One dip was observed at 2.87 GHz and the second one at 2.883 GHz (Figure 5.10b). In Figure 5.10c), where the magnetic field was stronger, one dip was found at 2.861 GHz and the second dip was at 2.88 GHz. When the magnet was 5mm away from the sample (Figure 5.10d), and the magnetic field applied to the sample was further increased, the frequency between the two dips kept increasing. The first dip was at 2.845 GHz and the second one at 2.891 GHz. As observed, the frequency between the two fluorescent dips increases as the magnetic field gets strong [165]. This was expected, as described in Chapter 2 (shown in Figure 2.26). Therefore, my system can detect magnetic fields; therefore, magnetometry could be achieved with LSFM ODMR.

5.4.5 Effect of RF Signal Power in LSFM ODMR

The amplitude of the LSFM ODMR fluorescence dip in respect to the sweeping frequency signal power is shown in Figure 5.11. The pattern of the amplitude reduction in LSFM ODMR follows the amplitude reduction of the wide-field ODMR; however, the amplitude is 0 at -39 dBm (instead of -44 dBm for the wide-field ODMR). A higher drop of fluorescence is observed in the LSFM ODMR spectra, compared to the wide-field ODMR; however, further investigation is required to determine whether the reduction of contrast is related to the LS illumination or the sample preparation protocol used. The LSFM ODMR contrast versus the sweeping frequency signal power present a sinewave over the data similar to the one shown in the wide-field ODMR contrast (Figure 5.8).

The effect of the microwave power on the linewidth of the ODMR spectrum fluorescent dip was investigated by plotting the ODMR spectra for microwave powers of 1

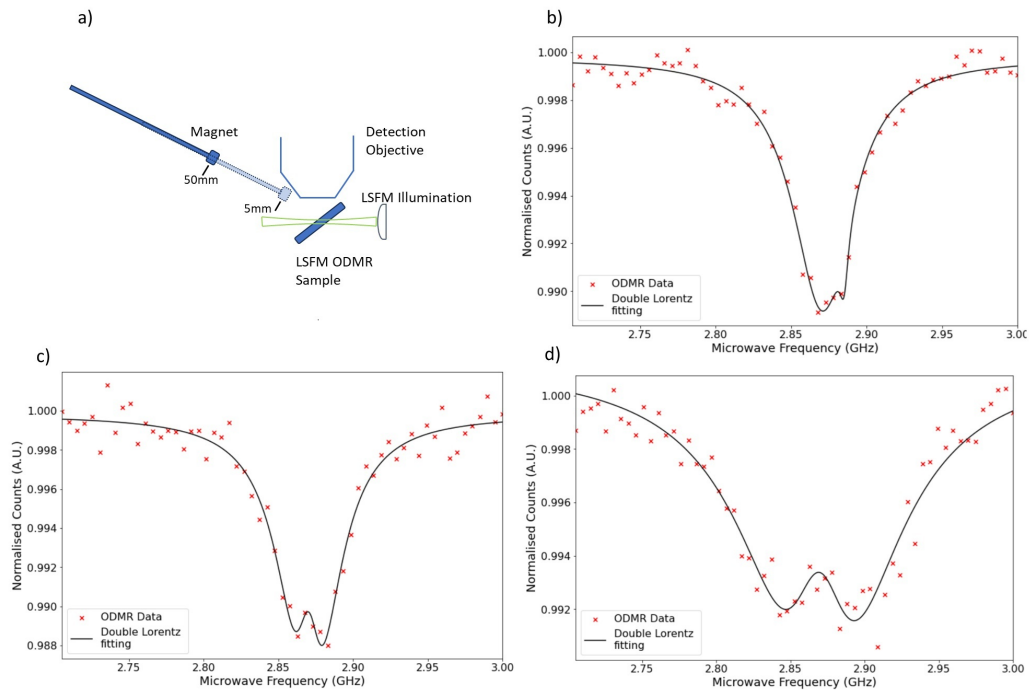


Figure 5.10: Effect of a magnetic field on the Light sheet fluorescent microscopy optically detected magnetic resonance measurements. The red marks represent the measured data points and the continuous line represents the Lorentzian fit. a) The experimental methods for the examination of the effect of a magnet on optically detected magnetic resonance recordings, b) Magnet at a distance of 50 mm away from the sample. The contrast of the ODMR spectrum is 0.011 and $R^2 = 0.98$. c) Magnet 20 mm away from the sample. The contrast of the ODMR spectrum is 0.011 and $R^2 = 0.97$. d) Magnet at 5 mm away from the sample. The contrast of the ODMR spectrum is 0.008 and $R^2 = 0.94$

dBm and -29dBm (Figure 5.12). The phenomenon observed in the investigation of the effect of microwave power on ODMR spectrum sensitivity in wide-field ODMR is also shown here. The reduction of microwave power results in the reduction of contrast, but it creates a narrower linewidth. This confirms that a system should be optimised in a way that both the microwave power and laser power are tuned to maximise ODMR sensitivity.

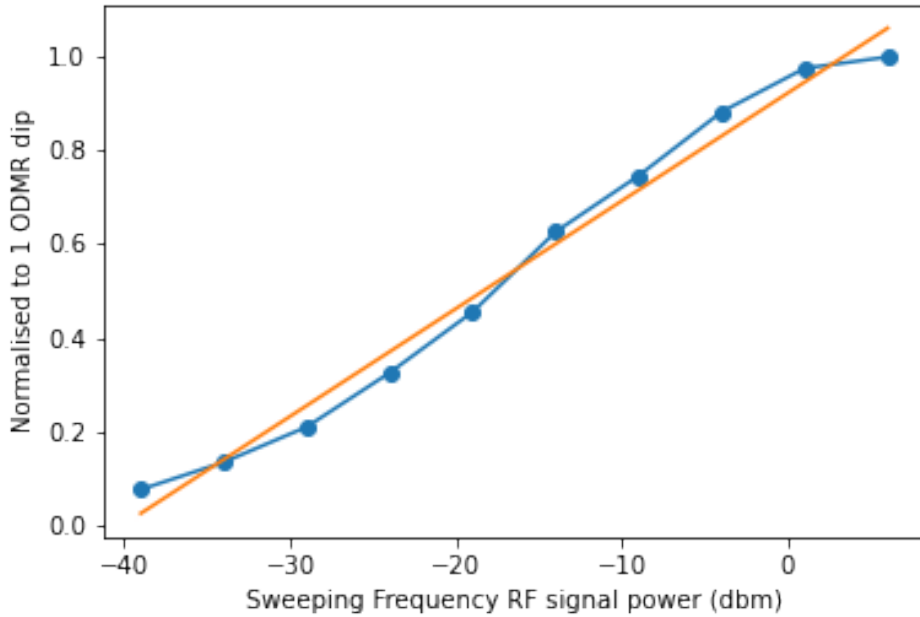


Figure 5.11: Effect of RF Sweeping frequency power on the light-sheet fluorescent microscope optically detected magnetic resonance spectrum recording. x-axis indicates the power of the RF signal in dBm and the y-axis shows the normalised magnitude of the optically detected magnetic resonance dip. Blue dots represent the measured data, and the orange continuous line is the linear fit, $R^2 = 0.985$

5.5 Summary and Discussion

A RF subsystem has been constructed to work in synchronisation with the LSFM microscope and enables ODMR spectrum measurements. The RF subsystem consists of two microwave generators, one for generating the sweeping frequency RF signal and one for generating the reference signal. An RF switch is used to switch between the two signals and an amplifier is used to amplify the signal that the FND sample sees. The optical subsystem is the detection path of the LSFM microscope. The sample preparation protocol presented in the work of R. Corbyn [12] was used and a custom made LSFM sample holder was made to enable LS illumination.

ODMR spectrum recordings were demonstrated with both wide-field illumination and LS illumination. An entire FOV ODMR as well as smaller RIO and single FND/FND clusters ODMR were presented in both wide-field illumination and LS illumination. The

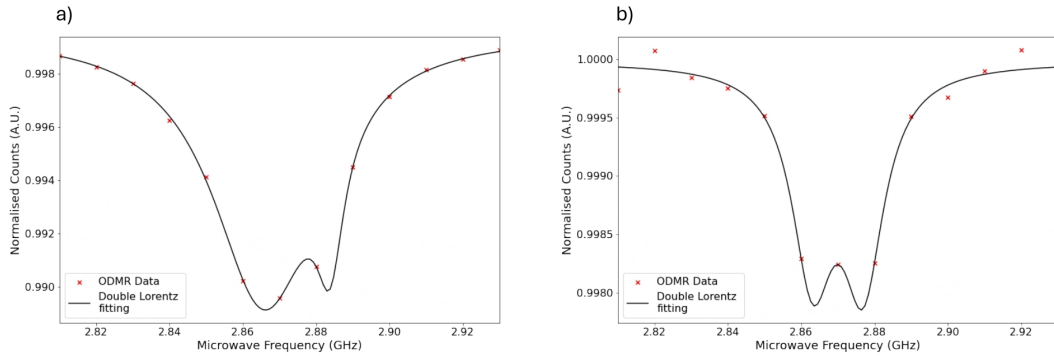


Figure 5.12: Light sheet fluorescent microscopy optically detected magnetic resonance with different RF sweeping frequency power. The red marks represent the measured data points and the continuous line represents the Lorentzian fit. a) Entire field of view optically detected magnetic resonance with RF power of 1 dBm. The contrast of the ODMR spectrum is 0.01 and $R^2 = 0.99$. b) Entire field of view optically detected magnetic resonance with a power of -29 dBm. The contrast of the ODMR spectrum is 0.017 and $R^2 = 0.98$.

effect of signal power, and magnetic field were examined, showing that LSFM ODMR is possible and paving the way to fast 3D wide-field ODMR sensing. The effect of the sample temperature was also observed in the wide-field and LSFM ODRM spectra.

Previous research shows that wide-field ODMR with LS illumination has been achieved [18] with a frame time of 2.2 ms, a FOV of 0.5 mm^2 and a "few micron" spatial resolution. However, this is not a SPIM illumination and beam scanning is not possible. My wide-field ODMR allows extraction of ODMR into a FOV up to 1.6 mm^2 , with similar spatial resolution. A larger FOV translates into the extraction of ODMR measurements from larger samples, leading to magnetic and temperature sensing in larger specimens. The frame time the LSFM ODMR spectrum measurement system can achieve is 25 ms; however due to hardware synchronisation issues the ODMR spectra were extracted with a frame time of 220 ms. My LSFM ODMR microscope also allows 3D ODMR measurements, achieved by scanning the LS at every completed ODMR recording. Such 3D ODMR measurements would provide even more information about the imaged specimen. Through the SLM modulation available on both the illumination beams, the ODMR illumination beam could be focused to the region of interest, providing higher illumination intensity and thus improving the ODMR sensi-

Chapter 5. Optically Detected Magnetic Resonance

tivity. Four-point ODMR [164] could also improve the speed of ODMR data recording and thus enable the sequential LSFM imaging and ODMR measurements.

Chapter 6

Conclusions

6.1 Summary

My work emphasised on the design, construction and operation of a LS fluorescent microscope that images freely moving organisms through a millimetric field of view with cellular resolution. Fundamentals of microscopy were investigated and the trade-off between the imaging FOV and resolution were stated. Confocal microscopy, spinning disk confocal microscopy and LSFM were investigated to examine whether such a microscope can fulfill our requirements. LSFM proved to be the best candidate because of the high imaging speed required to capture useful information from freely moving organisms, the large FOV, and the low photodamage.

The geometry of LSFM allows it to be a very configurable microscope. A plethora of LSFM designs have been presented in the past, each tailored to satisfy imaging sample requirements. My design was based on a selective plane illumination microscope (SPIM), where the LS is created when a laser beam passes through a cylindrical lens. LS created by a cylindrical lens is more suitable for imaging optically transparent samples, hence it is preferable for illumination *C. elegans*, a transparent roundworm. An upright configuration with single detection and dual-illumination were selected. Dual-illumination ensured a large FOV imaging while keeping the resolution at a cellular level, while the upright configuration lets the *C. elegans* move freely.

A mathematical model of a dual illumination, single detection LSFM was made.

The model was based on a 2 mm FOV and a 3 μm lateral resolution and a 21 μm axial resolution. Axial resolution in this case is defined by the thickness of the LS at the first zero crossings (the maximum LS thickness that is used for image acquisition). The output of the mathematical modelling was the NA of the illumination and detection objectives and the magnification required to ensure the desired imaging specifications. The laser beam modulation and scanning was achieved through the refraction of the beams of both illumination paths from a SLM. A SLM in the illumination path paves the way to an adaptive LSFM, where Bessel, Airy and Lattice beams can be used for illumination and the sample can be illuminated with the tiling method.

The characterisation of the constructed LSFM proved that synchronised laser scanning can be achieved through SLM refraction. The LS scanning was synchronised with the detection objective position to ensure that the two are in-focus. The LS thickness was modelled to be 21 μm at the zero-crossing (the edge of the effective FOV); therefore, the axial resolution of the LSFM was designed to be 21 μm . The actual LS thickness was measured by volumetric imaging of NDs with a stationary LS. Due to aberrations at the edge of the FOV, the LS thickness could not be accurately measured. The axial resolution of the LSFM was measured by volumetric imaging of NDs. The resulted axial resolution was approx. 21 μm at the centre of the FOV, showing that the modelled axial resolution agrees with the actual axial resolution. The lateral resolution of the detection objective (with lateral being in parallel to the imaging plane and axial being perpendicular to the imaging plane) was modelled to be 2.12 μm . The lateral resolutions measured was approximately 4 μm at the centre of the FOV and approximately 6 μm at the edge of the FOV. This gap between the model and reality could be due to the aberrations observed at the edge of the FOV, the depth of imaging (0 to 0.9 mm with 0 being the plane closer to the detection objective and 0.9 mm the further away from the objective), and the fact that our sample was not completely transparent. Additionally, volumetric imaging of *C. Elegans* was achieved by excitation of mCherry and imaging of neurons. Anatomical features were identified (head, pharynx, intestine, nerve ring, and embryos).

An ODMR measurement system was incorporated to the LSFM microscope. Al-

though a LS illumination wide-field ODMR has been reported [18], a millimetric FOV LSFM ODMR has not been reported yet. The difference between my work and the work in [18] is that I present a SPIM illumination that can do z-direction scanning, while in [18] a LS geometry is used for illumination within a bulk diamond sample without z-scanning capabilities. Both my work and [18] present similar spatial resolution (few microns), while the temporal resolution presented in [18] is in the millisecond scale (2.2 ms). My ODMR spectrum measurement setup can achieve a temporal resolution of 25 ms; however, due to hardware synchronisation issues, a single frame time of 220 ms is presented. In my work ODMR measurements can be recorded from a maximum FOV of 1.6mm×1.6mm (depending on the illumination area) in the wide-field mode and 1.2 mm×0.2 mm in the LSFM mode. An LSFM ODMR means that 3D ODMR measurements can be recorded and thus provide volumetric sensing. My results showed that LSFM ODMR is possible and that the effect of a magnetic field can be recorded. Additionally, the effect of the sample's temperature was observed in the ODRM spectra. This could pave the way for *in-vivo* high imaging volume sensing, resulting in new information about 3D magnetic sensing and thermometry.

6.2 Limitations

Restriction to laboratory access due to the measures against COVID 19 were a major setback to my project. My PhD started in October 2018 and by March 2020, where COVID measures were introduced, the microscope design was completed and all components were ordered and positioned on the optical table. I had access to the lab at the end of September 2020 for two days per week and got complete access to the lab in March 2021. Additionally, my access to the lab was denied from January 2020 to March 2020 and from October 2020 to January 2021 due to maintenance and laser interlock installation. The absence from the lab had a direct impact to the progress of my project since a major part of my project was laboratory based. This includes the alignment of the microscope, the characterisation of the AO elements (SLM and DM), the microscope, and the ODMR spectrum measurement setup. An additional setback

due to COVID measures, was the organisation of the biological lab, used for growing *C. elegans* and *E. coli*. The biolab was operational by April 2022 (four months before the completion of my PhD).

Hardware limitation also had a major impact on my project. The detection objective stage, Dover Motion DOF-5, was not reliable nor it operated properly; therefore, it was replaced with a 25 mm Dovetail Translation Stage (Thorlabs, DTS25/M), controlled by a K-Cube Brushed DC Servo Motor Controller (Thorlabs, KDC101) by a 12 mm Travel DC Servo Motor Actuator (Thorlabs, Z812B). Troubleshooting the objective stage and looking for an alternative stage took a significant time from the progress of the project. In addition, we found it challenging to record ODMR data using the PrimeBSI camera, thus we used the Thorlabs CS235MU Kiralux 2.3 MP Monochrome CMOS Camera. Unfortunately, the troubleshooting of the hardware problems occurred during my PhD could not produce any useful data.

6.3 Future work

The SLM in the detection path enables the sample illumination via various beams, such as Bessel beam [168], Airy beam [169] and lattice [170]. With a software adaptation my microscope could use such beams for sample illumination, paving the way for further biological research, since the resolution of imaging would be improved. SLM could also allow tiling [171] LSFM imaging which could either increase or maintain the same FOV but improve the imaging resolution by illuminating the sample through a series of thinner LSs, instead of a single LS [171].

ODMR measurements recorded through LSFM illumination is a new method of ODMR data extraction. I showed that the LSFM microscope can result in ODMR recordings; however, further research would allow the investigation of temperature sensing and magnetic field sensing. This would allow the *in vivo* temperature and magnetic field sensing of whole organisms, such as *C. elegans*. A correlation of free movement and neural activity to *in-vivo* temperature can be investigated.

Appendix A

Python Coding - LSFM Mode in SLMtools

Two Python codes are presented in this Appendix. An SLMtools adaptation introduces a LSFM window and enables SLMtools to scan either a single LS or dual LS with sequential illumination. For each LS scan a trigger is produced by a NI DAQ card and an image is captured. The processes repeats until the complete scan range is imaged. Through the SLMtools LSFM window, a start/stop positions are selected as well as the scanning step size. Additionally, a code that enables loading of LUT for the Meadowlark SLM with an HDMI connection is included in the SLMtools.

A.1 SLMtools LSFM Window

```
# LSFM CODE START
def make_LSFM_tab(self):
    grpbox_lsfm = QGroupBox('LSFM')
    l1 = QGridLayout()

    self.scan_start = 0
    self.scan_end = 0
    self.scan_steps = 0
```

Appendix A. Python Coding - LSFM Mode in SLMtools

```
self.lsfm_goto = 0

lab1 = QLabel('Z Start (um)')
lab2 = QLabel('Z End (um)')
lab3 = QLabel('Step size (um)')
lab4 = QLabel('GoTo (um)')

lestart = QLineEdit(str(0))
# lestart.editingFinished.connect(lambda: start_edit())
leend = QLineEdit(str(1))
# leend.editingFinished.connect(lambda: end_edit())
lesteps = QLineEdit(str(1))
# lesteps.editingFinished.connect(lambda: steps_edit())
legoto = QLineEdit(str(0))
# legoto.editingFinished.connect(lambda: goto_edit())

l1.addWidget(lab1, 0, 1)
l1.addWidget(lab2, 0, 2)
l1.addWidget(lab3, 0, 3)
l1.addWidget(lab4, 3, 1)

l1.addWidget(lestart, 1, 1)
l1.addWidget(leend, 1, 2)
l1.addWidget(lesteps, 1, 3)
l1.addWidget(legoto, 4, 1)

start = QPushButton('Start scan')
stop = QPushButton('Stop Scan')
load_lut = QPushButton('load LUT')
load_lut.setCheckable(True)
```

Appendix A. Python Coding - LSFM Mode in SLMtools

```
load_lut.toggle()
goto = QPushButton('Go')

l1.addWidget(start, 2, 1)
l1.addWidget(stop, 2, 2)
l1.addWidget(load_lut, 2, 3)
l1.addWidget(goto, 4, 2)

start.clicked.connect(lambda: start_button())
stop.clicked.connect(lambda: stop_button())
load_lut.clicked.connect(lambda: load_lut_button())
goto.clicked.connect(lambda: go_button())

self.scan_stop = 0

def start_button():

    lestart_int = int(lestart.text())
    leend_int = int(leend.text())

    lesteps_int = int(lesteps.text())

    #zern_rad_min = 0
    #zern_rad_max = 2 * np.pi
    steps_no = (leend_int - lestart_int) / lesteps_int
    #angular_shift = (zern_rad_max - zern_rad_min) / steps_no
    steps_no_int = int(steps_no)
```

Appendix A. Python Coding - LSFM Mode in SLMtools

```
# the light sheet translation for 200 as a tilt value is 867.28 (the rel.
shift = (leend_int - lestart_int)/abs(steps_no_int)

#stop scan
self.scan_stop = 0

#daq control for camera triggering

task_do = nidaqmx.Task()
task_do.do_channels.add_do_chan("Dev1/port1/line0")
task_do.start()

tast_di = nidaqmx.Task()
tast_di.di_channels.add_di_chan("Dev1/port2/line4")
tast_di.start()

for i in range(abs(steps_no_int)+ 1):
    if (self.scan_stop == 0):
        for j in range(len(self.slm.pupils)):

            p = self.slm.pupils[j]
            pp = PupilPanel(p, self.pupilsTab, self)

            self.pupilsTab.removeTab(len(self.slm.pupils) - 1)
            self.pupilsTab.setCurrentIndex(j)

            x = (lestart_int + i * shift)*(200/-600)
            pp.pupil.aberration[1] = 60
```

Appendix A. Python Coding - LSFM Mode in SLMtools

```
pp.pupil.aberration[2] = x
pp.pupil.set_aberration(pp.pupil.aberration)
pp.phase_display.update_phase(pp.pupil.rzern.n,
                              pp.pupil.aberration,
                              redraw=True)

#QtTest.QTest.qWait(150)
value_do = True
task_do.write(value_do)
QtTest.QTest.qWait(50)
value_do = False
task_do.write(value_do)
#QtTest.QTest.qWait(150)

pp.pupil.aberration[2] = 0
pp.pupil.aberration[1] = 0
pp.pupil.set_aberration(pp.pupil.aberration)
pp.phase_display.update_phase(pp.pupil.rzern.n,
                              pp.pupil.aberration,
                              redraw=True)

print(x)

#QtTest.QTest.qWait(500) # time.sleep() alternative that do

print('scan ended')
```

Appendix A. Python Coding - LSFM Mode in SLMtools

```
task_do.stop
task_do.close()
tast_di.close()

return

def stop_button():
    self.scan_stop = 1

def load_lut_button():

    Blink_c_wrapperdll = ctypes.WinDLL(
        "C:\Program Files\Meadowlark Optics\Blink 1920 HDMI\SDK\Blink_C_wrap

    lut_file = 'C:\Program Files\Meadowlark Optics\Blink 1920 HDMI\LUT Files

    Blink_c_wrapperdll.Create_SDK()

    com_port = ctypes.c_char_p()
    file_path = ctypes.c_char_p()

    com_port = 'COM4'
    file_path = lut_file

    Blink_c_wrapperdll.Load_lut(com_port, file_path)
    print('load LUT')
    Blink_c_wrapperdll.Delete_SDK()

    return
```

Appendix A. Python Coding - LSFM Mode in SLMtools

```
def go_button():
    for j in range(len(self.slm.pupils)):
        legoto_int = int(legoto.text())

        p = self.slm.pupils[j]
        pp = PupilPanel(p, self.pupilsTab, self)

        self.pupilsTab.removeTab(len(self.slm.pupils) - 1)
        self.pupilsTab.setCurrentIndex(j)

        x = legoto_int*(200/-600) #the light sheet translation for 200 as a
        pp.pupil.aberration[1] = 60
        pp.pupil.aberration[2] = x
        pp.pupil.set_aberration(pp.pupil.aberration)
        pp.phase_display.update_phase(pp.pupil.rzern.n,
                                     pp.pupil.aberration,
                                     redraw=True)

        print('go')

    return

grpbox_lsfm.setLayout(l1)
return grpbox_lsfm

def make_objective_tab(self):

    return
```

```
# LSFM CODE END
```

A.2 SLM dll Loading Code

```
import ctypes
```

```
Blink_c_wrapperdll = ctypes.WinDLL("C:\Program Files\Meadowlark Optics\Blink 1920 HD  
lut_file = 'C:\Program Files\Meadowlark Optics\Blink 1920 HDMI\LUT Files\linear.bl  
Blink_c_wrapperdll.Create_SDK()  
com_port = ctypes.c_char_p()  
file_path = ctypes.c_char_p()  
com_port = 'COM4'  
file_path = lut_file  
Blink_c_wrapperdll.Load_lut(com_port, file_path)
```

Appendix B

PrimeBSI Camera Troubleshooting

The PrimeBSI camera was not showing ODMR spectrum. After two months of troubleshooting, in collaboration with Teledyne engineers, the PrimeBSI camera was replaced with a Thorlabs CS235MU. The Thorlabs CS235MU camera was capable of recording ODMR spectrum using the same experimental configuration. In this Appendix Chapter I describe the PrimeBSI troubleshooting process.

The first data attempt was conducted with the camera gain set to Corrected Multi-Sampling (CMS) mode and the exposure time was set to 100ms, as suggested by the Teledyne engineers. CMS trades off dynamic range to ensure lower read noise. Next, the possibility of the pixel noise filters effect on ODMR spectrum measurements was examined. PrimeBSI's filtering works by examining 3x3 pixel regions, if a pixel's value is above or below the median value by a given percentage, the pixel's value is replaced by the median. Four filtering options are available, the dark low, dark high, bright low, and bright high. It was initially suggested to use the default filter settings; however after a failure in recording an ODMR spectrum, the filters were turned off. All combinations of filters being turned ON/OFF were examined. The effect of Clear Mode was also investigated, where clear mode continuously clears the sensors while there is no imaging acquisition. Prime BSI offers four Expose Out Modes, the First row, where the camera triggers ready when the first row of a single frame is being exposed, Any Row, where

Appendix B. PrimeBSI Camera Troubleshooting

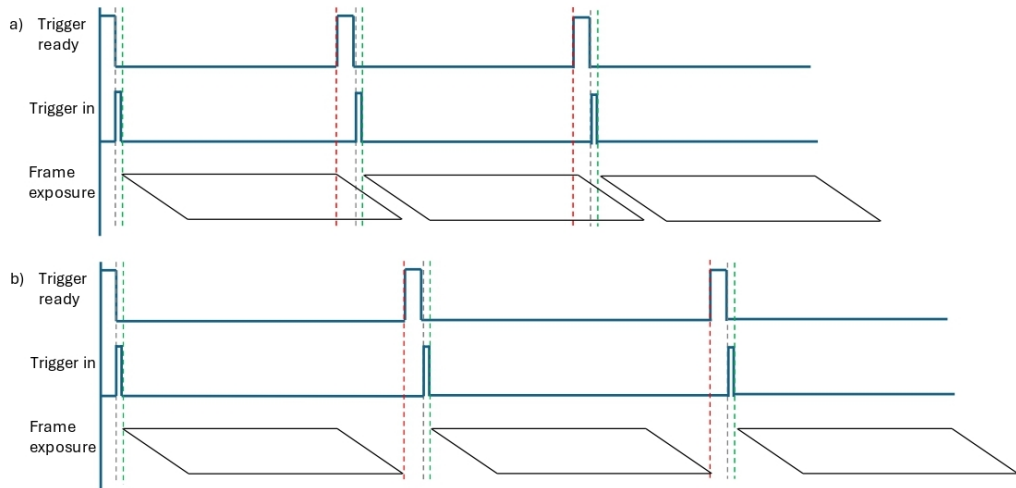


Figure B.1: The red dashed line shows the end exposure of the first row, triggering that the camera is ready to move to the next read. The gray dashed line represents the start of the trigger in, that triggers that the camera is ready for the next acquisition, and the green line shows the start of the next acquisition. a) First Row Mode. b) Any Row Mode. The figure was extracted using data from the Prime BSI manual [1].

the camera triggers ready at the end of last row exposure (First Row and Any Row principle of operation is shown in Figure B.1), Line Output Mode is used when the programmable scan mode is used, and Rolling Shutter Mode, which is similar to the First Row Mode, but the expose out signal is high when all rows are exposing. All Exposure Out Modes were investigated without acquiring an ODMR spectrum. [1]

From a software/hardware standpoint, it was ensured that the correct channels were selected in the experiment control software. All signals were investigated using BNC T-connectors to make sure that the signal responsible for triggering the camera was 5V and that the Camera In trigger and, the Camera ready trigger were synchronised as expected. ODMR spectrum was not recorded with the PrimeBSI camera.

Appendix C

ODMR Sample Preparation Protocol

Step	Action
1	Scratch the PCB to remove the insulating material (Figure 5.2a))
2	Glue a square coverslip (22 mm) on the PCB
3	Solder the copper wire at the scratched position
4	Clean a circular coverslip with isopropanol
5	Drop 20 μL of 1:10 90 nm FND on the circular coverslip
6	Wait until evaporation
7	Place the circular coverslip in a hotplate at 35-38 $^{\circ}\text{C}$ to speed that process up
8	Mix while evaporation occurs to spread the FNDs
9	Drop 10 μL of distilled water on the sample (circular coverslip
10	Place the circular coverslip on the rectangular coverslip with the FNDs facing towards the thin wire
11	wait for the sample to settle (10-15 minutes)
12	Seal the sample

Table C.1: Fluorescent nanodiamond sample preparation procedure for ODMR measurements.

Bibliography

- [1] Teledyne Photometrics. Prime bsi scientific cmos user manual.
- [2] Frederic Leblond, Scott C. Davis, Pablo A. Valdés, and Brian W. Pogue. Pre-clinical whole-body fluorescence imaging: Review of instruments, methods and applications. *Journal of Photochemistry and Photobiology B: Biology*, 98:77–94, 1 2010.
- [3] Vasilis Ntziachristos, Jorge Ripoll, Lihong V. Wang, and Ralph Weissleder. Looking and listening to light: The evolution of whole-body photonic imaging. *Nature Biotechnology*, 23:313–320, 3 2005.
- [4] Rory M Power and Jan Huisken. A guide to light-sheet fluorescence microscopy for multiscale imaging. *Nature Methods*, 14(4):360–373, 2017.
- [5] Zhouzhou Zhang, Xiao Yao, Xinxin Yin, Zhangcan Ding, Tianyi Huang, Yan Huo, Runan Ji, Hanchuan Peng, and Zengcai V. Guo. Multi-scale light-sheet fluorescence microscopy for fast whole brain imaging. *Frontiers in Neuroanatomy*, 15, 9 2021.
- [6] ZEISS. Light sheet fluorescence microscopy for multiview imaging of living and cleared specimens.
- [7] Masfer H. Alkahtani, Fahad Alghannam, Linkun Jiang, Abdulrahman Almethen, Arfaan A. Rampersaud, Robert Brick, Carmen L. Gomes, Marlan O. Scully, and Philip R. Hemmer. Fluorescent nanodiamonds: past, present, and future. *Nanophotonics*, 7(8):1423–1453, jul 2018.

Bibliography

- [8] Sheemah Kazi. A review article on nanodiamonds discussing their properties and applications. *International Journal of Pharmaceutical Science Invention ISSN*, 3:40–45, 2014.
- [9] Kostiantyn Turcheniuk and Vadym N. Mochalin. Biomedical applications of nanodiamond (review). *Nanotechnology*, 28, 6 2017.
- [10] Mayeul Chipaux, Kiran J. van der Laan, Simon R. Hemelaar, Masoumeh Hasani, Tingting Zheng, and Romana Schirhagl. Nanodiamonds and their applications in cells. *Small*, 14, 6 2018.
- [11] Graeme Johnstone and Brian Patton. Using an autocollimator to align 4f systems, June 2022. Available at: <https://pureportal.strath.ac.uk/en/publications/using-an-autocollimator-to-align-4f-systems>.
- [12] Ryan Corbyn. *Optimising Temperature and Electromagnetic sensing using Nanodiamonds and Fluorescence Microscopy*. Phd thesis, University of Strathclyde, 2023. Available at: <https://stax.strath.ac.uk/concern/theses/ft848r215?locale=fr>.
- [13] College of Arts and Sciences Department of Biology. Introduction to c.elegans anatomy, 2014. Accessed on 09 November 2018.
- [14] Jacek Z. Kubiak. *Cell Cycle in Development*. Springer, 2011.
- [15] Jeong-Hoon Hahm, Sunhee Kim, Race DiLoreto, Cheng Shi, Seung-Jae V. Lee, Coleen T. Murphy, and Hong Gil Nam. C. elegans maximum velocity correlates with healthspan and is maintained in worms with an insulin receptor mutation. *Nature Communications*, 6(1), nov 2015.
- [16] Z.F. Altun and D.H. 2024. Handbook of C. elegans Anatomy. In WormAtlas. Hall. Handbook of c. elegans anatomy. in wormatlas. <http://www.wormatlas.org/hermaphrodite/hermaphroditehomepage.htm>.

Bibliography

- [17] Ann K. Corsi, Bruce Wightman, and Martin Chalfie. A transparent window into biology: A primer on *Caenorhabditis elegans*. *WormBook*, pages 1–31, doi/10.1895/wormbook.1.177.1, 2015. <http://www.wormbook.org>.
- [18] Andrew Horsley, Patrick Appel, Janik Wolters, Jocelyn Achard, Alexandre Tallaire, Patrick Maletinsky, and Philipp Treutlein. Microwave device characterization using a widefield diamond microscope. *Physical Review Applied*, 10(4):044039.
- [19] S. C. Scholten, A. J. Healey, I. O. Robertson, G. J. Abrahams, D. A. Broadway, and J.-P. Tetienne. Widefield quantum microscopy with nitrogen-vacancy centers in diamond: Strengths, limitations, and prospects. *Journal of Applied Physics*, 130(15):150902.
- [20] Wesley Wei-Wen Hsiao, Yuen Yung Hui, Pei-Chang Tsai, and Huan-Cheng Chang. Fluorescent nanodiamond: A versatile tool for long-term cell tracking, super-resolution imaging, and nanoscale temperature sensing. *Accounts of Chemical Research*, 49(3):400–407.
- [21] Long-Jyun Su, Meng-Shiue Wu, Yuen Yung Hui, Be-Ming Chang, Lei Pan, Pei-Chen Hsu, Yit-Tsong Chen, Hong-Nerng Ho, Yen-Hua Huang, Thai-Yen Ling, Hsao-Hsun Hsu, and Huan-Cheng Chang. Fluorescent nanodiamonds enable quantitative tracking of human mesenchymal stem cells in miniature pigs. *Scientific Reports*, 7(1):45607.
- [22] Sandra Claveau, Jean-Rémi Bertrand, and François Treussart. Fluorescent nanodiamond applications for cellular process sensing and cell tracking. *Micromachines*, 9(5):247.
- [23] Graeme E. Johnstone, Gemma S. Cairns, and Brian R. Patton. Nanodiamonds enable adaptive-optics enhanced, super-resolution, twophoton excitation microscopy. *Royal Society Open Science*, 6, 7 2019.
- [24] Kubitscheck Ulrich. *Fluorescence Microscopy From Principles to Biological Applications*. Wiley-VCH, Boschstr. 12, 69469 Weinheim, Germany, 2017.

Bibliography

- [25] Valérie Pineau Noël, Shadi Masoumi, Elahe Parham, Gabriel Genest, Ludovick Bégin, Marc-André Vigneault, and Daniel C. Côté. Tools and tutorial on practical ray tracing for microscopy. *Neurophotonics*, 8, 1 2021.
- [26] Daniel Côté. Dcc-lab-raytracing. Last accessed 28 February 2024.
- [27] Tatiana Latychevskaia. Lateral and axial resolution criteria in incoherent and coherent optics and holography, near- and far-field regimes. 2019.
- [28] Martin Weigert, Kaushikaram Subramanian, Sebastian T. Bundschuh, Eugene W. Myers, and Moritz Kreysing. Biobeam—multiplexed wave-optical simulations of light-sheet microscopy. *PLOS Computational Biology*, 14(4):e1006079.
- [29] Brian J. Thompson. *Fundamentals OF Light Microscopy and Eelectronic Imaging*. Taylor Francis Group, LLC, Third Avenue, New York, NY 10158-0012, 2006.
- [30] Garbellotto Chiara. *A versatile light-sheet microscope, platform for advanced 3D fluorescence imaging and research*. Phd thesis, University of Glasgow, 2021. Available at <https://theses.gla.ac.uk/82429/>.
- [31] Evgenii Glushkov, Vytautas Navikas, and Aleksandra Radenovic. Fluorescent nanodiamonds as versatile intracellular temperature sensors. *CHIMIA International Journal for Chemistry*, 73(1):73–77, feb 2019.
- [32] Sarath Raman Nair, Lachlan J. Rogers, Xavier Vidal, Reece P. Roberts, Hiroshi Abe, Takeshi Ohshima, Takashi Yatsui, Andrew D. Greentree, Jan Jeske, and Thomas Volz. Amplification by stimulated emission of nitrogen-vacancy centres in a diamond-loaded fibre cavity. *Nanophotonics*, 9(15):4505–4518.
- [33] Ankit Rohatgi. Webplotdigitizer: Version 4.6, 2022.
- [34] Shu-Jung Yu, Ming-Wei Kang, Huan-Cheng Chang, Kuan-Ming Chen, and Yueh-Chung Yu. Bright fluorescent nanodiamonds: No photobleaching and low cytotoxicity. *Journal of the American Chemical Society*, 127(50):17604–17605, dec 2005.

Bibliography

- [35] Jana M. Say, Carlo Bradac, Torsten Gaebel, James R. Rabeau, and Louise J. Brown. Processing 15-nm nanodiamonds containing nitrogen-vacancy centres for single-molecule FRET. *Australian Journal of Chemistry*, 65(5):496.
- [36] A. Gruber, A. Dräbenstedt, C. Tietz, L. Fleury, J. Wrachtrup, and C. Von Borczyskowski. Scanning confocal optical microscopy and magnetic resonance on single defect centers. *Science*, 276(5321):2012–2014.
- [37] Nitin Mohan, Chao-Sheng Chen, Hsiao-Han Hsieh, Yi-Chun Wu, and Huan-Cheng Chang. In vivo imaging and toxicity assessments of fluorescent nanodiamonds in *Caenorhabditis elegans*. *Nano Letters*, 10(9):3692–3699, sep 2010.
- [38] Vadym N. Mochalin, Olga Shenderova, Dean Ho, and Yury Gogotsi. The properties and applications of nanodiamonds. *Nature Nanotechnology*, 7(1):11–23, dec 2011.
- [39] Nathan C Shaner, Robert E Campbell, Paul A Steinbach, Ben N G Giepmans, Amy E Palmer, and Roger Y Tsien. Improved monomeric red, orange and yellow fluorescent proteins derived from *discosoma* sp. red fluorescent protein. *Nature Biotechnology*, 22(12):1567–1572.
- [40] Milton Laikin. *Lens Design*. CPC Press, 6000 Broken Sound Parkway NW, Suite 300, Boca Raton, FL 33487-2742, 2006.
- [41] Keith Morris Suzanne Bell. *An Introduction to MICROSCOPY*. CPC Press, 6000 Broken Sound Parkway NW, Suite 300, Boca Raton, FL 33487-2742, 2010.
- [42] E. G. Rochow T. G. Rochow. *An Introduction to Microscopy by Means of Light, Electrons, X-Rays, or Ultrasound*. PLENUM PRESS' NEW YORK AND LONDON, 227 West 17th Street, New York, N.Y. 10011, 1979.
- [43] Martin J Booth. Adaptive optical microscopy: the ongoing quest for a perfect image. *Light: Science & Applications*, 3(4):e165–e165.

Bibliography

- [44] Martin J Booth. Adaptive optics in microscopy. *Philosophical Transactions of the Royal Society A: Mathematical, Physical and Engineering Sciences*, 365(1861):2829–2843, Sep 2007.
- [45] Kainan Yao, Jianli Wang, Xinyue Liu, and Wei Liu. Closed-loop adaptive optics system with a single liquid crystal spatial light modulator. *Optics Express*, 22(14):17216.
- [46] L Burger, I Litvin, S Ngcobo, and A Forbes. Implementation of a spatial light modulator for intracavity beam shaping. *Journal of Optics*, 17(1):015604.
- [47] Shrilekha Vedhakarishnan, Maria Vinas, Sara Aissati, and Susana Marcos. Vision with spatial light modulator simulating multifocal contact lenses in an adaptive optics system. *Biomedical Optics Express*, 12(5):2859.
- [48] Jerome Mertz, Hari Paudel, and Thomas G. Bifano. Field of view advantage of conjugate adaptive optics in microscopy applications. *Applied Optics*, 54(11):3498.
- [49] Yuanyuan Dai, Jacopo Antonello, and Martin J. Booth. Calibration of a phase-only spatial light modulator for both phase and retardance modulation. *Optics Express*, 27(13):17912.
- [50] Meadowlark Optics. User manual 1920x1152 xy phaser series spatial light modulator with hdmi controller. Available at <https://www.meadowlark.com/1920-1152-spatial-light-modulator-p-119>. Accessed on 07 January 2020.
- [51] Photonics Encyclopedia. Waveplates. Available at <https://www.rp-photonics.com/waveplates.html>. Accessed on 07 January 2020.
- [52] Edmund Optics. Introduction to adaptive optics and deformable mirrors. Available at <https://www.edmundoptics.co.uk/knowledge-center/application-notes/optics/introduction-to-adaptive-optics-and-deformable-mirrors/>. Accessed on 08 January 2020.

Bibliography

- [53] Gagan Raju and Nirmal Mazumder. Digging deeper through biological specimens using adaptive optics-based optical microscopy. *Photonics*, 10(2):178.
- [54] Soongyu Yi, Jin Xiang, Ming Zhou, Zhicheng Wu, Lan Yang, and Zongfu Yu. Angle-based wavefront sensing enabled by the near fields of flat optics. *Nature Communications*, 12(1):6002.
- [55] Bohumil Stoklasa, Libor Motka, Jaroslav Rehacek, Zdenek Hradil, and Luis Lorenzo Sánchez-Soto. Wavefront sensing reveals optical coherence. *Nature Communications*, 5(1):3275.
- [56] Santiago Vallmitjana, Antonio Marzoa, Salvador Bosch, and Eva Acosta. Testing two techniques for wavefront analysis. specific applications and comparative study. *Optica Pura y Aplicada*, 50(4):327–335.
- [57] Cerro Tololo. Wave-front sensors. Available at <http://www.ctio.noao.edu/atokovin/tutorial/part3/wfs.html>. Accessed on 09 January 2020.
- [58] Robert K. Tyson. *Topics in Adaptive Optics*. IntechOpen, Rijeka, Jan 2012.
- [59] Andreas Ettinger and Torsten Wittmann. Fluorescence live cell imaging. In *Methods in Cell Biology*, volume 123, pages 77–94. Elsevier.
- [60] Han-Yuan Lin, Li-An Chu, Hsuan Yang, Kuo-Jen Hsu, Yen-Yin Lin, Keng-Hui Lin, Shi-Wei Chu, and Ann-Shyn Chiang. Imaging through the whole brain of drosophila at $\lambda/20$ super-resolution. *iScience*, 14:164–170.
- [61] Cheng Huang, Jessica R. Maxey, Supriyo Sinha, Joan Savall, Yiyang Gong, and Mark J. Schnitzer. Long-term optical brain imaging in live adult fruit flies. *Nature Communications*, 9(1):872.
- [62] Laura Breimann, Friedrich Preusser, and Stephan Preibisch. Light-microscopy methods in *c. elegans* research. *Current Opinion in Systems Biology*, 13:82–92.
- [63] Phototoxicity revisited. *Nature Methods*, 15:751, Oct 2018.

Bibliography

- [64] Jaroslav Icha, Michael Weber, Jennifer C. Waters, and Caren Norden. Phototoxicity in live fluorescence microscopy, and how to avoid it. *BioEssays*, 39, 8 2017.
- [65] Nikon MicroscopyU. Fluorophore photobleaching literature references. Accessed on 01 November 2022.
- [66] Christian A. Combs. Fluorescence microscopy: A concise guide to current imaging methods. *Current Protocols in Neuroscience*, 50(1).
- [67] Omar E. Olarte, Jordi Andilla, Emilio J. Gualda, and Pablo Loza-Alvarez. Light-sheet microscopy: a tutorial. *Advances in Optics and Photonics*, 10(1):111, jan 2018.
- [68] Adam K. Glaser, Ye Chen, Chengbo Yin, Linpeng Wei, Lindsey A. Barner, Nicholas P. Reder, and Jonathan T. C. Liu. Multidirectional digital scanned light-sheet microscopy enables uniform fluorescence excitation and contrast-enhanced imaging. *Scientific Reports*, 8(1):13878.
- [69] Yicong Wu, Peter Wawrzusin, Justin Senseney, Robert S Fischer, Ryan Christensen, Anthony Santella, Andrew G York, Peter W Winter, Clare M Waterman, Zhirong Bao, Daniel A Colón-Ramos, Matthew McAuliffe, and Hari Shroff. Spatially isotropic four-dimensional imaging with dual-view plane illumination microscopy. *Nature Biotechnology*, 31(11):1032–1038, November 2013.
- [70] Michael Weber and Jan Huisken. Light sheet microscopy for real-time developmental biology. *Current Opinion in Genetics and Development*, 21:566–572, 10 2011.
- [71] Youngbum Kim, Eun Ji Lee, Shrawan Roy, Anir S. Sharbirin, Lars Gunnar Ranz, Thomas Dieing, and Jeongyong Kim. Measurement of lateral and axial resolution of confocal raman microscope using dispersed carbon nanotubes and suspended graphene. *Current Applied Physics*, 20:71–77, 1 2020.

Bibliography

- [72] Jan Huisken, Jim Swoger, Filippo Del Bene, Joachim Wittbrodt, and Ernst H. K. Stelzer. Optical sectioning deep inside live embryos by selective plane illumination microscopy. *Science*, 305(5686):1007–1009, aug 2004.
- [73] Jaroslav Icha, Michael Weber, Jennifer C. Waters, and Caren Norden. Phototoxicity in live fluorescence microscopy, and how to avoid it. *BioEssays*, 39(8):1700003.
- [74] Jan Huisken and Didier Y. R. Stainier. Even fluorescence excitation by multidirectional selective plane illumination microscopy (mspim). *Opt. Lett.*, 32(17):2608–2610, Sep 2007.
- [75] Rory M. Power and Jan Huisken. Adaptable, illumination patterning light sheet microscopy. *Scientific Reports*, 8(1):9615.
- [76] Yan Fu, Haifeng Wang, Riyi Shi, and Ji-Xin Cheng. Characterization of photodamage in coherent anti-stokes raman scattering microscopy. *Optics Express*, 14(9):3942.
- [77] Hosein Kafian, Sina Mozaffari-Jovin, Mohammad Bagheri, and Seyed Ali Mousavi Shaegh. Light-sheet fluorescent microscopy: fundamentals, developments and applications. *Physica Scripta*, 98(8):082001.
- [78] Philipp J. Keller, Annette D. Schmidt, Joachim Wittbrodt, and Ernst H.K. Stelzer. Reconstruction of zebrafish early embryonic development by scanned light sheet microscopy. *Science*, 322(5904):1065–1069, oct 2008.
- [79] Philipp J Keller, Annette D Schmidt, Anthony Santella, Khaled Khairy, Zhirong Bao, Joachim Wittbrodt, and Ernst H K Stelzer. Fast, high-contrast imaging of animal development with scanned light sheet-based structured-illumination microscopy. *Nature Methods*, 7(8):637–642, jul 2010.
- [80] Matteo Bernardello, Emilio J. Gualda, and Pablo Loza-Alvarez. Modular multi-modal platform for classical and high throughput light sheet microscopy. *Scientific Reports*, 12(1):1969.

Bibliography

- [81] John M. Girkin and Mariana T. Carvalho. The light-sheet microscopy revolution. *Journal of Optics (United Kingdom)*, 20, 5 2018.
- [82] Ernst H. K. Stelzer, Frederic Strobl, Bo-Jui Chang, Friedrich Preusser, Stephan Preibisch, Katie McDole, and Reto Fiolka. Light sheet fluorescence microscopy. *Nature Reviews Methods Primers*, 1(1):73.
- [83] John Lim, Hwee Kuan Lee, Weimiao Yu, and Sohail Ahmed. Light sheet fluorescence microscopy (lsfm): Past, present and future. *Analyst*, 139:4758–4768, 8 2014.
- [84] Florian O. Fahrbach, Fabian F. Voigt, Benjamin Schmid, Fritjof Helmchen, and Jan Huiskens. Rapid 3d light-sheet microscopy with a tunable lens. *Opt. Express*, 21(18):21010–21026, Sep 2013.
- [85] Michaela Mickoleit, Benjamin Schmid, Michael Weber, Florian O Fahrbach, Sonja Hombach, Sven Reischauer, and Jan Huiskens. High-resolution reconstruction of the beating zebrafish heart. *Nature Methods*, 11(9):919–922, jul 2014.
- [86] Florian O. Fahrbach, Fabian F. Voigt, Benjamin Schmid, Fritjof Helmchen, and Jan Huiskens. Rapid 3d light-sheet microscopy with a tunable lens. *Optics Express*, 21(18):21010.
- [87] Quirin S, Vladimirov N., Yang C-T, D. Peterka, R. Yueste, and M. Ahrens. Calcium imaging of neural circuits with extended depth-of-field light-sheet microscopy. *Optics letters*, 41:855–858, March 2016.
- [88] Omar E. Olarte, Jordi Andilla, David Artigas, and Pablo Loza-Alvarez. Decoupled illumination detection in light sheet microscopy for fast volumetric imaging. *Optica*, 2(8):702, aug 2015.
- [89] Brian R. Patton, Daniel Burke, David Oswald, Travis J. Gould, Joerg Bewersdorf, and Martin J. Booth. Three-dimensional sted microscopy of aberrating tissue using dual adaptive optics. *Optics Express*, 24:8862, 4 2016.

Bibliography

- [90] Dean Wilding, Paolo Pozzi, Oleg Soloviev, Gleb Vdovin, and Michel Verhaegen. Light-sheet optimization for microscopy. In Thomas G. Bifano, Joel Kubby, and Sylvain Gigan, editors, *Adaptive Optics and Wavefront Control for Biological Systems II*. SPIE, mar 2016.
- [91] Cyril Bourgenot, Christopher D. Saunter, Jonathan M. Taylor, John M. Girkin, and Gordon D. Love. 3d adaptive optics in a light sheet microscope. *Optics Express*, 20(12):13252.
- [92] Dean Wilding, Paolo Pozzi, Oleg Soloviev, Gleb Vdovin, and Michel Verhaegen. Adaptive illumination based on direct wavefront sensing in a light-sheet fluorescence microscope. *Optics Express*, 24(22):24896, oct 2016.
- [93] Loïc A Royer, William C Lemon, Raghav K Chhetri, Yinan Wan, Michael Coleman, Eugene W Myers, and Philipp J Keller. Adaptive light-sheet microscopy for long-term, high-resolution imaging in living organisms. *Nature Biotechnology*, 34(12):1267–1278, oct 2016.
- [94] Mostafa Aakhte, Ehsan A. Akhlaghi, and H.-Arno J. Müller. SSPIM: a beam shaping toolbox for structured selective plane illumination microscopy. *Scientific Reports*, 8(1), jul 2018.
- [95] Chiara Garbellotto and Jonathan M. Taylor. Multi-purpose SLM-light-sheet microscope. *Biomedical Optics Express*, 9(11):5419, oct 2018.
- [96] Raphael Jorand, Gwénaële Le Corre, Jordi Andilla, Amina Maandhui, Céline Frongia, Valérie Lobjois, Bernard Ducommun, and Corinne Lorenzo. Deep and clear optical imaging of thick inhomogeneous samples. *PLoS ONE*, 7(4):e35795, apr 2012.
- [97] Ashley James Tyler. *The Design and Construction of a Scanning Probe Nitrogen Vacancy Centre Magnetometer*. Phd thesis, University of Nottingham, 2021. Available at <https://eprints.nottingham.ac.uk/66040/>.

Bibliography

- [98] Victor Marcel Acosta. *Optical Magnetometry with Nitrogen-Vacancy Centers in Diamond*. Phd thesis, University of Nottingham, 2011. Available at <https://eprints.nottingham.ac.uk/66040/>.
- [99] Daniel Riedel. *Engineering of the photonic environment of single nitrogen-vacancy centers in diamond*. Phd thesis, Uni Basel, 2017. <http://edoc.unibas.ch>.
- [100] Zaroni Andrea Marchese Chiara. Nitrogen vacancy center defects in diamond sensor characterization and magnetic field imaging, 2018. Available at <https://www.politesi.polimi.it/handle/10589/144251>.
- [101] Jelle Storteboom, Philip Dolan, Stefania Castelletto, Xiangping Li, and Min Gu. Lifetime investigation of single nitrogen vacancy centres in nanodiamonds. *Optics Express*, 23(9):11327.
- [102] Romana Schirhagl, Kevin Chang, Michael Loretz, and Christian L. Degen. Nitrogen-vacancy centers in diamond: Nanoscale sensors for physics and biology. *Annual Review of Physical Chemistry*, 65:83–105, 2014.
- [103] Saravanan Sengottuvel, Mariusz Mrózek, Mirosław Sawczak, Maciej J. Głowacki, Mateusz Ficek, Wojciech Gawlik, and Adam M. Wojciechowski. Wide-field magnetometry using nitrogen-vacancy color centers with randomly oriented microdiamonds. *Scientific Reports*, 12, 12 2022.
- [104] David Kordahl, Lance W.Q. Xu, Shery L.Y. Chang, and Christian Dwyer. Prospects for detecting individual defect centers using spatially resolved electron energy loss spectroscopy. *Physical Review B*, 100, 10 2019.
- [105] Matthew E. Trusheim and Dirk Englund. Wide-field strain imaging with preferentially aligned nitrogen-vacancy centers in polycrystalline diamond. *New Journal of Physics*, 18, 12 2016.
- [106] Yushi Nishimura, Keisuke Oshimi, Yumi Umehara, Yuka Kumon, Kazu Miyaji, Hiroshi Yukawa, Yutaka Shikano, Tsutomu Matsubara, Masazumi Fujiwara, Yoshinobu Baba, and Yoshio Teki. Wide-field fluorescent nanodiamond spin

Bibliography

- measurements toward real-time large-area intracellular thermometry. *Scientific Reports*, 11, 12 2021.
- [107] Shinichi Hayashi and Yasushi Okada. Ultrafast superresolution fluorescence imaging with spinning disk confocal microscope optics. *Molecular Biology of the Cell*, 26(9):1743–1751.
- [108] John Oreopoulos, Richard Berman, and Mark Browne. Spinning-disk confocal microscopy. In *Methods in Cell Biology*, volume 123, pages 153–175. Elsevier.
- [109] Yufeng Gao, Lina Liu, Yixuan Yin, Jiuling Liao, Jia Yu, Ting Wu, Shiwei Ye, Hui Li, and Wei Zheng. Adaptive optics via pupil ring segmentation improves spherical aberration correction for two-photon imaging of optically cleared tissues. *Optics Express*, 28(23):34935.
- [110] Na Ji, Takashi R. Sato, and Eric Betzig. Characterization and adaptive optical correction of aberrations during in vivo imaging in the mouse cortex. *Proceedings of the National Academy of Sciences*, 109(1):22–27.
- [111] Aurore Masson, Paul Escande, Céline Frongia, Grégory Clouvel, Bernard Ducommun, and Corinne Lorenzo. High-resolution in-depth imaging of optically cleared thick samples using an adaptive SPIM. *Scientific Reports*, 5(1):16898.
- [112] Xiaodong Tao, Bautista Fernandez, Oscar Azucena, Min Fu, Denise Garcia, Yi Zuo, Diana C. Chen, and Joel Kubby. Adaptive optics confocal microscopy using direct wavefront sensing. *Opt. Lett.*, 36(7):1062–1064, Apr 2011.
- [113] Maxime Malivert, Fabrice Harms, Cynthia Veilly, Jerome Legrand, Ziqiang Li, Emmanuelle Bayer, Daniel Choquet, and Mathieu Ducros. Active image optimization for lattice light sheet microscopy in thick samples. *Biomedical Optics Express*, 13(12):6211.
- [114] Zheng Wang, Jintao Zhang, Xiaojuan Feng, and Li Xing. Microwave Heating Effect on Diamond Samples of Nitrogen-Vacancy Centers. *ACS Omega*, 7(35):31538–31543, September 2022.

Bibliography

- [115] Zhen Xian Fan, Li Xing, Fei Xiang Wu, Xiao Juan Feng, and Jin Tao Zhang. Microwave Field Characteristics of Nitrogen-Vacancy Centers in Diamond for Living Cell Temperature Measurement. preprint, Engineering, December 2023.
- [116] Hossein Babashah, Hoda Shirzad, Elena Losero, Valentin Goblot, Christophe Galland, and Mayeul Chipaux. Optically detected magnetic resonance with an open source platform. *SciPost Physics Core*, 6(4):065, October 2023.
- [117] Soya Saijo, Yuichiro Matsuzaki, Shiro Saito, Ikuya Hanano, Hideyuki Watanabe, Norikazu Mizuochi, and Junko Ishi-Hayase. AC Magnetic Field Sensing Using Continuous-Wave Optically Detected Magnetic Resonance of Nitrogen Vacancy Centers in Diamond, January 2018. arXiv:1801.05865 [quant-ph].
- [118] H. Tabuchi, Y. Matsuzaki, N. Furuya, Y. Nakano, H. Watanabe, N. Tokuda, N. Mizuochi, and J. Ishi-Hayase. Temperature Sensing with RF-Dressed States of Nitrogen-Vacancy Centers in Diamond. *Journal of Applied Physics*, 133(2):024401, January 2023. arXiv:2205.06976 [quant-ph].
- [119] J. Van Krugten, K.-K.H. Taris, and Erwin J.G. Peterman. Imaging adult *C. elegans* live using light-sheet microscopy. *Journal of Microscopy*, 281(3):214–223.
- [120] Jayson J. Smith, Isabel W. Kenny, Carsten Wolff, Rachel Cray, Abhishek Kumar, David R. Sherwood, and David Q. Matus. A light sheet fluorescence microscopy protocol for caenorhabditis elegans larvae and adults. *Frontiers in Cell and Developmental Biology*, 10:1012820.
- [121] Steven Ruzin. Digital imaging for biologists - capturing images. Available at <http://microscopy.berkeley.edu/courses/dib/sections/02Images/sampling.html>. Accessed on 11 August 2020.
- [122] Alexander Franzen. Componentlibrary - a vector graphics library for illustrations of optics experiments. Available at <https://www.gwoptics.org/ComponentLibrary/>. Accessed 28 February 2024.

Bibliography

- [123] Trimble. Sketchup. Available at <https://www.sketchup.com/>. Accessed on 28 February 2024.
- [124] Jan M. Binder, Alexander Stark, Nikolas Tomek, Jochen Scheuer, Florian Frank, Kay D. Jahnke, Christoph Müller, Simon Schmitt, Mathias H. Metsch, Thomas Uden, Tobias Gehring, Alexander Huck, Ulrik L. Andersen, Lachlan J. Rogers, and Fedor Jelezko. Qudi: A modular python suite for experiment control and data processing. *SoftwareX*, 6:85–90, 2017.
- [125] Nico Stuurman, N. Amodaj, and R.D. Vale. Micro-manager: Open source software for light microscope imaging. *Microscopy Today*, 15:42–43, 05 2007.
- [126] Antonello Jacopo. slmtools, 2020. Available at <https://github.com/jacopoantonello/slmtools>.
- [127] Jan Schniete, Aimee Franssen, John Dempster, Trevor J Bushell, William Bradshaw Amos, and Gail McConnell. Fast optical sectioning for widefield fluorescence mesoscopy with the mesolens based on HiLo microscopy. *Scientific Reports*, 8(1), nov 2018.
- [128] Eliana Battistella, Jan Schniete, Katrina Wesenraft, Juan Quintana, and Gail McConnell. Title: Light-sheet mesoscopy with the mesolens provides fast sub-cellular resolution imaging throughout large tissue volumes.
- [129] Hans-Ulrich Dodt, Ulrich Leischner, Anja Schierloh, Nina Jährling, Christoph Peter Mauch, Katrin Deininger, Jan Michael Deussing, Matthias Eder, Walter Zieglgänsberger, and Klaus Becker. Ultramicroscopy: three-dimensional visualization of neuronal networks in the whole mouse brain. *Nature Methods*, 4(4):331–336.
- [130] Stephan Daetwyler and Reto Paul Fiolka. Light-sheets and smart microscopy, an exciting future is dawning. *Communications Biology*, 6(1):502.

Bibliography

- [131] Eugene Frumker and Yaron Silberberg. Phase and amplitude pulse shaping with two-dimensional phase-only spatial light modulators. *Journal of the Optical Society of America B*, 24(12):2940.
- [132] Meadowlark Optics. *User Manual 1920x1152 XY Phase Series Spatial Light Modulator With PCIe Controller*. Meadowlark Optics, Inc., 5964 Iris Parkway, Frederick, CO 80530, USA.
- [133] Meadowlark Optics. *User Manual 1920x1152 XY Phase Series Spatial Light Modulator With HDMI Controller*. Meadowlark Optics, Inc., 5964 Iris Parkway, Frederick, CO 80530, USA.
- [134] Vasudevan Lakshminarayanan and Andre Fleck. Zernike polynomials: A guide. *Journal of Modern Optics*, 58:545–561, 4 2011.
- [135] Daniel Burke, Brian Patton, Fang Huang, Joerg Bewersdorf, and Martin J. Booth. Adaptive optics correction of specimen-induced aberrations in single-molecule switching microscopy. *Optica*, 2:177, 2 2015.
- [136] Hossein Hassani, Mansoureh Ghodsi, and Gareth Howell. A note on standard deviation and standard error. *Teaching Mathematics and its Applications*, 29:108–112, 3 2010.
- [137] Theresa Stiernagle. Maintenance of *C. elegans*. *WormBook : the online review of C. elegans biology*, pages 1–11, 2006.
- [138] Thermo Fisher. Preparation e.coli culture glycerol stocks. *Thermo Scientific - Part of Thermo Fisher Scientific*, 2012.
- [139] University of Minnesota. Caenorhabditis genetics center. Available at <https://cgc.umn.edu/strains?vt=all/>. Accessed on 10 October 2023.
- [140] FPBase. Tagrfp. Available at <https://www.fpbases.org/protein/tagrfp/>. Accessed on 10 October 2023.
- [141] FPBase. mcherry. Available at: <https://www.fpbases.org/protein/mcherry/>. Accessed on 10 October 2023.

Bibliography

- [142] Timothy Walston and Jeff Hardin. An agar mount for observation of *Caenorhabditis elegans* embryos. *Cold Spring Harbor Protocols*, 2010(12):pdb.prot5540.
- [143] Chun Hao Chen and Chun Liang Pan. Live-cell imaging of pvd dendritic growth cone in post-embryonic *c. elegans*. *STAR Protocols*, 2, 6 2021.
- [144] Victor Escrich, Begoña Ezcurra, Eva Gómez-Orte, Cristina Romero-Aranda, Antonio Miranda-Vizueté, and Juan Cabello. 4d microscopy: Unraveling *caenorhabditis elegans* embryonic development using nomarski microscopy. *Journal of Visualized Experiments*, 2020:1–14, 10 2020.
- [145] Mengting Li, Qihang Song, Yinghao Xiao, Junnan Wu, Weibing Kuang, Yingjun Zhang, and Zhen-Li Huang. Luckyprofiler: an imagej plug-in capable of quantifying fwhm resolution easily and effectively for super-resolution images. *Biomedical Optics Express*, 13:4310, 8 2022.
- [146] Venkatakaushik Voleti, Kripa B. Patel, Wenze Li, Citlali Perez Campos, Srinidhi Bharadwaj, Hang Yu, Caitlin Ford, Malte J. Casper, Richard Wenwei Yan, Wenxuan Liang, Chentao Wen, Koutarou D. Kimura, Kimara L. Targoff, and Elizabeth M.C. Hillman. Real-time volumetric microscopy of in vivo dynamics and large-scale samples with scape 2.0. *Nature Methods*, 16:1054–1062, 10 2019.
- [147] Adrian Negrean and Huibert D. Mansvelder. Optimal lens design and use in laser-scanning microscopy. *Biomedical Optics Express*, 5(5):1588.
- [148] Adrian Negrean and Huibert D. Mansvelder. Optimal lens design and use in laser-scanning microscopy. *Biomedical Optics Express*, 5:1588, 5 2014.
- [149] Milton Laikin. *Lens Design*. CPC Press, 6000 Broken Sound Parkway NW, Suite 300, Boca Raton, FL 33487-2742, 2006.
- [150] Matthias Rieckher, Ilias Kyparissidis-Kokkinidis, Athanasios Zacharopoulos, Georgios Kourmoulakis, Nektarios Tavernarakis, Jorge Ripoll, and Giannis Zacharakis. A customized light sheet microscope to measure spatio-temporal protein dynamics in small model organisms. *PLOS ONE*, 10(5):e0127869.

Bibliography

- [151] Alison R Frand, Sascha Russel, and Gary Ruvkun. Functional genomic analysis of *c. elegans* molting. *PLoS Biology*, 3(10):e312.
- [152] Dominic J. Hare, Michael W. M. Jones, Verena C. Wimmer, Nicole L. Jenkins, Martin D. De Jonge, Ashley I. Bush, and Gawain McColl. High-resolution complementary chemical imaging of bio-elements in *Caenorhabditis elegans*. *Metallomics*, 8(2):156–160.
- [153] Sherry G. Clendenon, Pamela A. Young, Michael Ferkowicz, Carrie Phillips, and Kenneth W. Dunn. Deep tissue fluorescent imaging in scattering specimens using confocal microscopy. *Microscopy and Microanalysis*, 17:614–617, 8 2011.
- [154] Aljaž Kavčič, Maja Garvas, Matevž Marinčič, Katrin Unger, Anna Maria Coclite, Boris Majaron, and Matjaž Humar. Deep tissue localization and sensing using optical microcavity probes. *Nature Communications*, 13, 12 2022.
- [155] Enrico F. Semeraro, Lisa Marx, Johannes Mandl, Moritz P. K. Frewein, Haden L. Scott, Sylvain Prévost, Helmut Bergler, Karl Lohner, and Georg Pabst. Evolution of the analytical scattering model of live *Escherichia coli*. *Journal of Applied Crystallography*, 54(2):473–485.
- [156] Volodymyr Nikolenko, Darcy S. Peterka, Roberto Araya, Alan Woodruff, and Rafael Yuste. Spatial light modulator microscopy. *Cold Spring Harbor Protocols*, 2013(12):pdb.top079517.
- [157] S. Fineschi, G. Naletto, M. Romoli, V. Da Deppo, E. Antonucci, D. Moses, A.M. Malvezzi, G. Nicolini, D. Spadaro, L. Teriaca, V. Andretta, G. Capobianco, G. Crescenzo, M. Focardi, F. Frassetto, F. Landini, G. Massone, R. Melich, P. Nicolosi, M. Pancrazzi, M.G. Pelizzo, L. Poletto, U. Schühle, M. Uslenghi, S. Vives, S.K. Solanki, P. Heinzl, A. Berlicki, S. Cesare, D. Morea, S. Mottini, P. Sandri, A. Alvarez-Herrero, and M. Castronuovo. Optical design of the multi-wavelength imaging coronagraph metis for the solar orbiter mission. *Experimental Astronomy*, 49(3):239–263.

Bibliography

- [158] Yang Liu, Bingxi Liu, John Green, Carly Duffy, Ming Song, James D. Lauderdale, and Peter Kner. Volumetric light sheet imaging with adaptive optics correction. *Biomedical Optics Express*, 14(4):1757.
- [159] Yee Lian Chew, Xiaochen Fan, Jürgen Götz, and Hannah R. Nicholas. Aging in the nervous system of *Caenorhabditis elegans*. *Communicative & Integrative Biology*, 6(5):e25288.
- [160] Claire Bernardin Souibgui, Anthony Zoropogui, Jeremy Voisin, Sebastien Ribun, Valentin Vasselon, Petar Pujic, Veronica Rodriguez-Nava, Patrick Belly, Benoit Cournoyer, and Didier Blaha. Virulence test using nematodes to prescreen *Nocardia* species capable of inducing neurodegeneration and behavioral disorders. *PeerJ*, 5:e3823.
- [161] Shamala Ravikumar, R Surekha, and Rooban Thavarajah. Mounting media: An overview. *Journal of Dr. NTR University of Health Sciences*, 3(5):1.
- [162] Hannah L. Stern, Qiushi Gu, John Jarman, Simone Eizagirre Barker, Noah Mendelson, Dipankar Chugh, Sam Schott, Hoe H. Tan, Henning Sirringhaus, Igor Aharonovich, and Mete Atatüre. Room-temperature optically detected magnetic resonance of single defects in hexagonal boron nitride. *Nature Communications*, 13(1):618, February 2022.
- [163] Zachary R. Jones, Nicholas J. Niemuth, Margaret E. Robinson, Olga A. Shenderova, Rebecca D. Klaper, and Robert J. Hamers. Selective imaging of diamond nanoparticles within complex matrices using magnetically induced fluorescence contrast. *Environmental Science: Nano*, 7(2):525–534.
- [164] Yushi Nishimura, Keisuke Oshimi, Yumi Umehara, Yuka Kumon, Kazu Miyaji, Hiroshi Yukawa, Yutaka Shikano, Tsutomu Matsubara, Masazumi Fujiwara, Yoshinobu Baba, and Yoshio Teki. Wide-field fluorescent nanodiamond spin measurements toward real-time large-area intracellular thermometry. *Scientific Reports*, 11(1):4248, February 2021.

Bibliography

- [165] Haimei Zhang, Carina Belvin, Wanyi Li, Jennifer Wang, Julia Wainwright, Robbie Berg, and Joshua Bridger. Little bits of diamond: Optically detected magnetic resonance of nitrogen-vacancy centers. *American Journal of Physics*, 86(3):225–236.
- [166] Saravanan Sengottuvel, Mariusz Mrózek, Mirosław Sawczak, Maciej J. Głowacki, Mateusz Ficek, Wojciech Gawlik, and Adam M. Wojciechowski. Wide-field magnetometry using nitrogen-vacancy color centers with randomly oriented micro-diamonds. *Scientific Reports*, 12(1):17997.
- [167] K. Jensen, V. M. Acosta, A. Jarmola, and D. Budker. Light narrowing of magnetic resonances in ensembles of nitrogen-vacancy centers in diamond. *Physical Review B*, 87(1):014115.
- [168] Tobias Meinert and Alexander Rohrbach. Light-sheet microscopy with length-adaptive Bessel beams. *Biomedical Optics Express*, 10(2):670.
- [169] Tom Vettenburg, Heather I C Dalgarno, Jonathan Nylk, Clara Coll-Lladó, David E K Ferrier, Tomáš Čížmár, Frank J Gunn-Moore, and Kishan Dholakia. Light-sheet microscopy using an airy beam. *Nature Methods*, 11(5):541–544.
- [170] Bi-Chang Chen, Wesley R. Legant, Kai Wang, Lin Shao, Daniel E. Milkie, Michael W. Davidson, Chris Janetopoulos, Xufeng S. Wu, John A. Hammer, Zhe Liu, Brian P. English, Yuko Mimori-Kiyosue, Daniel P. Romero, Alex T. Ritter, Jennifer Lippincott-Schwartz, Lillian Fritz-Laylin, R. Dyche Mullins, Diana M. Mitchell, Joshua N. Bembenek, Anne-Cecile Reymann, Ralph Böhme, Stephan W. Grill, Jennifer T. Wang, Geraldine Seydoux, U. Serdar Tulu, Daniel P. Kiehart, and Eric Betzig. Lattice light-sheet microscopy: Imaging molecules to embryos at high spatiotemporal resolution. *Science*, 346(6208):1257998.
- [171] Yanlu Chen, Xiaoliang Li, Dongdong Zhang, Chunhui Wang, Ruili Feng, Xuzhao Li, Yao Wen, Hao Xu, Xinyi Shirley Zhang, Xiao Yang, Yongyi Chen, Yi Feng, Bo Zhou, Bi-Chang Chen, Kai Lei, Shang Cai, Jie-Min Jia, and Liang Gao. A

Bibliography

versatile tiling light sheet microscope for imaging of cleared tissues. *Cell Reports*, 33(5):108349.